



HAL
open science

Ab-Initio Calculations of Many body effects in electronic spectre.

Matteo Gatti

► **To cite this version:**

Matteo Gatti. Ab-Initio Calculations of Many body effects in electronic spectre.. Optics [physics.optics]. Ecole Polytechnique X, 2007. English. NNT : . pastel-00004109

HAL Id: pastel-00004109

<https://pastel.hal.science/pastel-00004109>

Submitted on 22 Jul 2010

HAL is a multi-disciplinary open access archive for the deposit and dissemination of scientific research documents, whether they are published or not. The documents may come from teaching and research institutions in France or abroad, or from public or private research centers.

L'archive ouverte pluridisciplinaire **HAL**, est destinée au dépôt et à la diffusion de documents scientifiques de niveau recherche, publiés ou non, émanant des établissements d'enseignement et de recherche français ou étrangers, des laboratoires publics ou privés.

Correlation effects in valence electron spectroscopy
of transition metal oxides:
many-body perturbation theory
and alternative approaches

Matteo Gatti

La science n'est pas que scientifique
(Edgar Morin, Science avec conscience)

Da chimico un giorno avevo il potere
di sposare gli elementi e di farli reagire,
ma gli uomini mai mi riuscì di capire
perché si combinassero attraverso l'amore.
Affidando ad un gioco la gioia e il dolore.
Guardate il sorriso guardate il colore
come giocan sul viso di chi cerca l'amore.
(Fabrizio de André, Un chimico,
Non al denaro non all'amore né al cielo)

Moi, se dit le petit prince,
si j'avais cinquante-trois minutes à dépenser,
je marcherais tout doucement vers une fontaine...
(Antoine de Saint-Exupéry, Le petit prince)

Contents

Preface	ix
1 Introduction	1
1.1 The many-body problem	1
1.2 Spectroscopies	7
1.2.1 Photoemission	8
1.2.2 Absorption and electron energy loss	13
1.3 Beyond the independent-particle picture	16
1.3.1 From Hartree-Fock to dynamical quasiparticles	16
1.3.2 From Wigner and Mott to strong correlations	20
2 Ground-state properties	27
2.1 The variational principle	27
2.2 Density-functional theory	30
2.2.1 The Kohn-Sham system	32
2.2.2 Approximations of the exchange-correlation potential	34
2.2.3 Optimized effective potential method	36
2.2.4 DFT in practice	38
3 One-particle excitations	41
3.1 The Green's function	41
3.2 Hedin's equations and the GW approximation	45
3.3 GW in practice	51
3.3.1 Calculations in the quasiparticle framework	51
3.3.2 Dynamical screening and the frequency integration	54
3.3.3 Core-valence interaction	56
3.4 Self-consistent quasiparticle calculations	57
3.5 The COHSEX approximation	59
3.5.1 Self-consistent COHSEX in practice	62
4 Models for strongly correlated systems	67
4.1 LDA+U	67
4.1.1 What is U ? A GW perspective	70
4.2 Dynamical mean-field theory	72

4.2.1	DMFT for the Hubbard model	72
4.2.2	DMFT for electronic structure calculations (LDA + DMFT)	76
4.3	Spectral density-functional theory	78
5	Neutral excitations	83
5.1	Linear response	84
5.2	Microscopic-macroscopic connection	86
5.3	The Bethe-Salpeter equation	90
5.3.1	BSE in practice	92
5.4	Time-dependent density-functional theory	95
5.4.1	A kernel from many-body perturbation theory	98
5.5	Time-dependent current-density-functional theory	102
6	Vanadium dioxide	105
6.1	The phase transition	106
6.2	Peierls or Mott-Hubbard?	110
6.3	Measurements of the electronic properties	112
6.3.1	Valence states	112
6.3.2	Conduction states	115
6.4	LDA ground-state calculations	116
6.4.1	Pseudopotential generation	116
6.4.2	Ground-state atomic structures	119
6.4.3	Kohn-Sham eigenvalues	121
6.4.4	LDA validation of the molecular orbital picture	124
6.5	Standard GW calculations	125
6.6	Self-consistent quasiparticle calculations	133
6.7	Comparison with experiments and previous results	141
6.7.1	X-ray absorption spectra	146
6.8	Calculation of electron energy-loss spectra	148
6.8.1	Methodological issues	148
6.8.2	The satellite in the photoemission spectrum of the metal	152
7	Effective potentials and kernels for spectroscopy	159
7.1	Generalization of the Sham-Schlüter equation	160
7.2	The photoemission potential	164
7.3	Transforming nonlocality into frequency dependence	166
7.3.1	A scissor operator in a two-level system	167
7.3.2	Screened exchange in homogeneous electron gas	173
7.4	Spectral density-functional theory	178
7.5	Density-matrix functional theory	179
7.6	Time-dependent density-functional theory	180
7.6.1	The absorption kernel	182
7.7	Time-dependent current-density-functional theory	184

8	Conclusions	189
A	Derivation of some equations in MBPT	193
A.1	Equation of motion of the Green's function	193
A.2	Schwinger's functional derivative	195
A.3	The Dyson equation	196
A.4	Derivative of the identity	197
A.5	Hedin's equations	197
A.6	How to get a two-point Bethe-Salpeter equation?	199
B	Density functional in the Dyson equation	201
C	Integral equations	203
C.1	Linearization of the generalized Sham-Schlüter equation	204
C.2	Screened-exchange self-energy in HEG	206
	List of Publications	209
	Bibliography	211
	List of Figures	231
	Notations and units	235

Preface

Theoretical spectroscopy [1] has become one of the most active research field in condensed-matter physics. In spectroscopic measurements an electronic system is excited by means of an external perturbation and its subsequent response is measured. These measurements give access to a great deal of information about the properties of the system. The calculation of the electronic excitations [2] is hence a very powerful tool to study the properties of the materials. On the one hand, it permits to provide an interpretation of the experimental spectra and organize the information one can extract from the experimental measurements. On the other hand, when experimental results are still missing, reliable theoretical simulations allow one to formulate predictions about the electronic and optical properties of new materials. For this reason it is essential to adopt parameter-free approaches that can be used as a “theoretical microscope” to understand the physical properties of the materials.

In particular, in this thesis I will deal mostly with photoemission spectroscopy. In a photoemission experiment a photon is absorbed by a sample and an electron is emitted. By measuring the kinetic energy of the electron, one has access to the electronic properties of the system. If the electrons in the sample were independent particles, the emitted electron would give rise just to a delta peak in the experimental spectrum, in correspondence to the one-particle energy level it was occupying in the system. Instead, structures displayed by photoemission spectra are much more complex and hence richer of information. Therefore, their interpretation allows one to gain physical insights on the electronic interactions in the system.

In a photoemission experiment the emitted electron leaves a hole (i.e. a positive charge in correspondence to a depletion of negative charge) in the system. The presence of the hole induces a relaxation of the other electrons that screen this new positive charge. So the measured kinetic energy of the emitted electron is different with respect to the independent-particle situation. This in turn leads to a shift and a renormalization of the independent-particle peak, which broadens and loses part of its weight. When in the spectrum a main structure is still identifiable as deriving from the independent-particle peak, it can be still associated to a one-particle-like excitation, a quasiparticle. In this case, one can describe these excitations by

means of a one-particle Schrödinger equation with a complicated effective potential, the self-energy, which is a nonlocal, complex and energy-dependent operator. Moreover, the photon energy, besides creating and screening a hole, can be used also to simultaneously induce other excitations in the system. In this case, other structures, the satellites, appear in the spectrum at lower energies (in this case in fact the electron is emitted with a smaller kinetic energy).

When, on the contrary, the effect of the Coulomb interaction is very strong, the independent-particle peak is completely smeared out. The electrons are so correlated each other that a picture based on one-particle excitations is no more a convenient starting point in the description of the electronic properties of the system. In this case, one generally resorts to models, like the Hubbard model, that have been specifically devised to deal with strongly correlated materials.

First-principles methods currently employed in theoretical spectroscopy are the result of a long history. Essentially, on one side they are based on the density-functional theory (DFT), and its extension to time-dependent potentials (TDDFT); on the other side, they make use of the techniques developed in the context of the many-body perturbation theory (MBPT) in the 1960s.

In this thesis I have tried to explore new applications of these first-principles theoretical spectroscopy methods to systems where electronic correlation plays an important role. In particular, I have considered the electronic properties of vanadium dioxide (VO_2), a paradigm for materials where one expects to find a strong influence of the electronic correlations on the properties of the system. The description of the complex phase transition that characterizes vanadium dioxide represents a longstanding problem, in which the importance of electronic correlation is still debated. Model approaches are able to catch only some features of its properties, but a consistent interpretation calls for an *ab initio* calculation.

But, as soon as one tries to extend the field of applications of a certain method, new kinds of problems naturally arise. In fact, I have found that the standard methods for the calculation of quasiparticle band structures fail to explain the photoemission spectra of vanadium dioxide. This failure is widely illustrated and deeply discussed. In particular, I will address the open issue of performing self-consistent calculations in the MBPT framework. I will prove that the reasons of the bad result of the standard approach reside in some approximations that are normally employed in the actual implementation of the theoretical approaches, and not in the physical picture on which the methods rely. A way to overcome the limitations of the standard methods has been the use of the quasiparticle self-consistent scheme recently developed by F. Bruneval in [3]. I will show that in this way it is possible to provide a consistent first-principles interpretation of the experimental spectra also for vanadium dioxide.

This result is important because it permits to extend the validity of the quasiparticle picture also to systems where the many-body character of the electronic structure is supposed to be particularly relevant. But, on the other side, first-principles calculations are very expensive, especially in systems where correlation is important and one has to go beyond standard approaches. These computational limitations become evident already in the case of VO₂ and have led me to look for alternatives.

The great advantage of MBPT is its clear physical picture. This has turned out to be very helpful in understanding the electronic properties of VO₂. But this has also a price to pay. In fact one often has to calculate more information than actually needed. For instance, in order to describe photoemission spectra one would need the spectral function $A(\omega)$. But in MBPT the spectral function $A(\omega)$ is usually obtained only as a contraction of the more complex Green's function $G(\mathbf{r}, \mathbf{r}', \omega)$, which is the quantity one actually calculates. Therefore, one would like to combine the advantages of MBPT with a more efficient scheme for a direct calculation of the particular properties of interest, such as $A(\omega)$.

I will hence introduce a general scheme to define effective potentials and kernels (i.e. variations of potentials) that are able to provide shortcuts for theoretical spectroscopy calculations. As a particular example, I will consider the case of an effective potential for a direct calculation of $A(\omega)$ that one needs for photoemission. This photoemission potential turns out to be dynamical but local and real. Therefore it represents an important simplification with respect to the self-energy (which is nonlocal and complex).

I will discuss in particular the frequency dependence of this potential. I will show that the spatial nonlocality of the self-energy can be converted into the frequency dependence of the effective potential. By considering other examples of effective potentials and kernels, I will conclude that this is a common situation that one encounters when an effective potential or kernel with a reduced number of spatial degrees of freedom is used to describe electronic excitations. Moreover, I will show that this new general approach is a powerful tool. In particular, I will present a new very compact derivation of a kernel that is known to well describe absorption and energy-loss spectra of a wide range of materials.

The thesis is organized as follows. In the first chapter I will introduce the complexity inherent the many-body problem that one has to solve. Further, I will present the main spectroscopic techniques for the determination of the electronic properties of materials. In the following chapters, I will briefly review the first-principles approaches currently employed in spectroscopic calculations, ranging from the GW approximation to linear response in TDDFT. Moreover, I will introduce also some concepts behind the alternative model approaches, like the Hubbard model. In general, I will focus on the main physical ideas on which the different methods are grounded. I will present some of the most recent results one can find in literature and some

of main issues currently debated. For the rest, I will refer to the reviews, the books and the theses (such as [3][4][5]) where it is possible to study the details of the different methods.

Once the state-of-the-art theoretical framework has been summarized, I will present my calculations on vanadium oxide. I will show how the many-body *ab initio* theories are able to provide a consistent picture of the electronic properties of this system. Finally, I will discuss the new scheme I have derived to define effective potentials and kernels that permit a direct calculation of the electronic spectra. This will lead me to draw some conclusions about the results presented in the thesis and to delineate some future perspectives of the work, with possible new developments and applications.

Chapter 1

Introduction

1.1 The many-body problem

“The underlying physical laws necessary for the mathematical theory of a large part of physics and the whole of chemistry are thus completely known, and the difficulty is only that the exact application of these laws leads to equations much too complicated to be soluble.”

This famous statement of P.A.M Dirac is dated 1929 [6]. Nonetheless, it is still capable to summarize large part of the present-day research in physics and will serve as a guideline for this thesis too.

The 1920s had been not only the decade of the “Jazz age” [7], but also the years when the “scientific revolution” [8] of quantum mechanics had taken place. Nowadays, we know that atoms are made of electrons and nuclei. Their interactions are accurately known and fully described thanks to quantum mechanics. As a matter of fact, the stationary states $\delta E/\delta\Psi = 0$ of a system of N electrons, moving in the static potential V_{ext} created by the presence of N_{at} nuclei, are solutions of the time-independent Schrödinger equation

$$\left[\sum_{i=1}^N \left(-\frac{1}{2} \nabla_i^2 + V_{ext}(\mathbf{r}_i) \right) + \frac{1}{2} \sum_{i \neq j}^N v(|\mathbf{r}_i - \mathbf{r}_j|) \right] \Psi(\mathbf{r}_1, \dots, \mathbf{r}_N) = E \Psi(\mathbf{r}_1, \dots, \mathbf{r}_N). \quad (1.1)$$

By solving this equation, quantum mechanics allows every condensed-matter physicist to tell, for example, a copper pot from a plastic bottle, a block of ice from sea-sand, a piece of wood from a block of steel, and so on. In fact, *in principle*, the Schrödinger equation permits to understand the properties of all the materials on a microscopic level.

In Eq. (1.1) spin and relativistic effects have been neglected. In fact their role is not essential in the context of this thesis. More importantly, the

1. Introduction

Schrödinger equation (1.1) is already the result of another relevant simplification. Due to their smaller mass, electrons in a solid move with time scales that are much shorter than those of nuclei. Equivalently, ionic energy scales are much smaller than the electronic ones. Therefore, in first approximation (known as the Born-Oppenheimer approximation [9]), electronic and ionic dynamics can be decoupled, assuming fixed ionic positions. The electrons follow instantaneously (“adiabatically”) the motion of the nuclei. Hence, the ionic coordinates $\{\mathbf{R}\} = \mathbf{R}_1, \dots, \mathbf{R}_{N_{at}}$ enter Eq. (1.1) as parameters.

The eigenvalues of the Schrödinger equation (1.1) are the energies of the electronic system. As functions of the ionic coordinates $\{\mathbf{R}\}$, they define the adiabatic surfaces $E = E[\{\mathbf{R}\}]$, where the ionic dynamics takes place. The Born-Oppenheimer approximation is valid when these adiabatic surfaces are not degenerate in the ionic configuration space. Near the degeneracy points, the system is nonadiabatic and one has to take into account effects beyond the adiabatic approximation (e.g. Jahn-Teller effects [10]).

In any case, even in the framework of the Born-Oppenheimer approximation, the solution of equation (1.1) still remains a typical complex problem [11]. Its complexity (but also its interest) stems from the Coulomb interaction term v . In absence of interaction, in fact, the Schrödinger equation is decoupled into many one-particle problems for independent electrons. The presence of the Coulomb interaction is instead the cause of the high-dimensionality character of the solution of the Schrödinger equation (1.1). The many-body wavefunction $\Psi(\mathbf{r}_1, \dots, \mathbf{r}_N)$ is a function of $3N$ variable, where N in a solid is of the order of the Avogadro’s number, that is 10^{23} . For these reasons the Schrödinger equation (1.1) is at the same time exact and generally too complicated to be solved, rightly as stated by Dirac.

For the Coulomb interaction, electrons, once put together, can behave in a very different way with respect to when they were alone. For instance, assembling many carbon atoms can lead to the formation of an incredible variety of different compounds: diamond, graphite, nanotubes, nanoribbons, fullerenes, etc. All these materials have completely different properties one from the other, due to the different kind of hybridization and bonding of the valence electrons. In general, any many-particle system can display properties that are very different from the properties of single electrons that constitute it. This great richness is the main motivation and the deep interest to study the many-body problem.

Nevertheless, a many-electron system, despite its peculiar complexity, can sometimes exhibit a prominent single-particle behavior. Typical examples are the discontinuities with respect to the number of atoms and electrons shown by the distributions of mass abundances or ionization potentials in metal clusters [12] or fullerenes [13] (see Fig. 1.1). There are certain sizes of clusters, like C_{60} , with an exceptional stability. They are evidenced by distinct peaks in the mass-abundance distributions. As in an atom, this particular stability can be associated to the filling of all the one-particle

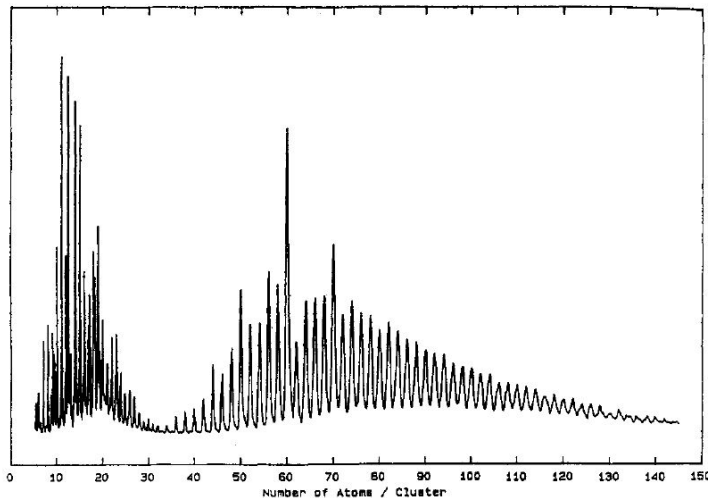


Figure 1.1: Mass abundances of carbon clusters as a function of the number of carbon atoms. The evident discontinuities are a hint of shell effects. From Ref. [14].

levels in a shell, in correspondence to some particular “magic number”. This shell structure is hence a clue of a relevant single-particle character of the electronic system.

So, in a first approximation, electrons in a solid can be considered as independent particles moving in the periodic potential created by the ions and the other electrons (if, in particular, the periodic potential is a constant, then the Sommerfeld free-electron model of metals is recovered [15]). This assumption, the so-called “Bloch paradigm” [16], historically led to the introduction of the concepts of energy bands, $\epsilon_{n\mathbf{k}}$, and Bloch states [17], $\psi_{n\mathbf{k}}(\mathbf{r}) = u_{n\mathbf{k}}(\mathbf{r})e^{i\mathbf{k}\mathbf{r}}$, solutions of the single-particle Schrödinger equation

$$\left(-\frac{1}{2}\nabla^2 + V_{ext}(\mathbf{r})\right)\psi_{n\mathbf{k}}(\mathbf{r}) = \epsilon_{n\mathbf{k}}\psi_{n\mathbf{k}}(\mathbf{r}), \quad (1.2)$$

where $V_{ext}(\mathbf{r})$ and $u_{n\mathbf{k}}(\mathbf{r})$ have the same spatial periodicity.

Despite its crude approximation, this one-electron model has been extremely successful, providing, for instance, a first explanation to the low-temperature limit of the metallic resistance, or to the different Hall coefficients. Moreover, this one-particle band model permitted the first classification of pure solids at low temperatures into metals and insulators [18]. This classification is based on a simple electron-counting criterion. Valence electrons fill the bands starting from the lowest in energy. Each band can accommodate $2N_{cell}$ electrons, where N_{cell} is the number of primitive cells in the solid. Therefore, if the number of valence electrons per primitive cell is odd, then the crystal is a metal, with the last band that is only partially

1. Introduction

filled. Instead, if all the bands are completely filled or empty, then the system is an insulator and there is an even number of electrons per primitive cells.

The development of empirical pseudopotentials [19] and many different methods of band calculations [15] allowed people to make quantitative descriptions of material properties, often with good precision. The technological silicon revolution [20] of the last century might not have been possible without this band-structure paradigm [16]. Even today, band-structure theory in solid-state physics textbooks [15] is still studied within the Bloch paradigm. Moreover, the Bloch model is often taken as a reference in the interpretation of the effects beyond the independent-electron assumption. The historical success of the Bloch paradigm may even turn to be misleading. This is rightly the case when one makes use of the Kohn-Sham equations in density-functional theory as an exact independent-particle band-structure model. In Secs. 2.2 and 7.2 I will discuss why this interpretation is wrong.

Yet the Bloch paradigm has shown all its limitations and all the conclusions based on this independent-particle model have been deeply revised. For instance, further studies have demonstrated that the electron-counting criterion to distinguish metals and insulators is too rough. It has been shown instead that the insulating character is strictly connected to the concept of electronic localization in the configuration space (that is the functional space of the N -particle wavefunctions Ψ) [21]. In an insulator the many-body wavefunction Ψ is a sum of functions localized in disconnected regions of the configuration space (and not necessarily of the real space). The modern theory of insulators [22][23] is now based on the theory of geometrical phases [24], that allows one to make a link between the concepts of localization and polarization in an insulator.

The one-particle band-structure paradigm itself has been deeply revised by the introduction of the concept of quasiparticles [25][26][27], which provides a proper interpretation of the results of photoemission experiments (see Sec. 1.2.1). Electrons are not independent particles in a solid, but the Coulomb interaction between them is screened by the presence of all the other electrons, which form a “polarization cloud” around each electron. Electrons and their clouds constitute the quasiparticles, more weakly interacting than bare electrons. But, since it is still possible to relate each quasiparticle with an electron, the qualitative one-particle picture is partly retained. One can still talk of a quasiparticle band structure, even beyond the independent-particle picture. When instead the interactions among electrons are so strong to induce radical deviations from the independent-particle model, the quasiparticle picture breaks down. It is no more possible to relate the elementary excitations measured for example in a photoemission experiment with one-particle properties. In this case, in principle, one is no more allowed to talk in terms of band structures and the system is said to be “strongly correlated”.

1.1 The many-body problem

In a first place, the effect of the Coulomb interaction on the electronic distribution can be analyzed on a pure statistical basis. The electron number density

$$\rho(\mathbf{r}) = N \int d\mathbf{r}_2, \dots, d\mathbf{r}_N |\Psi(\mathbf{r}, \mathbf{r}_2, \dots, \mathbf{r}_N)|^2 \quad (1.3)$$

is (proportional to)¹ the probability to find an electron in the volume $d\mathbf{r}$. If the electrons were independent, the probability to find *an* electron in \mathbf{r} would be the sum of the single probabilities to find in the same volume *one* of the N electrons:

$$\rho(\mathbf{r}) = \sum_{n=1}^N |\psi(\mathbf{r})|^2. \quad (1.4)$$

Moreover, the pair density $\rho_2(\mathbf{r}, \mathbf{r}')$ defines the probability to find an electron in \mathbf{r} *and* another in \mathbf{r}' . If the electrons were independent classical particles, their positions would be uncorrelated. Therefore ρ_2 would be the product of the probabilities to find an electron in \mathbf{r} and another in \mathbf{r}' : $\rho_2(\mathbf{r}, \mathbf{r}') = \rho(\mathbf{r})\rho(\mathbf{r}')$. Instead, since electrons interact, the probability to find an electron in \mathbf{r}' *does* depend on the probability to find an electron in \mathbf{r} . Hence one has:

$$\rho_2(\mathbf{r}, \mathbf{r}') = \rho(\mathbf{r})\bar{\rho}_2(\mathbf{r}'|\mathbf{r}), \quad (1.5)$$

where $\bar{\rho}_2$ is the probability to find an electron in \mathbf{r}' given that there is an electron in \mathbf{r} . The presence of an electron in \mathbf{r} reduces the probability to find an electron in \mathbf{r}' : $\rho_2(\mathbf{r}, \mathbf{r}') < \rho(\mathbf{r})\rho(\mathbf{r}')$. One says that the electron creates a hole. The exchange-correlation hole $\rho_{xc}(\mathbf{r}, \mathbf{r}')$ describes rightly the change of electron density in \mathbf{r}' due to the presence of an electron in \mathbf{r} :

$$\bar{\rho}_2(\mathbf{r}'|\mathbf{r}) = \rho(\mathbf{r}') + \rho_{xc}(\mathbf{r}, \mathbf{r}'). \quad (1.6)$$

The exchange-correlation hole contains exactly one particle. In fact it satisfies the sum rule:

$$\int d\mathbf{r}' \rho_{xc}(\mathbf{r}, \mathbf{r}') = -1, \quad (1.7)$$

and, analogously, it holds that

$$\int d\mathbf{r}' \bar{\rho}_2(\mathbf{r}'|\mathbf{r}) = N - 1. \quad (1.8)$$

The presence of the exchange-correlation hole ρ_{xc} is an expression of the fact that electrons in a solid are not uncorrelated. Its existence is due to

¹ In the following, the fact that, in order to talk in terms of probability distributions, one should consider the proper normalizations, such as

$$\frac{1}{N} \int d\mathbf{r} \rho(\mathbf{r}) = 1$$

will be implicitly assumed.

1. Introduction

two different physical effects. First, since electrons are fermions, the Pauli principle assures that electrons don't get too close each other and hence the effect of the Coulomb interaction is also diminished. This effect is called exchange. The exchange effect is rightly related to the fermionic character of the electrons. Even for an ideal fermionic system without Coulomb interaction, the Pauli principle would be still effective and the exchange hole still present. Moreover, in real systems for the presence of the Coulomb interaction electrons are further kept apart because they repel each other. This further effect, beyond exchange, which is strictly due to the effect of the Coulomb interaction, is called correlation.

If the electrons were independent classical particles, the interaction energy would be the Hartree energy:

$$E_H = \frac{1}{2} \int d\mathbf{r}d\mathbf{r}' \frac{\rho(\mathbf{r})\rho(\mathbf{r}')}{|\mathbf{r} - \mathbf{r}'|}. \quad (1.9)$$

Instead, the Coulomb energy is smaller than E_H because the interaction is weaker for the presence of the exchange-correlation hole. The pair-correlation function $\bar{g}(\mathbf{r}, \mathbf{r}')$, defined by:

$$\rho_2(\mathbf{r}, \mathbf{r}') = \rho(\mathbf{r})\bar{g}(\mathbf{r}, \mathbf{r}')\rho(\mathbf{r}'), \quad (1.10)$$

describes rightly this screening of the interparticle interaction. In fact, in a many-body system, the Coulomb interaction between two charge distributions $\rho(\mathbf{r})$ and $\rho(\mathbf{r}')$ is not mediated by $1/|\mathbf{r} - \mathbf{r}'|$, but rather by $\bar{g}(\mathbf{r}, \mathbf{r}')/|\mathbf{r} - \mathbf{r}'|$. Since the pair-correlation function has a screening effect, it holds: $0 < \bar{g} < 1$. Only when two charge distributions are far apart and the effect of the interaction is negligible, one has:

$$\lim_{|\mathbf{r} - \mathbf{r}'| \rightarrow \infty} \bar{g}(\mathbf{r}, \mathbf{r}') = 1. \quad (1.11)$$

Figure 1.2 shows the pair-correlation function $\bar{g}(\mathbf{r}, \mathbf{r}')$ and the exchange-correlation hole $\rho_{xc}(\mathbf{r}, \mathbf{r}')$ in a real system – bulk silicon – calculated by an accurate Montecarlo simulation [28]. One clearly sees that around each electron it is $\bar{g} < 1$ and a deep exchange-correlation hole is created.

Therefore, electrons cannot be considered as independent particles, not even in “simple” semiconductors like bulk silicon.

In the next sections of the chapter I will deal more deeply with the effects of the electronic correlations on the properties of the electronic systems. I will introduce photoemission, absorption and electron-energy loss spectroscopy as prototypical spectroscopy methods to study the excited-state properties of an electronic system. I will first give an independent-particle interpretation of these measures. By considering model systems, like the homogeneous electron gas, I will then discuss how electronic correlation can induce from moderate to drastic deviations [16] with respect to the

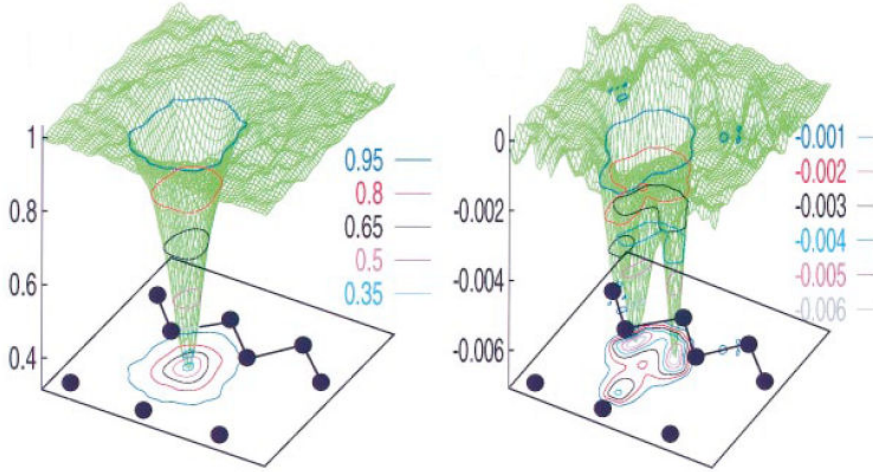


Figure 1.2: The pair-correlation function $\bar{g}(\mathbf{r}, \mathbf{r}')$ and the exchange-correlation hole $\rho_{xc}(\mathbf{r}, \mathbf{r}')$, with one electron fixed at the tetrahedral interstitial site in the (110) plane of bulk silicon. The atoms and bonds are schematically represented for bond chains along the [111] direction. From quantum Montecarlo calculations of Ref. [28].

independent-particle model. This will constitute the main motivation to introduce in the following chapters the theoretical spectroscopy methods that are suitable to interpret experimental spectra beyond the independent-particle picture.

1.2 Spectroscopies

In a spectroscopy experiment one perturbs the sample and measures the response of the electronic system. In this way it is possible to have access to a great deal of information on the electronic properties of the system. In general, a beam of particles (photons or electrons) impinges on the sample. By measuring the energy (or other properties) of the outgoing particles (again photons or electrons), one can determine the elementary excitations that the perturbation induces in the system (see Tab. 1.1).

In photoemission (PES) the sample absorbs one photon and emits an electron (called photoelectron). The missing electron leaves a hole in the system, which is hence in an excited state. In an independent-particle picture, photoemission spectra can be interpreted by calculating the density of occupied states. The inverse photoemission can be considered as the time-reversal of photoemission: the system absorbs an electron and a photon is emitted. In this way one measures the empty states. In absorption experi-

1. Introduction

	In	Out	n. e^- in the sample
Direct photoemission	photon	electron	$N \rightarrow N - 1$
Inverse photoemission	electron	photon	$N \rightarrow N + 1$
Absorption	photon	photon	$N \rightarrow N$
Electron energy loss	electron	electron	$N \rightarrow N$

Table 1.1: Classification of different kinds of spectroscopies according to the probe used ('in') and the particle collected after the interaction with the target ('out'). Moreover, the last column indicates the change in the number of electrons in the sample.

ments the incident beam of light loses photons that have been absorbed by the system. Their energy has been used to excite an electron from valence to conduction: an electron-hole pair is created in the system. Finally, in electron energy-loss spectroscopy experiments (EELS) an electron undergoes an inelastic scattering with the sample and one measures its loss of energy and its change of direction. Again, the energy lost by the probe has been used to induce an excitation of the system. From all these examples, it is clear that a spectroscopy experiment always leaves the system in an excited state.

These different kinds of spectroscopies can be classified in two categories depending on whether the sample changes or not its number of electrons. Direct and inverse photoemission experiments belong to the former. Absorption and EELS to the latter.

If the number of electrons of the sample changes, one measures mainly one-particle elementary excitations: the quasiparticles. If it is conserved, one has access to information on collective neutral excitations: excitons (electron-hole pairs) and plasmons (coherent electronic-density oscillations). In the many-body framework, in the former case one measures the spectral properties of one-particle Green's functions (see Chapter 3). In the latter, the key quantities are the response functions, a particular class of two-particle Green's functions (see Chapter 5). I will deal with one- and two-particle Green's function in the next chapters. For the moment, I will present a brief introduction of these spectroscopy methods.

1.2.1 Photoemission

The photoelectron spectroscopy owes its origin to the discovery of the photoelectric effect by Hertz [29] and its explanation to Einstein [30], which worthed him the Nobel prize.

In an independent-particle picture, by measuring the kinetic energy of the emitted electron, one obtains directly the energy of the one-particle level that the electron was occupying before being extracted from the sample. Instead, the distribution of kinetic energies one actually obtains is somewhat

different with respect to this simple picture. In fact, the emitted electron leaves a hole in the electronic system. A hole is a depletion of negative charge, so its charge is positive. Therefore, this hole induces a relaxation of all the other electrons that screen this new positive charge in the system. So the presence of the hole corresponds to an excited state of the system, with a finite lifetime. For this reason, in a photoemission spectrum one doesn't find a simple line (a delta peak) in correspondence to a particular one-particle energy, but a peak with a finite width, which gives a measure of the interactions due to the presence of a hole. This peak is called the quasiparticle peak. Moreover, sometimes the measured kinetic energy of the emitted electron is even lower. In fact, in these cases the photon energy has been used not only to create and screen a hole, but also to produce other excitations in the system. In particular, these excitations can have a collective nature, like in the case of an additional excitation of a plasmon. In these cases, the energy of the incoming photon has been spent to create simultaneously at least two different excitations in the system. So on a simple statistical basis one can figure out that these simultaneous events generally occur with a smaller probability. They hence give rise to structures in the spectrum that not only have lower energies but also reduced intensities than the quasiparticle peak. For this reason they are called satellites. When instead the Coulomb interaction induces strong correlation effects in the system, the one-particle nature of the excitation is completely lost. In the photoemission spectrum it is not possible anymore to clearly distinguish a prominent quasiparticle peak, but only excitations with an intrinsically many-body character show up.

A photoemission experiment can be interpreted as a three-step process: an electron in the system is excited by the incoming photon, travels towards the surface and finally escapes into the vacuum. The photoemission intensity is then the product of the probabilities of these three steps.

In order to have information on the “intrinsic” electronic properties of the sample, one can isolate the first step, assuming that the photoelectron, once excited by the photon, doesn't lose energy on the way to the surface and propagates as a free particle outside the sample. This assumption is called sudden approximation.

In this framework, the measured photocurrent $J_{\mathbf{p}}(\omega)$ is given by the probability per unit time of emitting an electron with momentum \mathbf{p} when the sample is irradiated with photons of frequency ω . Using Fermi's golden rule, one has [31][32]:

$$J_{\mathbf{p}}(\omega) = \sum_s |\langle N-1, s; \mathbf{p} | \Delta | N \rangle|^2 \delta(E_{\mathbf{p}} - E_s - \omega), \quad (1.12)$$

where $\Delta = -i\mathbf{A}\nabla$ is the coupling to the photon field. The perturbation induces a transition from the initial state $|N\rangle$ with N electrons in the ground state to the final state $|N-1, s; \mathbf{p}\rangle$. The final state is represented by a system

1. Introduction

with the photoelectron with momentum \mathbf{p} and the sample in the excited state s with $N - 1$ electrons. The energy conservation is assured by requiring that the photon energy ω is equal to the kinetic energy of the photoelectron $E_{\mathbf{p}}$ minus the electron binding energy, $E_s = E(N) - E(N - 1, s)$, for the electron in the state s : $\omega = E_{\mathbf{p}} - E_s$. So, by knowing ω and measuring $E_{\mathbf{p}}$, one can have access to information on the excited state s .

In second quantization Δ can be rewritten as:

$$\Delta = \sum_{ij} \Delta_{ij} \hat{c}_i^\dagger \hat{c}_j, \quad (1.13)$$

where the creation and annihilation operators \hat{c}^\dagger and \hat{c} have been introduced. In the sudden approximation the photoelectron is considered completely decoupled from the sample, therefore the final state is the simple product:

$$|N - 1, s; \mathbf{p}\rangle = \hat{c}_{\mathbf{p}}^\dagger |N - 1, s\rangle. \quad (1.14)$$

One further assumes that the photoelectron doesn't interact with the hole left behind and doesn't change the state of the $N - 1$ electron system. So $\hat{c}_{\mathbf{p}} |N\rangle = 0$ and $\hat{c}_{\mathbf{p}} \hat{c}_i^\dagger |N\rangle = (\delta_{\mathbf{p}i} - \hat{c}_i^\dagger \hat{c}_{\mathbf{p}}) |N\rangle = \delta_{\mathbf{p}i} |N\rangle$. Then:

$$\langle N - 1, s; \mathbf{p} | \Delta | N \rangle = \sum_j \Delta_{\mathbf{p}j} \langle N - 1, s | \hat{c}_j | N \rangle. \quad (1.15)$$

Introducing the matrix elements of spectral function $A_{ij}(\omega)$ (for $\omega < \mu$):

$$A_{ij}(\omega) = \sum_s \langle N | \hat{c}_i^\dagger | N - 1, s \rangle \langle N - 1, s | \hat{c}_j | N \rangle \delta(\omega - E_s), \quad (1.16)$$

the total photocurrent $J_{\mathbf{p}}(\omega)$ can be rewritten as:

$$J_{\mathbf{p}}(\omega) = \sum_{ij} \Delta_{\mathbf{p}i} A_{ij}(E_{\mathbf{p}} - \omega) \Delta_{j\mathbf{p}}. \quad (1.17)$$

For each state s , the spectral function (1.16) gives the probability to remove an electron from the ground state $|N\rangle$ and leave the system in the excited state $|N - 1, s\rangle$.

Generally one considers the dipole matrix elements as constants $\bar{\Delta}$ and the diagonal elements of A in the basis where Δ is constant as the most relevant. Therefore:

$$J_{\mathbf{p}}(\omega) = |\bar{\Delta}|^2 \sum_i A_{ii}(E_{\mathbf{p}} - \omega). \quad (1.18)$$

The total intensity of the spectrum is the product of the trace of the spectral function A and the matrix element $\bar{\Delta}$, which depends on the energy, momentum and polarization of the incoming photon. Therefore, when the matrix

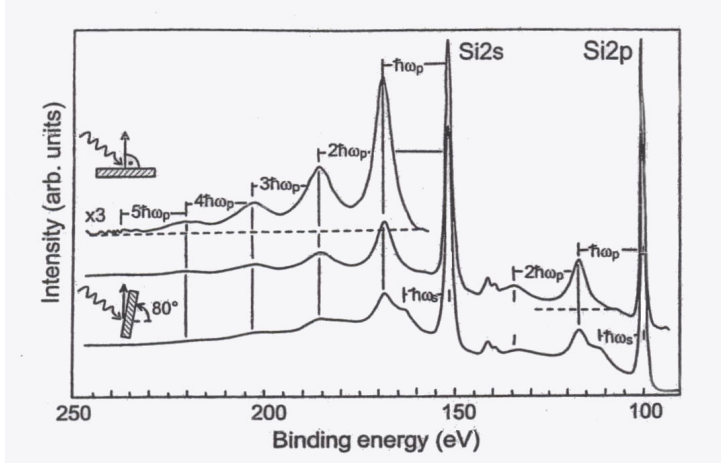


Figure 1.3: Si $2p$ and Si $2s$ photoemission spectra of the Si(111)7x7 surface. At normal emission, spectra are dominated by bulk properties. At grazing emission (80°) surface features can be seen. Besides prominent quasiparticle peaks, multiple losses by bulk ($\omega_p = 16$ eV) and surface ($\omega_s = \omega_p/\sqrt{2}$) plasmons are visible as satellites. From Ref. [33].

elements are not zero, photoemission measurements give direct insights on the spectral function A .

In an independent-particle picture the many-body wavefunctions are Slater determinants. In this case the matrix elements (1.16) become simply

$$A_{ij}(\omega) = \delta_{ij}\delta(\omega - E_i)\theta(\mu - \omega). \quad (1.19)$$

So the total photocurrent

$$J_{\mathbf{p}}(\omega) = |\bar{\Delta}|^2 \sum_i^{occ} \delta(E_{\mathbf{p}} - \omega - E_i) \quad (1.20)$$

turns out to be given by a series of delta peaks in correspondence to the energies E_i of the one-particle Hamiltonian. The photoemission spectrum is hence described by the density of occupied states:

$$\text{DOS}(E_{\mathbf{p}} - \omega) = \sum_i^{occ} \delta(E_{\mathbf{p}} - \omega - E_i), \quad (1.21)$$

evaluated at the energy $E_{\mathbf{p}} - \omega$.

Beyond the independent-particle picture, the many-body wavefunctions are generally a linear combination of many Slater determinants. So for each excited state s , there are many nonvanishing contributions to the spectral function (1.16) that form a more complex structure around the energy E_s . If in this more complex structure a main peak is still identifiable (see Fig.

1. Introduction

1.3), then one can associate this peak with a quasiparticle excitation.² The quasiparticle peaks are called the coherent part of the spectrum, because they correspond to one-particle-like excitations of the system. The spectral function can also display satellites (the incoherent part of the spectrum), that cannot be attributed to a one-particle excitation. When in a spectrum it is not possible to recognize anymore any one-particle-like feature, it is said that the electronic system is strongly correlated. In this case the quasiparticle paradigm is no more valid. Satellites due to features of the spectral function are called shake-up satellites and it is said that they are due to intrinsic losses [34][35]. They are due to direct excitations of the system for the incoming photon. When one considers, beyond the sudden approximations, scattering processes of the photoelectron on its way out of the solid, new features in the photoemission spectrum can appear. In this case one talks of extrinsic losses.

Besides the kinetic energy of the photoelectron, $E_{\mathbf{p}}$, also its direction of propagation can be measured, determining the angles θ and φ with respect to the direction perpendicular to the surface (see Fig. 1.4). In this case the experiment is called angular-resolved photoemission spectroscopy (ARPES). The component parallel to the surface of the crystal momentum \mathbf{k} is conserved: $\mathbf{k}_{\parallel} = \mathbf{p}_{\parallel} = \sqrt{2E_{\mathbf{p}}}\sin\theta$. The perpendicular component instead is not conserved. So the knowledge of \mathbf{p}_{\perp} doesn't permit to recover immediately the initial \mathbf{k}_{\perp} , with the exception of the normal emission condition when $\mathbf{p}_{\parallel} = 0$ and hence $\mathbf{p}_{\perp} = \mathbf{k}_{\perp}$. Otherwise one can vary the photon energy at fixed \mathbf{p}_{\parallel} , determining in this way the energy dispersion in the normal direction. In any case, combining the measurement of $E_{\mathbf{p}}$ and \mathbf{p}_{\parallel} , from ARPES measurements one can access the complete energy dispersion $E_s(\mathbf{k})$ of the bands in the solid.

PES is a surface sensitive technique: the electron escape depth is of order 10-50 Å for kinetic energies of 10-2000 eV [36]. Avoiding surface effects is crucial in order to obtain bulk information [37]. This can be achieved by working at high photon energies, where one has however worse resolution in energy and momentum, and using atomically flat and clean surfaces. At the same time, higher photon energies are more in the range of validity of the sudden approximation. The photoelectron is emitted with a high kinetic energy and therefore its removal process can be considered instantaneous. Therefore, instead of using UV photons produced by gas-discharge lamps, in PES one may prefer to use X-rays. In contrast, most of ARPES experiments are performed in the UV range, where the resolution is better [38], since $\Delta\mathbf{k}_{\parallel} = \sqrt{2E_{\mathbf{p}}}\cos\theta\Delta\theta$, where $\Delta\theta$ is the acceptance angle of the analyzer. So, at a lower $E_{\mathbf{p}}$, $\Delta\mathbf{k}_{\parallel}$ is smaller.

² In Chapter 3 the concept of quasiparticle will emerge as naturally associated with the one-particle Green's function G , whose imaginary part is the spectral function A .

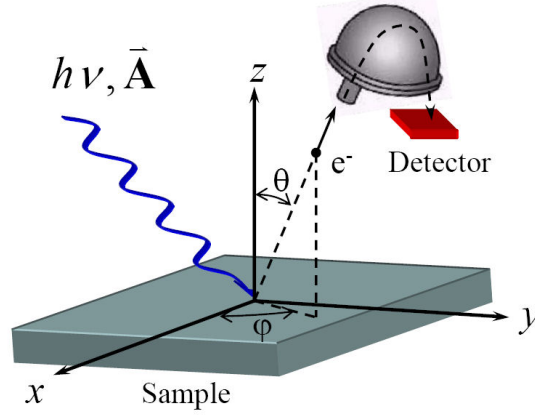


Figure 1.4: Schematic representation of an ARPES experiment.

1.2.2 Absorption and electron energy loss

In optical spectroscopies photons are used to probe the properties of the system. A photon impinging on a sample can be either absorbed, or reflected or transmitted. When it is absorbed, its energy is used to create a neutral excitation of the system. In fact, in an independent-particle picture, an electron is excited from occupied to empty states, conserving its crystal momentum (photons have a negligible momentum). Since, contrary to photoemission, the electron remains in the sample, it cannot be considered decoupled from the other electrons.

Optical spectroscopies can be interpreted on the basis of the macroscopic Maxwell equations [4][39]. In a medium, an electric field, polarized along the \hat{x} direction, is a damped wave:

$$\mathbf{E}(x, t) = E_0 \hat{e} e^{i\frac{\omega}{c}(nx-ct)} = E_0 \hat{e} e^{i\frac{\omega}{c}(n_1x-ct)} e^{-\frac{\omega}{c}n_2x}, \quad (1.22)$$

where n is the complex refractive index $n = n_1 + in_2$. So the intensity of the field is exponentially decaying:

$$I(x) = |\mathbf{E}(x)|^2 = E_0^2 e^{-2\frac{\omega}{c}n_2x}. \quad (1.23)$$

The absorption coefficient α is the inverse of the distance where the intensity of the field is reduced by $1/e$:

$$\alpha = \frac{2\omega n_2}{c}. \quad (1.24)$$

Or, introducing the (macroscopic) dielectric function $\epsilon_M = \epsilon_1 + i\epsilon_2 = n^2$:

$$\alpha = \frac{\epsilon_2 \omega}{n_1 c}. \quad (1.25)$$

1. Introduction

Since n_1 can be normally assumed constant in the frequency range of interest, the absorption spectra are expressed in terms of $\epsilon_2 = \text{Im}\epsilon_M$.

Measurements in a transmission configuration require very thin films, so ϵ_2 is generally not obtained by measuring directly the absorption coefficient α . It is instead measured in a reflection configuration or by ellipsometry, where one uses linearly polarized incident photons.

In the independent-particle approximation, in the dipole approximation, Fermi's golden rule [5][40]:

$$\epsilon_2^{(T)}(\omega) = \frac{8\pi^2}{\Omega\omega^2} \sum_{ij} |\langle\psi_j|\hat{\mathbf{e}} \cdot \mathbf{v}|\psi_i\rangle|^2 \delta(E_j - E_i - \omega) \quad (1.26)$$

explains the absorption spectra in the linear regime as a sum of one-particle independent transitions from $|\psi_i\rangle$ to $|\psi_j\rangle$, due to the interaction with a transverse electromagnetic plane wave of frequency ω and polarization $\hat{\mathbf{e}}$. In general $\epsilon_2^{(T)}$ is a tensor.

Since in an absorption experiment, contrary to photoemission, the excited electron remains inside the system, it cannot be considered as a free electron decoupled from the others, as in the independent-particle picture associated to Fermi's golden rule (1.26). In particular, one has to take into account the interaction between the electron and the hole that the excitation of the electron has created, the so-called excitonic effects. I will discuss in Chapter 5 how to deal with these two-particle interactions in the framework of the two-particle Green's functions.

In electron energy-loss spectroscopy, instead, the probe is a high-energy electron which undergoes a scattering interaction since the moment it approaches the sample. The probability that an impinging electron of velocity \mathbf{v} transfers in a unit time an energy W and a momentum \mathbf{q} to an excitation of the system can be expressed by the energy-loss rate [4][41]:

$$\frac{dW}{dt} = \frac{1}{(2\pi)^3} \int d\omega d\mathbf{q} \frac{\omega}{q^2} \text{Im} \left\{ -\frac{1}{\epsilon_M(\mathbf{q}, \omega)} \right\} \delta(\omega + \mathbf{q} \cdot \mathbf{v}). \quad (1.27)$$

In Eq. (1.27) one assumes that the impinging electron is a classical particle and can be treated in a nonrelativistic approximation, also neglecting quantum indetermination effects on its position. The energy-loss rate is then the product of a kinematic factor and the loss function $L(\omega)$:

$$L(\omega) = -\text{Im} \left\{ \frac{1}{\epsilon_M(\mathbf{q}, \omega)} \right\} = \frac{\epsilon_2(\mathbf{q}, \omega)}{\epsilon_1^2(\mathbf{q}, \omega) + \epsilon_2^2(\mathbf{q}, \omega)}. \quad (1.28)$$

From Eq. (1.28) one can conclude that spectral features in EELS can be seen in the case that either ϵ_2 has a peak corresponding to some interband transition or ϵ_2 is small and $\epsilon_1 = 0$. The latter condition determines the frequencies of the collective plasmon excitations. In energy-loss experiments

one can therefore excite plasmons, that are longitudinal excitations and are not generally observed in optical spectroscopy, since photons are a transverse perturbation.

Using Fermi's golden rule, the imaginary part of the longitudinal dielectric function can be evaluated as [5][40]:

$$\epsilon_2^{(L)}(\mathbf{q}, \omega) = \frac{8\pi^2}{\Omega q^2} \sum_{ij} |\langle \psi_j | e^{i\mathbf{q}\mathbf{r}} | \psi_i \rangle|^2 \delta(E_j - E_i - \omega). \quad (1.29)$$

In this picture plasmon peaks in EELS are associated to coherent oscillations of independent particles. I will discuss in Chapter 5 how to go beyond the independent-particle description of EELS.

In the long wavelength limit $\mathbf{q} \rightarrow 0$ the transverse and longitudinal dielectric functions (1.26) and (1.29) coincide, since [42]:

$$\mathbf{v} = \lim_{\mathbf{q} \rightarrow 0} \frac{1}{q} [\hat{H}, e^{i\mathbf{q}\mathbf{r}}]. \quad (1.30)$$

This is due to the invariance for $\mathbf{q} \rightarrow 0$ between the velocity gauge (transverse perturbation $\mathbf{A} \cdot \mathbf{v}$) and the length gauge (longitudinal perturbation $\mathbf{E} \cdot \mathbf{r}$).

A particular situation is the EELS for the core states. In fact, at high energies $\epsilon_2(\mathbf{q}, \omega) \rightarrow 0$ and $\epsilon_1(\mathbf{q}, \omega) \rightarrow 1$. This observation determines a simplification of the loss function (1.28):

$$L(\omega) = -\text{Im} \left\{ \frac{1}{\epsilon_M(\mathbf{q}, \omega)} \right\} \rightarrow \epsilon_2(\mathbf{q}, \omega). \quad (1.31)$$

In other words, for core states, the absorption and the loss function for vanishing \mathbf{q} become indistinguishable. The same occurs in the case of finite systems, as I will discuss in Sec. 5.2.

Analogously, X-ray absorption spectra (XAS) are due to an excitation of a core level ψ_c . The spectrum is obtained from (1.26) [43]:

$$\epsilon_2(\omega) = \frac{8\pi^2}{\Omega \omega^2} \sum_i^{unocc} |\langle \psi_i | \hat{\mathbf{e}} \cdot \mathbf{v} | \psi_c \rangle|^2 \delta(E_c - E_i - \omega) \quad (1.32)$$

For simplicity I consider here a system with a single ion per unit cell. The generalization to the multiatomic case is straightforward (see e.g. [44]). The core state ψ_c has a very strong atomic character. Neglecting spin-orbit effects: $\psi_c(\mathbf{r}) = R_{nl}(r)Y_{lm}(\theta, \varphi)$, where R_{nl} is a radial function and Y_{lm} a spherical harmonic function. Projecting also the final state $\psi_i(\mathbf{r})$ on the spherical harmonics:

$$\psi_i(\mathbf{r}) = \sum_{n', l', m'} c_{n'l'm'}^i R_{n'l'}(r) Y_{l'm'}(\theta, \varphi) \quad (1.33)$$

1. Introduction

one has that Eq. (1.32) can be rewritten as:

$$\begin{aligned} \epsilon_2(\omega) = & \frac{8\pi^2}{\Omega\omega^2} \sum_i^{unocc} \delta(\omega - E_i + E_c) \times \\ & \times \sum_{\substack{n',l',m' \\ n'',l'',m''}} c_{n'l'm'}^{*i} c_{n''l''m''}^i \langle n'l'm' | \hat{\mathbf{e}} \cdot \mathbf{v} | nlm \rangle \langle nlm | \hat{\mathbf{e}} \cdot \mathbf{v} | n''l''m'' \rangle \end{aligned} \quad (1.34)$$

where the simplified notation $|nlm\rangle = R_{nl}Y_{lm}$ has been adopted (when spin-orbit effects are important one replaces the atomic state $|nlm\rangle$ in (1.34) with $|nljm_j\rangle$).

In the matrix elements in (1.34) dipole selection rules apply. So, for instance, if the core state has an orbital angular momentum l , only the components with $l', l'' = l \pm 1$ survive. Once the dipole selection rules have been taken into account and assuming that the matrix elements of the same symmetry are a constant, one finds that the X-ray absorption spectra probe the density of unoccupied states localized on the atomic site and projected on a particular angular momentum component $l \pm 1$:

$$\epsilon_2(\omega) = \frac{8\pi^2}{\Omega\omega^2} \sum_i^{unocc} |c_{l\pm 1}^i|^2 \delta(\omega - E_i + E_c) \quad (1.35)$$

Often taking into account spin-orbit effects for the core level can be important. For instance, the core level $2p$ is split by the spin-orbit coupling into the $2p_{1/2}$ and $2p_{3/2}$ levels. The spin-orbit constant varies from 1.88 eV in K to 15.7 eV in Zn [45], so it generally cannot be neglected. Since there are two times as much $2p$ orbitals with $j = 3/2$ than $2p$ orbitals with $j = 1/2$, in the independent-particle picture excitations from the former should give rise to a peak of double intensity than the peak stemming from excitations from the latter. Moreover, the two peaks in the XAS should result separated by an energy exactly equal to the spin-orbit splitting. However electronic interactions can have important effects also on X-ray absorption spectra [46] and give rise to spectra that are different with respect to these expectations based on an independent-particle picture.

1.3 Beyond the independent-particle picture

1.3.1 From Hartree-Fock to dynamical quasiparticles

In the Hartree-Fock approximation [47][48] one considers electrons as independent fermions. Exchange is fully taken into account, but correlation is completely neglected. In this noninteracting model for fermions, the many-body wavefunction Ψ is a Slater determinant:

$$\Psi(\mathbf{r}_1, \dots, \mathbf{r}_N) = \sum_P \text{sgn}(P) \prod_{i=1}^N \psi_i(\mathbf{r}_{P(i)}), \quad (1.36)$$

1.3 Beyond the independent-particle picture

where the sum is over all the permutations P of N one-particle wavefunctions ψ_i and $\text{sgn}(P)$ is the sign of the permutation (+ if even and $-$ if odd). In general, the quantum number i of the state ψ_i accounts also for the spin σ_i .

The Hartree-Fock equations determine the set of one-particle orbitals ψ_i that minimize the total energy of the system:

$$\left[-\frac{\nabla^2}{2} + V_{\text{ext}}(\mathbf{r})\right]\psi_i(\mathbf{r}) + V_H(\mathbf{r})\psi_i(\mathbf{r}) + \int d\mathbf{r}' V_x(\mathbf{r}, \mathbf{r}')\psi_i(\mathbf{r}') = E_i\psi_i(\mathbf{r}), \quad (1.37)$$

where

$$V_H(\mathbf{r}) = \sum_j \int d\mathbf{r}' \psi_j^*(\mathbf{r}') \frac{1}{|\mathbf{r} - \mathbf{r}'|} \psi_j(\mathbf{r}') \quad (1.38)$$

and

$$\int d\mathbf{r}' V_x(\mathbf{r}, \mathbf{r}')\psi_i(\mathbf{r}') = - \sum_j \delta_{\sigma_i, \sigma_j} \int d\mathbf{r}' \psi_j^*(\mathbf{r}') \frac{1}{|\mathbf{r} - \mathbf{r}'|} \psi_j(\mathbf{r}')\psi_i(\mathbf{r}'). \quad (1.39)$$

In this approximation, the electrons move as independent particles in the mean field generated by the presence of all the other electrons. The Hartree potential V_H is due to the classic Coulomb interaction between electrons, while the nonlocal exchange potential V_x is a consequence of the Pauli exclusion principle. For this reason it involves only electrons with the same spin (in (1.39) for the presence of the delta function it must hold: $\sigma_i = \sigma_j$). Moreover, the exchange term is essential to cancel the self-interaction contained in the Hartree term (1.38). In fact, if in the sum (1.38) over the j orbitals one doesn't exclude explicitly the term $j = i$ when $V_H(\mathbf{r})$ acts on the orbital i , one would have that the electron sitting on the orbital i would interact with itself, which is prohibited. But, since it has an opposite sign, the term $j = i$ included in the sum (1.39) for V_x cancels exactly this spurious self-interaction.

The Hartree-Fock approximation corresponds to a first-order contribution to the total energy in a perturbative expansion in the Coulomb interaction v . Atomic total energies or molecular equilibrium geometries are often pretty good when calculated in the Hartree-Fock approximation. Considering an atom, such as Ne, correlation, which is all beyond the Hartree-Fock approximation, accounts for only 0.3% of the total energy [49]. Nevertheless, neglecting correlation effects can have dramatic consequences.

The jellium model describes a solid by means of a gas of interacting electrons embedded in a uniform background of positive charges. A single parameter, the Wigner-Seitz radius r_s ,

$$r_s = \left(\frac{3}{4\pi\rho}\right)^{\frac{1}{3}}, \quad (1.40)$$

which defines an average inter-electronic distance, characterizes this homogeneous electron gas (HEG). The shorter r_s is, the denser the gas is. The jellium is in particular a good model for simple metals, where $3 < r_s < 6$.

1. Introduction

Since the jellium is homogeneous and isotropic, the one-particle energies are functions of the norm of the wavevector \mathbf{k} . In the Hartree-Fock approximation they are:

$$E(k) = \frac{k^2}{2} - \frac{2k_F}{\pi} F\left(\frac{k}{k_F}\right), \quad (1.41)$$

where:

$$F(x) = \frac{1}{2} + \frac{1-x^2}{4x} \ln \left| \frac{1+x}{1-x} \right|. \quad (1.42)$$

The derivative $dE(k)/dk$ has a logarithmic divergence at $k = k_F$ (dF/dx is divergent for $x = 1$). Therefore, the electronic effective mass $m^* = \pi k (dF/dx)^{-1}$ [50] vanishes at the Fermi energy E_F , which is in clear contrast with experimental findings in simple metals. This divergence of the derivative is due to the infinite-range character of the Coulomb interaction v . For the same reason, also the second-order contribution to the total energy, evaluated in an expansion in v , is divergent. In the limit of small r_s , the perturbative series can be resummed avoiding the divergence [51], by considering the physical observation that the Coulomb interaction is actually screened by the presence of the other electrons. The screened interaction has a finite range and this prevents the divergences.

In photoemission experiments (or inverse photoemission) one measures the energy to remove (or add) an electron from the system (see Sec. 1.2.1). The electron removal energy I_k is defined as the energy needed to extract an electron from the energy level k (or, equivalently, to create a hole in the level k). The smallest electron removal energy I_k is the ionization potential I . I_k is given by the difference between the total energy of the system with $N - 1$ electrons, where one electron has been removed from the level k , and the total energy of the system with N electrons in the ground state: $I_k = E(N - 1_k) - E(N)$. Thanks to Koopmans' theorem [52], in the Hartree-Fock approximation one has that I_k is equal to the absolute value of the eigenvalue for the energy level k : $I_k = -E_k$. Analogously, the electron addition energy $A_l = E(N) - E(N + 1_l)$ is the energy gained when an electron is added on the energy level l . In Hartree-Fock one has: $A_l = -E_l$. The largest A_l is the electronic affinity A of the system.

Therefore, Koopmans' theorem gives us a direct physical meaning of the Hartree-Fock eigenvalues E_i . Anyway, in this calculation of the excitation energies based on Koopmans' theorem, there is an important approximation. In fact one assumes that in the $N \pm 1$ electron systems, the orbitals don't relax for the presence of an extra electron or an extra hole. This approximation results to be too crude. In particular, in finite systems one finds that, due to the relaxation of the other orbitals, ionization potentials are smaller than the values obtained by Koopmans' theorem. But in finite system, in which the extra particle is localized, one could deal with relaxation effects by performing explicitly two calculations for the N and $N \pm 1$ electron systems

1.3 Beyond the independent-particle picture

(this method is called Δ -self-consistent field). In this way, even though the calculations are done within the Hartree-Fock approximation, a large part of the error is corrected, because for finite systems the Hartree relaxation of the wavefunctions is essential. In solids, instead, where $N \rightarrow \infty$, the extra particle would live on a Bloch state which is delocalized all over the system. So one cannot apply the Δ -self-consistent-field method [53], but has rather to take into account dynamical correlation effects by introducing the concepts of polarization and screening of the Coulomb interaction.

In an insulator, the band gap E_g is defined as the difference between the ionization potential I and the electron affinity A :

$$E_{gap} = I - A = \min_{kl} [E(N - 1_k) + E(N + 1_l) - 2E(N)]. \quad (1.43)$$

When E_{gap} is calculated as Hartree-Fock eigenvalue differences, it is always much larger than the experimental value. In diamond, for instance, the experimental minimum direct gap is 7.3 eV. In Hartree-Fock it is 15 eV [2].

Going beyond the Hartree-Fock approximation, one has indeed to take into account correlation effects beyond the independent-particle model, the relaxation of the system for the presence of an extra particle, the screening of the Coulomb interaction.

In the Hartree-Fock approximation excitations have an infinite lifetime, rightly because there is no relaxation and the potentials are static. The excitation spectrum, as measured by a photoemission experiment, would be a series of delta peaks.

When instead the interactions beyond the Hartree-Fock mean field are taken into account, the presence of an extra particle is screened by the relaxation of all the other electrons. In this way one is led to replace bare particles (electrons and holes) with quasiparticles. Whereas electrons interact through the bare Coulomb interaction v , quasiparticles interact through the screened interaction W , which is weaker and more short-ranged.

As a matter of fact, in an interacting system, the motion of the extra electron is followed by the other particles, screening the Coulomb interaction. The additional electron, by moving around, polarizes the system. In a self-consistent manner, the response of the system through its polarization changes the effective properties of the electron, that becomes a dressed, renormalized quasiparticle. This feedback interaction is again a signature of the complex character of the many-body problem [11]. Each quasiparticle can be visually represented as formed by an electron and its screening cloud.

This description also clarifies the physical origin of the exchange-correlation hole $\rho_{xc}(\mathbf{r}, \mathbf{r}')$ and the pair-correlation function $\bar{g}(\mathbf{r}, \mathbf{r}')$, which I had introduced in the previous section on a pure statistical basis (see Eqs. (1.6) and (1.10)).

The quasiparticles are no more eigenstates of the full Hamiltonian (1.1) of the system. So their lifetime is finite. They interact with other quasiparticles or with collective excitations of the system. In the excitation spectrum

1. Introduction

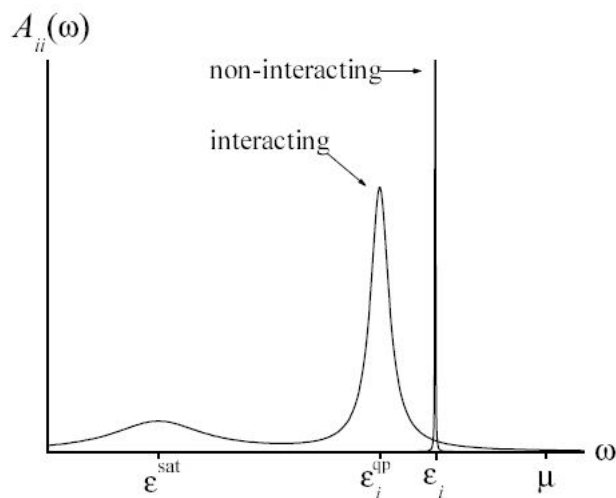


Figure 1.5: In an independent particle model, excitations measured by photoemission are series of delta peaks. When interactions are taken into account, the peak is shifted, and, since the lifetime of the excitation is finite, it is broadened. It has become a quasiparticle peak. Moreover, in addition to the main quasiparticle peak, new structures can appear. They are the satellites. From Ref. [54].

the delta peak of the independent-particle model is broadened and renormalized (see Fig. 1.5). Moreover, in addition to the quasiparticle peak, the interaction between the different excitations can produce also further structures: the satellites. In particular, the presence of satellites in the spectral function is due to the fact that screening of Coulomb interaction is essentially a dynamical effect. This, in turn, can lead to a transfer of spectral weight from the coherent one-quasiparticle part of the spectrum to the incoherent part associated to satellites.

A photoemission spectrum is much richer than in an independent-particle model. In fact, the fingerprints of electronic interactions are immediately visible in a one-particle excitation spectrum (see Fig. 1.5). For this reason it is particularly important to be able to extract the information contained in these spectra, in order to describe the electronic properties of the many-electron system.

1.3.2 From Wigner and Mott to strong correlations

The homogeneous electron gas, in the high-density limit (small r_s), when the kinetic energy dominates, is the simplest model for metals. But, since the kinetic energy has a r_s^{-2} dependence and the Coulomb energy is proportional to r_s^{-1} , in the dilute limit (large r_s), the latter prevails. In this limit, the

1.3 Beyond the independent-particle picture

electrons are trapped by the Coulomb repulsion with their neighbors. They form an ordered lattice (a “collective phase” [55]), called Wigner lattice [56], and oscillate around their lattice sites. So they have a very different behavior than in a metal, where they are almost free to travel around the system. The Wigner lattice is the first example of strongly correlated system, a system where the Coulomb interaction prevails and induces localization over delocalization, spatial order over disorder. Where one may expect a metal, an insulator is instead found.

Using the simple electron counting, based on the Bloch band-structure model, NiO should be a metal. Instead it is an insulator [57]. This is a clear evidence that the Bloch independent-particle picture is not valid in NiO.

This situation can be easily generalized to other examples. Mott [57], in particular, considered a simple cubic lattice of hydrogen atoms. Since there is one electron per primitive cell, in the Bloch picture this system should be always metallic. Instead, increasing the lattice constant, at a certain point the system becomes an insulator (a Mott insulator). Each electron remains localized around its proton. Since there is no more overlap between different orbitals, the electrons cannot travel from one site to another. When the overlap is large enough, the electrons tend to delocalize to gain in kinetic energy. Otherwise, the Coulomb repulsion prevents two electrons from being on the same site. They remain trapped on the site of their proton. This is clearly the same situation as the one that occurs in the homogeneous electron gas in the dilute limit, when the Wigner crystal is formed.

The Hubbard model [58] formalized the ideas of Mott. In its simplest formulation only one energy level is considered. It is hence the same situation as in the Mott example, where one deals with hydrogen atoms. In this case, the one-band Hubbard model is described by the Hamiltonian:

$$\hat{H} = -t \sum_{\langle ij \rangle \sigma} (\hat{c}_{i\sigma}^\dagger \hat{c}_{j\sigma} + h.c.) + U \sum_i \hat{n}_{i\uparrow} \hat{n}_{i\downarrow}. \quad (1.44)$$

The first term is the kinetic energy. In the formalism of the second quantization (with creation and annihilation operators \hat{c}^\dagger and \hat{c}), one electron moves from the site i to the site j – and vice versa – with probability t (the hopping term, in a tight-binding approach). The sum is limited to pairs of nearest neighbors and one assumes a regular lattice where the hopping t is just a constant. In particular, the spin $\sigma = \{\uparrow, \downarrow\}$ has been explicitly evidenced. As a matter of fact, for the Pauli principle, two electrons can be on the same hydrogen atom only if they have opposite spin. The second term in the Hubbard Hamiltonian (1.44), where $\hat{n}_{i\sigma} = \hat{c}_{i\sigma}^\dagger \hat{c}_{i\sigma}$, describes the energy penalty U to pay in case of a double occupation of a site. U is the on-site Coulomb repulsion energy.

In this way one formulates a simplification of the full many-body Hamiltonian (1.1), by introducing another effective Hamiltonian, with a reduced

1. Introduction

number of degrees of freedom and a spatial discretization. One then introduces in this model Hamiltonian some coupling constants, like the Hubbard U , which have also to account for the other degrees of freedom that are not explicitly included in the new effective Hamiltonian.

The competition between the kinetic term t and interaction term U determines the properties of the system. The phase diagram of the Hubbard model depends on the ratio U/t and on the electron density. In particular, the U/t ratio is increased when the lattice constant of the array of H atoms is increased (and vice versa). For small densities (less than one electron per site) the number of holes is always different from zero. For large densities (more than one electron per site) there is always a site with double occupation. In both cases charge fluctuations are always possible and the electrons can travel around without further costs. Hence, the system is always metallic. When there is exactly one electron per site (“half filling”), as in the Mott example, there is a phase transition from a metal when $t \gg U$ to a Mott insulator when $U \gg t$. If the electrons move slowly (i.e. their kinetic energy is small), they stay longer on a site and they experience more the repulsion with the other electron on the site. If this energy cost becomes too large, it can become convenient to stop moving and localize on the site. The system hence becomes an insulator.

The Hubbard model describes the competition between localized and itinerant electronic character, particle-like and wave-like behaviors. The independent-particle system ($U = 0$) is diagonal in momentum space. In this case the system is characterized by one band of width W , centered at the Fermi energy E_F . The Hamiltonian can be exactly diagonalized:

$$\hat{H} = \sum_{\mathbf{k}\sigma} \epsilon_{\mathbf{k}} \hat{c}_{\mathbf{k}\sigma}^\dagger \hat{c}_{\mathbf{k}\sigma}. \quad (1.45)$$

In a simple d dimensional cubic lattice, the band dispersion is given by $\epsilon_{\mathbf{k}} = -2t \sum_d \cos(k_d a)$ (where a is the lattice constant). This band dispersion yields a bandwidth $W = 2td$.

In the atomic limit ($t = 0$) the system becomes diagonal in real space. The one-particle excitation spectrum is characterized by two delta peaks at $E_F \pm U/2$. They correspond to the possibility to add or remove an electron from the atom. Close to the atomic limit, the electronic motion can be treated as a perturbation. One starts from atomic excitations that get broadened by orbital overlaps and give rise to “incoherent bands” (Hubbard bands), which remain better described in real space than in momentum space. In this case, one assists to the breakdown of the one-particle picture. The excitation spectrum doesn’t show anymore features with a clear single peak that can be assigned to a single particle-like excitation. The metal-insulator transition occurs when $U \sim W$, with a closure of the gap between the two Hubbard bands that get progressively closer each other.

1.3 Beyond the independent-particle picture

Furthermore, close to the atomic limit, different energy scales can become important at low temperatures. The system can display a great sensibility to external parameters that can induce various phase transitions. In particular, the Mott transition is often accompanied by a long-range antiferromagnetic ordering. This symmetry breaking is not a correlation effect, but it is due to the possibility of hopping between different sites. When $U \gg t$, at half filling each site is occupied by an electron. A hopping between two neighboring sites cannot occur if the two electrons have parallel spins. On the contrary, the hopping is mostly favored when the electrons have antiparallel spins. This explains why a Mott insulator is often antiferromagnetic. In this case, the symmetry breaking leads to a doubling of a unit cell and one is left with an insulator with a completely filled valence band [59].

Moreover, if in particular structural changes occur, in the Mott-Hubbard model they can be only a consequence of the electronic metal-insulator transition. Hence they are a secondary manifestation of electronic correlation. This is in contrast to the Peierls model [60], where instead the lattice degrees of freedom are at the origin of a metal-insulator transition. The Peierls model can be easily understood by considering an infinite linear chain of atoms. If the atoms are slightly displaced, for instance leading to a dimerization, the first Brillouin zone results halved. The band dispersion is modified by the distortion. The change in the band structure can be calculated in a nearly-free-electron model, by considering the distortion as a small perturbation. In this case the distortion yields a opening of a band gap in the middle of the ordinary Brillouin zone and induces a metal-insulator transition in case the gap is opened in coincidence with the top valence of the undistorted band structure. One therefore can conclude that a metallic one-dimensional chain is unstable with respect to lattice distortions. The Peierls model can be straightforwardly generalized to the three-dimensional case [60].

Concerning real systems, in materials characterized by partially filled d and f shells, where narrow bands are present, correlation is expected to play an important role (see Fig. 1.6). In particular, recently much attention has been given to the high- T_c superconductors, which are considered as doped Mott insulators. Moreover, transition-metal oxides are often good candidates to be Mott insulators [61]. In fact, for the metallic element of the compound the direct overlap between $3d$ orbitals is small. Generally the hopping between these orbitals is mediated by the hybridization with the oxygen $2p$ orbitals. The hopping t is then in general quite small. It can be estimated by the ratio between the overlap integral $2p-3d$, calculated in a tight-binding approach, and the charge transfer energy: $\epsilon_d - \epsilon_p$, which is the difference between the average position of the oxygen $2p$ and the transition metal $3d$ band. When $\epsilon_d - \epsilon_p$ is large, bonding states are mainly from oxygen $2p$ orbitals and antibonding states from the metal $3d$ states. In this case the hopping is small. The on-site Hubbard U depends instead on the effective screening from the $4s$ states of the metal. The larger is the difference $\epsilon_s - \epsilon_d$,

1. Introduction

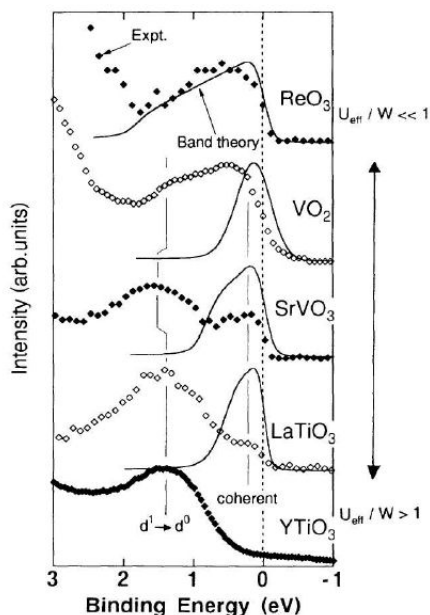


Figure 1.6: Photoemission spectra (dots) of different metallic d^1 compounds. Going upside-down, the ratio U/W increases and correlation effects become more important. While the coherent quasiparticle peak becomes more and more weak, the incoherent satellites becomes more and more pronounced. Solid curves are independent-particle calculations. From Ref. [64]

the less efficient is the screening and larger is U . The interplay of these factors determines whether a transition-metal oxide is a Mott insulator (as for “early” transition metals, as Ti, V, Cr...) or a charge-transfer insulator (as for “late” transition metals, as Ni and Cu) [62][61]. While in the former case, in the Mott-Hubbard picture, the band gap is originated only by $d-d$ interactions, in the latter case also O $2p$ states are involved, since they lie in the gap between occupied and unoccupied d states [63]. So, going beyond the Mott-Hubbard model, in charge-transfer insulators one has to take into account also charge fluctuations within the unit cell between the oxygen and the transition-metal sites [62].

In Fig. 1.6 a series of photoemission spectra for different d^1 compounds is presented [64]. Since from one compound to another the lattice-structure properties are different, the overlap between d orbitals and the consequent width W of the d bands have different sizes. Increasing the ratio U/W (which is equivalent to the ratio U/t), localized atomic-like excitations (the Hubbard bands) appear in the photoemission spectra, together with quasiparticle peaks, closer to the Fermi energy.

Photoemission spectroscopy confirms to be an invaluable tool to study

1.3 Beyond the independent-particle picture

the effects of correlation on the electronic properties of a solid. In chapter 3 I will present a brief introduction to the many-body perturbation theory where the key ingredients are the one-particle Green's function, which represent the natural quantities one can use to interpret photoemission spectra beyond the independent-particle model.

In this first chapter I have introduced the complexity inherent the many-body problem. I have underlined that this complexity is actually the origin of its great interest. I have discussed the limits of an independent-particle picture to describe some prototypical spectroscopy experiments and the need to introduce new quantities able to interpret the physical effects that emerge from spectroscopy results. This will be in particular the subject of Chapters 3 and 5. For instance, in the interpretation of photoemission, one needs to go beyond an interpretation based on the density of one-particle states and introduces the spectral function $A(\omega)$. In Chapter 3 the spectral function will be rigorously defined as imaginary part of the Green's function G and the framework where it possible to calculate G and A will be illustrated. In the next chapter I will instead present some theoretical tools to determine the ground state of an interacting electronic system, which represents the starting point for any theoretical spectroscopy calculation.

Chapter 2

Ground-state properties

In order to simulate spectroscopy measurements one has to calculate the excited states of the electronic system. But, first of all, the ground state has to be determined. In this chapter I introduce the key ideas of the density-functional theory (DFT). DFT is the practical first-principles scheme that is currently employed in the calculation of the ground-state properties. DFT is a “minimum-information theory”. Instead of dealing with the many-body wavefunction $\Psi(\mathbf{r}_1, \dots, \mathbf{r}_N)$, DFT leads to calculate directly the simplest quantity, i.e. the electronic density $\rho(\mathbf{r})$, that one needs in order to have access to the ground-state properties. This is an important aspect of DFT that I will further discuss in Chapter 7.

Many books (see e.g. [65]) and reviews (see e.g. [66]) have been written on DFT. In particular, in the review of van Leeuwen [67] a complete introduction also to the mathematical details of the theory can be found.

2.1 The variational principle

Determining the ground state of a system of N electrons means finding the lowest eigenvalue E_0 of the Schrödinger equation (1.1). This corresponds to the calculation of the wavefunction Ψ_0 that yields the minimum:

$$E_0 = \min_{\Psi} E[\Psi] = \min_{\Psi} \langle \Psi | \hat{H} | \Psi \rangle = \min_{\Psi} \langle \Psi | \hat{T} + \hat{V}_{ext} + \hat{W} | \Psi \rangle \quad (2.1)$$

of the sum of the kinetic energy \hat{T} , the external potential \hat{V}_{ext} and the electron-electron interaction \hat{W} . A particular case is represented by the Hartree-Fock approximation, where one restricts the search of the minimum to the set of wavefunctions that are Slater determinants (see Eq. (1.36)).

However, since the Coulomb potential $v(|\mathbf{r}_i - \mathbf{r}_j|)$ is a two-particle interaction, the knowledge of the full many-body wavefunction Ψ_0 is actually not required for the determination of E_0 . The total energy can be in fact

2. Ground-state properties

calculated as:

$$E = -\frac{1}{2} \int d\mathbf{r} \nabla^2 \gamma(\mathbf{r}, \mathbf{r}') \Big|_{\mathbf{r}'=\mathbf{r}} + \int d\mathbf{r} \rho(\mathbf{r}) V_{ext}(\mathbf{r}) + \int d\mathbf{r} d\mathbf{r}' \rho_2(\mathbf{r}, \mathbf{r}') v(|\mathbf{r} - \mathbf{r}'|), \quad (2.2)$$

in terms of the pair density $\rho_2(\mathbf{r}, \mathbf{r}')$, the one-particle density matrix $\gamma(\mathbf{r}, \mathbf{r}')$, and the density $\rho(\mathbf{r})$. The total energy in this way turns out to be a functional, $E = E[D_2]$, of the two-particle density matrix D_2 :

$$\begin{aligned} D_2(\mathbf{r}_1, \mathbf{r}_2; \mathbf{r}'_1, \mathbf{r}'_2) &= \\ &= N(N-1) \int d\mathbf{r}_3 \dots \mathbf{r}_N \Psi^*(\mathbf{r}_1, \mathbf{r}_2, \mathbf{r}_3, \dots, \mathbf{r}_N) \Psi(\mathbf{r}'_1, \mathbf{r}'_2, \mathbf{r}_3, \dots, \mathbf{r}_N). \end{aligned} \quad (2.3)$$

In fact ρ_2 , γ and ρ are all directly linked to D_2 :

$$\rho_2(\mathbf{r}, \mathbf{r}') = D_2(\mathbf{r}, \mathbf{r}'; \mathbf{r}, \mathbf{r}'); \quad (2.4)$$

$$\gamma(\mathbf{r}, \mathbf{r}') = \frac{1}{N-1} \int d\mathbf{r}_2 D_2(\mathbf{r}, \mathbf{r}_2; \mathbf{r}', \mathbf{r}_2); \quad (2.5)$$

$$\rho(\mathbf{r}) = \frac{1}{N-1} \int d\mathbf{r}_2 D_2(\mathbf{r}, \mathbf{r}_2; \mathbf{r}, \mathbf{r}_2). \quad (2.6)$$

Therefore, the calculation of the ground-state energy could be thought as a variational search of a minimum with respect to the much simpler D_2 instead of the complicate Ψ :

$$E_0 = \min_{D_2} E[D_2] = \min_{D_2} \langle \Psi | \hat{H} | \Psi \rangle. \quad (2.7)$$

Actually, this search has to be restricted to the two-particle density matrix D_2 obtained from normalisable and antisymmetric wavefunctions Ψ (otherwise an arbitrary function of N variables could lead to a lower minimum). This is a constraint known as the N -representability condition of D_2 . In other words, this constrained-search approach, formally introduced by Levy [68], is a two-step procedure. One should first look for the Ψ that generate D_2 and then calculate the minimum of the functional $E[D_2]$:

$$E_0 = \min_{D_2} \left\{ \min_{\Psi \rightarrow D_2} \langle \Psi | \hat{H} | \Psi \rangle \right\}. \quad (2.8)$$

This N -representability condition could be made operational if it were reformulated as a Lagrange multiplier. One should introduce the proper constraint in (2.8), but this general issue for the two-particle density matrix D_2 has not been solved yet.

Instead, it is possible to use the density matrix $\gamma(\mathbf{r}, \mathbf{r}')$ as the key variable. The ground-state energy E_0 in this case becomes:

$$E_0 = \min_{\gamma} E[\gamma] = \min_{\gamma} \left\{ -\frac{1}{2} \int d\mathbf{r} \nabla^2 \gamma(\mathbf{r}, \mathbf{r}') \Big|_{\mathbf{r}'=\mathbf{r}} + \int d\mathbf{r} \gamma(\mathbf{r}, \mathbf{r}) V_{ext}(\mathbf{r}) + W[\gamma] \right\}. \quad (2.9)$$

2.1 The variational principle

Here one has to pay the price that now the explicit functional dependence with respect to γ of the interaction term $W[\gamma]$

$$W[\gamma] = \min_{\Psi \rightarrow \gamma} \langle \Psi | \hat{W} | \Psi \rangle \quad (2.10)$$

is not known anymore and has to be approximated. Different strategies to find good approximations are currently studied [69]. Anyway, the N -representability constraint for the density matrix can be expressed easily in terms of the natural orbitals φ_i and the occupation numbers n_i :

$$\gamma(\mathbf{r}, \mathbf{r}') = \sum_{i=1}^{\infty} n_i \varphi_i^*(\mathbf{r}) \varphi_i(\mathbf{r}'), \quad (2.11)$$

where the natural orbitals φ_i and the occupation numbers n_i are solutions of the equation:

$$\int d\mathbf{r}_2 \gamma(\mathbf{r}_1, \mathbf{r}_2) \varphi_i(\mathbf{r}_2) = n_i \varphi_i(\mathbf{r}_1), \quad (2.12)$$

and the n_i are subject to the double constraint:

$$\sum_{i=1}^{\infty} n_i = N \quad 0 \leq n_i \leq 1. \quad (2.13)$$

The first condition can be transformed easily into a Lagrange multiplier, together with the orthonormality condition on the φ_i . The variational principle can be then applied to the following quantity [70]:

$$\frac{\delta}{\delta \gamma} \left\{ E[\gamma] - \mu \left(\sum_{i=1}^{\infty} n_i - N \right) - \sum_{i,j=1}^{\infty} \epsilon_{ij} \left(\int d\mathbf{r} \varphi_i^*(\mathbf{r}) \varphi_j(\mathbf{r}) - \delta_{ij} \right) \right\} = 0. \quad (2.14)$$

The Gilbert's theorem [71] guarantees that the ground-state expectation value of any observable of the system is a unique functional of the density matrix γ . In this way a density-matrix functional theory is established. Its great advantage is that the kinetic energy is still a known functional of γ . On the other side, the theory has two technical disadvantages that make more difficult its application to concrete calculations. First, the second constraint in (2.13) allows for border minima in the occupation number optimization and in this case the minimum does not stem from the variational principle condition (2.14). There may be solutions ("pinned states" [69]), corresponding to occupation numbers which are exactly equal to 0 or 1, that do not satisfy Eq. (2.14). Second, the density matrix is idempotent if and only if it corresponds to a Slater determinant [72]. In other words, given a density matrix γ of an interacting system, it is not possible to define a fictitious system of noninteracting particles that yields the same γ . In density-functional theory, as I will discuss in the next section, the introduction of such a fictitious noninteracting system (the Kohn-Sham system), capable to reproduce

2. Ground-state properties

a given density ρ of an interacting system, has represented a fundamental breakthrough, which cannot be analogously exploited in the density-matrix framework (see also Sec. 7.5).

2.2 Density-functional theory

The density-functional theory (DFT) is minimum-information theory. The Hohenberg-Kohn theorem [73] proves that the electronic density $\rho(\mathbf{r})$ is the simplest quantity that in principle one needs to know in order to calculate all the ground-state properties, such as the ground-state energy E_0 . Moreover, thanks to the Kohn-Sham scheme [74], a very efficient method has been devised to calculate $\rho(\mathbf{r})$. This scheme is based on a one-particle Schrödinger equation with an effective potential, the Kohn-Sham potential $V_{KS}(\mathbf{r})$. Finally, already a very simple approximation such as the local-density approximation (LDA) [74], has turned out to be very successful, even beyond any initial expectations. These three observations justify the enormous success of DFT in condensed-matter physics.

In the previous section I have shown that for the calculation of the ground-state energy one doesn't need to solve the full many-body Schrödinger equation, but much simpler quantities can be used to get the same result. Hohenberg and Kohn [73] have determined the simplest of these possible variables. The Hohenberg-Kohn theorem proves that, for a system with a nondegenerate ground state, there exists a one-to-one correspondence, up to an additive constant, between the ground-state density $\rho(\mathbf{r})$ and the static external potential $V_{ext}(\mathbf{r})$. Since there is also a one-to-one correspondence between the external potential and the ground-state many-body wavefunction Ψ , Ψ can be written as a functional of the density $\Psi = \Psi[\rho]$.

The Hohenberg-Kohn theorem is valid only for the densities that are the ground state of some potential. These densities are called V -representable. While the V -representability condition assesses the existence of the one-to-one mapping between ρ and V_{ext} , the Hohenberg-Kohn theorem establishes its uniqueness. In general all reasonable densities are V representable. In the worst case, the potential has degenerate ground states such that the given ρ is representable as a linear combination of the degenerate ground-state densities (the density is then called “ensemble- V -representable”) [75].

The Hohenberg-Kohn theorem has been then generalized in many ways: to cases where the ground states is degenerate, or where the system is spin-polarized, to relativistic DFT [76], to multicomponent DFT [77], to DFT for superconductors [78], and so on. In particular, in Sec. 5.4 I will discuss the extension of DFT to situations where a time-dependent potential is applied to the system.

The Hohenberg-Kohn theorem introduces a dramatic simplification. Instead of having to calculate Ψ , that is a function of $3N$ variables, one has

2.2 Density-functional theory

to calculate only a function of 3 variables, and yet obtains the same desired ground-state properties, such as the ground-state energy E_0 . From this point of view, Ψ and ρ are perfectly equivalent.

However, from the practical point of view, the functional dependence of the ground-state properties with respect to ρ is in general not known. In the case of the ground-state energy one has [79]:

$$E_0 = \min_{\rho} E[\rho] = \min_{\rho} \left\{ \int d\mathbf{r} \rho(\mathbf{r}) V_{ext}(\mathbf{r}) + F[\rho] \right\}, \quad (2.15)$$

where the functional

$$F[\rho] = \min_{\Psi \rightarrow \rho} \langle \Psi | \hat{T} + \hat{W} | \Psi \rangle \quad (2.16)$$

has an unknown dependence with respect to density. $F[\rho]$ is a universal functional, in the sense that it doesn't depend on the external potential. Thanks to the one-to-one mapping between the density and the external potential, the total energy can be thought as a functional of V_{ext} . Therefore, from a mathematical point of view, F is the Legendre transform [67] of E and one can prove that:

$$\frac{\delta E}{\delta V_{ext}(\mathbf{r})} = \rho(\mathbf{r}) \quad (2.17)$$

and

$$\frac{\delta F}{\delta \rho(\mathbf{r})} = -V_{ext}(\mathbf{r}). \quad (2.18)$$

In fact:

$$\frac{\delta E}{\delta V_{ext}(\mathbf{r})} = \frac{\delta \langle \Psi | \hat{H} | \Psi \rangle}{\delta V_{ext}(\mathbf{r})} = E \frac{\delta \langle \Psi | \Psi \rangle}{\delta V_{ext}(\mathbf{r})} + \rho(\mathbf{r}) = \rho(\mathbf{r})$$

and (see Eq. (2.15)):

$$\frac{\delta F}{\delta \rho(\mathbf{r})} = \int d\mathbf{r}' \frac{\delta E}{\delta V_{ext}(\mathbf{r}')} \frac{\delta V_{ext}(\mathbf{r}')}{\delta \rho(\mathbf{r})} - \int d\mathbf{r}' \rho(\mathbf{r}') \frac{\delta V_{ext}(\mathbf{r}')}{\delta \rho(\mathbf{r})} - V_{ext}(\mathbf{r}) = -V_{ext}(\mathbf{r}).$$

The N -representability condition for the density

$$\int d\mathbf{r} \rho(\mathbf{r}) = N \quad (2.19)$$

can be easily added as a Lagrange multiplier to the energy functional $E[\rho]$ and the minimum could be calculated once an approximation to $F[\rho]$ has been chosen. In the case of the so-called density-only approaches [80], in fact one tries to approximate directly $F[\rho]$.

A historical approximation, in this context, is the Thomas-Fermi-Dirac method [81][82][83], where one approximates $F[\rho]$ with:

$$F[\rho] = \frac{3}{10} (3\pi^2)^{\frac{2}{3}} \int d\mathbf{r} \rho^{\frac{5}{3}}(\mathbf{r}) + \frac{1}{2} \int d\mathbf{r} d\mathbf{r}' \frac{\rho(\mathbf{r})\rho(\mathbf{r}')}{|\mathbf{r} - \mathbf{r}'|} - \frac{3}{4} \left(\frac{3}{\pi}\right)^{\frac{1}{3}} \int d\mathbf{r} \rho^{\frac{4}{3}}(\mathbf{r}). \quad (2.20)$$

2. Ground-state properties

In this sum the first and last terms are the kinetic and exchange energies. They are approximated through a local-density approximation, valid in principle only for slowly varying densities. In this approximation, both energy contributions are calculated considering at each space point \mathbf{r} the corresponding energy per particle of the homogeneous electron gas of density $\bar{n} = n(\mathbf{r})$ and then integrating over all the points \mathbf{r} . The remaining term in (2.20) is then the classical Hartree energy $E_H[\rho]$ (see Eq. (1.9)).

The density-only strategy would be very tempting, since calculations would scale linearly with the number of atoms in the system. The main problem consists in finding a good approximation to the kinetic energy, beyond the local-density approximation. From the virial theorem [67] one in fact knows that the kinetic energy is of the same order as the total energy. For example, the Von Weizsacker [84] kinetic functional:

$$T[\rho] = \frac{1}{8} \int d\mathbf{r} \frac{(\nabla\rho(\mathbf{r}))^2}{\rho(\mathbf{r})} \quad (2.21)$$

is a first generalization towards the inclusion of corrections of higher order gradients of the density [85], but it is still not enough to obtain satisfactory results.

2.2.1 The Kohn-Sham system

In order to overcome the problem of finding an approximation of $F[\rho]$ directly based on the density, Kohn and Sham [74] formulated an alternative efficient strategy. They proposed to introduce a fictitious system of noninteracting electrons subjected to an effective external potential, V_{KS} , with the property that it yields the same density as the real interacting system.

Whether this is always possible is a subtle question. Recent works [67] have shown that for every interacting V -representable density there is a noninteracting V -representable density arbitrarily close to it.

In the noninteracting Kohn-Sham system $\dot{W} = 0$, then Eq. (2.18) becomes:

$$\frac{\delta F_{KS}}{\delta\rho(\mathbf{r})} = \frac{\delta T_{KS}}{\delta\rho(\mathbf{r})} = -V_{KS}(\mathbf{r}). \quad (2.22)$$

Defining:

$$E_{xc}[\rho] = F[\rho] - T_{KS}[\rho] - E_H[\rho] \quad (2.23)$$

and differentiating (2.23) with respect to the density ρ :

$$V_{xc}(\mathbf{r}) = -V_{ext}(\mathbf{r}) + V_{KS}(\mathbf{r}) - V_H(\mathbf{r}), \quad (2.24)$$

one finds the definition of the effective Kohn-Sham potential V_{KS} in terms of the external potential V_{ext} , the Hartree potential V_H :

$$V_H(\mathbf{r}) = \int d\mathbf{r}' v(|\mathbf{r} - \mathbf{r}'|) \rho(\mathbf{r}'), \quad (2.25)$$

2.2 Density-functional theory

and the exchange-correlation potential V_{xc} :

$$V_{xc}(\mathbf{r}) = \frac{\delta E_{xc}}{\delta \rho(\mathbf{r})}, \quad (2.26)$$

which is not known analytically and has to be approximated.

Since in the Kohn-Sham system the fictitious electrons are noninteracting, the many-body wavefunction Ψ_{KS} is a Slater determinant (1.36), formed by the Kohn-Sham orbitals φ_i . The variational principle can be reformulated directly in term of the φ_i :

$$\frac{\delta}{\delta \varphi_i} \left[E - \sum_{k,l=1}^N \epsilon_{kl} \left(\int d\mathbf{r} \varphi_k^*(\mathbf{r}) \varphi_l(\mathbf{r}) - \delta_{kl} \right) \right] = 0. \quad (2.27)$$

In this way one obtains the Kohn-Sham equations

$$\left(-\frac{\nabla^2}{2} + V_{KS}[\rho](\mathbf{r}) \right) \varphi_i(\mathbf{r}) = \epsilon_i \varphi_i(\mathbf{r}), \quad (2.28)$$

whose solution permits to get the exact density of the interacting system as:

$$\rho(\mathbf{r}) = \sum_{i=1}^N |\varphi_i(\mathbf{r})|^2. \quad (2.29)$$

This is indeed a noteworthy result: the solution of the many-body Schrödinger equation has been converted in a set of self-consistent one-particle Schrödinger equations in the effective potential V_{KS} .

In (2.28) the eigenvalues ϵ_i are a by-product of the Kohn-Sham approach. They are the Lagrange multipliers appearing in Eq. (2.27). Since an analogous of Koopmans' theorem doesn't hold for the Kohn-Sham equations, the eigenvalues don't have a physical meaning. There is the sole exception of the highest occupied ϵ_N , which is equal to the ionization energy of the system [86]:

$$\epsilon_N = -I. \quad (2.30)$$

This is a consequence of the fact that the ionization energy determines the asymptotic form of the density in the vacuum and this is well reproduced in DFT. In particular, in the Kohn-Sham scheme it depends on highest occupied eigenvalue.

Therefore, strictly speaking, the Kohn-Sham eigenvalues in any case are not excitations energies. Nevertheless they are often interpreted in terms of band structure. And this can be at the origin of relevant misunderstandings.

The functional dependence of V_{xc} with respect to the density ρ is highly non-analytical and nonlocal. A small variation of a density in a point \mathbf{r} can induce a great variation of the potential in a point \mathbf{r}' [54]. This observation is at the basis of many pathologies of the exact V_{xc} . Its effects have been

2. Ground-state properties

analyzed for instance in the case of two widely separated open-shell atoms or in an insulator subjected to a uniform electric field [87].

In a solid the addition of an electron induces an infinitesimal change to the density. Nevertheless the potential changes of a finite constant value:

$$\Delta = V_{xc}^{N+1}(\mathbf{r}) - V_{xc}^N(\mathbf{r}) + O(1/N). \quad (2.31)$$

This is the origin of the so-called band gap problem of DFT [88][89]. The gap in an insulator is the difference between the ionization potential I and the affinity A : $E_{gap} = I - A$ (see Eq. (1.43)). Since the affinity of a system of N electrons is equal to the ionization potential of the system of $N + 1$ electrons, using Eq. (2.30), one has:

$$E_{gap} = \epsilon_{N+1}^{N+1} - \epsilon_N^N. \quad (2.32)$$

Hence:

$$E_{gap} = \epsilon_{N+1}^{N+1} - \epsilon_{N+1}^N + \epsilon_{N+1}^N - \epsilon_N^N = \Delta + E_{gap}^{KS}, \quad (2.33)$$

where E_{gap}^{KS} is what one obtains by solving the Kohn-Sham equations (with N particles) as difference between the lowest unoccupied and the highest occupied eigenvalues. This explicitly demonstrates that in any case $E_{gap}^{KS} \neq E_{gap}$.

Not even in a metallic system the Kohn-Sham eigenvalues can be interpreted as quasiparticle energies. For example, the Kohn-Sham equations applied to the homogeneous electron gas would yield the same bad results as the Hartree approximation. In fact the Kohn-Sham potential is local and static and hence a constant number in any homogeneous system. Instead, the correct theory to define quasiparticle band structures, for both insulators and metals, relies upon the Green's-function formalism and will be introduced in the next chapter.

2.2.2 Approximations of the exchange-correlation potential

The Kohn-Sham scheme is a very efficient method for ground-state calculations. The whole complexity of the many-body problem has been reduced to find a good approximation of the exchange-correlation potential V_{xc} .

The simplest approximation introduced by Kohn and Sham is the local-density approximation (LDA), the same approximation that Thomas and Fermi had applied to the kinetic energy (see Eq. (2.20)). The great advantage of the Kohn-Sham LDA with respect to the Thomas-Fermi approach is that one has to approximate a much smaller quantity, E_{xc} , than the kinetic energy. So also the error introduced by the approximation will be much smaller. In LDA the exchange-correlation energy is:

$$E_{xc}^{LDA}[\rho] = \int d\mathbf{r} \rho(\mathbf{r}) \varepsilon_{xc}^{HEG}(\rho(\mathbf{r})). \quad (2.34)$$

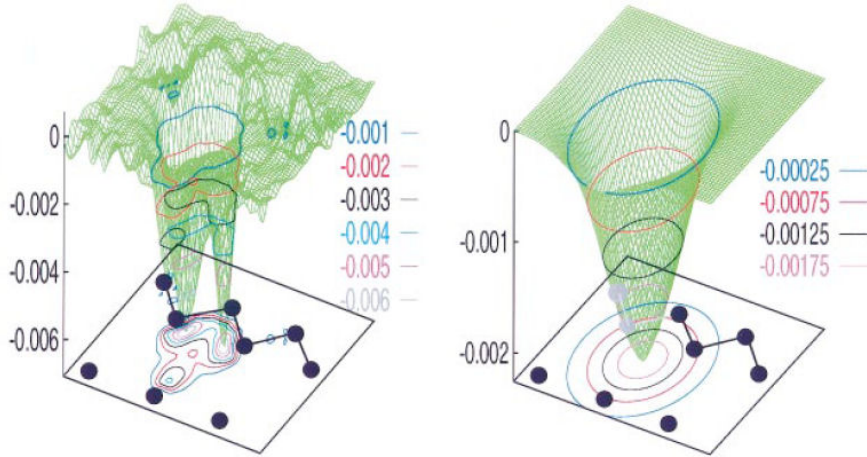


Figure 2.1: Comparison of an accurate Montecarlo calculation and an LDA approximation for the exchange-correlation hole for an electron at the tetrahedral interstitial site in the (110) plane of bulk silicon. The atoms and bonds are schematically represented for bond chains along the [111] direction. From Ref. [28].

The true system is locally approximated by a homogeneous electron gas with density $\bar{\rho} = \rho(\mathbf{r})$. The exchange-correlation energy per particle of the homogeneous electron gas, ε_{xc}^{HEG} , can be accurately calculated with quantum Montecarlo methods [90]. The results of these calculations are then parametrized in order to be used in practical LDA calculations [91].

LDA resulted to be more accurate than the initial expectations, which had defined its domain of validity to systems with a slowly varying density. Its accuracy relies on cancellations of the errors in the approximations of the exchange and correlation terms (LDA underestimates exchange and overestimates correlation [49]) and from the fact that LDA satisfies the sum rules for the exchange-correlation hole ρ_{xc} (see Eq. (1.6)) [92][93]. As Fig. 2.1 shows, even though LDA is not able to yield a good description of the shape of the exchange-correlation hole, it provides a very good estimate of its spherical average, which is what one actually needs in ground-state calculations [92][93].

In order to take better into account systems where the density varies more strongly, LDA has been generalized to the so called generalized-gradient approximation (GGA) [94]. In this approximation ε_{xc}^{HEG} becomes a function of the density and its gradients, with some free parameters that are obtained either from sum rules or fitted to experiments. GGA is widely used in chemistry because it improves the calculations of dissociation energies. Anyway, a systematic improvement with respect to LDA cannot be found.

2. Ground-state properties

In particular, both LDA and GGA suffer from a self-interaction problem: each electron feels the potential of *all* the electrons instead of *all the other* electrons. The consequences of this problem are different. In particular, the approximated Kohn-Sham potential decays more rapidly than r^{-1} , as the exact one does. This is the origin of the fact that Rydberg series cannot be described, negative ions are not bound, and ionization potentials are often too small.

The correct asymptotic behavior of the exchange-correlation potential (for closed-shell systems with spherical symmetry) has been obtained using the adiabatic-connection fluctuation-dissipation (ACDF) theorem [95]. Moreover, potentials derived in this framework are able to describe correctly dispersion forces [96][97][98], where the nonlocality in the functional dependence of the correlation energy with the density and a correct balance between the approximations for exchange and correlation are crucial [99]. Nevertheless, the ACDF approach is very cumbersome and has been used only for few applications.

Alternative approximations that remedy the self-interaction deficiency of LDA/GGA are the self-interaction correction (SIC) scheme [100] and the exact-exchange (EXX) approximation [101]. In the former one explicitly subtracts from the DFT energy functional the spurious self-interaction for each occupied state. The self-interaction correction vanishes for extended states, but it is important for spatially localized states. In this sense, the SIC is linked to the gain in energy associated with localization [102]. The exact-exchange approximation tracks in a DFT framework the spirit of self-interaction correction of the Fock exchange term (1.39) with respect to the Hartree term (1.38). In the following section I will show how EXX arises naturally as a particular approximation to the energy functional in the optimized effective potential (OEP) approach. In Sec. 7.1 I will discuss an alternative equivalent derivation of the OEP-EXX scheme (see Eq. (7.10)).

2.2.3 Optimized effective potential method

The optimized effective potential (OEP) method was originally created in order to approximate the Hartree-Fock method by constructing a local potential whose eigenfunctions minimize the Hartree-Fock energy [103][104]. It has then been applied in the DFT framework.

In the OEP context the DFT energy functional is thought as an explicit orbital functional $E[\{\varphi_i, \epsilon_i\}]$, and hence only an implicit density functional. Thanks to the Hohenberg-Kohn theorem, the variational condition (2.15) can be formulated in terms of the Kohn-Sham potential [105]:

$$\frac{\delta E[\varphi_i, \epsilon_i]}{\delta V_{KS}(\mathbf{r})} = 0. \quad (2.35)$$

2.2 Density-functional theory

The functional derivative is then calculated using a chain rule:

$$\frac{\delta E}{\delta V_{KS}(\mathbf{r})} = \sum_j \int d\mathbf{r}' \left[\frac{\delta E}{\delta \varphi_j^*(\mathbf{r}')} \frac{\delta \varphi_j^*(\mathbf{r}')}{\delta V_{KS}(\mathbf{r})} + h.c. \right] + \frac{\partial E}{\partial \epsilon_j} \frac{\delta \epsilon_j}{\delta V_{KS}(\mathbf{r})}. \quad (2.36)$$

After some algebra [105] and making use of the constraint that the orbitals φ_i are solution of the Kohn-Sham equation with a local potential, one finds the OEP equation for V_{xc} :

$$\int d\mathbf{r}' \chi_{KS}(\mathbf{r}, \mathbf{r}', \omega = 0) V_{xc}(\mathbf{r}') = \Lambda_{xc}(\mathbf{r}), \quad (2.37)$$

where:

$$\chi_{KS}(\mathbf{r}, \mathbf{r}', \omega = 0) = \frac{\delta \rho(\mathbf{r})}{\delta V_{KS}(\mathbf{r}')} \quad (2.38)$$

is the static independent-particle response function (see Sec. 5.4) and

$$\Lambda_{xc}(\mathbf{r}) = \sum_{k \neq j} \left[|\varphi_j(\mathbf{r})|^2 \frac{\partial E_{xc}}{\partial \epsilon_j} - \varphi_j^*(\mathbf{r}) \int d\mathbf{r}' \frac{\varphi_k(\mathbf{r}') \varphi_k^*(\mathbf{r}')}{\epsilon_k - \epsilon_j} \frac{\delta E_{xc}}{\delta \varphi_j^*(\mathbf{r}')} + h.c. \right]. \quad (2.39)$$

A simplification of the OEP equation (2.38), the KLI approximation, has been introduced by Krieger *et al.* [106]. It consists in neglecting the derivative $\partial E_{xc}/\partial \epsilon_j$ and in assuming constant the energy denominators $\epsilon_k - \epsilon_j = \Delta \bar{\epsilon}$.

Also the unoccupied Kohn-Sham states, which don't contribute to the electronic density, enter Eq. (2.37). So, even in the KLI framework, the determination of V_{xc} in the OEP scheme remains a much more involved calculation than the LDA approximation.

The OEP method is currently employed in the exact-exchange approximation (EXX) [101], where only the exchange part of E_{xc} is taken into account:

$$E_x[\{\varphi_i\}] = -\frac{1}{2} \sum_{i,j=1}^N \int d\mathbf{r} d\mathbf{r}' \frac{\varphi_j^*(\mathbf{r}) \varphi_i^*(\mathbf{r}') \varphi_i(\mathbf{r}) \varphi_j(\mathbf{r}')}{|\mathbf{r} - \mathbf{r}'|}. \quad (2.40)$$

The Kohn-Sham exchange potential can be then obtained using the chain-rule differentiation:

$$V_x(\mathbf{r}) = \frac{\delta E_x}{\delta \rho(\mathbf{r})} = \sum_k \int d\mathbf{r}_1 d\mathbf{r}_2 \left[\frac{\delta E_x}{\delta \varphi_k(\mathbf{r}_1)} \frac{\delta \varphi_k(\mathbf{r}_1)}{\delta V_{KS}(\mathbf{r}_2)} + h.c. \right] \frac{\delta V_{KS}(\mathbf{r}_2)}{\delta \rho(\mathbf{r})} \quad (2.41)$$

Even though the functional dependence of E_x with respect to the orbitals φ_i is the same as in Hartree-Fock, the energy calculated in Hartree-Fock is always lower (at most equal) than the energy obtained in EXX. In fact, in the OEP framework the orbitals φ_i are subject to a further constraint: being

2. Ground-state properties

solution of the Kohn-Sham equation where the potential is local. In Hartree-Fock this constraint is not used, and in fact the Hartree-Fock potential is nonlocal. Therefore the variational minimization in Hartree-Fock is applied to a larger class of orbitals and this leads to lower energies.

In the EXX approximation the self-interaction deficiency of LDA/GGA is exactly eliminated and this can be important for the determination of some ground-state properties.

In any case, any OEP scheme, EXX included, can be used only to describe ground-state properties. It is not supposed to produce reliable results also for excited-state properties, in particular for quasiparticle energies measured in photoemission. Nevertheless, promising results for Kohn-Sham band gaps in *sp* semiconductors had been obtained in the EXX approximation [107][108]. However, the true band gap E_{gap} is given by the sum of the exact Kohn-Sham gap E_{gap}^{KS} and the derivative discontinuity Δ of the (exact) exchange-correlation potential V_{xc} (see Eq. (2.33)). So the fact that band gaps obtained in the EXX approximation, E_{gap}^{EXX} , have been found similar to E_{gap} implies only that the error introduced by the EXX approximation in the Kohn-Sham scheme is similar to the derivative discontinuity. Since

$$E_{gap} = E_{gap}^{EXX} + (E_{gap}^{KS} - E_{gap}^{EXX}) + \Delta, \quad (2.42)$$

in order to have $E_{gap} = E_{gap}^{EXX}$, it must be: $E_{gap}^{EXX} - E_{gap}^{KS} = \Delta$. This is a fortuitous coincidence that holds only in *sp* semiconductors in the EXX approximation. In fact, when EXX calculations have been performed for other systems, like noble-gas solids [109], one finds $E_{gap}^{EXX} < E_{gap}$. Also when, beyond EXX, effects due to correlation have been included in the OEP scheme [110][111], a confirmation that $E_{gap}^{OEP} < E_{gap}$ has been found. Moreover, whereas Δ calculated in LDA is zero, the derivative discontinuity calculated in EXX, Δ_{EXX} , is quite large. Adding Δ_{EXX} to E_{gap}^{EXX} , one finds a result close to the band gap calculated in Hartree-Fock [110], which is much larger than the experimental value.

When one has a good estimate of the exact Kohn-Sham gap E_{gap}^{KS} , the derivative discontinuity Δ (see Eq. (2.33)) contributes for 30% to 50% to the band gap E_{gap} [110][112]. Therefore, in order to calculate quasiparticle energies one cannot use a Kohn-Sham scheme. The natural framework is instead given by the one-particle Green's-function theory, as it will be discussed in the next chapter.

2.2.4 DFT in practice

Once an approximation of the exchange-correlation potential has been chosen, the Kohn-Sham equations are solved by representing the wavefunctions φ_i over a (finite) basis. One is then led to diagonalize a matrix equation. Thanks to the Bloch theorem, the simplest choice in a solid is to use a

2.2 Density-functional theory

plane-wave basis set:

$$\varphi_{n\mathbf{k}}(\mathbf{r}) = \frac{1}{\sqrt{N_{\mathbf{k}}\Omega_c}} \sum_{\mathbf{G}} u_{n\mathbf{k}}(\mathbf{G}) e^{i(\mathbf{k}+\mathbf{G})\mathbf{r}}, \quad (2.43)$$

where:

$$u_{n\mathbf{k}}(\mathbf{G}) = \frac{1}{\Omega_c} \int_{\Omega_c} d\mathbf{r} e^{-i\mathbf{G}\mathbf{r}} u_{n\mathbf{k}}(\mathbf{r}) \quad (2.44)$$

is a lattice periodic function (Ω_c is the volume of unit cell). The number of plane waves is determined by the cutoff energy E_{cut} :

$$\frac{(\mathbf{k} + \mathbf{G})^2}{2} < E_{cut}. \quad (2.45)$$

In other words, the cutoff energy defines the sphere to which all the plane waves of the basis belong. So, increasing E_{cut} , one can improve systematically the quality of the basis set.

The key quantity in DFT is the density $\rho(\mathbf{r})$:

$$\rho(\mathbf{r}) = \sum_n \frac{1}{\Omega_{\mathbf{k}}} \int_{\Omega_{\mathbf{k}}} d\mathbf{k} f(\epsilon_F - \epsilon_{n\mathbf{k}}) \varphi_{n\mathbf{k}}^*(\mathbf{r}) \varphi_{n\mathbf{k}}(\mathbf{r}), \quad (2.46)$$

where the Fermi distribution f assures that only occupied states are considered in the sum over the bands. The \mathbf{k} integration over the Brillouin zone in (2.46) is in practice replaced by a finite sum over special grids of \mathbf{k} points in the irreducible Brillouin zone. A common recipe to build grids of \mathbf{k} points is given by Monkhorst and Pack [113]. Using (2.43), one explicitly has:

$$\rho(\mathbf{r}) = \sum_n \sum_{\mathbf{k}} \sum_{\mathbf{G}\mathbf{G}'}^{IBz} w_{\mathbf{k}} f(\epsilon_F - \epsilon_{n\mathbf{k}}) u_{n\mathbf{k}}^*(\mathbf{G}) u_{n\mathbf{k}}(\mathbf{G}') e^{i(\mathbf{G}-\mathbf{G}')\mathbf{r}}, \quad (2.47)$$

where the weights $w_{\mathbf{k}}$ of the special \mathbf{k} points of the grid have been introduced. Moreover, from (2.47) one realizes that, since both \mathbf{G} and \mathbf{G}' have to belong to the sphere defined in (2.45), the density has to be represented on a sphere of double radius than the one for the wavefunctions.

In a typical convergence study, one increases the number of plane waves and \mathbf{k} points used to represent the wavefunctions until the results don't vary anymore. In case one deals with metals, a proper smearing technique of the Fermi distribution has to be used to facilitate the convergence with the \mathbf{k} points.

In order to be able to use a plane-wave basis set, one has to adopt a pseudopotential approximation. The use of pseudopotentials has in fact the double advantage of reducing both number of plane waves required to achieve convergence and the number of electrons involved in the calculation.

In this way, the density ρ is partitioned in valence and core parts. Since core electrons don't take part to the chemical bonding, one can reasonably

2. Ground-state properties

assume that core electrons in a solid occupy the same orbitals as in the atom (frozen-core approximation). Therefore in the calculations only valence electrons are explicitly considered. The core electrons keep the valence electrons away from the nuclei. Summing this repulsive effect to the attractive interaction between the nuclei and the valence electrons gives rise to a much weaker total potential: the pseudopotential. Each atom results formed by a ionic core (given by the nucleus and the core electrons) and valence electrons, described by pseudowavefunctions, that interact with the ionic core through the pseudopotential.

There are many different recipes to build *ab initio* pseudopotentials (for a detailed introduction, see, for instance, Refs. [5][114]). In particular, in this thesis I have considered norm-conserving pseudopotentials [115] (see Sec. 6.4.1). In this scheme one calculates the pseudopotential and the pseudowavefunctions to be used in the solid from the solution of the Kohn-Sham equation for the pseudoatom that yields the same eigenvalues as the ones obtained by solving the Kohn-Sham equation for the real atom. In particular one requires that all-electron wavefunctions and pseudowavefunctions have the same norm, assuring that both give rise to the same electronic density. Outside a cutoff radius r_c^l , defined for each component of angular momentum l and larger than the outermost node of the all-electron radial wavefunction, the all-electron wavefunction and the pseudowavefunction coincide. For $r < r_c^l$ the pseudowavefunctions are built in such a way that they are still smooth and nodeless.

Solving the Kohn-Sham equations in this scheme finally permits to calculate the ground-state electronic energy as:

$$E_0 = -\frac{1}{2} \sum_i \int d\mathbf{r} \varphi_i^*(\mathbf{r}) \nabla^2 \varphi_i(\mathbf{r}) + \frac{1}{2} \int d\mathbf{r} d\mathbf{r}' \frac{\rho(\mathbf{r}) \rho(\mathbf{r}')}{|\mathbf{r} - \mathbf{r}'|} + \int d\mathbf{r} V_{ext}(\mathbf{r}) \rho(\mathbf{r}) + E_{xc}[\rho]. \quad (2.48)$$

In order to get the total energy of the system, E_{tot} one has also to add to E_0 the (constant) Coulomb repulsion term between ions. In particular, if the external potential V_{ext} depends on a parameter α , one can calculate the total energy as a function of α , $E_{tot} = E_{tot}(\alpha)$, in order to find its minimum with respect to α . Typical properties that can be accessed in this way are the lattice constants (see Sec. 6.4.2), forces (through the Hellman-Feynman theorem [116]), phonons, etc.

Chapter 3

One-particle excitations

In many-body perturbation theory (MBPT) the key variables are the Green's functions. In particular, in this chapter I introduce the one-particle Green's function G , which permits to calculate the spectral function and the quasi-particle energies associated to the one-particle excitations measured in photoemission (see Sec. 1.2.1). Thanks to Schwinger's functional-derivative method, I will derive a closed set of equations (Hedin's equations) that account, in principle exactly, for all the many-body effects in an electronic system. Following the main ideas of Hedin, I will stress the importance of the screening of the Coulomb interaction. I will then introduce the GW approximation and some details of its standard implementation. Moreover, I will discuss the recently developed schemes to perform self-consistent quasiparticle calculations, in particular the one based on Hedin's COHSEX approximation (for a more detailed introduction I refer to the thesis of F. Bruneval [3]).

Besides standard MBPT textbooks (such e.g. [117]), the fundamental review of Hedin and Lundqvist [118] and the more recent review of Strinati [119] present a complete introduction to MBPT and the main physical ideas behind it. The reviews of Aulbur et al. [120] and Aryasetiawan and Gunnarsson [121] provide also a collection of results obtained in the GW approximation. The work of Farid [122] describes the mathematical foundations of the Green's-function theory.

3.1 The Green's function

The time-ordered one-particle Green's function at zero temperature is defined as:

$$G(1, 2) = -i\langle N|T[\hat{\psi}(1)\hat{\psi}^+(2)]|N\rangle, \quad (3.1)$$

where $|N\rangle$ is the exact ground state of the interacting system and $\hat{\psi}$ are field operators in the Heisenberg picture (1 is a shorthand notation for $\mathbf{r}_1 t_1 \sigma_1$).

3. One-particle excitations

The T -product orders operators with the one at latest time on the left and adds a sign -1 for each interchange of operators. Explicitly:

$$G(1, 2) = -i[\theta(t_1 - t_2)\langle N|\hat{\psi}(1)\hat{\psi}^+(2)|N\rangle - \theta(t_2 - t_1)\langle N|\hat{\psi}^+(2)\hat{\psi}(1)|N\rangle]. \quad (3.2)$$

For $t_2 > t_1$, G describes the propagation of an extra hole from \mathbf{r}_1 to \mathbf{r}_2 and, for $t_1 > t_2$, the propagation of an extra electron from \mathbf{r}_2 to \mathbf{r}_1 . Therefore, it is the key variable in order to provide an interpretation of the one-particle excitations of the system.

In particular the definition (3.1) will be considered in the case of time-independent Hamiltonian (for a generalization see App. A.2). Also two other Green's functions are often introduced as [117]:

$$G^R(1, 2) = -i\theta(t_1 - t_2)\langle N|\{\hat{\psi}(1), \hat{\psi}^+(2)\}|N\rangle, \quad (3.3)$$

$$G^A(1, 2) = +i\theta(t_2 - t_1)\langle N|\{\hat{\psi}(1), \hat{\psi}^+(2)\}|N\rangle, \quad (3.4)$$

where the braces are anticommutators. They are known respectively as the retarded (or causal) Green's function, G^R , and the advanced Green's function G^A .

The one-particle Green's function G contains a great deal of useful information [117]. Thanks to G we can calculate also the ground-state expectation value of any one-particle operator and the ground-state energy of the system.

With a time-independent Hamiltonian, any one-particle operator \hat{A} in second quantization can be written as:

$$\hat{A} = \lim_{\mathbf{r}' \rightarrow \mathbf{r}} \int d\mathbf{r} A(\mathbf{r}) \hat{\psi}^+(\mathbf{r}') \hat{\psi}(\mathbf{r}). \quad (3.5)$$

The limit here has to be considered explicitly in case $A(\mathbf{r})$ contains differential operators. So, comparing (3.5) and (3.1), one can immediately realize that the expectation value $\langle A \rangle = \langle N|\hat{A}|N\rangle$ can be expressed in terms of the one-particle Green's function as:

$$\langle A \rangle = -i \lim_{\mathbf{r}' \rightarrow \mathbf{r}} \lim_{t' \rightarrow t^+} \int d\mathbf{r} A(\mathbf{r}) G(\mathbf{r}, \mathbf{r}', t, t'). \quad (3.6)$$

For example, the expectation value of the electronic density:

$$\hat{\rho}(\mathbf{r}_1) = \int d\mathbf{r} \delta(\mathbf{r} - \mathbf{r}_1) \hat{\psi}^+(\mathbf{r}) \hat{\psi}(\mathbf{r}) \quad (3.7)$$

is the diagonal in space and time of the Green's function:

$$\rho(\mathbf{r}_1) = -iG(\mathbf{r}_1, \mathbf{r}_1, t, t^+). \quad (3.8)$$

Similarly, although the Hamiltonian contains two-particle operators, the ground-state total energy E_0 of the system can be calculated from the

3.1 The Green's function

one-particle Green's function G thanks to the Galitskii-Migdal equation [117][123]:

$$E_0 = \frac{1}{2} \int d\mathbf{r} \lim_{\mathbf{r}' \rightarrow \mathbf{r}} \lim_{t' \rightarrow t^+} \left[\frac{\partial}{\partial t} - ih_0(\mathbf{r}) \right] G(\mathbf{r}, \mathbf{r}', t, t'). \quad (3.9)$$

If the Hamiltonian is time independent, G depends only on the difference $\tau = t - t'$. Inserting in Eq. (3.2) a completeness relation in the Fock space, one has:

$$\begin{aligned} G(\mathbf{r}_1, \mathbf{r}_2, \tau) &= (-i)\theta(\tau) \sum_s \langle N | \hat{\psi}(1) | N+1, s \rangle \langle N+1, s | \hat{\psi}^+(2) | N \rangle + \\ &\quad - (-i)\theta(-\tau) \sum_s \langle N | \hat{\psi}^+(2) | N-1, s \rangle \langle N-1, s | \hat{\psi}(1) | N \rangle. \end{aligned} \quad (3.10)$$

Moreover, since:

$$\theta(\pm\tau) = \mp \frac{1}{2\pi i} \int_{-\infty}^{+\infty} d\omega \frac{e^{-i\omega\tau}}{\omega \pm i\eta} \quad (3.11)$$

for $\eta \rightarrow 0^+$ [72], from the Fourier transform of (3.10), one obtains the Lehmann representation [124] for the one-particle Green's function:

$$G(\mathbf{r}_1, \mathbf{r}_2, \omega) = \sum_s \frac{f_s(\mathbf{r}_1) f_s^*(\mathbf{r}_2)}{\omega - \tilde{E}_s + i\eta \text{sgn}(\tilde{E}_s - \mu)}, \quad (3.12)$$

where, if $\tilde{E}_s > \mu$, $f_s(\mathbf{r}) = \langle N | \hat{\psi}(\mathbf{r}) | N+1, s \rangle$ and $\tilde{E}_s = E_{N+1,s} - E_N$; if $\tilde{E}_s < \mu$, $f_s(\mathbf{r}) = \langle N-1, s | \hat{\psi}(\mathbf{r}) | N \rangle$ and $\tilde{E}_s = -E_{N-1,s} + E_N$. The Lehmann amplitudes f_s form a complete set, but in general they are not orthogonal. G has poles at the electron addition and removal energies \tilde{E}_s . The poles lie slightly above the real axis for frequencies below μ and slightly below the real axis for frequencies above μ .

It is possible to derive a Lehmann representation also for the retarded and advanced Green's functions (3.3)-(3.4):

$$G^R(\mathbf{r}_1, \mathbf{r}_2, \omega) = \sum_s \frac{f_s(\mathbf{r}_1) f_s^*(\mathbf{r}_2)}{\omega - \tilde{E}_s + i\eta} \quad (3.13)$$

$$G^A(\mathbf{r}_1, \mathbf{r}_2, \omega) = \sum_s \frac{f_s(\mathbf{r}_1) f_s^*(\mathbf{r}_2)}{\omega - \tilde{E}_s - i\eta} \quad (3.14)$$

from which one can see that G^R is analytic for $\text{Im}\omega > 0$ and G^A is analytic for $\text{Im}\omega < 0$, because their poles lie all in the other complex half plane.

The spectral function A that one measures in photoemission experiments (see Sec 1.2.1) is proportional to the imaginary part of the Green's function:

$$A(\mathbf{r}_1, \mathbf{r}_2, \omega) = \frac{1}{\pi} \text{sgn}(\mu - \omega) \text{Im}G(\mathbf{r}_1, \mathbf{r}_2, \omega). \quad (3.15)$$

3. One-particle excitations

From the Lehmann representation (3.12), the spectral function can be written as:

$$A(\mathbf{r}_1, \mathbf{r}_2, \omega) = \sum_s f_s(\mathbf{r}_1) f_s^*(\mathbf{r}_2) \delta(\tilde{E}_s - \omega). \quad (3.16)$$

From this expression one can immediately realize that the spectral function is hence the quantity directly related to the one-particle excitations, described by the Lehmann amplitudes f_s and the electron addition and removal energies \tilde{E}_s .

It is important to note that for energy ranges where in the thermodynamic limit \tilde{E}_s form a continuum, one should consider the analytic continuation of G in the complex plane (for the mathematical details see [122]). A meaningful Green's function on the real axis is defined only as the limit of its analytic continuation in the complex plane:

$$G(\omega) = \lim_{\eta \rightarrow 0} G(\omega + i\eta \text{sgn}(\omega - \mu)). \quad (3.17)$$

So the Green's function turns out to be:

$$G(\mathbf{r}_1, \mathbf{r}_2, z) = \int d\omega' \frac{A(\mathbf{r}_1, \mathbf{r}_2, \omega')}{z - \omega'}, \quad (3.18)$$

G displays a branch cut along the real axis across which G is discontinuous and

$$A(\omega) = \lim_{\eta \rightarrow 0} \frac{1}{2\pi i} [G(\omega - i\eta) - G(\omega + i\eta)]. \quad (3.19)$$

The spectral function satisfies the normalization condition:

$$\int_{-\infty}^{+\infty} d\omega A(\mathbf{r}_1, \mathbf{r}_2, \omega) = \delta(\mathbf{r}_1 - \mathbf{r}_2) \quad (3.20)$$

and from its diagonal one can extract important information such as the electronic density:

$$\rho(\mathbf{r}) = \int_{-\infty}^{\mu} d\omega A(\mathbf{r}, \mathbf{r}, \omega). \quad (3.21)$$

If the system is noninteracting, then the many-body states $|N\rangle$ are Slater determinants (see Sec. 1.3.1). In this case $f_s = \langle N | \hat{\psi}(\mathbf{r}) | N + 1, s \rangle \neq 0$ only if $|N + 1, s\rangle = c_s^\dagger |N\rangle$ (analogously for $E_s < \mu$). So the Lehmann amplitudes are the true eigenfunctions of the one-particle Hamiltonian. Moreover, the spectral function calculated on the basis of these one-particle states consists in delta peaks at the energies \tilde{E}_s . In the general case, instead, the many-body states are a combination of many Slater determinants and the spectral function is given by the overlap of many different contributions that lead to a spreading and a renormalization of the delta peaks (see Fig. 1.5).

3.2 Hedin's equations and the GW approximation

The time evolution of G corresponds to the propagation of an electron (or a hole). Its equation of motion (see App. A.1):

$$\left[i \frac{\partial}{\partial t_1} - h_0(1) \right] G(1, 2) = \delta(1, 2) - i \int d3v(1, 3) G_2(1, 3, 2, 3^+), \quad (3.22)$$

where $h_0 = -\nabla^2/2 + V_{ext}$ is the one-particle term of the Hamiltonian, describes the fact that the electron, moving around, polarizes the system creating electron-hole pairs along its way. For this reason the equation of motion of the one-particle Green's function involves also a two-particle quantity: the two-particle Green's function G_2 , which describes the creation and annihilation of pairs of particles. Further deriving the equation of motion for G_2 , one would find a hierarchy of equations involving Green's functions of increasing orders: G_3, G_4, \dots . In fact, for example the electron-hole pair created by the propagation of the first electron would induce a cascade of other electron-hole pairs.

Eq. (3.22) could be evaluated using diagrammatic techniques based on the Wick theorem [117][125]. In order to keep more contact with the physics of the interacting system, I will follow here an equivalent alternative method, based on Schwinger's functional derivative [126].

Even though G is still unknown, from (3.22) we know that its evolution leads to a polarization of the system. The main physical idea of Schwinger is that the same polarization of the system could be obtained by a time-dependent perturbing external potential V_{per} , which, in the spirit of the linear-response theory, will be let vanish at the end of the derivation. So the one-particle term of the Hamiltonian h_0 contains now also V_{per} .

It is possible to demonstrate (see App. A.2) that the variation of G with respect to the perturbation V_{per} is:

$$\frac{\delta G(1, 2)}{\delta V_{per}(3)} = G(1, 2)G(3, 3^+) - G_2(1, 3, 2, 3^+). \quad (3.23)$$

Inserting (3.23) in (3.22), one finds:

$$\begin{aligned} \left[i \frac{\partial}{\partial t_1} - h_0(1) + i \int d3v(1, 3)G(3, 3^+) \right] G(1, 2) = \\ = \delta(1, 2) + i \int d3v(1^+, 3) \frac{\delta G(1, 2)}{\delta V_{per}(3)}. \end{aligned} \quad (3.24)$$

Since $-iG(3, 3^+) = \rho(3)$, one can recognize that the term:

$$-i \int d3v(1, 3)G(3, 3^+) = V_H(1) \quad (3.25)$$

3. One-particle excitations

is the classical Hartree potential. So the effects of the perturbation V_{per} can be split into a classical contribution (the first term in the right-hand-side of Eq. (3.23)) and a contribution beyond the classical independent-particle picture. The quantum effects are hence all contained in the last term of (3.24), which can be cast in the equivalent way, by defining the self-energy Σ as:

$$i \int d3v(1^+, 3) \frac{\delta G(1, 2)}{\delta V_{per}(3)} = \int d3 \Sigma(1, 3) G(3, 2). \quad (3.26)$$

The self-energy therefore turns out to be the effective nonlocal and dynamical potential that describes all the effects of exchange and correlation in the system. It is the effective potential that the extra particle feels for the polarization that its propagation induces for the exchange effects, due to the fact that it is a fermion.

With the introduction of the Hartree potential V_H and the self-energy Σ , Eq. (3.24) can be then rewritten as:

$$\left[i \frac{\partial}{\partial t_1} - h_0(1) - V_H(1) \right] G(1, 2) = \delta(1, 2) + \int d3 \Sigma(1, 3) G(3, 2). \quad (3.27)$$

The Hartree Green's function is defined as the resolvent of the Hartree Hamiltonian (but calculated with the exact electronic density ρ), where one has $\Sigma = 0$:

$$\left[i \frac{\partial}{\partial t_1} - h_0(1) - V_H(1) \right] G_H(1, 2) = \delta(1, 2). \quad (3.28)$$

Combining Eqs. (3.27) with (3.28) one finds (see App. A.3):

$$G_H^{-1}(1, 2) - G^{-1}(1, 2) = \Sigma(1, 2). \quad (3.29)$$

The self-energy describes a renormalization effect: the difference between the propagation of an independent (Hartree) particle and the propagation of an interacting fermionic particle. Eq. (3.29) is generally rewritten as a Dyson equation linking G_H and G :

$$G(1, 2) = G_H(1, 2) + \int d34 G_H(1, 3) \Sigma(3, 4) G(4, 2), \quad (3.30)$$

where $d34$ is a shorthand notation for $d\mathbf{r}_3 dt_3 d\mathbf{r}_4 dt_4$ that will be regularly adopted in the following.

The self-energy appearing in these equations is still unknown. Eq. (3.26) can be easily solved with respect to Σ :

$$\Sigma(1, 2) = i \int d34 v(1^+, 3) \frac{\delta G(1, 4)}{\delta V_{per}(3)} G^{-1}(4, 2). \quad (3.31)$$

Since (see App. A.4):

$$\frac{\delta G(1, 2)}{\delta V_{per}(3)} = - \int d45 G(1, 4) \frac{\delta G^{-1}(4, 5)}{\delta V_{per}(3)} G(5, 2), \quad (3.32)$$

3.2 Hedin's equations and the GW approximation

from Eq. (3.31) one has:

$$\Sigma(1, 2) = -i \int d34v(1^+, 3)G(1, 4) \frac{\delta G^{-1}(4, 2)}{\delta V_{per}(3)}. \quad (3.33)$$

Thanks to the definition of the reducible vertex $\tilde{\Gamma}$

$$\tilde{\Gamma}(1, 2, 3) = -\frac{\delta G^{-1}(1, 2)}{\delta V_{per}(3)}, \quad (3.34)$$

equation (3.33) can be rewritten as:

$$\Sigma(1, 2) = -i \int d34v(1^+, 3)G(1, 4)\tilde{\Gamma}(4, 2, 3). \quad (3.35)$$

Moreover, using the Dyson equation (3.29), the chain rule:

$$\frac{\delta \Sigma(1, 2)}{\delta V_{per}(3)} = \int d45 \frac{\delta \Sigma(1, 2)}{\delta G(4, 5)} \frac{\delta G(4, 5)}{\delta V_{per}(3)}, \quad (3.36)$$

and Eq. (3.32) together with the definition (3.34), the following equation for the reducible vertex $\tilde{\Gamma}$ can be obtained:

$$\begin{aligned} \tilde{\Gamma}(1, 2, 3) = \delta(1, 3)\delta(1, 2) + \int d4567 \left[-iv(1, 4)\delta(1, 2)\delta(4, 5) + \frac{\delta \Sigma(1, 2)}{\delta G(4, 5)} \right] \times \\ \times G(4, 6)\tilde{\Gamma}(6, 7, 3)G(7, 5). \end{aligned} \quad (3.37)$$

In Eq. (3.37) the terms beyond the delta functions express the change of the induced potentials due to the propagation of the extra particle. In other words, the extra particle polarizing the system makes also the other particle move and this reaction modifies self-consistently the potentials that the extra particle feels.

The three equations (3.30), (3.35) and (3.37) define a closed set of equations in the three variables G , Σ and $\tilde{\Gamma}$. One should iterate them self-consistently in order to calculate G . The simplest approximation, beyond the Hartree approximation, consists in taking for the self-energy:

$$\Sigma(1, 2) = iG(1, 2)v(1^+, 2). \quad (3.38)$$

In this case one neglects the so-called vertex effects, by assuming $\tilde{\Gamma}(1, 2, 3) = \delta(1, 2)\delta(1, 3)$. This assumption corresponds to the Hartree-Fock approximation and (3.38) is nothing else than the Fock exchange operator V_x (see Eq. 1.39):

$$\Sigma_x(\mathbf{r}_1, \mathbf{r}_2) = -\sum_i \theta(\mu - E_i) \phi_i(\mathbf{r}_1) \phi_i^*(\mathbf{r}_2) v(|\mathbf{r}_1 - \mathbf{r}_2|). \quad (3.39)$$

As already discussed (see Sec. 1.3.1), the eigenvalues of the Hartree-Fock equation are not good estimates of the spectral properties of solids. An

3. One-particle excitations

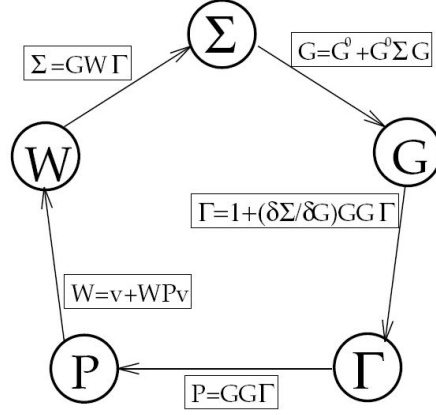


Figure 3.1: Hedin's pentagon connecting the Green's function G , the self-energy Σ , the vertex Γ , the polarizability P and the screened interaction W . From Ref. [120].

order-by-order expansion in v turns out to be ill-defined, as in the case of the homogeneous electron gas. Instead, Lars Hedin [127] introduced a fundamental breakthrough by realizing that, instead of the bare Coulomb interaction v , one should consider an expansion in the screened potential W :

$$W(1, 2) = \int d3 \epsilon^{-1}(1, 3) v(3, 2), \quad (3.40)$$

where ϵ^{-1} is the inverse of the (microscopic) dielectric function, which describes the screening of the bare Coulomb potential v .

In this way (see App. A.5) a closed set of five equations in five variables, Hedin's equations, can be obtained (see also Fig. 3.1). They are:

$$\Sigma(1, 2) = i \int d34 G(1, 4) W(3, 1^+) \Gamma(4, 2, 3), \quad (3.41)$$

$$G(1, 2) = G_H(1, 2) + \int d34 G_H(1, 3) \Sigma(3, 4) G(4, 2), \quad (3.42)$$

$$\Gamma(1, 2, 3) = \delta(1, 2) \delta(1, 3) + \int d4567 \frac{\delta \Sigma(1, 2)}{\delta G(4, 5)} G(4, 6) G(7, 5) \Gamma(6, 7, 3), \quad (3.43)$$

$$P(1, 2) = -i \int d34 G(2, 3) G(4, 2) \Gamma(3, 4, 1), \quad (3.44)$$

$$W(1, 2) = v(1, 2) + \int d34 v(1, 3) P(3, 4) W(4, 2). \quad (3.45)$$

This five equations describe all the physics of the many-body system in a closed form.

Besides the Green's function G , the self-energy Σ and the screened potential W , in Hedin's equations (3.41)-(3.45) the irreducible vertex Γ and

3.2 Hedin's equations and the GW approximation

the (time-ordered) irreducible polarizability P have been introduced:

$$\Gamma(1, 2, 3) = -\frac{\delta G^{-1}(1, 2)}{\delta V_{tot}(3)} = \delta(1, 3)\delta(1, 2) + \frac{\delta \Sigma(1, 2)}{\delta V_{tot}(3)}, \quad (3.46)$$

$$P(1, 2) = \frac{\delta \rho(1)}{\delta V_{tot}(2)}, \quad (3.47)$$

where $V_{tot} = V_{per} + V_H$ is the total classical potential. Γ describes the change of the potentials with respect to the change of the total classical potential V_{tot} . Since the induced potential, through a screening effect, counteracts the perturbing potential, the change of the potentials in Γ is expected to be smaller than in the reducible vertex $\tilde{\Gamma}$, where one considers V_{per} instead of V_{tot} (see Eq. (3.34)). The polarizability P contains the effects of polarization of the system. From its equation in (3.44), one can see that the polarization is made of interacting particles

When a charge is added to an electronic system, the first effect is the polarization of the system. By neglecting the electron-hole interaction in the electron-hole pairs that constitute the polarization and the exchange-correlation effects in the induced interaction between the extra charge and the polarization charge of the system, one finds the GW approximation introduced by Hedin [127]:

$$\Sigma(1, 2) = iG(1, 2)W(1^+, 2). \quad (3.48)$$

The GW approximation corresponds to neglect vertex effects, i.e. to take for the vertex the simplest expression:

$$\Gamma(1, 2, 3) = \delta(1, 2)\delta(1, 3) \quad (3.49)$$

in both P (see Eq. (3.44)) and Σ (see Eq. (3.41)). In particular, the form of this approximation for P is known as random-phase approximation (RPA) and yields for the polarizability:

$$P(1, 2) = P_0(1, 2) = -iG(1, 2)G(2, 1). \quad (3.50)$$

The important difference with respect to the Hartree-Fock approximation (see Eq. (3.38)) is the fact that in GW one takes explicitly into account the existence of polarization effects that screen the propagation of the extra particle. While in Hartree-Fock there is no polarization and no relaxation of the system and the self-energy is static, GW is a dynamically screened approximation. In GW one sets the irreducible vertex $\Gamma = 1$, in Hartree-Fock $\tilde{\Gamma} = 1$. The latter is a more drastic approximation because Γ contains the response of the potentials to the variation of the total potential V_{tot} (i.e. external plus induced Hartree potential) which is smaller than the response

3. One-particle excitations

of the potentials to the variation of the external potential alone ($V_{tot} < V_{per}$), since the variations of the electronic density tend to oppose to the perturbation. Then, the fact for example that beyond GW the exact polarization is made by interacting electron-hole pairs can be considered as an effect of second order and hence neglected. And, for instance, missing vertex corrections in the self-energy give rise to self-screening errors [128].

The formalism based on the Green's functions permits also to revise the concept of electronic correlation as discussed in the Introduction (see Sec. 1.1). There the idea of correlation had been introduced in terms of static probabilities. If two electrons are correlated, then the probability to find them in the positions \mathbf{r}_1 and \mathbf{r}_2 is not the simple product of the single probabilities. Here the idea of correlation instead emerges as tightly connected to the dynamical propagation of particles. Two electrons are correlated because their propagation in the system is not independent. On the contrary, one has to take into account the polarization effects due to the dynamical relaxation of all the other particles that an electron encounters along its trajectory. If in the former picture it is as one had taken an instantaneous photograph of the electronic system at a certain fixed moment, in the Green's-function approach one is instead watching the dynamical evolution (the "movie") of the electronic system.

Even using the GW approximation to the self-energy, the Dyson equation is still a self-consistent equation in G that one could solve iteratively. In this sense the starting point is arbitrary. In fact, it is possible to start with the Green's function of any noninteracting system and iterate self-consistently (keeping the vertex $\Gamma = 1$). In particular, Hedin obtained the GW approximation by iterating Hedin's equations starting from $\Sigma = 0$, i.e. from the Hartree Green's function G_H . Modern calculations, starting from the works of Strinati, Mattausch and Hanke [129] and then Hybertsen and Louie [130][131] and Godby, Schlüter and Sham [112] [132], instead use a "best G, best W" approach [133]. In this philosophy one dismisses the idea of a strict iterative solution of Hedin's equations. Instead, one builds the GW self-energy from the best mean-field results at disposal, in general the LDA Kohn-Sham eigenvalues and eigenfunctions, and calculates the GW quasiparticle energies as a first-order correction with respect to LDA. Other possibilities are to start from GGA [134][135], EXX [136][137] or hybrid-functional [138] results. The "best G, best W" approach (also known as "one-shot GW", or G_0W_0) has become the standard method for GW calculations. In general it yields results for quasiparticle energies in good agreement with experiment (see Fig. 3.2) and hence is the method of choice for band-structure calculations [120].

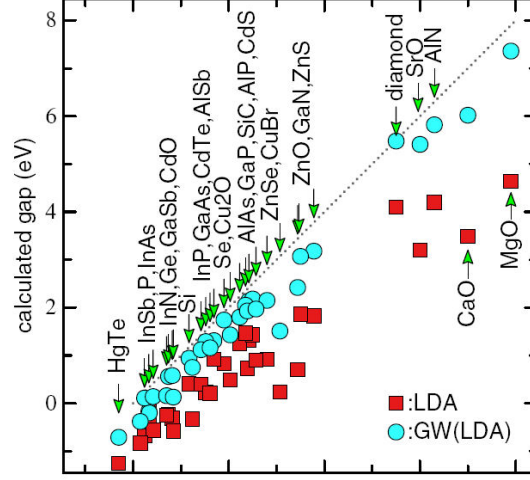


Figure 3.2: Comparison between the calculated and the experimental band gaps for a certain number of materials. In case of perfect agreement between theory and experiment, the dot, corresponding to the theoretical result, should stay on the diagonal line. Instead, all the LDA results (red squares) show an evident underestimation of the band gap. The GW values are in much better agreement with the experiment. From all-electron perturbative GW calculations of Ref. [139].

3.3 GW in practice

3.3.1 Calculations in the quasiparticle framework

The Fourier transform of the Dyson equation (3.27) gives:

$$[\omega - h_0(\mathbf{r}_1) - V_H(\mathbf{r}_1)]G(\mathbf{r}_1, \mathbf{r}_2, \omega) - \int d\mathbf{r}_3 \Sigma(\mathbf{r}_1, \mathbf{r}_3, \omega)G(\mathbf{r}_3, \mathbf{r}_2, \omega) = \delta(\mathbf{r}_1 - \mathbf{r}_2). \quad (3.51)$$

Eq. (3.51) can be analytically continued in the complex plane [122]. A formal solution of this equation in the complex plane is then given by:

$$G(\mathbf{r}_1, \mathbf{r}_2, z) = \sum_{\lambda} \frac{\Phi_{\lambda}(\mathbf{r}_1, z)\tilde{\Phi}_{\lambda}(\mathbf{r}_2, z)}{z - E_{\lambda}(z)}, \quad (3.52)$$

where the right and left eigenfunctions Φ_{λ} and $\tilde{\Phi}_{\lambda}$ are solutions of:

$$\begin{aligned} [h_0(\mathbf{r}_1) + V_H(\mathbf{r}_1)]\Phi_{\lambda}(\mathbf{r}_1, z) + \int d\mathbf{r}_2 \Sigma(\mathbf{r}_1, \mathbf{r}_2, z)\Phi_{\lambda}(\mathbf{r}_2, z) &= E_{\lambda}(z)\Phi_{\lambda}(\mathbf{r}_1, z), \\ [h_0(\mathbf{r}_1) + V_H(\mathbf{r}_1)]\tilde{\Phi}_{\lambda}(\mathbf{r}_1, z) + \int d\mathbf{r}_2 \tilde{\Phi}_{\lambda}(\mathbf{r}_2, z)\Sigma(\mathbf{r}_2, \mathbf{r}_1, z) &= E_{\lambda}(z)\tilde{\Phi}_{\lambda}(\mathbf{r}_1, z). \end{aligned} \quad (3.53)$$

3. One-particle excitations

Right and left eigenfunctions form a biorthonormal set:

$$\int d\mathbf{r} \tilde{\Phi}_\lambda(\mathbf{r}, z) \Phi_{\lambda'}(\mathbf{r}, z) = \delta_{\lambda\lambda'}. \quad (3.54)$$

In the quasiparticle approximation one assumes that the complex poles of the Green's function G :

$$E_s = E_\lambda(E_s) \quad (3.55)$$

(or, more in general, local minima of $|z - E_\lambda(z)|$ [140]) represent the dominant contribution to G . In this way one finds the quasiparticle equation:

$$[h_0(\mathbf{r}_1) + V_H(\mathbf{r}_1)]\phi_s(\mathbf{r}_1) + \int d\mathbf{r}_2 \Sigma(\mathbf{r}_1, \mathbf{r}_2, E_s)\phi_s(\mathbf{r}_2) = E_s\phi_s(\mathbf{r}_1). \quad (3.56)$$

Even though the quasiparticle equation is a single-particle equation, the quasiparticles don't correspond to stationary one-particle eigenstates of the many-body Hamiltonian \hat{H} (1.1), but they are formed by a macroscopically large number of almost degenerate stationary eigenstates of \hat{H} [122]. In the Lehmann representation in the thermodynamic limit one has a series of infinite close-lying poles on the real axis that merge to form a branch-cut. An alternative representation is given by a complex pole, the quasiparticle energy E_s solution of Eq. (3.55), whose real part gives the position of the peak associated to this pole and its imaginary part the width of the peak [2] (see Fig. 3.3). The real part of the quasiparticle energy represents the energy measured in photoemission, its imaginary part is connected to the lifetime of the excitation.

The quasiparticle equation (3.56) can be directly compared with the Kohn-Sham equation (2.28):

$$[h_0(\mathbf{r}_1) + V_H(\mathbf{r}_1)]\varphi_s(\mathbf{r}_1) + V_{xc}(\mathbf{r}_1)\varphi_s(\mathbf{r}_1) = \epsilon_s\varphi_s(\mathbf{r}_1). \quad (3.57)$$

The overlap between LDA and GW wavefunctions has been claimed to be larger than 99.9 % [131] in simple semiconductors, even though later calculations have shown that this is not always the case [141]. In any case, assuming that the quasiparticle wavefunctions ϕ_s can be approximated by the Kohn-Sham orbitals φ_s : $\phi_s \approx \varphi_s$, one can calculate the corrections to the Kohn-Sham eigenvalues ϵ_s to the first order in $\Sigma - V_{xc}$:

$$\langle \varphi_s | \Sigma(E_s) - V_{xc} | \varphi_s \rangle = E_s - \epsilon_s. \quad (3.58)$$

Generally, in order to solve this nonlinear equation in E_s , Σ is expanded in a Taylor series around ϵ_s and only the linear term is kept:

$$\langle \Sigma(E_s) \rangle = \langle \Sigma(\epsilon_s) \rangle + \left\langle \frac{\partial \Sigma(\omega)}{\partial \omega} \right|_{\omega=\epsilon_s} (E_s - \epsilon_s) + O((E_s - \epsilon_s)^2). \quad (3.59)$$

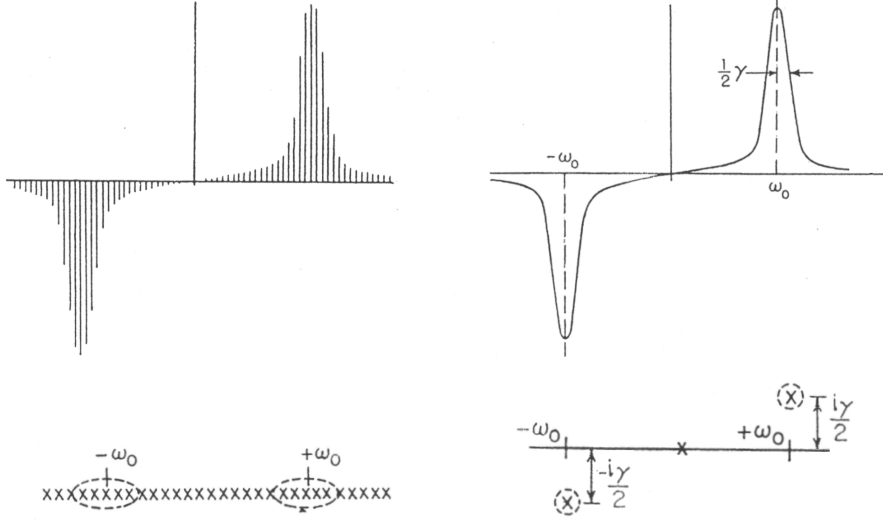


Figure 3.3: Schematic comparison between the Lehmann representation (on the left) and the quasiparticle pole representation (on the right). In the upper panels the residues of the imaginary part of a complex function are drawn; in the bottom panels the crosses identify the position of the poles. A series of close lying poles on the real axis in the Lehmann representation can be equivalently represented by a single pole in the complex plane (see also Ref. [2]). The imaginary part of pole in the complex plane gives the width of peak. From Ref. [142].

So the quasiparticle energies E_s can be finally evaluated as:

$$E_s = \epsilon_s + Z_s \langle \varphi_s | \Sigma(E_s) - V_{xc} | \varphi_s \rangle, \quad (3.60)$$

where the renormalization factor Z_s is:

$$Z_s = \left(1 - \left\langle \frac{\partial \Sigma(\omega)}{\partial \omega} \Big|_{\omega=\epsilon_s} \right\rangle \right)^{-1}. \quad (3.61)$$

Also the spectral function A can be expanded in the one-particle Kohn-Sham orbitals:

$$A_{ij}(\omega) = \int d\mathbf{r} d\mathbf{r}' \varphi_i^*(\mathbf{r}) A(\mathbf{r}, \mathbf{r}', \omega) \varphi_j(\mathbf{r}'). \quad (3.62)$$

Neglecting the nondiagonal parts of Σ [35], one has:

$$A_{ii}(\omega) = \frac{1}{\pi} \frac{|\text{Im}\Sigma_i(\omega)|}{(\omega - \epsilon_i - \text{Re}\Sigma_i(\omega))^2 + (\text{Im}\Sigma_i(\omega))^2}. \quad (3.63)$$

Structures in the spectral function (3.63) are given by the crossings between the curves $y = \text{Re}\Sigma_i(\omega)$ and $y = \omega - \epsilon_i$. In particular, when near the crossing

3. One-particle excitations

$|\text{Im}\Sigma_i(\omega)|$ is small the spectral function displays a peak. So $A_{ii}(\omega)$ has a peak at $\omega = \text{Re}E_i = \epsilon_i + \text{Re}\Sigma_i(E_i)$ of width $|\text{Im}\Sigma_i(E_i)|$. The integral of the region under the peak is equal to $\text{Re}Z_i$, where Z_i is the renormalization factor (see Eq. (3.61)). The incoherent part of the spectrum measures $1 - \text{Re}Z_i$. In particular, if $\omega - \epsilon_i - \text{Re}\Sigma_i(\omega)$ is zero or close to zero at some other energies, and $\text{Im}\Sigma_i(\omega)$ is not too large, then other structures, the satellites, appear in the spectrum.

3.3.2 Dynamical screening and the frequency integration

The GW self-energy (3.48) can be split into an exchange term Σ_x and a correlation term $\Sigma_c(\omega)$: $\Sigma(\omega) = \Sigma_x + \Sigma_c(\omega)$. While $\Sigma_x = iGv$ is static (see Eq. (3.39)), in order to evaluate $\Sigma_c(\omega)$, one has to calculate the convolution integral of G and $W_p = W - v$:

$$\Sigma_c(\mathbf{r}_1, \mathbf{r}_3, \omega) = \frac{i}{2\pi} \int d\omega' e^{i\eta\omega'} G(\mathbf{r}_1, \mathbf{r}_2, \omega + \omega') W_p(\mathbf{r}_1, \mathbf{r}_2, \omega'). \quad (3.64)$$

Since, in order to obtain Σ_c , one has to perform the frequency integration (3.64), the fine details of the energy dependence of W_p are often not important. So one can approximate the imaginary part of the inverse dielectric function ϵ^{-1} as a single-pole function in ω . This is based on the observation that the spectra of electron energy loss, which measure the imaginary part of ϵ^{-1} (see Sec. 1.2.2), typically display a single peak corresponding to the plasmon resonance [143][144]. In the reciprocal space ϵ^{-1} reads:

$$\epsilon_{\mathbf{G}, \mathbf{G}'}^{-1}(\mathbf{q}, \omega) = \int d\mathbf{r} d\mathbf{r}' e^{-i(\mathbf{q} + \mathbf{G})\mathbf{r}} \epsilon^{-1}(\mathbf{r}, \mathbf{r}', \omega) e^{+i(\mathbf{q} + \mathbf{G}')\mathbf{r}'} \quad (3.65)$$

where \mathbf{G} and \mathbf{G}' are vectors of the reciprocal lattice and \mathbf{q} belongs to the first Brillouin zone. For each element of $\epsilon^{-1}(\omega)$ in (3.65) the pole position and its strength are two free parameters. They can be calculated by fitting ϵ^{-1} at two points along the imaginary axis, generally 0 and the classical plasmon frequency, as proposed by Godby and Needs [145] and done in this thesis, or by employing sum rules and using the dielectric matrix calculated only at $\omega = 0$ [131][146].

This plasmon-pole approximation has been devised for quasiparticle calculations, where one is interested in the calculation of GW corrections. It cannot be used for the calculation of the spectral function (see Eq. (3.63)), because in this approximation $\text{Im}\Sigma = 0$ everywhere with the sole exception of the pole. In this case, and in general when the plasmon-pole approximation turns out to be insufficient, different methods of frequency integration have been proposed.

In particular, the frequency integral (3.64) can be evaluated using the residue theorem [3][147]. It can be calculated using the contour C that runs along the real axis, a quarter of circle in the first quadrant of the complex

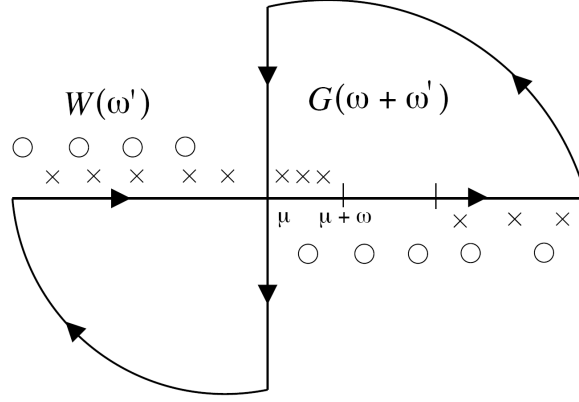


Figure 3.4: Path of the contour integration for $\Sigma_c(\omega)$. Poles of G are marked with crosses and poles of W with open circles. From Ref. [3].

plane, the imaginary axis and another quarter of circle in the third quadrant (see Fig. 3.4). From the Cauchy theorem, if $f(z)$ is the analytic continuation of $G(\omega')W_p(\omega')$ in the complex plane, one has that the integral along the contour C is equal to the sum of residues of the poles z_p contained inside the contour:

$$\int_C f(z)dz = 2\pi i \sum_{z=z_p} \text{Res} f(z). \quad (3.66)$$

The spectral representation of W_p is given by [121]:

$$W_p(\mathbf{r}_1, \mathbf{r}_2, \omega) = \int_{-\infty}^{+\infty} d\omega' \frac{D(\mathbf{r}, \mathbf{r}', \omega)}{\omega - \omega' + i\eta \text{sgn}(\omega)}, \quad (3.67)$$

where $D(\mathbf{r}, \mathbf{r}', \omega) = -1/\pi \text{sgn}(\omega) \text{Im} W_p(\mathbf{r}_1, \mathbf{r}_2, \omega)$. Moreover, from the parity of W it follows $D(\mathbf{r}, \mathbf{r}', -\omega) = -D(\mathbf{r}, \mathbf{r}', \omega)$. From Eq. (3.67) one can see that in the first and third quadrants W_p has no poles (see also Fig. 3.4). So all the poles inside the contour stem from the first-order poles of G . Splitting the integral along the contour C into the different pieces, one finds:

$$\begin{aligned} \Sigma_c &= \frac{i}{2\pi} \int_{-\infty}^{+\infty} G(z)W_p(z)dz = \\ &= \frac{i}{2\pi} \left[2\pi i \sum_p \lim_{z \rightarrow z_p} G(z)W_p(z)(z - z_p) - \int_{+i\infty}^{-i\infty} G(z)W_p(z)dz, \right] \end{aligned} \quad (3.68)$$

since the integrals along the quarters of circle in the first and third quadrants vanish. In order to get Σ_c , one has to perform the integration along the imaginary axis, where G and W_p are well behaved, and to evaluate the residues in the poles z_p . In practical calculations, while the frequency dependence

3. One-particle excitations

of G is known analytically, $W_p(z)$ has to be calculated numerically. This requires to calculate $\epsilon^{-1}(z)$ for a large enough number of frequencies z along the imaginary axis and along the real axis and then interpolate between the calculated values to obtain $W_p(z)$. Of course this method is much more expensive than the plasmon-pole approximation where one has to evaluate ϵ^{-1} only at two different frequencies. But, on the other side, it yields an accurate evaluation of the frequency integral (3.64). And this is particularly important to assess the validity of the plasmon-pole approximation or to calculate the spectral function $A(\omega)$.

Much cheaper alternative approaches for the calculation of $\Sigma(\omega)$ are instead based on particular models of the screened interaction W . In the scheme proposed by Gygi and Baldereschi [148], for example, W is separated into a short-range term of a metallic inhomogeneous electron gas W^{IEG} and a long-range correction δW : $W = W^{IEG} + \delta W$. The short-range term of the self-energy iGW^{IEG} , according to Sham and Kohn [140], can be approximated by a local and energy-dependent potential. In the Gygi-Baldereschi model this local potential is further approximated by considering only its value at the Fermi energy, which corresponds to the exchange-correlation potential $V_{xc}(\mathbf{r})$ calculated in LDA. Additionally, for the long-range correction δW one takes a static approximation. Moreover, only diagonal terms $\mathbf{G} = \mathbf{G}'$ are taken into account: $\delta W(\mathbf{q}) = \delta\epsilon^{-1}(\mathbf{q}, \omega = 0)v(\mathbf{q})$, where $\delta\epsilon^{-1}$ is the diagonal part of the difference between the inverse electronic dielectric function of a model semiconductor and of a homogeneous electron gas with the same average density. In the model semiconductor one makes use of some parameters, in particular the static value of the dielectric constant, which is taken from the experiment.

3.3.3 Core-valence interaction

Since the works of Hybertsen and Louie [131] and Godby, Sham and Schlüter [132] most of the GW calculations have been carried out in a pseudopotential framework. A recent work of Ku and Eguluz [149] had questioned the validity of the pseudopotential approximation in the context of GW calculations, showing large discrepancies between their all-electron results and older pseudopotential calculations. In case of a core-valence partitioning, the Green's function G and polarizability P are obtained from the sum of two contributions deriving from core and valence: $G = G_v + G_c$ and $P = P_v + P_c$. So the self-energy is [131]:

$$\Sigma = iG_cW + iG_vW_vP_cW_v + iG_vW_v. \quad (3.69)$$

In a pseudopotential GW calculation only the last term is treated explicitly. The other two terms are instead treated at the LDA level in the pseudopotential. The first term is the screened core-valence interaction. Since for core electrons the screening is ineffective, it is essentially a core-valence exchange

3.4 Self-consistent quasiparticle calculations

interaction. It depends mostly on the spatial overlap between valence and core orbitals. In order to make this term small, it is important to take care of core states whose overlap with valence states is not negligible. In particular, this prescription applies to semicore states, i.e. states that belong to the same shell of some valence states, as in the case of d states [150]. The second term corresponds to a core contribution to the polarization of valence electrons and is generally smaller. Ku and Eguiluz [149] raised some doubts for the replacement $iG_cW + iG_vW_vP_cW_v \rightarrow V_{xc}$ because their all-electron calculations presented large discrepancies with respect to previous pseudopotential-based results. They found in fact a strong underestimation of the band gap in bulk silicon. Further works, carried out both in all-electron and in the pseudopotential contexts, have then shown that the discrepancies tend to become smaller when all-electron calculations are more converged [151][152] and more states are included in valence in pseudopotential calculations [153]. Therefore, a pseudopotential calculation, if properly performed, can still be considered reliable.

3.4 Self-consistent quasiparticle calculations

In a fully self-consistent GW calculation one should update both the eigenvalues and the eigenfunctions until those that enter the construction of the potentials (the Hartree term and the self-energy) are equal to the ones obtained by the solution of the Dyson equation. It is formidable task. In fact, since the self-energy is non-Hermitian, self-consistency requires the calculation of both the left and right eigenfunctions (see Eq. (3.53)). Moreover, one should diagonalize the Hamiltonian at each energy, since the GW self-energy is also frequency dependent.

Fully self-consistent calculations have been carried out only few times for the homogeneous electron gas [154], in the Hubbard model [155][156], for simple semiconductors and metals [157][149], and for some atoms and molecules [151][158]. But even when the self-consistency issue is taken into account, one often still assumes that the LDA wavefunctions are a good approximation to the quasiparticle wavefunctions and hence the self-energy is kept diagonal in the LDA basis [149]. In this case only the eigenvalues entering the Green's function and the dielectric matrix are updated self-consistently [159]. This can be partially motivated by the fact that the main changes in the band structure generally come from an update of the eigenvalues [141]. Already in the works of Hybertsen and Louie [131] there is a discussion about the update of the quasiparticle energies in the self-energy. Self-consistency in the energies has been considered many times since then.

There are also reasons of principle to avoid performing fully self-consistent GW calculations. Self-consistency has been shown to be essential in order to satisfy conservation laws that are fundamental for e.g. total-energy calcu-

3. One-particle excitations

lations [160][161]. But, on the contrary, a self-consistent GW calculation of the spectral properties of the homogeneous electron gas has yielded results that are worse than the ones obtained by the standard perturbative GW scheme [154] or at the GW_0 level, where only G is updated self-consistently [162]. The self-consistent calculation ends up with broad, featureless structures in the spectral function, the disappearance of the plasmon satellite and a larger bandwidth. This result has been explained with the fact that the GW self-energy is dynamical. The frequency dependence of the self-energy leads to a transfer of the spectral weight from the main quasiparticle peak to the side of the spectrum. The fact that self-consistent GW calculations deteriorate the results concerning the spectral properties suggests that one should consider vertex corrections beyond the GW approximation. In fact it has been found that self-consistency and vertex corrections have opposite effects [156][163][164].

On the other hand, the standard GW method, based on a perturbative scheme, relies on the quality of the underlying starting point and therefore it is in this sense arbitrary, even though well grounded on a pragmatic point of view. The underestimation of the band gap in LDA can lead to an overestimation of the screening in W (which is calculated in RPA) and hence yield a too small GW correction [165]. In cases of wrong band ordering or wrong band occupations, the Kohn-Sham LDA itself can be a problematic starting point [166]. A way to overcome these difficulties is to improve the “best G , best W ” approach by performing self-consistent quasiparticle calculations. In this case one considers static and Hermitian approximations to the self-energy in order to build the best mean-field Hamiltonian. In this way, the self-consistent calculation becomes feasible and the problems connected to the frequency dependence of Σ are avoided. In fact, in the updated Green’s function only the quasiparticle contributions are kept and the incoherent parts of the spectral function are discarded. Of course, the self-consistent loop leads to “forget” the LDA starting point.

In this framework mainly two approximations have been proposed and tested [141][167][168]. One is based on the COHSEX approximation introduced by Hedin [127] (see Sec. 3.5). The other is the recent quasiparticle self-consistent GW (QPscGW) scheme proposed by Faleev *et al.* [169][139] in 2004.

In these procedures one has to build and diagonalize the full approximate static Hamiltonian $h_0 + V_H + \Sigma$ until the self-consistency requirement between input and output eigenvalues and eigenvectors is fulfilled. In the QPscGW scheme one adopts a GW self-energy and evaluates its matrix elements as:

$$\langle \phi_i | \Sigma | \phi_j \rangle = \frac{1}{2} \text{Re}[\langle \phi_i | \Sigma(E_i) | \phi_j \rangle + \langle \phi_i | \Sigma(E_j) | \phi_j \rangle], \quad (3.70)$$

where Re means that only the Hermitian part is retained. While off-diagonal matrix elements are approximated, the diagonal elements are the true GW

3.5 The COHSEX approximation

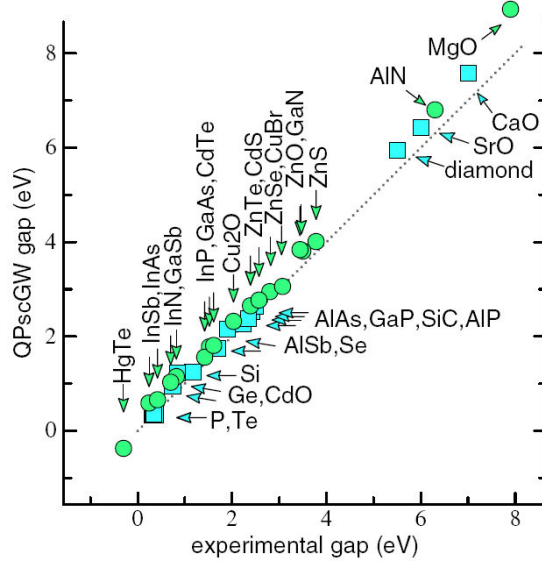


Figure 3.5: Comparison between experimental and band gaps and the ones calculated in the QPscGW approximation. The agreement is very good. See also Fig. 3.2. From Ref. [139].

ones. The QPscGW scheme leads to results in very good agreement with experiment, with small systematic errors with a overestimation of the band gap (see Fig. 3.5). Faleev *et al.* [139] claim that this slight overestimation can be explained as due to the need of inclusion of electron-hole interactions beyond RPA through vertex corrections.

3.5 The COHSEX approximation

An alternative quasiparticle approach to QPscGW is the COHSEX approximation to the self-energy. COHSEX is a static approximation of the GW self-energy that has been introduced by Hedin [127],

In Hartree-Fock particles interact through the bare potential v , and the self-energy Σ_x is (see Eq. (3.38)):

$$\Sigma_x(\mathbf{r}_1, \mathbf{r}_2) = \frac{i}{2\pi} \int d\tau e^{i\omega\tau} G(\mathbf{r}_1, \mathbf{r}_2, \tau) v(\mathbf{r}_1, \mathbf{r}_2) \delta(\tau + \eta). \quad (3.71)$$

A first improvement with respect to Hartree-Fock would be to consider instead of v a statically screened potential. By replacing $v(\mathbf{r}_1, \mathbf{r}_2)$ in Eq. (3.71) with $W(\mathbf{r}_1, \mathbf{r}_2, \omega = 0)$, one would get a screened exchange (SEX) self-energy:

$$\Sigma_{SEX}(\mathbf{r}_1, \mathbf{r}_2) = \frac{i}{2\pi} \int d\tau e^{i\omega\tau} G(\mathbf{r}_1, \mathbf{r}_2, \tau) W(\mathbf{r}_1, \mathbf{r}_2, \omega = 0) \delta(\tau + \eta). \quad (3.72)$$

3. One-particle excitations

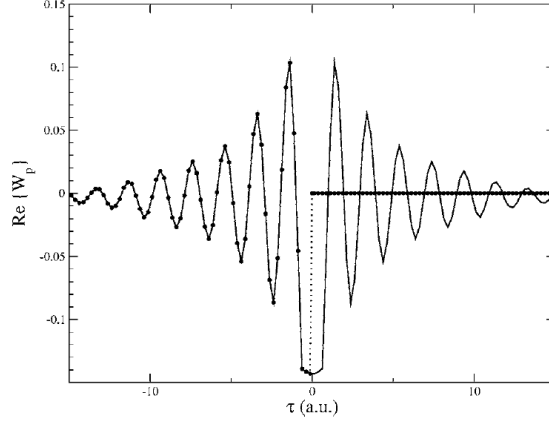


Figure 3.6: Real part of the screened potential $W_{p,\mathbf{G},\mathbf{G}'}(\mathbf{q}, \tau)$ in aluminum. Comparison between time-ordered W_p (solid line) and advanced W_p (dots) for $\mathbf{G} = \mathbf{G}' = 0$ and $\mathbf{q}=(0.25,0,0)$. From Ref. [141].

Σ_{SEX} hence has the same structure as the Hartree-Fock self-energy. Similarly it involves only occupied states.

As in Hartree-Fock, in the SEX approximation one still has a completely instantaneous interaction. This has as a consequence the $\delta(\tau + \eta)$ factor in Eq. (3.72). In the SEX approximation, for the presence of the small η in the δ factor, W is evaluated at the time $\tau = 0^-$, which corresponds to an advanced screened potential [141] (see Fig. 3.6). This breaks the particle-hole symmetry in (the time-ordered) W . In the COHSEX approximation of Hedin [127], this symmetry is restored by taking as self-energy:

$$\begin{aligned} \Sigma_{COHSEX}(\mathbf{r}_1, \mathbf{r}_2, \tau) = & iG(\mathbf{r}_1, \mathbf{r}_2, \tau)v(\mathbf{r}_1, \mathbf{r}_2, \tau + \eta) + \\ & + iG(\mathbf{r}_1, \mathbf{r}_2, \tau) \int d\tau' W_p(\mathbf{r}_1, \mathbf{r}_2, \tau')\delta(\tau), \end{aligned} \quad (3.73)$$

where $W_p = W - v$ is the polarization potential. In other words, one replaces W_p in the W entering Eq. (3.72) with its integrated value times a $\delta(\tau)$ function [118]. Inserting in (3.73) the explicit expression (3.2) for $G(\mathbf{r}_1, \mathbf{r}_2, \tau)$ and taking the Fourier transform, one has:

$$\begin{aligned} \Sigma_{COHSEX}(\mathbf{r}_1, \mathbf{r}_2) = & -\langle N | \hat{\psi}^+(\mathbf{r}_2) \hat{\psi}(\mathbf{r}_1) | N \rangle v(\mathbf{r}_1, \mathbf{r}_2) + \\ & + \frac{1}{2} \left[\langle N | \hat{\psi}(\mathbf{r}_1) \hat{\psi}^+(\mathbf{r}_2) | N \rangle - \langle N | \hat{\psi}^+(\mathbf{r}_2) \hat{\psi}(\mathbf{r}_1) | N \rangle \right] W_p(\mathbf{r}_1, \mathbf{r}_2, \omega = 0), \end{aligned} \quad (3.74)$$

where I have used the fact that $\theta(\tau)\delta(\tau) = -\theta(\tau)\delta(\tau) = \frac{1}{2}\delta(\tau)$. Adding and subtracting a term $\frac{1}{2}\langle N | \hat{\psi}^+(\mathbf{r}_2) \hat{\psi}(\mathbf{r}_1) | N \rangle W_p(\mathbf{r}_1, \mathbf{r}_2, \omega = 0)$, Eq. (3.74) can

3.5 The COHSEX approximation

be rewritten as:

$$\begin{aligned} \Sigma_{COHSEX}(\mathbf{r}_1, \mathbf{r}_2) = & -\langle N | \hat{\psi}^+(\mathbf{r}_2) \hat{\psi}(\mathbf{r}_1) | N \rangle W(\mathbf{r}_1, \mathbf{r}_2, \omega = 0) + \\ & + \frac{1}{2} \delta(\mathbf{r}_1 - \mathbf{r}_2) W_p(\mathbf{r}_1, \mathbf{r}_2, \omega = 0). \end{aligned} \quad (3.75)$$

In the COHSEX approximation the self-energy is static. It is the sum of two contributions: the screened-exchange (SEX) and the Coulomb-hole (COH) terms. They are:

$$\Sigma_{SEX}(\mathbf{r}_1, \mathbf{r}_2) = - \sum_i \theta(\mu - E_i) \phi_i(\mathbf{r}_1) \phi_i^*(\mathbf{r}_2) W(\mathbf{r}_1, \mathbf{r}_2, \omega = 0), \quad (3.76)$$

$$\Sigma_{COH}(\mathbf{r}_1, \mathbf{r}_2) = \frac{1}{2} \delta(\mathbf{r}_1 - \mathbf{r}_2) W_p(\mathbf{r}_1, \mathbf{r}_2, \omega = 0). \quad (3.77)$$

With respect to the SEX approximation, in the COHSEX approximation there is the additional term Σ_{COH} , which is local in space. It represents the classical interaction between an additional point charge and the surrounding polarization cloud that the point charge induces [2][3][127]. In homogeneous system Σ_{COH} is just a constant, determining a rigid shift of the band structure. But in all the other situations it introduces important corrections on top of the shift with respect to SEX calculations [141]. Neglecting the screening effects (i.e. setting $\epsilon^{-1} = 1$), one recovers the Hartree-Fock approximation, since in this case $\Sigma_{COH}=0$ and $\Sigma_{SEX} = iGv$.

Equivalently, the COHSEX self-energy can be seen directly as a static approximation of the GW self-energy. By combining the spectral representation (3.67) of the time-ordered W_p with the spectral representation (3.18) for G and performing the frequency integration (3.64), one obtains that the GW self-energy is given by the sum of two terms [118][121]:

$$\Sigma_1(\mathbf{r}_1, \mathbf{r}_2, \omega) = - \sum_i \theta(\mu - E_i) \phi_i(\mathbf{r}_1) \phi_i^*(\mathbf{r}_2) W(\mathbf{r}_1, \mathbf{r}_2, \omega - E_i), \quad (3.78)$$

$$\Sigma_2(\mathbf{r}_1, \mathbf{r}_2, \omega) = \sum_i \phi_i(\mathbf{r}_1) \phi_i^*(\mathbf{r}_2) \int_0^\infty d\omega' \frac{D(\mathbf{r}, \mathbf{r}', \omega')}{\omega - E_i - \omega'}. \quad (3.79)$$

The first term arises from the poles in G and the second from the poles in W [131]. The static COHSEX approximation for the two terms is obtained when in $\Sigma_1(\omega)$ and $\Sigma_2(\omega)$ one sets $\omega - E_i = 0$. This corresponds to assume that the main contribution to the self-energy $\Sigma(\omega)$ stems from the states E_i close to ω . So $\omega - E_i$ is small compared to main excitations in D which are at the plasmon energy [127][118]. Σ_1 can be in this way identified with Σ_{SEX} and Σ_2 with Σ_{COH} .

The COHSEX self-energy is known to overestimate the GW self-energy corrections by $\sim 20\%$ in simple semiconductors [131]. Since in the COHSEX approximation the self-energy is static and Hermitian a self-consistent

3. One-particle excitations

COHSEX calculation is feasible. It produces wavefunctions and quasiparticle energies that are expected to be not too far from the real ones. They can be therefore used as a reliable starting point for a perturbative GW calculation, which takes into account the dynamical effects that COHSEX neglects.

Other self-consistent schemes have been proposed in order to improve the LDA (or GGA) starting points. Here the aim should be to find a good compromise between the physical information included in the approximation used in the self-consistent calculation and its computational cost. For example, by replacing LDA with EXX one could hope to have a better starting point for a subsequent perturbative GW calculation [136]. But EXX is still within DFT, with a Kohn-Sham local potential. So one has still to assume that the Kohn-Sham wavefunctions are a good approximation to the quasiparticle wavefunctions. Besides, EXX lacks correlation and is computationally heavy (heavier than the last GW perturbative step), because in order to calculate V_{xc} in EXX one needs also unoccupied states. So EXX does not seem very convenient from either points of view. A better starting point than the EXX could be found in a generalized Kohn-Sham scheme [170], where one for instance can adopt a nonlocal and static potential, deriving from hybrid functionals. In this case one would have to perform a cheaper self-consistent calculation than in COHSEX, but at the price of introducing some parameters to mix the LDA V_{xc} with a nonlocal exchange term [138]. When, in particular, self-consistent calculations are done in the SEX approximation [171], from a computational point of view, the only difference with respect to COHSEX is the Coulomb-hole term, whose computational cost is insignificant, but has important effects, especially in inhomogeneous systems [141]. From the point of view of the quality of the approximation, the QP-scGW self-energy is the closest one to the GW self-energy. But performing a QPscGW calculation is much more expensive than in the COHSEX approximation. Moreover, the COHSEX+GW scheme has been shown [3][141] to lead results comparable with the ones obtained in the QPscGW approach.

Therefore, from this cost-benefit analysis the COHSEX approximation turns out to be a very good compromise. For this reason I will use it to perform quasiparticle self-consistent calculations. So I will describe this approach in some more details in the next section.

3.5.1 Self-consistent COHSEX in practice

The first step is a well-converged LDA calculation. For each \mathbf{k} point, the LDA wavefunctions $\varphi_{i\mathbf{k}}$ are then used as a basis to represent the COHSEX wavefunctions $\phi_{i\mathbf{k}}$:

$$|\phi_{i\mathbf{k}}\rangle = \sum_j c_{ij\mathbf{k}} |\varphi_{j\mathbf{k}}\rangle. \quad (3.80)$$

3.5 The COHSEX approximation

Since the starting point is LDA, at the first iteration this matrix is the identity. Moreover, at the first iteration also the quasiparticle energies E_i are given by the Kohn-Sham eigenvalues ϵ_i .

Then, at each step, using the quasiparticle wavefunctions $\phi_{i\mathbf{k}}$ and the quasiparticle energies E_i , one has to calculate the full Hamiltonian $\langle \phi_{i\mathbf{k}} | h_0 + V_H + \Sigma | \phi_{j\mathbf{k}} \rangle$, where Σ is the static and Hermitian COHSEX self-energy. In particular, $h_0 = V_{KS} - V_H - V_{xc}$ and one needs to calculate ϵ^{-1} and W at $\omega = 0$ to build Σ (see Eq. (3.74)). At the step n , the diagonalization of the Hamiltonian yields a new set of quasiparticle energies $E_i^{(n)}$ and coefficients $c_{ij\mathbf{k}}^{(n)}$ that link the new quasiparticle wavefunctions to the quasiparticle wavefunctions at the previous iteration:

$$|\phi_{i\mathbf{k}}^{(n)}\rangle = \sum_j c_{ij\mathbf{k}}^{(n)} |\phi_{j\mathbf{k}}^{(n-1)}\rangle. \quad (3.81)$$

So the matrix of the coefficients evolves through the self-consistent loop, by mixing for each quasiparticle wavefunction $\phi_{i\mathbf{k}}$ different contributions coming from the different LDA wavefunctions $\varphi_{i\mathbf{k}}$. Since the Hamiltonian is Hermitian, the matrix of the coefficients c_{ij} remains unitary. By converging the calculation, the Hamiltonian on the basis of the updated quasiparticle wavefunctions $\phi_{i\mathbf{k}}^{(n)}$ tends to be diagonal. One iterates the self-consistent loop until the new quasiparticle energies $E_i^{(n)}$ are close (within a fixed small difference, in general 1 meV) to quasiparticle energies at the previous step $E_i^{(n-1)}$. It is also possible to perform energy-only self-consistent calculations. In this case the wavefunctions remain the LDA ones and only the quasiparticle energies E_i are updated in the construction of the Hamiltonian.

Since in practical calculations the LDA basis is finite, one has to converge with the number of LDA wavefunctions used to represent the QP wavefunctions in Eq. (3.80). The number of these LDA wavefunctions corresponds to the number of states that one needs to recalculate self-consistently (for all the \mathbf{k} points). So, a self-consistent quasiparticle calculation is much more expensive than the standard GW perturbative calculations, where one evaluates the corrections only for the states (bands and \mathbf{k} points) of interest.

Moreover, in order to avoid undamped local oscillations of charge (while the total density is conserved), the practical experience evidenced the need to introduce a damping factor for the electronic density. The density used at the step N , $\rho^{(n)}$, is given by:

$$\rho^{(n)}(\mathbf{r}) = \alpha \sum_i |\phi_i^{(n)}(\mathbf{r})|^2 + (1 - \alpha) \sum_i |\phi_i^{(n-1)}(\mathbf{r})|^2. \quad (3.82)$$

Without damping (i.e. with $\alpha = 1$) one would have instead directly:

$$\rho^{(n)}(\mathbf{r}) = \sum_i |\phi_i^{(n)}(\mathbf{r})|^2. \quad (3.83)$$

3. One-particle excitations

Finally, the converged self-consistent COHSEX eigenfunctions and eigenvalues are used as an input for the last perturbative GW calculation that yields the final result.

Figure 3.7 shows the flowchart of the self-consistent COHSEX calculations, with the LDA prelude and the perturbative GW epilogue. For a more detailed explanation of the implementation scheme I refer to the thesis of F. Bruneval [3].

3.5 The COHSEX approximation

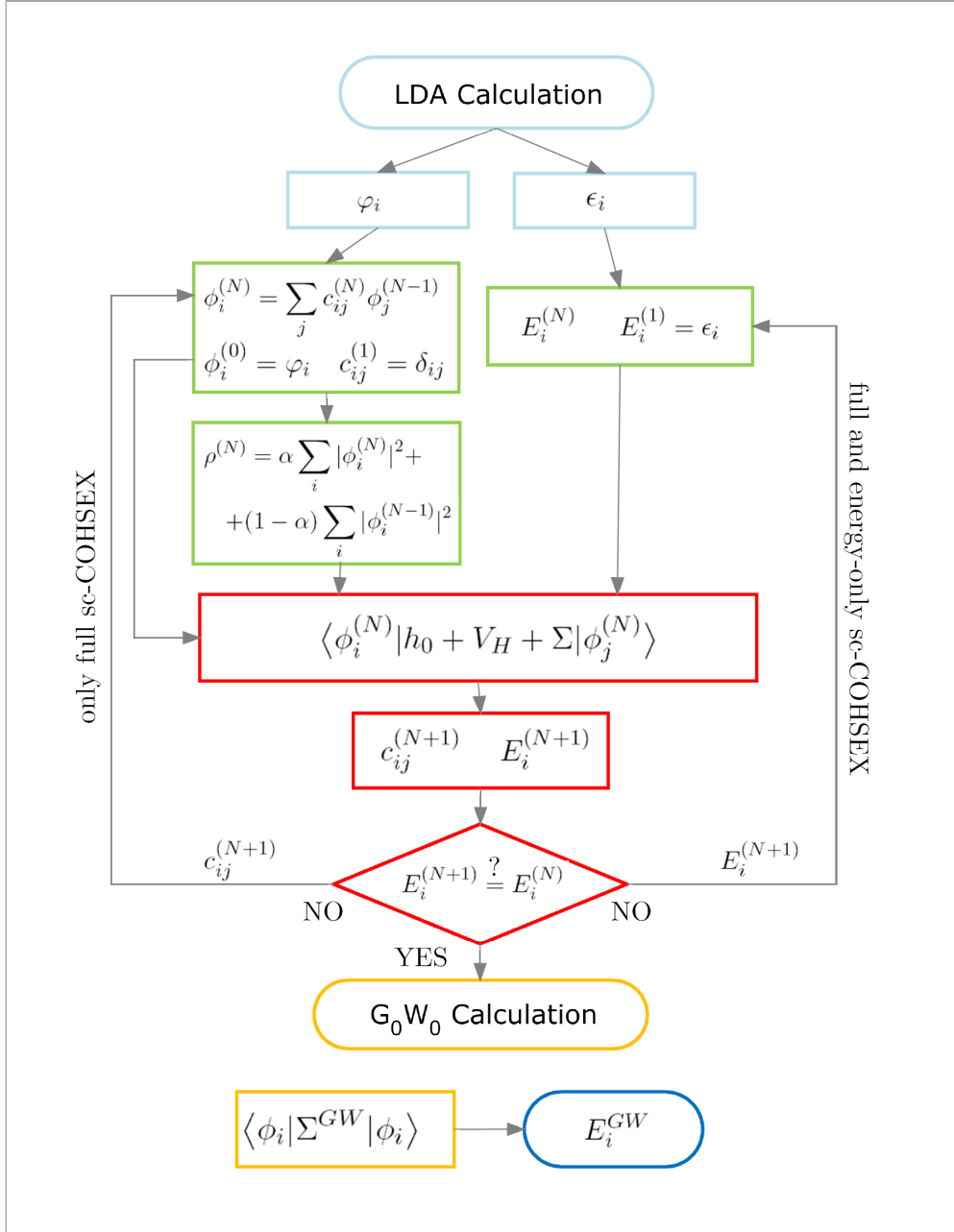


Figure 3.7: Flowchart of self-consistent COHSEX calculations.

Chapter 4

Models for strongly correlated systems

In strongly correlated systems, first-principles methods become often inapplicable, because of the high number of electrons involved in the calculations but mostly because good approximations for functionals describing strong correlations have not been found yet. In these cases also the quasiparticle paradigm can be insufficient to describe photoemission.

An alternative way can be to renounce to a first-principle description and introduce a model Hamiltonian (to describe at least the correlated orbitals). The Hubbard model is one of the most used model Hamiltonian to describe strongly correlated systems (see Sec. 1.3.2). In this model, correlated electrons interact via a strong on-site repulsive interaction weighted by an adjustable parameter U .

In this context, different schemes that takes LDA as starting point have been recently developed. In these approaches, the LDA electronic structure is used to adjust the parameters of the Hubbard Hamiltonian. This permits to take explicitly into account the Hubbard U for the orbitals that are thought to be strongly correlated. In this chapter, I will present the main ideas of two of such approaches: LDA+ U and dynamical mean-field theory (LDA+DMFT).

The review of Anisimov et al. [172] gives a general introduction to the LDA+ U method. Analogously, the reviews of Georges et al. [173] and Kotliar et al. [174] describe the state-of-the-art of DMFT.

4.1 LDA+ U

The first assumption of the LDA+ U scheme is the separation of electrons in two classes: electrons belonging to correlated d (or f) orbitals and electrons in delocalized s and p orbitals.

The LDA+ U method makes use of a Hubbard model Hamiltonian (see

4. Models for strongly correlated systems

Eq. (1.44)):

$$\hat{H} = -t \sum_{\langle ij \rangle \sigma} (\hat{c}_{i\sigma}^\dagger \hat{c}_{j\sigma} + h.c.) + U \sum_i \hat{n}_{i\uparrow} \hat{n}_{i\downarrow}. \quad (4.1)$$

The kinetic term is calculated with the Kohn-Sham LDA energy functional for all the orbitals. The LDA Coulomb interaction between d orbitals is then replaced by the on-site Hubbard term U . In practice, the “mean-field” LDA evaluation of the $d-d$ interaction is subtracted from the LDA energy functional. This is called the double-counting correction. The Hubbard term acting only on the d orbitals is added to the energy functional. In this way, as in the SIC approach in DFT (see Sec. 2.2.3), localized electrons move in a different potential than delocalized electrons. Anyway, in the LDA+U scheme the s and p orbitals have still an indirect effect. Even though they are not treated explicitly by the Hubbard term, they contribute to screen the atomic Coulomb interaction between d orbitals, which leads to a renormalization of the atomic Hubbard U .

The total LDA+U energy functional is [175]:

$$E_{LDA+U} = E_{LDA} + E_U - E_{dc} \quad (4.2)$$

Introducing the occupations n_i of the d orbitals on a site I , the LDA+U energy functional explicitly reads [176]:

$$E_{LDA+U} = E_{LDA} + \frac{1}{2}U \sum_{i \neq j} n_i n_j - U \frac{N(N-1)}{2}, \quad (4.3)$$

where $N = \sum_i n_i$ is the total number of d electrons in the site I . The last term of Eq. (4.3) is one of the possible expressions of the double-counting term, whose formulation is actually arbitrary.

The LDA+U potential is clearly an orbital-dependent potential. In fact it can be written as:

$$V_{LDA+U} = \sum_i V_i(\mathbf{r}) |i\rangle \langle i|, \quad (4.4)$$

where the projection operator on the orbital i has been explicitly introduced. V_{LDA+U} is a static nonlocal potential. The potential $V_i(\mathbf{r})$ acting on the orbital i can be obtained by taking the derivative of the energy functional E_{LDA+U} with respect to the charge density $\rho_i(\mathbf{r})$ related to the orbital i . For the s and p orbitals, $V_i(\mathbf{r})$ coincides with the LDA potential. For the d orbitals instead it is:

$$V_i(\mathbf{r}) = V_{LDA}(\mathbf{r}) + U \left(\frac{1}{2} - n_i \right). \quad (4.5)$$

Moreover, the eigenvalues are the derivatives of E_{LDA+U} with respect to the orbital occupations n_i [86]:

$$\epsilon_i = \epsilon_{i,LDA} + U \left(\frac{1}{2} - n_i \right). \quad (4.6)$$

So, in a non-self-consistent LDA+U calculation, the s and p orbitals, ϵ_i would have the LDA value. The occupied d orbitals have $n_i = 1$. Their energies are downshifted by $-U/2$ with respect to the LDA eigenvalues. Empty d orbitals have $n_i = 0$ and their energy are upshifted by $+U/2$. Full and empty d orbitals become respectively lower and upper Hubbard bands separated by a gap U . In actual calculations, the potential V_{LDA+U} enters the Kohn-Sham equations, which have to be solved self-consistently. In any case, the Hubbard correction $U(1/2 - n_i)$ in (4.5) tends to localize electrons on d orbitals where the occupation is larger than $1/2$.

This simplified model corresponds to a one-band Hubbard Hamiltonian. It has to be generalized [177][172] in order to take into account spin, exchange effects between different d orbitals, and the fact that d orbitals are not spherical and hence U depends on the particular type of d orbital. Then E_{LDA} is calculated considering explicitly the spin σ in the local-spin-density approximation (LSDA) to DFT. Moreover, the Hubbard term now contains also an exchange term. So it depends on the density matrix $\gamma_\sigma(\mathbf{r}, \mathbf{r}') = \sum_i \varphi_{i\sigma}^*(\mathbf{r}) \varphi_{i\sigma}(\mathbf{r}')$.

$$E_U = \frac{1}{2} \sum_{m_1\sigma} [\langle m_1 m_3 | V_{scr} | m_2 m_4 \rangle \gamma_{m_1 m_2 \sigma} \gamma_{m_3 m_4 \bar{\sigma}} + \langle m_1 m_3 | V_{scr} | m_2 m_4 \rangle - \langle m_1 m_3 | V_{scr} | m_4 m_2 \rangle] \gamma_{m_1 m_2 \sigma} \gamma_{m_3 m_4 \sigma} \quad (4.7)$$

where the matrix elements of the screened interaction V_{scr} are taken with respect to the components $|m\rangle$ with magnetic quantum number m of the d atomic orbital sitting on the site I (and $\bar{\sigma}$ stands for $-\sigma$). So $\gamma_{m_1 m_2 \sigma} = \sum_i \langle \varphi_{i\sigma} | m_1 \rangle \langle m_2 | \varphi_{i\sigma} \rangle$. The double-counting term becomes:

$$E_{dc} = U \frac{N(N-1)}{2} - J \sum_{\sigma} \frac{N_{\sigma}(N_{\sigma}-1)}{2}, \quad (4.8)$$

where $N_{\sigma} = \sum_m \gamma_{mm\sigma}$ and the Coulomb U and exchange J interaction parameters are (for d orbitals $l = 2$):

$$U = \frac{1}{(2l+1)^2} \sum_{m_1 m_2} \langle m_1 m_2 | V_{scr} | m_1 m_2 \rangle, \quad (4.9)$$

$$J = \frac{1}{2l(2l+1)} \sum_{m_1 \neq m_2} \langle m_1 m_2 | V_{scr} | m_2 m_1 \rangle. \quad (4.10)$$

4. Models for strongly correlated systems

The matrix elements of V_{scr} remain to be determined. If they are expanded in spherical harmonics, their values can be related directly with U and J , using Slater integrals. So, once the parameters U and J have been chosen (or evaluated in some way), the total functional E_{LDA+U} is completely determined.

Different ways to calculate U have been proposed. U is the energy cost for moving a d electron between two atoms with n d electrons each, renormalized by the screening due to the other s and p electrons [178]. In the most efficient situation, the screening has the effect to move one of these sp electrons in the opposite direction, with the consequence of reducing the energy cost of the d electron transfer. U is then the cost of the global reaction $2(d^n s^1) \rightarrow d^{n+1} s^0 + d^{n-1} s^2$. U can be calculated in the framework of constrained LDA by moving one d electron on a site and letting the system relax, with the further constraint that hopping of d electrons between the atom with the additional charge and the others is forbidden (in fact this term is already taken into account by the kinetic term in the Hubbard Hamiltonian).

While, thanks to its orbital dependence, LDA+ U is able to determine a gap opening in d and f systems, often it has the tendency to favor the anti-ferromagnetic solution, even in cases where no magnetic ordering is found in experiments [179]. Moreover, since its Hamiltonian is static, it is incapable to describe the transfer of spectral weight that occurs in metal-insulator transitions and which can be accounted for only by dynamical approaches.

4.1.1 What is U ? A GW perspective

Here it is interesting to make a bridge with the GW formalism. I follow the argument discussed by Anisimov *et al.* in [172]. The matrix element of the self-energy in the GW approximation on a d state can be written as:

$$\langle d|\Sigma(E_d)|d\rangle = \langle d|\Sigma_x|d\rangle + \sum_j^{occ} \langle dj|W_p^-(E_d-E_j)|jd\rangle + \sum_j^{unocc} \langle dj|W_p^+(E_d-E_j)|jd\rangle, \quad (4.11)$$

where the first term on the right-hand-side is the expectation value of the Fock operator Σ_x (see Eq. (3.39)) and

$$W_p^\pm(\mathbf{r}, \mathbf{r}', \omega) = \int_{-\infty}^{+\infty} d\omega' \frac{D(\mathbf{r}, \mathbf{r}', \omega')}{\omega - \omega' \pm i\eta}, \quad (4.12)$$

with $W_p = W - v$ (see Eq. (3.67)). Assuming that the d state is localized and well separated in energy from the other states, one can say that the most important contribution to the correlation term $\langle d|\Sigma_c|d\rangle$ in the sums of Eq. (4.11) is given by the diagonal one: $j = d$. If d is occupied, it is $\langle dd|W_p^-(0)|dd\rangle$. If it is unoccupied, it is $\langle dd|W_p^+(0)|dd\rangle$.

Since W_p is an even function of ω , it holds that [172]:

$$W_p^\pm(0) = \pm \frac{1}{2} W_p(0). \quad (4.13)$$

The conclusion is that the two d states result separated by an energy:

$$\Delta = \langle dd|v|dd\rangle + \langle dd|W_p(0)|dd\rangle = \langle dd|W(\omega = 0)|dd\rangle = U. \quad (4.14)$$

This is the physical interpretation of U in the GW framework: $U \approx \langle W(\omega = 0) \rangle$. The U calculated in constrained LDA is generally larger than the static limit of W (calculated in RPA) [180], where there is no constraint for the hopping of the d orbitals. In fact, since in static RPA $\omega = 0$ corresponds to a time length $\tau = \infty$, the hopping of d electrons between different sites is always possible on such a time scale [181].

Hence, in a GW perspective, the Hubbard U denotes the on-site static limit of the screened interaction W . Actually, since the screening, which is due to $\epsilon^{-1}(\omega)$, is frequency dependent (it becomes weaker at high energies – see Eq. (1.31)), also U should be a frequency-dependent function. In fact, it is possible to identify a frequency dependent $U(\omega)$ with the on-site matrix elements between the d orbitals of an effective screened interaction $W_r(\omega)$, where the screening entering W_r stems only from the s and p orbitals [182]. Explicitly, the polarizability P can be split into a component P_d due to the d orbitals and a component P_r due to all the other orbitals: $P = P_d + P_r$ (the same can be done with the Green's function: $G = G_d + G_r$). And, if W_r is defined as: $W_r = v + vP_rW_r$, then the total screened interaction W becomes: $W = W_r + W_rP_dW$. The GW self-energy in this way can be partitioned into three terms [182]:

$$iGW = iG_dW_d + iG_dW_r + iG_rW. \quad (4.15)$$

The second term is the main correction to the static Hubbard model. The last term, involving orbitals different from the d ones, is instead neglected in both the static and dynamical Hubbard models.

These arguments have provided a physical interpretation of the Hubbard U at a GW level. Here it is also interesting to make a brief reference to results concerning the GW performance in solving the Hubbard Hamiltonian (at different U/t ratios). In particular, in a series of papers, Verdozzi *et al.* [155], Pollehn *et al.* [183], and Schindlmayr *et al.* [156] have applied the GW approximation to analytically solvable finite Hubbard systems. Their results have shown that at low interaction strength (such as $U/t = 1.5$ [155]) GW results are in very good agreement with the exact results, concerning both the quasiparticle peaks and the satellites. Especially far from half filling, by increasing the interaction strength the agreement deteriorates (the amplitude of the satellites is overestimated and the quasiparticle peaks are shifted by a constant with respect to exact solutions). This shows the need to include vertex corrections beyond the GW approximation. For instance, for nearly filled (or nearly empty) band systems, the T-matrix approximation [184][185] in these finite Hubbard models is in good agreement with the exact results even at high U/t ratio. Whereas the screening in GW is calculated

4. Models for strongly correlated systems

at the RPA level, which is given by an infinite summation of ring diagrams [117], the T-matrix approximation corresponds to an infinite summation of ladder diagrams due to particle-particle (or hole-hole) multiple scattering, that can be important to deal with short-range correlations.

4.2 Dynamical mean-field theory

Dynamical mean-field theory (DMFT) is a method that is able to provide an approximate solution to the Hubbard Hamiltonian in the nontrivial regime $t \sim U$, where the competition between localized and itinerant electronic characters is the most important (see Sec. 1.3.2). The main idea is to map a lattice model (the Hubbard model) into an atomic impurity model (the Anderson impurity model) subjected to a self-consistency condition [173]. This mapping strategy can be understood similarly to the Kohn-Sham scheme where one introduces a reference system of noninteracting particles that reproduce the density of the real system.

I am not going to present rigorously the mathematical details of the method. The aim is just to introduce the main physical ideas underlying the theory. Moreover, I will adopt a T=0 K formalism, whereas in DMFT one normally makes use of a finite-temperature formalism.

4.2.1 DMFT for the Hubbard model

The starting point is the one-band Hubbard model on a cubic lattice (see Sec. 1.3.2):

$$\hat{H} = -t \sum_{\langle ij \rangle \sigma} (\hat{c}_{i\sigma}^\dagger \hat{c}_{j\sigma} + \hat{c}_{j\sigma}^\dagger \hat{c}_{i\sigma}) + U \sum_i \hat{n}_{i\uparrow} \hat{n}_{i\downarrow}. \quad (4.16)$$

The Green's function of the Hubbard model (in the reciprocal space) is:

$$G(\mathbf{k}, \omega) = \frac{1}{\omega - \epsilon_{\mathbf{k}} - \Sigma(\mathbf{k}, \omega)}, \quad (4.17)$$

where $\epsilon_{\mathbf{k}} = -2t \sum_d \cos(k_d a)$.

The key variable in DMFT is the local Green's function G_{loc} . It corresponds to the on-site part of the lattice Green's function G : $G_{loc} = G_{ii}$. In the reciprocal space:

$$G_{loc}(\omega) = \sum_{\mathbf{k}} \frac{1}{\omega - \epsilon_{\mathbf{k}} - \Sigma(\mathbf{k}, \omega)}. \quad (4.18)$$

The local G_{loc} can be represented by the Green's function G_{imp} of the Anderson impurity model [186]. In other words, in DMFT the Anderson model plays the role of reference system (like the Kohn-Sham system of

4.2 Dynamical mean-field theory

	DFT	DMFT
Key quantity	$\rho(\mathbf{r}) = -iG(\mathbf{r}, t, \mathbf{r}, t^+)$	$G_{loc}(\omega) = G_{ii}(\omega)$
Reference system	Kohn-Sham system	Anderson impurity model
Effective variables	$V_{xc}(\mathbf{r})$ and $G_{KS}(\mathbf{r}, t, \mathbf{r}', t')$	$\Sigma_{imp}(\omega)$ and $G_{imp}(\omega)$
Link to key quantity	$-iG_{KS}(\mathbf{r}, t, \mathbf{r}, t^+) = \rho(\mathbf{r})$	$G_{imp}(\omega) = G_{loc}(\omega)$

Table 4.1: In both DFT (where the key quantity is the density $\rho(\mathbf{r})$) and DMFT (where the key quantity is the on-site Green's function $G_{ii}(\omega)$) one introduces a fictitious reference system. In DFT it is the Kohn-Sham system, in DMFT it is the Anderson impurity model. In both cases the full many-body quantities (G and Σ) in the reference system are replaced by reduced effective variables ($V_{xc}(\mathbf{r})$ and G_{KS} in DFT; $\Sigma_{imp}(\omega)$ and $G_{imp}(\omega)$ in DMFT). The reference system doesn't reproduce all the properties of the real physical system, but only the quantity of interest.

DFT), with the property $G_{imp} = G_{loc}$ (see Tab. 4.1). In general, the Anderson impurity model describes a single impurity atom coupled to an effective bath of noninteracting delocalized conduction electrons. It is a single-site model, so G_{imp} is a single-site Green's function by definition. The Hamiltonian \hat{H}_{AIM} of the Anderson impurity model is made of three terms:

$$\hat{H}_{AIM} = \hat{H}_{atom} + \hat{H}_{bath} + \hat{H}_{coupling}. \quad (4.19)$$

Explicitly:

$$\hat{H}_{AIM} = \epsilon_d \sum_{\sigma} \hat{c}_{\sigma}^{\dagger} \hat{c}_{\sigma} + U \hat{n}_{c\uparrow} \hat{n}_{c\downarrow} + \sum_{l\sigma} \epsilon_l \hat{a}_{l\sigma}^{\dagger} \hat{a}_{l\sigma} + \sum_{l\sigma} V_l (\hat{a}_{l\sigma}^{\dagger} \hat{c}_{\sigma} + \hat{c}_{\sigma}^{\dagger} \hat{a}_{l\sigma}). \quad (4.20)$$

It describes the exchange of electrons between the bath (which has the electronic levels ϵ_l) and the impurity (which has one level ϵ_d). The probability of hopping between one level l of the bath and the impurity is given by V_l . When two electrons (with opposite spin) sit on the atomic level, they have to pay an energy cost equal to U (as in the Hubbard model).

G_{imp} is the full Green's function of the Anderson impurity model and is related to the noninteracting (i.e. with $U = 0$) Green's function of the impurity model $G_{0,imp}$ by the Dyson equation:

$$G_{imp}^{-1}(\omega) = G_{0,imp}^{-1}(\omega) - \Sigma_{imp}(\omega). \quad (4.21)$$

The noninteracting $G_{0,imp}$ is:

$$G_{0,imp}^{-1}(\omega) = \omega - \epsilon_d - \Delta(\omega), \quad (4.22)$$

where $\Delta(\omega)$ is:

$$\Delta(\omega) = \sum_l \frac{|V_l|^2}{\omega - \epsilon_l}. \quad (4.23)$$

4. Models for strongly correlated systems

It is possible to demonstrate that, with a proper choice of the parameters ϵ_l and V_l that enter \hat{H}_{AIM} , G_{imp} is equal to G_{loc} . In actual calculations $\Delta(\omega)$ (and hence $G_{0,imp}^{-1}(\omega)$) is not known *a priori* and must be found by solving a self-consistent problem. $\Delta(\omega)$ in the Anderson model is the hybridization function and in DMFT becomes the energy dependent mean field of the theory.

All these quantities live on a single-site model. They are functions that depend only on ω . The approximation introduced by DMFT is that one takes also for the self-energy of the Hubbard lattice model $\Sigma(\mathbf{k}, \omega)$, the self-energy of the impurity model $\Sigma_{imp}(\omega)$: $\Sigma(\mathbf{k}, \omega) = \Sigma_{imp}(\omega)$. In other words, one assumes that the on-site self-energy Σ_{ii} of the Hubbard model is given by: $\Sigma_{ii}(\omega) = \Sigma_{imp}$ and all the off-diagonal terms $i \neq j$ are zero: $\Sigma_{ij} = 0$. With this assumption $G_{loc}(\omega)$, defined in Eq. (4.18), becomes:

$$G_{loc}(\omega) = \sum_{\mathbf{k}} \frac{1}{\omega - \epsilon_{\mathbf{k}} - \Sigma_{imp}(\omega)}. \quad (4.24)$$

Using the fact that (see Eq. 4.18) $\Sigma_{imp} = G_{0,imp}^{-1} - G_{imp}^{-1} = G_{0,imp}^{-1} - G_{loc}^{-1}$ (since $G_{loc} = G_{imp}$), and the definition (4.21): $G_{0,imp}^{-1} = \omega - \epsilon_d - \Delta(\omega)$, the self-energy of the impurity Σ_{imp} can be rewritten as:

$$\Sigma_{imp}(\omega) = \omega - \epsilon_d - \Delta(\omega) - G_{loc}^{-1}(\omega). \quad (4.25)$$

Inserting this relation in (4.24), one has also:

$$G_{loc}(\omega) = \sum_{\mathbf{k}} \frac{1}{\epsilon_d + \Delta(\omega) + G_{loc}^{-1}(\omega) - \epsilon_{\mathbf{k}}}. \quad (4.26)$$

The two equations (4.21) and (4.24) permit to calculate G_{loc} and $G_{0,imp}$ self-consistently. The DMFT scheme to solve the lattice Hubbard Hamiltonian can be summarized as follows:

- the starting point is a guess for $G_{0,imp}$;
- the Anderson impurity model is solved (thanks to an “impurity solver”, a method based for example on Quantum Montecarlo techniques), yielding the full G_{imp} and the self-energy of the impurity model Σ_{imp} (from the Dyson equation (4.21)): $\Sigma_{imp} = G_{0,imp}^{-1} - G_{imp}^{-1}$. The possibility to solve the Anderson impurity model is clearly a key point in the DMFT scheme. Here there isn’t the possibility to discuss further the various methods to solve the impurity problem (for more details see [187][174]).
- the local Green’s function G_{loc} is calculated thanks to Eq. (4.24): $G_{loc}(\omega) = \sum_{\mathbf{k}} (\omega - \epsilon_{\mathbf{k}} - \Sigma_{imp}(\omega))^{-1}$;

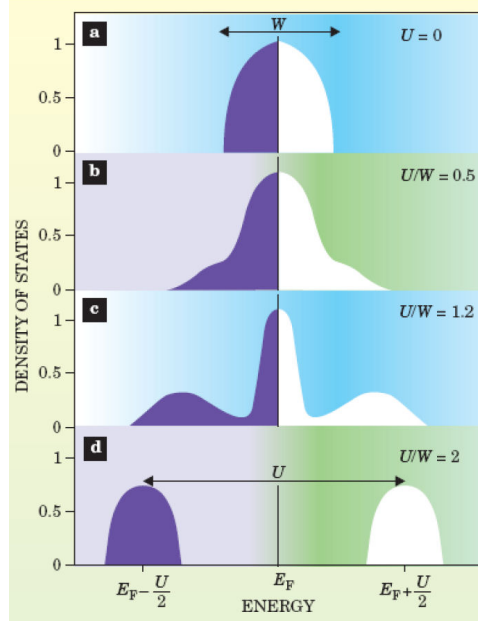


Figure 4.1: Densities of states of the Hubbard model for different U/W ratios, calculated using the DMFT single-site approximation. In the independent-particle limit ($U = 0$) the system is metallic, with one quasiparticle band at the Fermi level. In the atomic limit ($U \gg W$), there are two Hubbard bands at energy $E_F \pm U/2$. DMFT describes the transition between these two limits as due to a transfer of spectral weight from the quasiparticle band to the Hubbard bands, with the formation, in the intermediate regime, of a typical three-peak structure (as shown in the panel (c)). From Ref. [188].

- a new $G_{0,imp}$ is obtained by the Dyson equation (4.21), where one uses the condition $G_{imp} = G_{loc}$, so: $G_{0,imp} = (G_{loc}^{-1} + \Sigma_{imp})^{-1}$.

Once $G_{loc}(\omega)$ has been calculated self-consistently, one can have access to the spectral function (but also to the total energy) of the Hubbard model: $A(\omega) = \frac{1}{\pi} |\text{Im}G_{loc}(\omega)|$.

The DMFT assumption is that the self-energy of the lattice is a single-site function. This is clearly a drastic simplification that permits to find a self-consistent solution of the Hubbard model. But it is not an approximation in the independent-electron limit ($U = 0$), in the atomic limit ($t = 0$) and in the infinite dimensional lattice at any coupling t/U . In fact, in all these cases the true self-energy itself of the Hubbard model becomes a single-site quantity. The infinite dimensional limit, in particular, is not trivial and has been extensively studied [189][190]. In the three dimensional case the DMFT approximation fully accounts for the dynamical fluctuations (the possibility to add/remove an electron on a site), but neglects completely the spatial fluctuations (it is a single-site approximation).

4. Models for strongly correlated systems

The important result of DMFT for the Hubbard model is that DMFT is capable to provide a consistent solution for any value of the ratio t/U and, in this way, a complete explanation of the Mott transition at half-filling [187]. In the DMFT framework the transition is the result of the transfer of spectral weight from the quasiparticle peak to the Hubbard bands of the correlated metallic phase, that gives rise to a characteristic three-peak spectrum (see Fig. 4.1).

4.2.2 DMFT for electronic structure calculations (LDA + DMFT)

The DMFT method is used also for electronic structure calculations of real materials, by adopting the LDA+U Hubbard Hamiltonian [191][192]. While in the LDA+U framework the self-energy is static, the DMFT solution of the LDA+U Hamiltonian permits to account for dynamical fluctuations. In this sense, LDA+U can be considered as the static Hartree-Fock limit of DMFT [174]. In particular, in DMFT only the diagonal density-density terms of the LDA+U Hamiltonian (4.7) are retained. So the Hubbard term is:

$$\hat{H}_U = \frac{1}{2} \sum_{mm'\sigma} U_{mm'} \hat{n}_{m\sigma} \hat{n}_{m'\bar{\sigma}} + \frac{1}{2} \sum_{m \neq m'\sigma} (U_{mm'} - J_{mm'}) \hat{n}_{m\sigma} \hat{n}_{m'\sigma}, \quad (4.27)$$

where U and J account for the direct and exchange interactions:

$$U_{mm'} = \langle mm' | V_{scr} | mm' \rangle, \quad (4.28)$$

$$J_{mm'} = \langle mm' | V_{scr} | m'm \rangle. \quad (4.29)$$

In principle, also terms like $\sum_{m \neq m'\sigma} J_{mm'} \hat{c}_{m\sigma}^\dagger \hat{c}_{m\bar{\sigma}}^\dagger \hat{c}_{m'\sigma} \hat{c}_{m'\bar{\sigma}}$ should be taken into account but they are generally neglected [179].

The on-site Green's function of the solid G_{loc} is obtained by representing the full Green's function G on a localized basis, that is a basis whose functions are centered on the atomic positions $\{\mathbf{R}\}$: $\psi_{m\mathbf{R}}(\mathbf{r}) = \psi_m(\mathbf{r} - \mathbf{R})$. One has:

$$G(\mathbf{r}, \mathbf{r}'\omega) = \sum_{\mathbf{R}\mathbf{R}'} \sum_{mm'} \psi_{m\mathbf{R}} G_{mm'}(\mathbf{R} - \mathbf{R}', \omega) \psi_{m'\mathbf{R}'}. \quad (4.30)$$

G_{loc} corresponds to the on-site part, $\mathbf{R} = \mathbf{R}'$, of G : $[G_{loc}]_{mm'}(\omega) = G_{mm'}(\mathbf{0}, \omega)$, where one considers only the ‘‘correlated orbitals’’, that are a subset of the d (or f) orbitals. So $m = 2$ (or 3).

The Hubbard Hamiltonian is then solved in the DMFT self-consistent loop. The starting point is an initial guess for $G_{0,imp}$. In this case one takes as $G_{0,imp}$ the on-site part $G_{KS,loc}$ of the Kohn-Sham Green's function G_{KS} . Thanks to an impurity solver, one obtains G_{imp} and then $\Sigma_{imp} =$

4.2 Dynamical mean-field theory

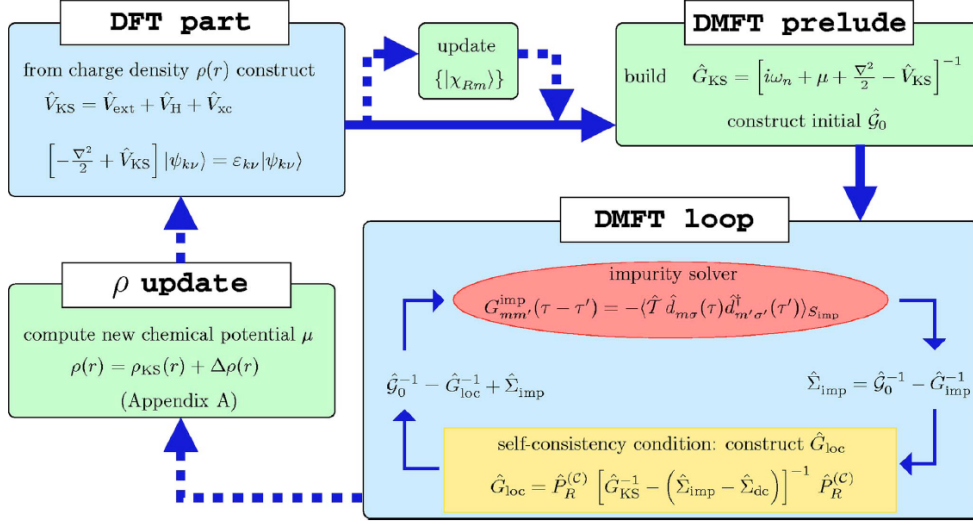


Figure 4.2: Self-consistent scheme of the LDA+DMFT method. From Ref. [193].

$G_{0,\text{imp}}^{-1} - G_{\text{imp}}^{-1}$. The local Hubbard Green's function G_{loc} is then calculated from:

$$[G_{\text{loc}}]_{mm'}(\omega) = \sum_{\mathbf{k}} \left[\frac{1}{G_{\text{KS}}^{-1}(\mathbf{k}, \omega) - (\Sigma_{\text{imp}}(\omega) - \Sigma_{\text{dc}})} \right]_{mm'}, \quad (4.31)$$

where G_{KS}^{-1} is a matrix on both sp and d orbitals and $\Sigma_{\text{imp}} - \Sigma_{\text{dc}}$ has only the block corresponding to the d orbitals. Given G_{loc} , one can recalculate $G_{0,\text{imp}} = (G_{\text{loc}}^{-1} + \Sigma_{\text{imp}})^{-1}$. When self-consistency is achieved in this DMFT loop, one should recalculate the density $\rho(\mathbf{r})$ from the Green's function G of the solid. With this updated density a new Kohn-Sham self-consistent calculation should be performed in order to update the parameters entering the Hubbard Hamiltonian, until full self-consistency is achieved between ρ , G_{loc} and $G_{0,\text{imp}}$. In actual calculations, the inclusion of self-consistency over the density is too expensive and generally people stop after the end of the first DMFT loop [194].

From Eq. (4.31) one can see that the corrections deriving from the solution of the Hubbard model to the Kohn-Sham eigenvalues $\epsilon_{\mathbf{k}}$ are the same for all the \mathbf{k} points. The fundamental assumption of DMFT is in fact that $\Sigma(\mathbf{k}, \omega) = \Sigma_{\text{imp}}(\omega)$. The self-energy of the solid turns out to be \mathbf{k} independent. This approximation may be too restrictive, especially when inter-site dynamical fluctuations are as important as on-site fluctuations. In these cases a generalization of DMFT to account for short-range fluctuations has been proposed [195]. In this extension of DMFT, called cluster-DMFT [196],

4. Models for strongly correlated systems

one redefines the local part of the Green's function G to consider. Instead of taking a single-site G_{loc} , the key variable becomes a Green's function defined on a cluster of sites. This generalization permits to reintroduce a \mathbf{k} dependence in the self-energy. But, of course, practical calculations become more demanding.

4.3 Spectral density-functional theory

In this section I will consider the spectral density-functional theory (SDFT) [197], that represents an exact framework where dynamical mean-field theory can be viewed as a particular approximation. I will introduce SDFT as an energy functional of the on-site Green's function G_{loc} (see Sec. 4.2) by comparing this functional with the DFT energy functional and the Luttinger-Ward functional, which is defined in the many-body framework.

In the many-body perturbation theory the total energy (or the action in case of a time-dependent Schrödinger equation) of an electronic system can be written as a functional of the Green's function G . Moreover, it is possible to require that the functional is stationary for a Green's function G solution of the Dyson equation: $G = G_H + G_H \Sigma G$. In particular, the Luttinger-Ward functional [198]:

$$\Gamma_{LW}[G] = \Phi[G] - \text{Tr}\{\Sigma G + \ln(\Sigma - G_H^{-1})\} - E_H[G] \quad (4.32)$$

has this property. In (4.32) E_H is the classical Hartree energy, the term calculated from the trace (i.e. integration over spatial, time and spin coordinates) is the kinetic energy plus the interaction with the external potential and $\Phi[G]$ accounts for the exchange-correlation effects. The functional derivative of Φ with respect to the Green's function G at the stationary point is the self-energy:

$$\Sigma(1, 2) = \frac{\delta\Phi}{\delta G(2, 1)}. \quad (4.33)$$

Baym and Kadanoff have shown that a self-energy with this property (i.e. a “ Φ -derivable” self-energy) is conserving [184][199], i.e. it respects conservation rules (for instance for the particle number). The choice of the total functional is not unique. It is possible to demonstrate [200] that other variational functionals having the same stationary point can be obtained from the Luttinger-Ward functional (4.32). For instance, Klein [201] has derived one of such alternative functionals, $\Gamma_K[G]$. These functionals are all equivalent in case one has the exact Green's function G and evaluates them at the stationary point. Otherwise, when an approximate Green's function is used, they give rise to different results.

In density-functional theory, instead, the total energy is a functional of the electronic density ρ , as discussed in Sec. 2.2. Since in particular G_{KS} is

4.3 Spectral density-functional theory

MBPT	
Key quantity	$G(\mathbf{r}, \mathbf{r}', \omega)$
Functional	$\Gamma_{LW}[G]$ or $\Gamma_K[G]$
Stationary condition	$\Sigma(1, 2) = \delta\Phi/\delta G(2, 1)$
SDFT	
Key quantity	$G_{loc}(\mathbf{r}, \mathbf{r}', \omega) = G(\mathbf{r}, \mathbf{r}', \omega)\Theta(\Omega_{loc})$
Functional	$\Gamma_{SDFT}[G_{loc}]$
Stationary condition	$V_{SDFT}(1, 2) = \delta\Phi_{SDFT}/\delta G_{loc}(2, 1)\Theta(\Omega_{loc})$
DFT	
Key quantity	$\rho(\mathbf{r}) = -iG(\mathbf{r}, t, \mathbf{r}, t^+)$
Functional	$\Gamma_{DFT}[\rho]$
Stationary condition	$V_{xc}(1, 2) = \delta\Phi_{DFT}/\delta\rho(1)$

Table 4.2: Summary of the key features of many-body perturbation theory (MBPT), spectral density-functional theory (SDFT), and density-functional theory (DFT) in the variational functional approach.

a functional of ρ , analogously to Eq. (4.32), one has:

$$\Gamma_{DFT}[\rho] = \Phi_{DFT}[\rho] - \text{Tr}\{V_{xc}G_{KS} + \ln(V_{xc} - G_H^{-1})\} - E_H[\rho]. \quad (4.34)$$

The Kohn-Sham equations are obtained as stationary point: $\delta\Gamma_{DFT}/\delta\rho = 0$, with

$$V_{xc}(1) = \frac{\delta\Phi_{DFT}}{\delta\rho(1)}. \quad (4.35)$$

In particular in this case the stationary point is a minimum (and not a saddle point as in the case of Γ_{LW} in (4.32)). At the stationary point, the term $\text{Tr}\{V_{xc}G_{KS} + \ln(V_{xc} - G_H^{-1})\}$ at $T=0$ reduces [174] to $-\text{Tr}\{\nabla^2 G_{KS} - V_{ext}\rho\}$, the usual sum of the (Kohn-Sham) kinetic energy and external potential.

In spectral density-functional theory (SDFT), instead, the key variable is G_{loc} , the ‘‘on-site’’ part of Green’s function [174][202][203][197]. In the real space it is: $G_{loc}(\mathbf{r}, \mathbf{r}', \omega) = G(\mathbf{r}, \mathbf{r}', \omega)\Theta(\Omega_{loc})$, where $\Theta(\Omega_{loc})$ is 1 when \mathbf{r} is in the unit cell Ω_c and \mathbf{r}' inside a volume Ω_{loc} , and 0 otherwise (see Fig. 4.3).

An auxiliary Green’s function G_{SDFT} is introduced with the property $G_{loc}(r, r', \omega) = G_{SDFT}(r, r', \omega)\Theta(\Omega_{loc})$. In other words, $G_{SDFT}(\mathbf{r}, \mathbf{r}', \omega) = G(\mathbf{r}, \mathbf{r}', \omega) = G_{loc}(\mathbf{r}, \mathbf{r}', \omega)$ for $\mathbf{r} \in \Omega_c$ and $\mathbf{r}' \in \Omega_{loc}$, while in the other spatial regions they can be different (G_{loc} in particular is 0). The Green’s function G_{SDFT} defines a reference system of particles moving under the potential $V_{SDFT}(\mathbf{r}, \mathbf{r}', \omega)$ (which is not zero where $\Omega_{loc} = 1$), with $G_{SDFT}^{-1}(\mathbf{r}, \mathbf{r}', \omega) = G_H^{-1}(\mathbf{r}, \mathbf{r}', \omega) - V_{SDFT}(\mathbf{r}, \mathbf{r}', \omega)$. The total energy can be calculated also as a functional of G_{loc} [197]:

$$\Gamma_{SDFT}[G_{loc}] = \Phi_{SDFT}[G_{loc}] - \text{Tr}\{V_{SDFT}G_{SDFT} + \ln(V_{SDFT} - G_H^{-1})\} - E_H[\rho], \quad (4.36)$$

4. Models for strongly correlated systems

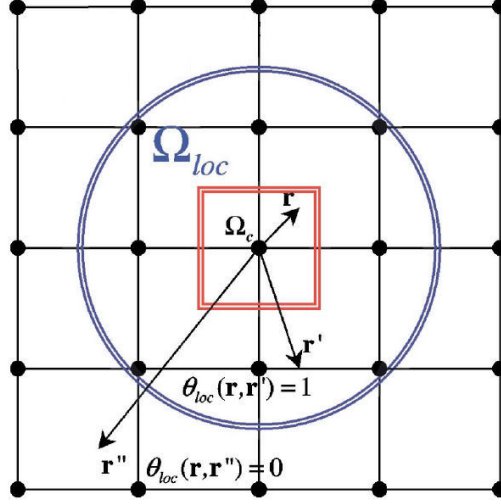


Figure 4.3: Definition of the region in the real space where $G_{loc}(\mathbf{r}, \mathbf{r}', \omega) \neq 0$. $\Theta(\Omega_{loc})$ ($\theta_{loc}(\mathbf{r}, \mathbf{r}')$ in the figure) is 1 when \mathbf{r} is in the unit cell Ω_c and \mathbf{r}' inside a volume Ω_{loc} , and is 0 otherwise. From Ref. [197].

with the usual partition into a term given by the kinetic energy plus the external potential energy, a classical Hartree term and the exchange-correlation interaction energy Φ_{SDFT} . Also in this case from the stationarity condition $\delta\Gamma_{SDFT}/\delta G_{loc} = 0$ one obtains the Dyson equation $G_{SDFT}^{-1}(\mathbf{r}, \mathbf{r}', \omega) = G_H^{-1}(\mathbf{r}, \mathbf{r}', \omega) - V_{SDFT}(\mathbf{r}, \mathbf{r}', \omega)$, with:

$$V_{SDFT}(1, 2) = \frac{\delta\Phi_{SDFT}}{\delta G_{loc}(2, 1)} \Theta(\Omega_{loc}). \quad (4.37)$$

The three functionals Γ_{LW} , Γ_{DFT} and Γ_{SDFT} are equivalent in yielding the total energy. Moreover, in all the cases one implicitly assumes that the corresponding key variable is “V-representable” (see Sec. 2.2 for the DFT case). They all are formally exact, as functionals of different variables, even though they introduce different partitioning of the total energy. In fact they define different kinetic energies and hence different exchange-correlation interaction energies. For instance, for the DFT functional, the kinetic term is the kinetic energy of the Kohn-Sham system, which is not the kinetic energy of the real system. Concerning their functional dependence, whereas Γ_{DFT} can never coincide with Γ_{LW} (unless the self-energy is static and local), clearly if $\Theta(\Omega_{loc}) = 1$ in the whole space, Γ_{SDFT} and Γ_{LW} trivially coincide, since in this case one has $G_{loc} = G$. The interaction functional Φ is in principle known only in the many-body case, through for example a diagrammatic representation in G and v . In DFT and SDFT the functional dependences of Φ_{DFT} and Φ_{SDFT} with respect to ρ and G_{loc} are instead not known.

4.3 Spectral density-functional theory

(Cluster) DMFT represents an explicit approximation of the SDFT functional Γ_{SDFT} [197], where one takes for the interaction energy Φ_{SDFT} the functional form of Φ : $\Phi_{SDFT}[G_{loc}] = \Phi[G_{loc}]$ and one approximates the kinetic part of Γ_{LW} with the corresponding term of Γ_{SDFT} . Equivalently, this corresponds to use the functional Γ_{LW} , where the functional dependence of Φ is restricted to G_{loc} . So cluster-DMFT is exact if the self-energy Σ is localized inside the region where $\Theta(\Omega_{loc}) = 1$. In this case, the functionals Γ_{LW} and Γ_{SDFT} coincide and $V_{SDFT} = \Sigma$.

In MBPT the GW self-energy is evaluated at the first order in W , but it retains all the long-range components of the Coulomb interaction. In DMFT, instead, only the on-site components are considered in the self-energy. But in the Hubbard model the on-site self-energy can be in principle exactly calculated at any perturbative level, thanks to the solution of the Anderson model through a proper impurity solver (see Sec. 4.2). A proposal of combining these complementary aspects of GW and DMFT has been elaborated by Biermann *et al.* [204][205], but practical applications, beyond model Hamiltonians [206], are still too computationally involved.

In Sec. 7.4, instead, I will show how it is possible to derive a formally exact equation for V_{SDFT} (which in the present formulation is defined only as functional derivative of an unknown quantity, Φ_{SDFT}) in terms of other quantities, such as Σ and G , which are *in principle* known, in the sense that one knows how to build controlled approximations.

Chapter 5

Neutral excitations

In this chapter I complete the introduction to the theoretical spectroscopy methods that deal with electronic excitations. In Chapter 3 the one-particle Green's function was the natural quantity to describe the one-particle excitations, as the ones that occur in photoemission experiments. Absorption and EELS instead involve neutral excitations and call for the definition of new quantities.

So, after a general introduction to linear-response theory and to the connection between microscopic theories and macroscopic measurements, I will present the formalism of the Bethe-Salpeter equation (BSE), which accounts for the two-particle nature of excitations measured in absorption experiments. I will then show that time-dependent density-functional theory (TDDFT) and time-dependent current-density-functional theory (TDCDFT) can be an efficient alternative to BSE to deal with perturbations that can be represented, respectively, by a scalar or a vector potential.

BSE relies on an intuitive physical picture that allows one to find working strategies, but calculations in the BSE framework are demanding. TDDFT is more efficient but finding good approximations is more difficult. So I will discuss how in the recent past it has been possible to derive better approximations for the simpler TDDFT approach from the working implementation of the more complex BSE.

An in-depth introduction to linear-response theory can be found in the book of Giuliani and Vignale [55]. In the review of Onida et al. [2], besides an introduction to DFT and MBPT methods, it is profitably discussed how it is possible to combine the advantages of both approaches. Botti et al. [207] have recently collected the results deriving from the application of TDDFT to extended systems. Different theses provide a detailed introduction to the different methods discussed in this chapter. So I refer directly to the works of S. Albrecht [5] for the BSE, F. Sottile [4] and F. Bruneval [3] for the combination of MBPT and TDDFT, A. Berger [208] and P. Romaniello [209] for TDCDFT.

5. Neutral excitations

5.1 Linear response

I consider here an electronic system, described by the many-body Hamiltonian \hat{H} (see Eq. (1.1)), subjected to a time-dependent external perturbation $\hat{H}_1(t)$. The total Hamiltonian becomes:

$$\hat{H}_{tot} = \hat{H} + \hat{H}_1(t). \quad (5.1)$$

In particular I will deal with perturbations that couple a field F with a probe \hat{P} :

$$\hat{H}_1(t) = \int d\mathbf{r}_1 F(\mathbf{r}_1, t) \hat{P}(\mathbf{r}_1, t). \quad (5.2)$$

Typically the perturbation is an electromagnetic field coupled with densities or currents. In this framework it is convenient to adopt an interaction picture. Operators evolve according to \hat{H} and states with $\hat{H}_1(t)$. The first-order variation of the expectation value of the observable \hat{O} due to the perturbation \hat{H}_1 is:

$$\delta\langle\hat{O}(1)\rangle = -i\theta(t_1 - t_2) \int d2 \langle N | [\hat{O}(1), \hat{H}_1(2)] | N \rangle, \quad (5.3)$$

where 1 is a shorthand notation for $\mathbf{r}_1 t_1 \sigma_1$. In linear-response theory one considers small variations δF of the field F . Using (5.3) it is hence possible to evaluate the variation $\delta\langle\hat{O}(1)\rangle$ from the Kubo formula [210]:

$$\delta\langle\hat{O}(1)\rangle = \int d2 \chi_{OP}(1, 2) \delta F(2), \quad (5.4)$$

where $\chi_{OP}(1, 2) = -i\theta(t_1 - t_2) \langle N | [\hat{O}(1), \hat{P}(2)] | N \rangle = \delta\langle\hat{O}(1)\rangle / \delta F(2)$ is a (causal or retarded) response function.

By inserting a completeness relation and taking the Fourier transform, the response function can be written in the Lehmann representation as:

$$\chi_{OP}(\mathbf{r}_1, \mathbf{r}_2, \omega) = \sum_s \left[\frac{O_s(\mathbf{r}_1) P_s^*(\mathbf{r}_2)}{\omega + E_0 - E_s + i\eta} - \frac{O_s^*(\mathbf{r}_1) P_s(\mathbf{r}_2)}{\omega + E_s - E_0 + i\eta} \right], \quad (5.5)$$

where:

$$O_s(\mathbf{r}_1) = \langle N | \hat{O}(\mathbf{r}_1) | N, s \rangle. \quad (5.6)$$

The response function has poles at the excitation energies $\pm(E_0 - E_s)$, corresponding to transitions between the ground state $|N\rangle$ and the excited state $|N, s\rangle$ of the unperturbed Hamiltonian \hat{H} . The first term in (5.5) is given by resonant transitions, the second by antiresonant transitions. While the poles of the one-particle Green's function G correspond to excitations that change the number of particles, the poles of the response function correspond to neutral excitations. As in the case of the Green's function G , in the thermodynamic limit χ_{OP} displays a branch cut along the real axis. The response

function χ_{OP} is built only using elements deriving from the unperturbed system (Eq. (5.5) is still in the interaction picture). This is possible thanks to fact that χ_{OP} is calculated in the linear-response regime.

As a consequence of its causality character, the response function $\chi_{OP}(\omega)$ is analytic in the complex upper half-plane. Thanks to this property, the real and imaginary parts of $\chi_{OP}(\omega)$ are related through the Kramers-Kronig relations [211][212]:

$$\text{Re}\chi_{OP}(\omega) = \frac{1}{\pi} \int_{-\infty}^{+\infty} d\omega' \frac{\text{Im}\chi_{OP}(\omega')}{\omega' - \omega}, \quad (5.7)$$

$$\text{Im}\chi_{OP}(\omega) = -\frac{1}{\pi} \int_{-\infty}^{+\infty} d\omega' \frac{\text{Re}\chi_{OP}(\omega')}{\omega' - \omega}. \quad (5.8)$$

In particular here we are interested in perturbations induced by electromagnetic fields, which can be represented generally by a scalar potential V_{per} and a vector potential \mathbf{A}'_{per} :

$$\begin{aligned} \hat{H}_1(t) = & \int d\mathbf{r} V_{per}(\mathbf{r}, t) \hat{\rho}(\mathbf{r}, t) + \\ & - \frac{1}{c} \int d\mathbf{r} \mathbf{A}'_{per}(\mathbf{r}, t) \hat{\mathbf{j}}(\mathbf{r}, t) + \frac{1}{2c^2} \int d\mathbf{r} \mathbf{A}'_{per}{}^2(\mathbf{r}, t) \hat{\rho}(\mathbf{r}, t). \end{aligned} \quad (5.9)$$

From now on, for simplicity of notation, I will set $\mathbf{A}_{per} = -(1/c)\mathbf{A}'_{per}$. The fields are coupled to the density ρ and the (paramagnetic) current \mathbf{j} :

$$\rho(1) = \langle \hat{\psi}^+(1) \hat{\psi}(1) \rangle = -iG(1, 1^+), \quad (5.10)$$

$$\mathbf{j}(1) = \langle \frac{1}{2i} [\hat{\psi}^+(1) \nabla \hat{\psi}(1) - (\nabla \hat{\psi}^+(1)) \hat{\psi}(1)] \rangle = \frac{1}{2i} [(\nabla_1 - \nabla_2)(-iG(1, 2))]_{2=1^+}. \quad (5.11)$$

The diamagnetic term $\mathbf{A}_{per}^2 \rho$ of (5.9) in linear response can be neglected (at the first order, for $\mathbf{A}_{per} \rightarrow 0$ it is 0).

The linear response of the density ρ and the total current \mathbf{J} (sum of the paramagnetic and diamagnetic terms):

$$\mathbf{J}(1) = \mathbf{j}(1) + \mathbf{A}_{per}(1)\rho(1), \quad (5.12)$$

thanks to (5.4), can be calculated as:

$$\delta\rho(1) = \int d2 \chi_{\rho\rho}(1, 2) \delta V_{per}(2) + \int d2 \vec{\chi}_{\rho\mathbf{j}}(1, 2) \delta \mathbf{A}_{per}(2), \quad (5.13)$$

$$\delta\mathbf{J}(1) = \int d2 \vec{\chi}_{\mathbf{j}\rho}(1, 2) \delta V_{per}(2) + \int d2 [\vec{\chi}_{\mathbf{j}\mathbf{j}}(1, 2) + \rho(1)\delta(1, 2)] \delta \mathbf{A}_{per}(2), \quad (5.14)$$

5. Neutral excitations

where the density-density $\chi_{\rho\rho}$, current-current $\overleftrightarrow{\chi}_{\mathbf{j}\mathbf{j}}$, density-current $\overrightarrow{\chi}_{\rho\mathbf{j}}$ and current-density $\overleftarrow{\chi}_{\mathbf{j}\rho}$ response functions have been introduced:

$$\begin{aligned}\chi_{\rho\rho}(1, 2) &= -i\theta(t_1 - t_2)\langle N | [\hat{\rho}(1), \hat{\rho}(2)] | N \rangle = \delta\rho(1)/\delta V_{per}(2), \\ \overleftrightarrow{\chi}_{\mathbf{j}\mathbf{j}}(1, 2) &= -i\theta(t_1 - t_2)\langle N | [\hat{\mathbf{j}}(1), \hat{\mathbf{j}}(2)] | N \rangle = \delta\mathbf{j}(1)/\delta\mathbf{A}_{per}(2), \\ \overrightarrow{\chi}_{\rho\mathbf{j}}(1, 2) &= -i\theta(t_1 - t_2)\langle N | [\hat{\rho}(1), \hat{\mathbf{j}}(2)] | N \rangle = \delta\rho(1)/\delta\mathbf{A}_{per}(2), \\ \overleftarrow{\chi}_{\mathbf{j}\rho}(1, 2) &= -i\theta(t_1 - t_2)\langle N | [\hat{\mathbf{j}}(1), \hat{\rho}(2)] | N \rangle = \delta\mathbf{j}(1)/\delta V_{per}(2).\end{aligned}\tag{5.15}$$

In particular, the density-density response function $\chi_{\rho\rho}$ is the causal version of the time-ordered polarizability χ , which has been defined in App. A.5. Up to the factors $\pm i\eta$ in the denominators (see Eq. (5.5)), the two coincide. Since from the context it is generally clear which one is needed, I will write directly $\chi_{\rho\rho}$ as χ .

Moreover, thanks to the conductivity sum rule:

$$\overleftrightarrow{\chi}_{\mathbf{j}\mathbf{j}}(\mathbf{r}_1, \mathbf{r}_2, \omega = 0) + \rho(\mathbf{r}_1)\delta(\mathbf{r}_1 - \mathbf{r}_2) = 0,\tag{5.16}$$

where one neglects a small Landau diamagnetic part [209], Eq. (5.14) can be simplified as:

$$\begin{aligned}\delta\mathbf{J}(\mathbf{r}_1, \omega) &= \int d\mathbf{r}_2 \overleftarrow{\chi}_{\mathbf{j}\rho}(\mathbf{r}_1, \mathbf{r}_2, \omega)\delta V_{per}(\mathbf{r}_2, \omega) + \\ &+ \int d\mathbf{r}_2 [\overleftrightarrow{\chi}_{\mathbf{j}\mathbf{j}}(\mathbf{r}_1, \mathbf{r}_2, \omega) - \overleftrightarrow{\chi}_{\mathbf{j}\mathbf{j}}(\mathbf{r}_1, \mathbf{r}_2, 0)]\delta\mathbf{A}_{per}(\mathbf{r}_2, \omega).\end{aligned}\tag{5.17}$$

5.2 Microscopic-macroscopic connection

In the previous section I have introduced the response functions. In the remaining sections of the chapter I will discuss different possibilities to calculate them. All these methods are based on microscopic theories and deal with microscopic variables. Instead experiments measure macroscopic quantities, which are properly averaged in space. It is important, and not trivial, to establish a bridge between these microscopic and macroscopic worlds. Since for perturbations with momentum transfer $\mathbf{q} \rightarrow 0$, the longitudinal and transverse responses (measured respectively in EELS and absorption experiments, see Sec. 1.2.2) coincide, I will consider here the simpler longitudinal case. For a more general discussion I refer to the work of Del Sole and Fiorino [213] and the review of Strinati [119].

The (longitudinal) microscopic dielectric function can be obtained by the density-density response function χ as (see App. A.5):

$$\epsilon^{-1}(12) = \delta(12) + \int d3v(13)\chi(32).\tag{5.18}$$

5.2 Microscopic-macroscopic connection

In a periodic solid this relation can be expressed in the Fourier space as (see also Eq. (3.65)):

$$\epsilon_{\mathbf{G},\mathbf{G}'}^{-1}(\mathbf{q},\omega) = \delta_{\mathbf{G},\mathbf{G}'} + v_{\mathbf{G}}(\mathbf{q})\chi_{\mathbf{G},\mathbf{G}'}(\mathbf{q},\omega), \quad (5.19)$$

where \mathbf{G} is a reciprocal lattice vector and \mathbf{q} belongs to first Brillouin zone.

When the system is perturbed by an external potential $V_{per}(\mathbf{q} + \mathbf{G}, \omega)$, the total potential (sum of the external and the induced potential) felt by a test-charge is:

$$V_{tot}(\mathbf{q} + \mathbf{G}, \omega) = \sum_{\mathbf{G}'} \epsilon_{\mathbf{G},\mathbf{G}'}^{-1}(\mathbf{q},\omega) V_{per}(\mathbf{q} + \mathbf{G}', \omega). \quad (5.20)$$

The total potential in general has different wave vector components than the perturbing potential for the presence of microscopic fluctuations induced by the inhomogeneities of the material. The difference between the microscopic potentials and their macroscopic average is called local fields. To connect the microscopic and the macroscopic quantities one has to take a spatial average over a distance that is large compared to the lattice parameters and small compared to the wavelength of the external perturbation [214]. Since the microscopic quantities are lattice periodic, this procedure reduces to take the spatial average over a unit cell.

A microscopic potential $V(\mathbf{r}, \omega)$ can be expanded in its Fourier components as:

$$V(\mathbf{r}, \omega) = \sum_{\mathbf{q}\mathbf{G}} V(\mathbf{q} + \mathbf{G}, \omega) e^{i(\mathbf{q}+\mathbf{G})\mathbf{r}}, \quad (5.21)$$

or:

$$V(\mathbf{r}, \omega) = \sum_{\mathbf{q}} e^{i\mathbf{q}\mathbf{r}} \sum_{\mathbf{G}} V(\mathbf{q} + \mathbf{G}, \omega) e^{i\mathbf{G}\mathbf{r}} = \sum_{\mathbf{q}} e^{i\mathbf{q}\mathbf{r}} V(\mathbf{q}, \mathbf{r}, \omega), \quad (5.22)$$

where:

$$V(\mathbf{q}, \mathbf{r}, \omega) = \sum_{\mathbf{G}} V(\mathbf{q} + \mathbf{G}, \omega) e^{i\mathbf{G}\mathbf{r}}. \quad (5.23)$$

$V(\mathbf{q}, \mathbf{r}, \omega)$ is periodic with respect to the Bravais lattice and hence is the quantity that one has to average to get the corresponding macroscopic potential $V_M(\mathbf{q}, \omega)$:

$$V_M(\mathbf{q}, \omega) = \frac{1}{\Omega_c} \int d\mathbf{r} V(\mathbf{q}, \mathbf{r}, \omega). \quad (5.24)$$

Inserting (5.23) in (5.24), one has:

$$V_M(\mathbf{q}, \omega) = \sum_{\mathbf{G}} V(\mathbf{q} + \mathbf{G}, \omega) \frac{1}{\Omega_c} \int d\mathbf{r} e^{i\mathbf{G}\mathbf{r}} = V(\mathbf{q} + \mathbf{0}, \omega). \quad (5.25)$$

Therefore the macroscopic averaged potential V_M is given by $\mathbf{G} = \mathbf{0}$ component of the corresponding microscopic potential V .

5. Neutral excitations

In particular, in the standard spectroscopy experiments discussed in this thesis, the external perturbing potential is a macroscopic quantity. For instance it can be the electromagnetic field impinging on a sample that one can measure in an absorption experiment. For the Eq. (5.25) only the $\mathbf{G} = 0$ component of $V_{per}(\mathbf{q} + \mathbf{G}, \omega)$ is different from 0. Therefore the macroscopic average $V_{tot,M}$ of the microscopic total potential V_{tot} in Eq. (5.20) is:

$$V_{tot,M}(\mathbf{q}, \omega) = \epsilon_{\mathbf{G}=0, \mathbf{G}'=0}^{-1}(\mathbf{q}, \omega) V_{per}(\mathbf{q}, \omega). \quad (5.26)$$

Eq. (5.26) is a relation between macroscopic potentials, so it defines the macroscopic inverse dielectric function ϵ_M^{-1} : $V_{tot,M} = \epsilon_M^{-1} V_{per}$. In this way one obtains:

$$\epsilon_M^{-1}(\mathbf{q}, \omega) = \epsilon_{\mathbf{G}=0, \mathbf{G}'=0}^{-1}(\mathbf{q}, \omega). \quad (5.27)$$

Therefore, the macroscopic dielectric function turns out to be defined as:

$$\epsilon_M(\mathbf{q}, \omega) = \frac{1}{\epsilon_{\mathbf{G}=0, \mathbf{G}'=0}^{-1}(\mathbf{q}, \omega)}. \quad (5.28)$$

This corresponds to the result found by Adler [215] and Wiser [216].

It is important to note here that, since V_{tot} is in general a microscopic quantity, because it contains the microscopic fluctuations due to the polarization of the medium, one could not obtain directly the macroscopic dielectric function ϵ_M from the inverse of the relation (5.20):

$$V_{per}(\mathbf{q} + \mathbf{G}, \omega) = \sum_{\mathbf{G}'} \epsilon_{\mathbf{G}, \mathbf{G}'}(\mathbf{q}, \omega) V_{tot}(\mathbf{q} + \mathbf{G}', \omega). \quad (5.29)$$

Since V_{per} is macroscopic, (5.29) is just:

$$V_{per}(\mathbf{q}, \omega) = \sum_{\mathbf{G}'} \epsilon_{\mathbf{G}=0, \mathbf{G}'}(\mathbf{q}, \omega) V_{tot}(\mathbf{q} + \mathbf{G}', \omega). \quad (5.30)$$

Hence:

$$V_{per}(\mathbf{q}, \omega) = \epsilon_{\mathbf{G}=0, \mathbf{G}'=0}(\mathbf{q}, \omega) V_{tot,M}(\mathbf{q}, \omega) + \sum_{\mathbf{G}' \neq 0} \epsilon_{\mathbf{G}=0, \mathbf{G}'}(\mathbf{q}, \omega) V_{tot}(\mathbf{q} + \mathbf{G}', \omega). \quad (5.31)$$

Since $V_{per} = \epsilon_M V_{tot,M}$, one has that $\epsilon_M = \epsilon_{\mathbf{G}=0, \mathbf{G}'=0}$ only if one neglects the off-diagonal terms ($\mathbf{G}' \neq 0$) in Eq. (5.31). These off-diagonal terms correspond to the rapidly oscillating contributions to the microscopic total potential. The terms $\mathbf{G}' \neq 0$ in Eq. (5.31) are responsible of the so-called crystal local-field effects (LFE). In fact, from Eq. (5.28), one has that $\epsilon_M = 1/\epsilon_{\mathbf{G}=0, \mathbf{G}'=0}^{-1} = \epsilon_{\mathbf{G}=0, \mathbf{G}'=0}$ only if $\epsilon_{\mathbf{G}, \mathbf{G}'}$ is diagonal, which corresponds to a dielectric function in the real space that depends only on the distance between \mathbf{r} and \mathbf{r}' : $\epsilon(|\mathbf{r} - \mathbf{r}'|)$.

5.2 Microscopic-macroscopic connection

It is possible to demonstrate [2][4][5] that ϵ_M can be directly obtained using a modified density-density response function $\bar{\chi}$:

$$\epsilon_M(\mathbf{q}, \omega) = 1 - v_{\mathbf{G}=0}(\mathbf{q})\bar{\chi}_{\mathbf{G}=0, \mathbf{G}'=0}(\mathbf{q}, \omega). \quad (5.32)$$

Whereas the density-density response function χ satisfies the Dyson equation (see App. A.5): $\chi = P + Pv\chi$, $\bar{\chi}$ is obtained from:

$$\bar{\chi} = P + P\bar{v}\bar{\chi}, \quad (5.33)$$

where the macroscopic component of \bar{v} is set to zero: $\bar{v}_{\mathbf{G}=0} = 0$. For the other components $\mathbf{G} \neq 0$, $\bar{v} = v$. Neglecting local-field effects, the macroscopic dielectric function is (see Eq. (5.31)):

$$\epsilon_M^{NLF}(\mathbf{q}, \omega) = \epsilon_{\mathbf{G}=0, \mathbf{G}'=0}(\mathbf{q}, \omega) = 1 - v_{\mathbf{G}=0}(\mathbf{q})P_{\mathbf{G}=0, \mathbf{G}'=0}(\mathbf{q}, \omega). \quad (5.34)$$

Therefore, comparing (5.32) and (5.34), one can see that it is the microscopic part of the Coulomb interaction \bar{v} that is responsible of the local-field effects. In fact, setting $\bar{v} = 0$ in (5.33) would imply that $\bar{\chi} = P$ and hence $\epsilon_M^{NLF} = \epsilon_M$.

Local-field effects are tightly related to spatial inhomogeneities in the system. Whenever a system is not homogeneous, even if the external field is slowly varying, the induced charges can have rapid spatial variations. This means that the off-diagonal elements of the dielectric function are important. Typical examples where local fields play an important role are layered systems [217], nanotubes [218] and finite systems like nanoclusters [219], which represent themselves an inhomogeneity in the vacuum space. Instead, bulk solids of *sp* semiconductors are often examples of homogeneous systems where local fields play a minor role [220].

These criteria actually apply only for polarizable systems, where the initial and final states involved in a particular transition are localized in a common spatial region [221]. On the contrary, even in very inhomogeneous systems, if the inhomogeneity is not much polarizable, the induced potentials are small and consequently local fields are not so important [4].

Absorption and electron energy-loss experiments measure $\text{Im}\epsilon_M$ and $-\text{Im}\epsilon_M^{-1}$, respectively (see Sec. 1.2.2). Once $\epsilon_{\mathbf{G}=0, \mathbf{G}'=0}$ has been calculated, the spectra are obtained from:

$$\text{Abs}(\omega) = \lim_{\mathbf{q} \rightarrow 0} \text{Im}\epsilon_M(\omega) = \lim_{\mathbf{q} \rightarrow 0} \text{Im} \frac{1}{\epsilon_{\mathbf{G}=0, \mathbf{G}'=0}^{-1}(\mathbf{q}, \omega)}, \quad (5.35)$$

$$\text{EELS}(\omega) = - \lim_{\mathbf{q} \rightarrow 0} \text{Im}\epsilon_M^{-1}(\omega) = - \lim_{\mathbf{q} \rightarrow 0} \text{Im}\epsilon_{\mathbf{G}=0, \mathbf{G}'=0}^{-1}(\mathbf{q}, \omega). \quad (5.36)$$

where, in particular, I considered the EELS at vanishing momentum transfer. Equivalently [4]:

$$\text{Abs}(\omega) = - \lim_{\mathbf{q} \rightarrow 0} \text{Im}[v_{\mathbf{G}=0}(\mathbf{q})\bar{\chi}_{\mathbf{G}=0, \mathbf{G}'=0}(\mathbf{q}, \omega)], \quad (5.37)$$

5. Neutral excitations

$$\text{EELS}(\omega) = - \lim_{\mathbf{q} \rightarrow 0} \text{Im}[v_{\mathbf{G}=0}(\mathbf{q})\chi_{\mathbf{G}=0, \mathbf{G}'=0}(\mathbf{q}, \omega)]. \quad (5.38)$$

The only difference between $\bar{\chi}$ and χ is the absence of the long-range term $v_{\mathbf{G}=0}$ of the Coulomb interaction in the Dyson equation (5.33). Therefore $v_{\mathbf{G}=0}$ is the responsible of the difference between absorption and EELS spectra in solids [222]. Bulk silicon absorbs in the energy range between 3-5 eV and the plasmon resonance is at 16.8 eV. In finite system, instead, the long range term has no importance. For this reason, when the limit $\mathbf{q} \rightarrow 0$ is assumed, EELS and absorption mathematically coincide in finite systems.

5.3 The Bethe-Salpeter equation

Photoemission experiments in Chapter 3 have been described in terms of a one-particle effective Hamiltonian for one-particle excitations: the quasiparticles. In case of absorption experiments, instead, one has to deal with neutral excitations due to the simultaneous creation of a quasidelectron and a quasihole (see Sec. 1.2.2). A one-particle description is no more adequate. In this section I will therefore introduce the effective two-particle Hamiltonian capable to deal with these neutral excitations.

In order to describe neutral excitation, in the MBPT framework the key variable is the two-particle correlation function, formally defined as functional derivative with respect to a nonlocal perturbation:

$$L(1, 2, 3, 4) = -i \frac{\delta G(1, 2)}{\delta V_{per}(3, 4)}. \quad (5.39)$$

Thanks to the rule of the derivative of the identity (see App. A.4), $\delta G/\delta V_{per} = -G(\delta G^{-1}/\delta V_{per})G$, Eq. (5.39) can be rewritten as:

$$L(1, 2, 3, 4) = +i \int d56 G(1, 5) \frac{\delta G^{-1}(5, 6)}{\delta V_{per}(3, 4)} G(6, 2). \quad (5.40)$$

This permits to use the Dyson equation:

$$G^{-1}(5, 6) = G_H^{-1}(5, 6) - V_{per}(5, 6) - \Sigma(5, 6), \quad (5.41)$$

and get:

$$L(1, 2, 3, 4) = +i \int d56 G(1, 5) \left[-\delta(3, 5)\delta(4, 6) + \frac{\delta[V_H(5)\delta(5, 6) + \Sigma(5, 6)]}{\delta V_{per}(3, 4)} \right] G(6, 2). \quad (5.42)$$

5.3 The Bethe-Salpeter equation

Then, using the chain rule $\delta\Sigma/\delta V_{per} = (\delta\Sigma/\delta G)(\delta G/\delta V_{per})$, one finds:

$$L(1, 2, 3, 4) = -iG(1, 3)G(4, 2) + \\ - i \int d5678 G(1, 5)G(6, 2) \frac{\delta[V_H(5)\delta(5, 6) + \Sigma(5, 6)]}{\delta G(7, 8)} L(7, 8, 3, 4). \quad (5.43)$$

$L_0(1, 2, 3, 4) = -iG(1, 3)G(4, 2)$ describes the free propagation of an electron and a hole that don't interact. So it is the two-particle correlation function for independent particles. With this definition, the Bethe-Salpeter equation (BSE) [223] reads:

$$L(1, 2, 3, 4) = L_0(1, 2, 3, 4) + \\ + \int d5678 L_0(1, 2, 5, 6)[v(5, 7)\delta(5, 6)\delta(7, 8) + \Xi(5, 6, 7, 8)]L(7, 8, 3, 4), \quad (5.44)$$

where the four-point many-body interaction kernel:

$$\Xi(5, 6, 7, 8) = i \frac{\delta\Sigma(5, 6)}{\delta G(7, 8)} \quad (5.45)$$

has been introduced. In the kernel of the BSE (5.44) the Coulomb term v is summed to Ξ . It links the two-particle correlation function L to its irreducible counterpart \tilde{L} : $L = \tilde{L} + \tilde{L}vL$. As above, $v = v_{\mathbf{G}=0} + \bar{v}$. \bar{v} is responsible of the local-field effects (see Eq. (5.33)) and $v_{\mathbf{G}=0}$ of the difference between absorption and EELS.

A connection between L and the (reducible) vertex $\tilde{\Gamma}$ (3.34) can be established when the particular case of a local perturbation $V_{per}(3)$ is considered in the definition of (5.39) of L [119]:

$$L(1, 2, 3, 3^+) = -i \frac{\delta G(1, 2)}{\delta V_{per}(3)} = +i \int d45 G(1, 4) \frac{\delta G^{-1}(4, 5)}{\delta V_{per}(3)} G(5, 2) = \\ = -i \int d45 G(1, 4) \tilde{\Gamma}(4, 5, 3) G(5, 2). \quad (5.46)$$

Analogously a similar link can be drawn between the irreducible \tilde{L} and the irreducible vertex $\tilde{\Gamma}$.

In spectroscopy experiments what is measured is the two-point response function

$$\chi(1, 2) = \frac{\delta\rho(1)}{\delta V_{per}(2)}. \quad (5.47)$$

χ is a contraction of the four-point L :

$$\chi(1, 2) = L(1, 1^+, 2, 2^+). \quad (5.48)$$

5. Neutral excitations

So calculating L through the Bethe-Salpeter equation (5.44) permits to obtain χ and hence the spectra.

Furthermore, in case of a transverse perturbation (as for an electromagnetic field at finite \mathbf{q}), the perturbation is given by the vector potential \mathbf{A} . Analogously to what has been shown for a scalar potential (see App. A.2), it is possible to demonstrate that (see Ref. [119]):

$$-i \frac{\delta G(1, 2)}{\delta \mathbf{A}(3)} = \frac{1}{2i} \left[(\nabla_3 - \nabla_4) L(1, 2, 3, 4) \right]_{4=3^+}. \quad (5.49)$$

Therefore, once L has been calculated thanks to the BSE (5.44), also the other two-point response functions can be obtained from proper contractions of L (see Eqs. (5.10)-(5.11)):

$$\overleftrightarrow{\chi}_{\mathbf{j}\mathbf{j}}(1, 3) = \frac{1}{2i} \frac{1}{2i} \left[(\nabla_1 - \nabla_2)(\nabla_3 - \nabla_4) L(1, 2, 3, 4) \right]_{2=1^+, 4=3^+}, \quad (5.50)$$

$$\overrightarrow{\chi}_{\rho\mathbf{j}}(1, 3) = \frac{1}{2i} \left[(\nabla_3 - \nabla_4) L(1, 1^+, 3, 4) \right]_{4=3^+}, \quad (5.51)$$

$$\overleftarrow{\chi}_{\mathbf{j}\rho}(1, 3) = \frac{1}{2i} \left[(\nabla_1 - \nabla_2) L(1, 2, 3, 3^+) \right]_{2=1^+}. \quad (5.52)$$

5.3.1 BSE in practice

In order to solve the Bethe-Salpeter equation (5.44) one has to approximate the many-body interaction kernel Ξ (5.45). The standard approximation consists in using the GW self-energy (see Eq. (3.48)). In this way the solution of the Bethe-Salpeter equation corresponds to the inclusion of vertex corrections in P (or χ , see Eq. (5.46)) through a second iteration of Hedin's equations. The kernel Ξ becomes:

$$\Xi(5, 6, 7, 8) = i \frac{\delta \Sigma(5, 6)}{\delta G(7, 8)} = - \frac{\delta [G(5, 6)W(5, 6)]}{\delta G(7, 8)}. \quad (5.53)$$

The derivative contains two terms: W and $G\delta W/\delta G$. The latter describes the change of the screening due to the excitation. At the level of the GW approximation it is a second-order effect and can be therefore neglected (but in this way the correlation functions are no more conserving [184]). With these approximations the Bethe-Salpeter equation becomes:

$$\begin{aligned} L(1, 2, 3, 4) &= L_0(1, 2, 3, 4) + \\ &+ \int d5678 L_0(1, 2, 5, 6) [v(5, 7)\delta(5, 6)\delta(7, 8) - W(5, 6)\delta(5, 7)\delta(6, 8)] L(7, 8, 3, 4). \end{aligned} \quad (5.54)$$

The kernel that connects the independent-particle correlation function L_0 to the interacting L is given by the sum of two terms [224][225]. The first is

5.3 The Bethe-Salpeter equation

the unscreened exchange term v and is repulsive. The second is the screened Coulomb electron-hole direct term W and is attractive. Without screening (5.54) reduces to a time-dependent Hartree-Fock approximation. Looking at the indexes of the delta functions of these two terms in (5.54), one immediately realizes that the BSE is still a purely four-point equation and cannot be contracted to obtain directly the two-point response function χ , which is what is experimentally measured. This represents the real bottleneck of the Bethe-Salpeter equation approach in practical calculations.

For simple semiconductors dynamical effects in the electron-hole screening in W and in the Green's function G tend to cancel [226][227], therefore they are usually neglected in both. So, instead of $W(1, 2)$, in (5.54) in the standard approach [228][5][229][230][231][232] one uses a statically screened instantaneous interaction:

$$\frac{1}{2\pi}W(\mathbf{r}_1, \mathbf{r}_2, \omega = 0)\delta(t_1 - t_2), \quad (5.55)$$

and for G the Green's function obtained by a perturbative GW calculation. This Green's function is built with Kohn-Sham orbitals and quasiparticle eigenvalues with GW perturbative corrections included and with the quasiparticle renormalization factors that are set to 1. Improperly, I will call it "quasiparticle" Green's function (see also App. A.6). In a more general case, one can consider a Green's function obtained from quasiparticle self-consistent calculations [233]. Including dynamical effects in the screening would give rise instead to a time-dependent interaction [234]. Since the kernel is no more Hermitian, in principle this would permit to describe for example excitonic lifetimes [226].

In a spectroscopy experiment one measures the response of the electronic system to an external perturbation. The Bethe-Salpeter equation shows that the first effect of the perturbation is the creation, inside the system, of electron-hole pairs. This first response of the system is expressed by the independent-particle term L_0 . The perturbation, then, generates an induced potential which alters the independent-particle picture through a self-consistent response that modifies the potentials acting on the system. In particular, in the BSE v derives from the variation of the Hartree potential and W from the variation of the self-energy. In fact, after the absorption of a photon, the electron still remains in the sample. So it can strongly interact with the hole, leading to the creation of an exciton. The electron and the hole cannot be considered as independent and one has to pass to a two-particle picture in order to take into account these excitonic effects.

Hanke and Sham [224][225] solved the Bethe-Salpeter equation (5.54) in a localized basis by inverting directly the four-point kernel at each frequency ω . When the dimension of the basis involved in the calculation becomes relevant, the inversion procedure is too expensive. The Bethe-Salpeter equation (5.54) can be solved also by diagonalizing a two-particle excitonic Hamilto-

5. Neutral excitations

nian, which moreover provides information about the excitonic eigenstates and eigenvalues. Alternative schemes based on the same excitonic Hamiltonian adopt the Haydock recursive algorithm [235][231][166] or \mathbf{k} -point interpolation procedures [232]. The two-particle Hamiltonian is obtained by calculating the matrix element of (5.54) in the transition space, which is constituted by couples of quasiparticle wavefunctions $\phi_v\phi_c$ [2][5]. In the transition space, the resonant parts (that involve transitions from valence v to conduction states c) of the two terms in the BSE kernel read (here I consider the microscopic Coulomb potential \bar{v} that yields \bar{L} , otherwise one would have v):

$$\bar{v}_{(vc),(v'c')} = 2 \int d\mathbf{r}_1 d\mathbf{r}_3 \phi_v^*(\mathbf{r}_1) \phi_c(\mathbf{r}_1) \bar{v}(|\mathbf{r}_1 - \mathbf{r}_3|) \phi_{v'}(\mathbf{r}_3) \phi_{c'}^*(\mathbf{r}_3), \quad (5.56)$$

where the factor 2 is due to spin degeneracy, and:

$$W_{(vc),(v'c')} = \int d\mathbf{r}_1 d\mathbf{r}_2 \phi_v^*(\mathbf{r}_1) \phi_{v'}(\mathbf{r}_1) W(\mathbf{r}_1, \mathbf{r}_2, \omega = 0) \phi_c(\mathbf{r}_2) \phi_{c'}^*(\mathbf{r}_2). \quad (5.57)$$

Written in this form, the two terms clearly show a different nature. While W is a direct (screened) interaction between valence and conduction charge densities, \bar{v} instead is a dipole interaction between valence-conduction charge fluctuations. In the transition space the Bethe-Salpeter equation becomes a Schrödinger equation [2][5]:

$$\sum_{(n_3 n_4)} H_{(n_1 n_2), (n_3 n_4)}^{2p} A_\lambda^{(n_3 n_4)} = E_\lambda A_\lambda^{(n_1 n_2)} \quad (5.58)$$

for the effective two-particle excitonic Hamiltonian, which is defined as:

$$H_{(n_1 n_2), (n_3 n_4)}^{2p} = \epsilon_{n_2} - \epsilon_{n_1} \delta_{n_1 n_3} \delta_{n_2 n_4} + (f_{n_1} - f_{n_2}) (\bar{v}_{(n_1 n_2), (n_3 n_4)} - W_{(n_1 n_2), (n_3 n_4)}). \quad (5.59)$$

After the excitonic Hamiltonian has been diagonalized, one can calculate the dielectric function, thanks to the two-point contraction (see Eq. (5.48)) of \bar{L} and Eq. (5.32). The final result is:

$$\epsilon_2(\omega) = \lim_{\mathbf{q} \rightarrow 0} \frac{8\pi}{q^2} \sum_\lambda \left| \sum_{vc} A_\lambda^{vc} \langle v | e^{-i\mathbf{q}\mathbf{r}} | c \rangle \right|^2 \delta(\omega - E_\lambda), \quad (5.60)$$

where, for simplicity, again only the resonant transitions $v \rightarrow c$ have been considered in the excitonic Hamiltonian. Comparing Eq. (5.60) with Eq. (1.26), one can see that the inclusion of the excitonic effects has two consequences on the spectra calculated using Fermi's golden rule. First, the energy of the transition is now E_λ which in general is different from the independent-particle value $\epsilon_c - \epsilon_v$. Second, the exciton wavefunctions coefficients A_λ^{vc} mix the independent-particle transitions $|v\rangle \rightarrow |c\rangle$. When the

5.4 Time-dependent density-functional theory

electron-hole interaction is not taken into account, the excitonic Hamiltonian is diagonal and A_{λ}^{vc} is different from zero for only one transition. In general, instead, an excitonic transition λ is made by different independent-particle transitions $|v\rangle \rightarrow |c\rangle$.

We can make here a parallel with the spectral function of the one-particle Green's function. When the system is noninteracting, it is a series of delta peaks corresponding to single Slater determinants. When the electronic interaction is switched on, the quasiparticle peak is made by the mixing of different contributions of many Slater determinants, rightly as an excitonic transition is obtained by the mixing of different independent-particle transitions.

This first-principles method based on the Bethe-Salpeter equations has been applied many times in the last ten years. It has yielded very successful results in the calculation of optical properties of solids with continuum or bound excitons (like, respectively, silicon [229] or solid argon [236]), surfaces [237], nanowires [238] and clusters [228] as well as in the calculation of electron energy-loss spectra [144]. Nevertheless it is a computationally heavy scheme and one would like to find a more efficient method that guarantees the same accuracy. In fact, spectra in the BSE framework are obtained from a contraction of a two-particle Green's function (see Eq. (5.48)). Therefore, one calculates more information than needed. An alternative method for the direct calculation of the spectra is represented by time-dependent density-functional theory (TDDFT), which I will introduce in the following section.

5.4 Time-dependent density-functional theory

It is possible to extend the (static) density-functional theory to the case of time-dependent external potentials. The time-dependent density-functional theory (TDDFT) is hence an alternative to the Bethe-Salpeter equation in dealing with neutral excitations. In fact, Runge and Gross [239] have proved that, for a given initial state, time-dependent potentials $V_{ext}(\mathbf{r}, t)$ and time-dependent densities $\rho(\mathbf{r}, t)$ are in a one-to-one correspondence (up to a purely time-dependent function). Any observable is a functional of the density $\rho(\mathbf{r}, t)$ and of the initial state, which, anyway, in our case will be always the ground state of the system.

In particular the action $A[\rho]$, which is defined on the Keldysh contour¹ [241], is a functional of the density, with the property:

$$\left. \frac{\delta A}{\delta \rho(\mathbf{r}, \tau)} \right|_{\rho(\mathbf{r}, t)} = V_{ext}(\mathbf{r}, t). \quad (5.61)$$

Since a given time-dependent density $\rho(\mathbf{r}, t)$ can be reproduced by a noninteracting system (which in general has also a different initial state) [242], it

¹For an introduction to the Keldysh contour formalism see e.g. [240].

5. Neutral excitations

is possible to generalize the Kohn-Sham scheme of DFT to time-dependent situations. If $A_{KS}[\rho]$ is the action functional relative of the noninteracting Kohn-Sham system:

$$\left. \frac{\delta A_{KS}}{\delta \rho(\mathbf{r}, \tau)} \right|_{\rho(\mathbf{r}, t)} = V_{KS}(\mathbf{r}, t), \quad (5.62)$$

defining $A_{xc}[\rho]$ as:

$$A[\rho] = A_{KS}[\rho] - \frac{1}{2} \int_C d12 \rho(1) \rho(2) v(1, 2) - A_{xc}[\rho], \quad (5.63)$$

one finds that the effective Kohn-Sham potential $V_{KS}(\mathbf{r}, t)$ in the time-dependent case is:

$$V_{KS}(\mathbf{r}, t) = V_H(\mathbf{r}, t) + V_{ext}(\mathbf{r}, t) + V_{xc}(\mathbf{r}, t), \quad (5.64)$$

where:

$$V_{xc}(\mathbf{r}, t) = \left. \frac{\delta A_{xc}}{\delta \rho(\mathbf{r}, \tau)} \right|_{\rho(\mathbf{r}, t)}. \quad (5.65)$$

So the solution of the set of effective one-particle equations:

$$\left[-\frac{1}{2} \nabla^2 + V_{KS}(\mathbf{r}, t) \right] \varphi_i(\mathbf{r}, t) = i \frac{\partial}{\partial t} \varphi_i(\mathbf{r}, t) \quad (5.66)$$

yields the time-dependent density of the system:

$$\rho(\mathbf{r}, t) = \sum_{i=1}^N |\varphi_i(\mathbf{r}, t)|^2. \quad (5.67)$$

As DFT leads to a dramatic simplification in the solution of the time-independent many-body Schrödinger equation (1.1), the same gain is obtained in TDDFT with respect to the time-dependent version of the many-body Schrödinger equation. But, as in the static case, $V_{xc}(\mathbf{r}, t)$ is unknown and to be approximated. The simplest approximation is the adiabatic local-density approximation (ALDA) [243], where at each instant t one takes for $V_{xc}(\mathbf{r}, t)$ the exchange-correlation potential calculated in LDA with density $\rho(\mathbf{r}, t)$:

$$V_{xc}^{ALDA}(\mathbf{r}, t) = V_{xc}^{LDA}(\rho(\mathbf{r}, t)). \quad (5.68)$$

TDDFT can be of course used to calculate the linear response of the system to an external time-dependent perturbation $V_{per}(\mathbf{r}, t)$. In this case the time-dependent external potential of the formal theory can be taken as the sum of the static ionic potential $V_{ext}(\mathbf{r})$ and the external perturbation: $V_{ext}(\mathbf{r}, t) = V_{ext}(\mathbf{r}) + V_{per}(\mathbf{r}, t)$. Thanks to the Runge-Gross theorem, the change of the density $\delta\rho$ due to a variation of the external perturbation δV_{per}

5.4 Time-dependent density-functional theory

can be obtained equivalently as the change of the density in the Kohn-Sham system as a result of a variation of V_{KS} :

$$\delta\rho(1) = \int d2\chi(1,2)\delta V_{ext}(2) = \int d2\chi_{KS}(1,2)\delta V_{KS}(2). \quad (5.69)$$

Using:

$$\frac{\delta V_{KS}(1)}{\delta V_{ext}(2)} = \delta(1,2) + \frac{\delta V_H(1)}{\delta V_{ext}(2)} + \frac{\delta V_{xc}(1)}{\delta V_{ext}(2)}, \quad (5.70)$$

one obtains the Dyson equation of linear response TDDFT [244]:

$$\chi(1,2) = \chi_{KS}(1,2) + \int d3d4\chi_{KS}(1,3)[v(3,4) + f_{xc}(3,4)]\chi(4,2), \quad (5.71)$$

where the exchange-correlation kernel f_{xc} has been defined as:

$$f_{xc}(1,2) = \frac{\delta V_{xc}(1)}{\delta\rho(2)}. \quad (5.72)$$

While the true excitation energies are the poles of χ (see Eq. (5.5)), the noninteracting Kohn-Sham response function χ_{KS} has poles at the Kohn-Sham eigenvalues differences.

TDDFT constitutes an in principle exact alternative to the Bethe-Salpeter equation for the calculation of the response function χ . The great advantage of TDDFT is its efficiency. Since it deals directly with variations of the density, the linear-response equation (5.71) is a two-point equation. BSE is instead an intrinsically four-point equation, because it describes two-particle interactions. On the other side, in the BSE the interaction kernel is in principle exactly known (even though it becomes soon computationally intractable) and, moreover, good approximations have been formulated in practice. In TDDFT, on the contrary, the f_{xc} kernel is unknown and one has to devise some approximations.

The independent-particle polarizability χ_{KS} is built using elements from a ground-state Kohn-Sham calculation (see also the general Lehmann representation (5.5) for response functions of interacting systems):

$$\begin{aligned} \chi_{KS,\mathbf{G}\mathbf{G}'}(\mathbf{q},\omega) &= \frac{1}{N_{\mathbf{k}}\Omega_c} \sum_{v\mathbf{c}\mathbf{k}} \langle\varphi_{v\mathbf{k}}|e^{-i(\mathbf{q}+\mathbf{G})\mathbf{r}}|\varphi_{c\mathbf{k}+\mathbf{q}}\rangle \langle\varphi_{c\mathbf{k}+\mathbf{q}}|e^{i(\mathbf{q}+\mathbf{G}')\mathbf{r}}|\varphi_{v\mathbf{k}}\rangle \times \\ &\times \frac{f_{v\mathbf{k}}(2 - f_{c\mathbf{k}+\mathbf{q}})}{2} \left[\frac{1}{\omega - (\epsilon_{c\mathbf{k}+\mathbf{q}} - \epsilon_{v\mathbf{k}}) + i\eta} - \frac{1}{\omega - (\epsilon_{v\mathbf{k}} - \epsilon_{c\mathbf{k}+\mathbf{q}}) + i\eta} \right], \end{aligned} \quad (5.73)$$

Since it is a polarizability for independent particles, χ_{KS} can be calculated by the product of two Kohn-Sham Green's functions $-iG_{KS}G_{KS}$, analogously to the RPA P_0 in MBPT, which is given by $-iGG$ (see Eq. (3.50)).

5. Neutral excitations

Once an approximation for the f_{xc} kernel has been chosen, one can solve the Dyson equation (5.71) to obtain χ and hence the spectra. Setting $f_{xc} = 0$ in Eq. (5.71) corresponds to the random-phase approximation (RPA), crystal local fields included. The time-dependent local-density approximation (TDLDA) is the simplest approximation to f_{xc} , where one has:

$$f_{xc}^{ALDA}(\mathbf{r}, \mathbf{r}', t, t') = \delta(\mathbf{r} - \mathbf{r}')\delta(t - t') \frac{\partial V_{xc}^{LDA}(\rho(\mathbf{r}))}{\partial \rho(\mathbf{r})}. \quad (5.74)$$

TDLDA often gives good results in the calculation of spectra for finite systems [245], electron energy-loss spectra [246] or, more generally, in the case of finite momentum-transfer \mathbf{q} [247]. When local fields are not essential, TDLDA and RPA results are similar [246]. TDLDA instead fails in the calculation of absorption spectra of solids [2][4]. What makes the difference between absorption and EELS spectra in extended systems is the long-range part of the Coulomb interaction $v_{\mathbf{G}=0}$. $v_{\mathbf{G}=0}$ is absent in the case of absorption (see Eqs. (5.33) and (5.35)). So, in this case, the only long-range term can derive from the exchange-correlation kernel f_{xc} . This long-range contribution is indeed essential to obtain good absorption spectra in solids [248]. In fact, in systems with a band gap, for $\mathbf{q} \rightarrow 0$ (as in absorption) the head (i.e. the element $\mathbf{G} = \mathbf{G}' = 0$) of $\chi_{KS} \rightarrow 0$ as q^2 . The ALDA kernel is instead a contact potential, which means that it is constant in \mathbf{q} . Hence its contribution, multiplied by χ_{KS} , vanishes in the limit $\mathbf{q} \rightarrow 0$. This explains the failure of TDLDA in the calculation of absorption spectra of solids. Besides, rightly for this reason, a kernel $f_{xc} \propto \frac{1}{q^2}$ for $\mathbf{q} \rightarrow 0$ is essential to get any correction to an independent-transition picture. In real space, this means that f_{xc} must have an infinite range, as the Coulomb potential which is proportional to $1/|\mathbf{r}_1 - \mathbf{r}_2|$. Some different ways to derive such a long-ranged kernel are reviewed in the next section.

5.4.1 A kernel from many-body perturbation theory

The derivation of an exchange-correlation kernel with the proper long-range contribution has been recently the subject of many different works [248][4][249][250][251][252][3][253][254][200]. They all aim at combining the respective advantages of BSE and TDDFT.

The idea is to design a f_{xc} kernel able to reproduce the good results of BSE. In the interpretation of MBPT, the effect of such a kernel is twofold. So f_{xc} can be split into two contributions [254]:

$$f_{xc} = f_{xc}^{(1)} + f_{xc}^{(2)}. \quad (5.75)$$

First, f_{xc} has to transform each couple of Kohn-Sham fictitious particles into a couple of (quasi)electron and (quasi)hole. From the independent Kohn-Sham response function χ_{KS} it has to give back the independent-particle

5.4 Time-dependent density-functional theory

P_0 :

$$f_{xc}^{(1)}(1, 2) = \chi_{KS}^{-1}(12) - P_0^{-1}(12). \quad (5.76)$$

Here P_0 is the causal version of the time-ordered RPA polarizability that defines the screening of W in GW: $P_0(1, 2) = -iG(1, 2)G(2, 1)$ (see Eq. (3.50)). In the BSE formalism $P_0(1, 2) = L_0(1, 1, 2, 2)$. In practice, P_0 , in the standard BSE approach, is built with two quasiparticle Green's functions, with Kohn-Sham wavefunctions and G_0W_0 quasiparticle energies. In essence, $f_{xc}^{(1)}$ has hence to shift Kohn-Sham eigenvalues into quasiparticle energies.

Second, f_{xc} has to describe the interactions between the (quasi)electron and the (quasi)hole. These are the excitonic effects that mix the independent transitions in P_0 .

$$f_{xc}^{(2)}(1, 2) = P_0^{-1}(1, 2) - P^{-1}(1, 2). \quad (5.77)$$

This is the role played by W in the Bethe-Salpeter equation. The effects of $f_{xc}^{(1)}$ and $f_{xc}^{(2)}$ are opposite: the former induces a blueshift of the spectrum (it opens the band gap), the latter essentially a redshift. Therefore in f_{xc} there must be strong cancellation effects between the two. But, so far, people have still found more convenient to start directly from P_0 (i.e. to calculate explicitly GW corrections) instead of trying to approximate $f_{xc}^{(1)}$. So it is in particular on the excitonic part $f_{xc}^{(2)}$ of the kernel that the efforts have been focused.

The excitonic kernel $f_{xc}^{(2)}$ can be derived exactly in the many-body framework. $f_{xc}^{(2)}$ and the vertex function Γ have the same role in P (see Hedin's equation (3.44) for P). They both account for the interaction between electrons and holes in the pairs that build up the polarizability. They are both the result of the self-consistent change of the potentials due to the perturbation.

I will follow here the derivation of F. Bruneval *et al.* in [253]. The irreducible vertex is (see Eq. (3.46)):

$$\Gamma(1, 2, 3) = \delta(1, 3)\delta(1, 2) + \frac{\delta\Sigma(1, 2)}{\delta V_{tot}(3)}. \quad (5.78)$$

Thanks to the Runge-Gross theorem it is possible to rewrite Γ as:

$$\Gamma(1, 2, 3) = \delta(1, 3)\delta(1, 2) + \int d4 \frac{\delta\Sigma(1, 2)}{\delta\rho(4)} \frac{\delta\rho(4)}{\delta V_{tot}(3)}, \quad (5.79)$$

where the one-to-one mapping between the perturbing potential and the density ρ has been explicitly exploited. In this way one gets two results. First, an explicit equation for the vertex that involves only three-point quantities:

$$\Gamma(1, 2, 3) = \delta(1, 3)\delta(1, 2) + \int d4 \frac{\delta\Sigma(1, 2)}{\delta\rho(4)} P(4, 3), \quad (5.80)$$

5. Neutral excitations

instead of the implicit integral equation with a four-point kernel (see Hedin's equation (3.43) for Γ). Second, inserting (5.80) in Hedin's equation for P and using (5.77), one obtains an explicit exact expression for $f_{xc}^{(2)}$:

$$f_{xc}^{(2)}(1, 2) = -i \int d345 P_0^{-1}(1, 3) G(3, 4) G(5, 3) \frac{\delta\Sigma(4, 5)}{\delta\rho(2)}. \quad (5.81)$$

The three point quantity $\delta\Sigma/\delta\rho$ plays here the same role as the interaction kernel Ξ of the BSE. Both stem from the change of the self-energy with the perturbation. Therefore, as in the standard Bethe-Salpeter, Σ is approximated at the GW level and the term $\delta W/\delta\rho$, which corresponds to the change of the screening for the perturbation, is neglected:

$$\frac{\delta\Sigma(1, 2)}{\delta\rho(3)} = iW(1, 2) \frac{\delta G(1, 2)}{\delta\rho(3)}. \quad (5.82)$$

For W , as in the BSE, one takes the static approximation. Moreover

$$\frac{\delta G(1, 2)}{\delta\rho(3)} = - \int d45 G(1, 4) \frac{\delta G^{-1}(4, 5)}{\delta\rho(3)} G(5, 2), \quad (5.83)$$

and $\delta G^{-1}/\delta\rho$ is approximated as if G^{-1} were the resolvent of a local potential: $\delta G^{-1}/\delta\rho = -P_0^{-1}$. Summing up the various pieces, the final approximation for the kernel is:

$$f_{xc}^{(2)}(1, 2) = \int d3456 P_0^{-1}(1, 3) G(3, 4) G(5, 3) \times \\ \times W(4, 5) G(4, 6) G(6, 5) P_0^{-1}(6, 2). \quad (5.84)$$

This kernel has indeed the correct long-range contribution, as shown for instance by Adragna *et al.* [250] in bulk silicon.

The same expression for $f_{xc}^{(2)}$ has been obtained in other different ways. The works of F. Sottile *et al.* [4][249] and G. Adragna *et al.* [250][251] suggested a direct comparison between the Bethe-Salpeter equation for the four-point irreducible polarizability \tilde{L} :

$$\tilde{L}(1, 2, 3, 4) = L_0(1, 2, 3, 4) + \\ - \int d5678 L_0(1, 2, 5, 6) \delta(5, 7) \delta(6, 8) W(5, 6) \tilde{L}(7, 8, 3, 4), \quad (5.85)$$

and the equivalent two-point equation in the TDDFT framework $P = P_0 + P_0 f_{xc}^{(2)} P$. Whereas the Bethe-Salpeter equation (5.85) cannot be contracted to a two-point one, it is possible to rewrite the TDDFT equation for P as a four-point equation for 4P , with $P(1, 2) = {}^4P(1, 1, 2, 2)$ (and analogously for P_0 and L_0):

$${}^4P(1, 2, 3, 4) = L_0(1, 2, 3, 4) + \\ + \int d5678 L_0(1, 2, 5, 6) \delta(5, 6) \delta(7, 8) f_{xc}^{(2)}(5, 7) {}^4P(7, 8, 3, 4). \quad (5.86)$$

5.4 Time-dependent density-functional theory

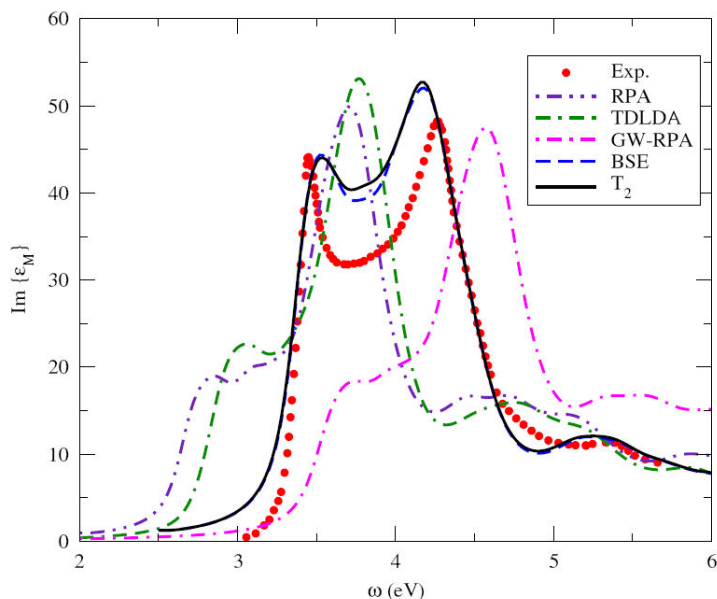


Figure 5.1: Comparison between the experimental absorption spectrum of bulk silicon (red dots) and theoretical spectra obtained in different approximation. RPA corresponds to set $f_{xc} = 0$ in Eq. (5.71); in TDLDA one uses the f_{xc} kernel (5.74) in Eq. (5.71); in GW-RPA one sets $W = 0$ in the Bethe-Salpeter equation (5.54); BSE is the result of Eq. (5.60); T_2 is obtained using the kernel (5.84). The two latter results are in very good agreement with the experimental spectrum. From Ref. [4].

In particular, in the derivation of F. Sottile [4] one directly maps the matrix elements $W_{(vc),(v'c')}$ of W in the BSE (see Eq. (5.57)) into the matrix elements $F_{(vc),(v'c')}$ of $f_{xc}^{(2)}$ in the TDDFT equation. This can be done for the transitions of interest. However, a complete mapping $-W \rightarrow f_{xc}^{(2)}$ is not possible. In fact, in the two four-point equations, $f_{xc}^{(2)}$ and W don't contract the same indexes. On the other side, the mapping between the two equations permits a flexibility that can be exploited to find even more efficient kernels [236].

In the approach of Adragna [251], instead, the two equations, (5.85) and (5.86), have been expanded in a perturbative series, respectively in W and $f_{xc}^{(2)}$. In this perturbative expansion one retains only the first-order terms in both. Requiring the equality of the two-point contraction of these first-order terms, one gets back the expression (5.84) for $f_{xc}^{(2)}$. This perturbative expansion can be derived on an equal footing also using a Kohn-Sham-based many-body diagrammatic technique [255][256], as shown in the work of Stub-

5. Neutral excitations

ner *et al.* [254]. Finally, the variational derivation of von Barth *et al.* [200] has demonstrated how the (total) f_{xc} kernel satisfies important conservation rules.

The f_{xc} kernel (5.84) yields similar spectra as the ones obtained by solving the Bethe-Salpeter equation. This kernel in fact has demonstrated to be as accurate as the BSE in the calculation of absorption (and electron energy loss) spectra of solids (see Fig. 5.1), surfaces [257], infinite molecular chains and finite systems [258]. Moreover, on a theoretical level, the insertion of the density-functional concept in the MBPT framework has permitted to derive a simpler equation for the vertex function (see Eq. (5.80)). This in turn has led to an exact expression (see Eq. (5.81)) for the TDDFT kernel in terms of many-body quantities. In this way it has been possible to establish a double, formally exact, link between MBPT and TDDFT and to mutually exploit the advantages of both.

Adopting the same philosophy of this section, in App. B I discuss how the density-functional concept can be exploited also to rewrite the Dyson equation (3.30) between G and G_H and obtain a new equation for G where the self-energy doesn't appear anymore.

5.5 Time-dependent current-density-functional theory

Time-dependent density-functional theory can deal only with longitudinal perturbations, represented by a scalar external potential V_{per} . It is instead incapable to treat situations where a transverse perturbation, represented by a vector potential \mathbf{A}_{per} , is applied to the system. Perturbations of this type are generally electromagnetic fields applied to the sample. In the case of optical absorption, the momentum transfer \mathbf{q} is vanishing, and one can still calculate the longitudinal response, which coincides with the transverse one. But for more general situations (also beyond the dipole approximation) this equivalence doesn't hold anymore.

There is also a more fundamental difficulty. DFT and TDDFT have been proven only for finite system. In the demonstrations one always asks for boundary conditions that cannot be always met in infinite systems. These difficulties arise in particular when one deals with situations where a spatially uniform electric field is applied to the system. The electric field can be both time-independent [87] or time-dependent [259]. In particular, in the latter case one finds that the external potential and the time-dependent density are no more in a one-to-one correspondence. It is possible to find situations where two different time-dependent electric fields give rise to the same density. In these cases the current density should be chosen as the basic variable. In fact, the two uniform electric fields still determine two different currents.

5.5 Time-dependent current-density-functional theory

Time-dependent current-density-functional theory (TDCDFT) considers an electronic system subjected to an arbitrary perturbing electromagnetic field, characterized by a scalar potential V_{per} and a vector potential $\hat{\mathbf{A}}_{per}$. Thanks to a gauge invariance, it is possible to choose a gauge in which the scalar potential is eliminated and the external perturbation is fully represented by the vector potential \mathbf{A}_{per} . Ghosh and Dhara [260] have demonstrated that, given an initial state, there is a one-to-one correspondence between external vector potentials $\mathbf{A}_{per}(\mathbf{r}, t)$ and current densities $\mathbf{j}(\mathbf{r}, t)$, up to a gauge transformation. This represents a generalization of the Runge-Gross theorem. In fact, any scalar potential with a gauge transformation can be represented by a longitudinal vector potential. Moreover, the current $\mathbf{j}(\mathbf{r}, t)$ determines the density $\rho(\mathbf{r}, t)$ thanks to the continuity equation:

$$\frac{\partial}{\partial t}\rho(\mathbf{r}, t) + \nabla \cdot \mathbf{j}(\mathbf{r}, t) = 0. \quad (5.87)$$

In TDCDFT all the observables are functionals of the current density and the initial state, which, again, will be always chosen as the unperturbed ground state of the system. Analogously to what has been done for TDDFT, it is possible [261] to introduce the action A , defined on the Keldysh contour, as a functional of the current \mathbf{j} , with the property:

$$\left. \frac{\delta A}{\delta \mathbf{j}(\mathbf{r}, \tau)} \right|_{\mathbf{j}(\mathbf{r}, t)} = \mathbf{A}_{per}(\mathbf{r}, t). \quad (5.88)$$

One then introduces the action A_{KS} for a noninteracting system and defines the exchange-correlation contribution A_{xc} to the action in the usual way:

$$A[\mathbf{j}] = A_{KS}[\mathbf{j}] - \frac{1}{2} \int d1 d2 \rho(1) \rho(2) v(1, 2) - A_{xc}[\mathbf{j}]. \quad (5.89)$$

By differentiating (5.89) one finds:

$$\mathbf{A}_{per}(\mathbf{r}, t) = \mathbf{A}_{KS}(\mathbf{r}, t) - \mathbf{A}_H(\mathbf{r}, t) - \mathbf{A}_{xc}(\mathbf{r}, t), \quad (5.90)$$

with:

$$\frac{\partial}{\partial t} \mathbf{A}_H(\mathbf{r}, t) + \nabla \int d\mathbf{r}' \rho(\mathbf{r}', t) v(|\mathbf{r} - \mathbf{r}'|) = 0, \quad (5.91)$$

and

$$\left. \frac{\delta A_{xc}}{\delta \mathbf{j}(\mathbf{r}, \tau)} \right|_{\mathbf{j}(\mathbf{r}, t)} = \mathbf{A}_{xc}(\mathbf{r}, t). \quad (5.92)$$

In (5.90) retardation effects, linked to the transverse component of the induced vector potential, are formally included in \mathbf{A}_{xc} , but they are often neglected [259][262][263]. Their macroscopic component, relevant in particular in extended system, can be formally added to the perturbing field [119][213].

5. Neutral excitations

The Kohn-Sham vector potential \mathbf{A}_{KS} is the effective potential of the Kohn-Sham system that has the same current $\mathbf{j}(\mathbf{r}, t)$ as the real system [264]. The solution of the Kohn-Sham equations

$$\left[\frac{1}{2}(-i\nabla + \mathbf{A}_{KS}(\mathbf{r}, t))^2 + v_{ext}(\mathbf{r}) \right] \varphi_i(\mathbf{r}, t) = i \frac{\partial}{\partial t} \varphi_i(\mathbf{r}, t) \quad (5.93)$$

permits to obtain the current density as:

$$\begin{aligned} \mathbf{j}(\mathbf{r}, t) = & \frac{1}{2i} \sum_{i=1}^N (\varphi_i^*(\mathbf{r}, t) \nabla \varphi_i(\mathbf{r}, t) - \varphi_i(\mathbf{r}, t) \nabla \varphi_i^*(\mathbf{r}, t)) + \\ & + \sum_{i=1}^N |\varphi_i(\mathbf{r}, t)|^2 \mathbf{A}_{KS}(\mathbf{r}, t). \end{aligned} \quad (5.94)$$

The response function $\overleftrightarrow{\chi}_{\mathbf{jj}}$ to the perturbation $\mathbf{A}_{per}(\mathbf{r}, t)$ can be calculated from a (tensorial) Dyson equation [261], which can be obtained similarly to derivation of the TDDFT linear-response equation (5.71):

$$\begin{aligned} \overleftrightarrow{\chi}_{\mathbf{jj}}(\mathbf{r}_1, \mathbf{r}_2, \omega) = & \overleftrightarrow{\chi}_{\mathbf{jj}, KS}(\mathbf{r}_1, \mathbf{r}_2, \omega) + \int d\mathbf{r}_3 d\mathbf{r}_4 \overleftrightarrow{\chi}_{\mathbf{jj}, KS}(\mathbf{r}_1, \mathbf{r}_3, \omega) \times \\ & \times \left[-\frac{1}{\omega} \nabla_3 \frac{1}{|\mathbf{r}_3 - \mathbf{r}_4|} \nabla_4 + \overleftrightarrow{f}_{xc}(\mathbf{r}_3, \mathbf{r}_4, \omega) \right] \overleftrightarrow{\chi}_{\mathbf{jj}}(\mathbf{r}_4, \mathbf{r}_2, \omega), \end{aligned} \quad (5.95)$$

where the unknown tensor exchange-correlation kernel:

$$\overleftrightarrow{f}_{xc}(1, 2) = \frac{\delta \mathbf{A}_{xc}(1)}{\delta \mathbf{j}(2)} \quad (5.96)$$

has been introduced.

The exchange-correlation kernel $\overleftrightarrow{f}_{xc}$ (and, equivalently, the exchange-correlation vector potential) can be approximated as a local functional of the current, making use of the homogeneous electron gas as reference system [265][266]. The use of this approximation has led to contrasting results. On one side, good results have been found for polarizabilities of polymers [267]. At the same time, TDCDFT permits an efficient description beyond TDLDA of the Drude peak in the spectra of metals in the nontrivial limit $\omega \rightarrow 0 \mathbf{q} \rightarrow 0$ [209][268]. On the other side, absorption spectra for bulk semiconductors are close to the ones obtained in TDLDA [208][269] and, moreover, one finds unphysical imaginary parts in the calculation of atomic excitation energies [270].

In Sec. 7.7 I will derive an exact expression for $\overleftrightarrow{f}_{xc}$ and I will suggest a new approximation of it, based on a many-body derivation, analogous to the one discussed in Sec. 5.4.1 for the TDDFT kernel.

Chapter 6

Vanadium dioxide

Vanadium dioxide (VO_2) is the prototype of several metal oxides. It can be considered as a paradigm for materials where the competition between the tendencies towards electronic localisation and delocalization plays a key role. At a temperature just above room temperature, VO_2 undergoes a double transition, from a metal to an insulator and from a rutile to a monoclinic structure. It has been long debated on which of the two components is the main responsible in driving the transition. Moreover, many experimental results are available that call for a reliable and consistent interpretation. But most of the state-of-the-art theoretical approaches were unable to describe this complex transition. Model interpretations succeeded in explaining only some aspects of the properties of VO_2 , but a consistent global description of the transition requires a first-principles calculation. In particular, in this work I focused on the calculation of the electronic properties of VO_2 . I adopted the parameter-free spectroscopy methods introduced in the previous chapters, in order to find an interpretation to a recent photoemission measurement. I will show that correlation effects in the photoemission spectra can indeed be correctly interpreted in this framework, provided that quasiparticle energies and wavefunctions are calculated self-consistently.

This chapter is organized as follows. I will first introduce the two components of the phase transition and briefly present some experimental results supporting each of the two historical interpretations of the transition. I will then discuss my results, from DFT-LDA for the ground state to a self-consistent quasiparticle calculation for the one-particle excitation properties. I will show how it has been possible to explain the various features of the spectra of the two phases in a consistent way. I will also put into evidence the practical computational limits of the approach. This has motivated a further work, aiming at finding simpler ways to calculate electronic spectra. It will constitute the subject of the next chapter.

6. Vanadium dioxide

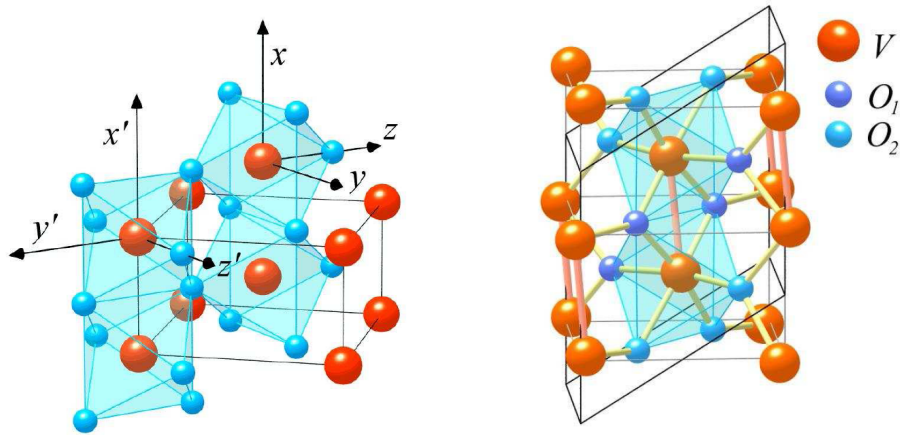


Figure 6.1: Atomic structures of the high-temperature rutile metallic phase (on the left) and the low-temperature monoclinic insulating phase (on the right). Vanadium atoms are shown as large red spheres, oxygen atoms as small blue (or light blue) spheres. The monoclinic structure is obtained by distorting the rutile structure along the c -axis (vertical axis in the figure) with the effect of doubling the unit cell. From Ref. [271].

6.1 The phase transition

Vanadium dioxide exhibits a first-order phase transition at a temperature of 340 K and ambient pressure. At high temperature it is a metal and its crystal structure is tetragonal (rutile). At low temperature it becomes an insulator and at the same time undergoes a structural transition to a monoclinic phase (see Fig. 6.1).

As a result, all its physical properties show a considerable change [272]. For instance, from the metal to the insulator, the resistivity has a jump of five orders of magnitude [273], the third-harmonic optical signal intensity decreases by a factor of 30 [274]. Similar changes occur for the magnetic susceptibility, the thermal expansion coefficients, the optical transmission and reflectivity, the Seebeck coefficients, etc.

Since its discovery in 1959 by Morin [275], this transition has attracted a great interest for both fundamental reasons and possible practical applications.

Vanadium dioxide is of technological interest because the phase transition occurs close to room temperature and is reversible (with typical hysteresis curves). Moreover, the transition can be obtained also in many other different manners, not only by varying the temperature. In fact, it has been achieved also by applying pressure [276], an electric field [277], or light [278]. Therefore, VO_2 has wide applications in the design of ultrafast electromagnetic switches [279, 280] and sensors [281] and, in general, in optoelectronics

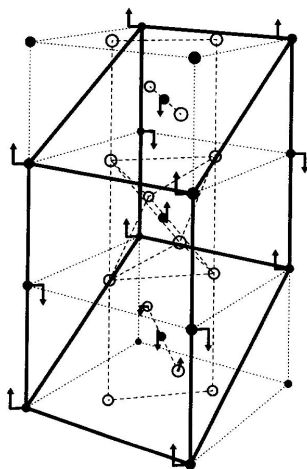


Figure 6.2: Structural distortion in the phase transition. V atoms are represented by full circles, O atoms by empty circles. The arrows indicate the distortion that leads from a tetragonal unit cell (dotted line) to a monoclinic one (solid line). From Ref. [286].

[282, 283].

Thin films of tungsten-doped vanadium dioxide have been proposed [284] as windows coatings that always allow visible light to pass, but reflect infrared light, which causes heating, when the temperature is above 29 degrees Celsius.

From the fundamental point of view, the nature of the transition has been at the center of an intense debate for more than four decades. The issue is whether the electronic correlation is so strong to localize the electrons into a Mott-Hubbard insulator [285], or the structural distortions alone are enough to induce the insulating phase (Peierls model) [286] (see Sec. 1.3.2); in other words, whether the effects on the electronic properties of VO_2 derive from the structural transition or the electronic transition itself induces also a structural distortion; whether the gap in the insulating phase is due to the structural deformation or to electronic correlation.

Before entering into the details of the debate, here I will present separately the two components (structural and electronic) of the phase transition. I will then briefly review experimental evidences supporting one or the other model.

In the rutile structure of the metallic phase (space group $P4_2/mnm$ or D_{4h}^{14} , No. 136 [287]), there are two VO_2 formulas per unit cell. If vanadium atoms are located at $(0, 0, 0)$ and $(\frac{1}{2}, \frac{1}{2}, \frac{1}{2})$, oxygens atoms are then at $\pm(u, u, 0)$ and $\pm(\frac{1}{2} + u, \frac{1}{2} - u, \frac{1}{2})$. A diffraction X-ray study [288] yields for the lattice parameters of the tetragonal cell the values: $a_R = b_R = 4.5546$

6. Vanadium dioxide

	x	y	z
V	0.242	0.975	0.025
O ₁	0.10	0.21	0.20
O ₂	0.39	0.69	0.29

Table 6.1: Atomic positions in the unit cell (reduced coordinates) for the monoclinic phase. After Ref. [271].

\AA and $c_R = 2.8514 \text{ \AA}$, and for the oxygen coordinates $u = 0.3001$.

In the phase transition the lattice is slightly distorted. The V atoms dimerize along the rutile c -axis, and the V dimers twist around the c -axis. In the rutile, V-V distances along the c -axis are 2.85 \AA , in the monoclinic phase they become 2.61 \AA and 3.16 \AA . The oxygen atoms, on the contrary, stay almost at their original positions and do not follow the displacements of the V atoms. The volume has a change of 0.044% [289]. The insulator is slightly denser. The effect of the distortion is hence a lowering of the symmetry and a unit cell doubling. Figure 6.1 shows a comparison of the two structures and Fig. 6.2 represents the effect of the distortion on the rutile structure.

In the monoclinic structure (space group $P2_1/c$ or C_{2h}^5 , No. 14 [287]) there are then four VO_2 formulas per unit cell, that occupy the positions: $\pm(x, y, z)$, $\pm(x, \frac{1}{2} - y, \frac{1}{2} + z)$. With this choice of the reference system [271], the primitive vectors are: $(0, 0, -a_M)$, $(-b_M, 0, 0)$, $(0, c_M \sin \beta_M, -c_M \cos \beta_M)$. The monoclinic cell is obtained from the tetragonal by observing that: $a_M \simeq 2c_R$, $b_M \simeq a_R$, $c_M \simeq a_R - c_R$. Lattice parameters for the monoclinic phase have been measured by X-ray diffraction [290]: $a_M = 5.743 \text{ \AA}$, $b_M = 4.517 \text{ \AA}$, $c_M = 5.375 \text{ \AA}$, $\beta_M = 122.61^\circ$. The different atomic positions are reported in Tab. 6.1.

Concerning the electronic phase transition, the first description has been formulated in a molecular orbital picture by Goodenough [291]. In this framework, bands in a solid are obtained from the overlap of atomic orbitals. In other words, the electronic wavefunctions of the solid are seen as linear combinations of the atomic wavefunctions. In VO_2 bands derive from the one-electron energy levels of the V^{4+} and O^{2-} ions. In particular, in the rutile structure, there are ten V $3d$ bands, originating from the five $3d$ orbitals of the two inequivalent V atoms per unit cell, and twelve O $2p$ bands from the four oxygen atoms (spin degeneracy – neither phase is magnetic – permits to occupy bands with 2 electrons each). In the solid these V $3d$ and O $2p$ orbitals hybridize, giving rise to bonding and antibonding bands of σ or π character. The oxygen $2p$ states are lower in energy than the vanadium $3d$ states and hence fill mainly the bonding bands. The $3d$ states, being around the Fermi level, play the major role in the determination of

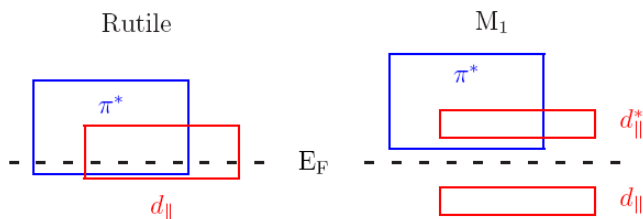


Figure 6.3: Band scheme around the Fermi level for VO_2 in a molecular orbital picture [291]. In the rutile phase the t_{2g} states $d_{||}$ and π^* overlap at the Fermi level giving rise to the metal. In the monoclinic phase (M_1 in the picture) a gap is opened between the $d_{||}$ and π^* levels as a consequence of the bonding-antibonding splitting of the $d_{||}$ state and the rising of the π^* one. From Ref. [271].

the physical properties of VO_2 .

In the molecular orbital picture, the crystalline ionic electric field perturbs the atomic states and, in particular, lifts the $2l+1$ degeneracy of the atomic states. In metallic vanadium dioxide, the rutile structure is obtained from a body-centered tetragonal lattice of V atoms, each of them surrounded by an octahedron formed by six O atoms. This octahedral crystal field splits the V $3d$ states into low energy t_{2g} levels and high energy e_g^σ levels. The t_{2g} are threefold degenerate, the e_g^σ are twofold degenerate. The difference in energy between the t_{2g} and the e_g^σ is due to the different degree of hybridization with the oxygens, which determines a different cost in the Coulomb repulsion energy. The hybridization is larger for the e_g^σ and, therefore, the bonding-antibonding splitting is larger for the e_g^σ , the bonding states being actually mostly O $2p$.

After [291], the t_{2g} state that points to the neighboring V atom along the c -axis is called $d_{||}$ (or a_{1g} in [292]). It derives from the $d_{x^2-y^2}$ orbital of the V atom. The other t_{2g} orbitals (d_{xz} and d_{yz}) are indicated as π^* (e_g^π in [292]). The $d_{||}$ state is hence mainly formed by d orbitals overlapping along the c -axis. It is a highly anisotropic state and leads to a narrow band. It is rightly the overlap of these d orbitals between adjacent vanadium atoms that causes an average V-V separation that is shorter than e.g. the Ti-Ti distance in TiO_2 (instead, the other V-V and V-O distances are not anomalous). The π^* orbitals, instead, point towards the oxygen atoms and are more hybridized with O p orbitals. They determine wider bands and more spherical states.

In VO_2 V has a d^1 configuration. A single d electron per V atom is shared by these bands. The t_{2g} levels ($d_{||}$ and π^*) are hence partially occupied, giving rise to a metal. Figure 6.3 shows a schematic representation of this band diagram in the molecular orbital picture.

6. Vanadium dioxide

In the insulating phase the number of atoms per unit cell is doubled. Therefore, also the total number of $3d$ and $2p$ orbitals is doubled. The effect of the transition on the electronic structure is twofold. First, the d_{\parallel} band is split into a bonding-antibonding combination. Second, the π^* states are shifted above the Fermi level. The combination of these two effects opens a gap of around 0.6 eV between the top of the bonding d_{\parallel} band and the bottom of the π^* band [293]. The system becomes an insulator (see Fig. 6.3).

6.2 Peierls or Mott-Hubbard?

Historically, different models have tried to reduce the complexity of this double phase transition and put into evidence its key factors. The Peierls and Mott-Hubbard models represent two complementary interpretations of the phase transition. In the former case the structural deformation drives the electronic transition. In the latter it is the other way round: it is the strong electronic correlation at the origin of the structural transition.

In the Peierls scheme [291], the upshift of the π^* levels is due to the tilting of the V pairs, which increases the hybridization with the O atoms and then the total π - π^* splitting. Moreover, the d_{\parallel} splitting into a bonding-antibonding combination is a direct consequence of the V-V dimerization.

Instead, in the Mott scheme [285], the π^* upshift decreases the screening of the Coulomb repulsion for the strongly correlated d_{\parallel} orbitals which are then susceptible to a Mott transition.

Therefore, the central issue is whether the splitting of d_{\parallel} is due to the V pairing or to the opening of a correlation gap.

In favor of the Mott model are the large latent heat at the transition (larger than expected from band-structure calculations) and the magnetic Pauli susceptibility, unusually high for a paramagnetic metal (which implies a high density of states at the Fermi level) [272]. Moreover, in the metallic VO₂ the resistivity has a linear dependence with the temperature without any saturation [294, 295], as it should in normal metals, when the mean free path becomes as short as the lattice constant [296]. So the high-temperature phase of vanadium dioxide should be actually defined as “bad metal”, a regime that could not be fully described by a Fermi liquid theory.

On the contrary, the lack of magnetic ordering in the insulator is strongly against the Mott hypothesis (see Sec. 1.3.2). The other vanadium oxide, V₂O₃, in the insulating phase is antiferromagnetic, as directly predicted by the Mott-Hubbard model and, for that reason, constitutes a prototype of Mott insulator.

On other hand, doping VO₂ with small amounts of CrO₂ ($\sim 0.2\%$) [297, 298] or the application of small uniaxial stress [299] lead to the formation of two new metastable structures at low temperature. Both are insulating.

6.2 Peierls or Mott-Hubbard?

One is triclinic (space group $P1$) and the other is again monoclinic (space group $B2/m C_{2h}^3$). The latter is called M_2 to distinguish it from the more stable monoclinic M_1 phase. In the M_2 phase the V atoms form two kinds of parallel chains along the c -axis, with a zig-zag displacement around the c -axis (and no V pairing) in one chain, and a V-V dimerization (and no tilting) in the other. In the M_1 phase, instead, both chains are equivalent: all the V ions are both paired and twisted. In the triclinic phase the two kinds of distortions happen in a not equivalent way in the different chains, giving rise to a lower symmetric structure.

Relevant in the M_2 phase is the presence of local magnetic moments, which, instead, are absent, in the more stable M_1 phase. The linear chains of equispaced V atoms in the M_2 structure can be in fact described as a non-interacting spin-1/2 Heisenberg model [298]. The two monoclinic phases are structurally very similar and the transition from one to the other is continuous. Therefore, the discovery of the magnetic M_2 phase has given new credit to the Mott picture [300, 301].

Very recent pump-probe measurements [302, 303, 304] on VO₂ thin films have shown that, contrary to previous experiments [305], the metal-insulator transition and the structural phase transition from monoclinic to rutile may not occur simultaneously, but, in any case, they disagree on which occurs first.

If the Peierls explanation is valid, a change of phonon modes is expected in the transition, as a clue of the importance of the structural degrees of freedom. But in VO₂ a direct study of the lattice dynamics is difficult: the large incoherent scattering cross section of vanadium makes difficult any coherent inelastic neutron scattering experiment.

An anisotropy in thermal expansion [289], with large thermal displacements [288], a lower Debye temperature than e.g. the neighboring rutile TiO₂, an elastic anisotropy in the metallic phase found by acoustic measurements [306], are all hints of a strong electron-phonon coupling, supporting the Peierls model hypothesis. In the metallic phase, the formation of a charge-density wave has been predicted [307], accompanied by a lattice instability at tetragonal R point $(\frac{1}{2}, 0, \frac{1}{2})$ [288, 308, 309]. This soft phonon mode has been also measured by diffuse X-ray scattering [310].

On the other hand, in a recent Raman spectroscopy study [311] no shift of Raman modes has been registered. The change is limited to the intensity of the peaks, giving no evidence of phonon softening. This result is in contrast with an older Raman study [312], which, on the contrary, supported the idea of strong electron-phonon coupling. The large discrepancies in the Raman spectra have been explained [313] as related to possible deviations from oxygen stoichiometry.

In any case, from this brief summary of the different experimental observations on VO₂, it is evident that no unique conclusion about the character of the transition can be firmly drawn. Even experimental results themselves

6. Vanadium dioxide

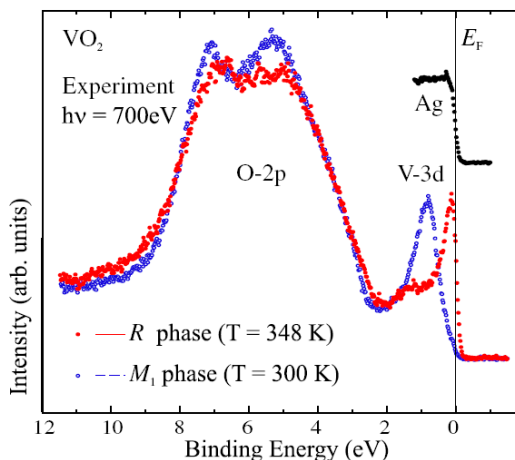


Figure 6.4: Photoemission spectra for the valence states of the metallic (red dots) and insulating phases (blue dots). The data have been taken, at normal emission, on a single crystal of VO₂ with photon energy of 700 eV. The Fermi level has been determined using a silver sample. From Ref. [293].

are often contradictory. No single model, neither Peierls nor Mott-Hubbard, is able to provide a complete and coherent explanation for all these experimental evidences.

Recently, this need to go beyond standard model approaches has been put forward by both experimental [293][314] and theoretical [292] works. These conclusions call for an *ab initio* study of the electronic properties. This is the scope of the following calculations.

6.3 Measurements of the electronic properties

6.3.1 Valence states

Many different direct photoemission studies can be found in literature [293, 315, 316, 317, 318, 319, 320, 321]. They measure the integrated excitation spectrum of the valence bands (see Sec. 1.2.1). Only two [322, 323] report also a partial angular-resolved photoemission analysis that would provide a direct measurement of the band dispersion. To my knowledge, no inverse photoemission data for conduction states are available.

All the photoemission spectra show a very broad O 2*p* structure at an energy between 2 eV and 10 eV below the Fermi level. Figure 6.4 reports the most recent measurement by Koethe *et al.* [293]. This O 2*p* structure has two main peaks (at 5.4 eV and 7.5 eV [318]) and is very similar in the metallic and insulating phases. The main difference between the two phases actually concerns the narrow V 3*d* peak. The maximum of this peak is at

6.3 Measurements of the electronic properties

Core level	Ref. [318]	Ref. [320]
V $2s$	630.02	
O $1s$	529.75	529.9
V $2p_{1/2}$	523.48	523.5
V $2p_{3/2}$	515.95	516.2
V $3s$	68.95	
V $3p$	40.53	40.4
O $2s$	21.73	22.0

Table 6.2: Binding energies (eV) of core and semicore states in monoclinic VO₂ from two different XPS measurements [318, 320]. For the rutile phase similar values are found [320].

a binding energy of around 0.9 eV [293] in the insulator and at the Fermi level for the metal (with a very high spectral weight [293]). In addition, the spectrum of the metal shows another feature at 1.3 eV [293, 315], between the V $3d$ peak and the O $2p$ broad structure, that cannot be ascribed to any V $3d$ state. It is hence a satellite.

On the other hand, all the various spectra differ much in the relative intensities of these peaks and on the spectral weight change in the transition. The origin of these large discrepancies can be traced back to the problem of the actual bulk sensitivity of the experiment, to the different photon energy employed (e.g. hard X-ray or helium lamp photons [315]), and also to stoichiometry problems. In fact, the most stable ionic form for vanadium is V³⁺, and not V⁴⁺, as it is for VO₂. Therefore, a loss of oxygen is possible at the relatively high temperature of the measurement for the metallic phase. The experiment has to be carried out very carefully.

Moreover, the X-ray photoelectron cross section is much larger for the V $3d$ than for the O $2p$ states. So, in principle, in this case one measures mostly the V $3d$ spectral weight [320]. This means that the O $2p$ broad band, measured by X-rays, shows a larger V $3d$ contribution than the actual hybridization. On the other side, this is compensated by the fact that in VO₂ there are six O $2p$ electrons and only one V $3d$ electron per formula unit.

Also core lines have been measured by X-ray spectroscopy [318, 320]. For completeness and later reference, their binding energy is reported in Tab. 6.2.

Information provided by photoemission is complemented by X-ray emission experiments (see Fig. 6.5). In this case the spectra are obtained by transitions between valence bands and core holes and, in an independent-particle picture, yield an alternative measurement of the valence states. In particular the transitions: V L α ($3d4s \rightarrow 2p_{3/2}$), V K β_5 ($4p \rightarrow 1s$), O K α

6. Vanadium dioxide

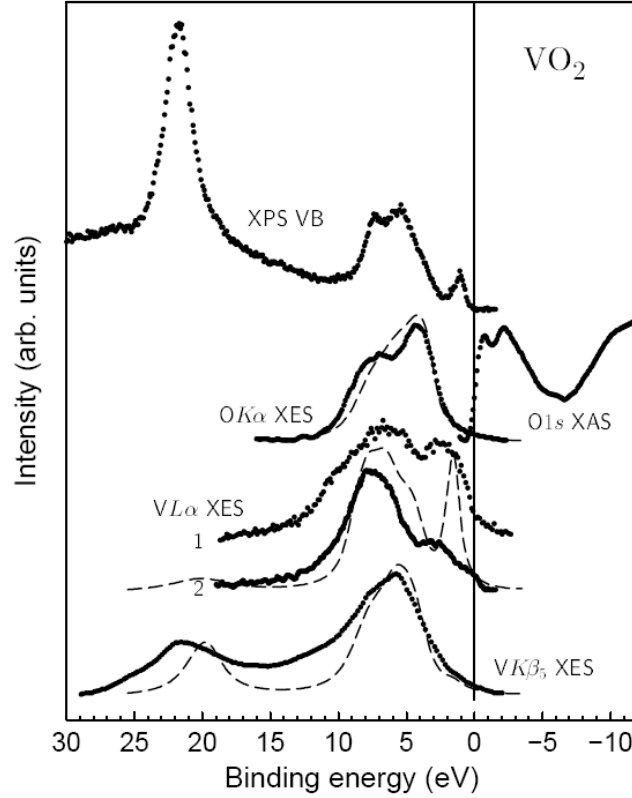


Figure 6.5: X-ray emission spectra for the monoclinic phase adjusted in order to have the same energy scale as the XPS spectrum used as reference (first curve from the top). The O $K\alpha$ and V $L\alpha$ spectra probe the distribution of the O $2p$ and V $3d$ states, respectively. At low binding energies, the XPS spectrum shown here corresponds to the blue curve of Fig. 6.4. The additional O $2s$ peak at a binding energy around 22 eV is also visible in this picture. The top of the O $K\alpha$ curve is at the same binding energy (around 4 eV) as a shoulder in the XPS spectrum (where O $2p$ cross section is smaller than the V $3d$ one and hence O $2p$ features are partially hidden). Two V $L\alpha$ curves are presented, corresponding to an emission after an electronic excitation (curve 1 in the picture) or a photon excitation (curve 2). The former also contains the V $L\beta$ ($3d4s \rightarrow 2p_{1/2}$) emission spectrum. The V $K\beta_5$ spectrum measures the V $4p$ states and shows their hybridization with the O $2p$ and O $2s$ states. Dash curves are theoretical LDA densities of states. From Ref. [318].

6.3 Measurements of the electronic properties

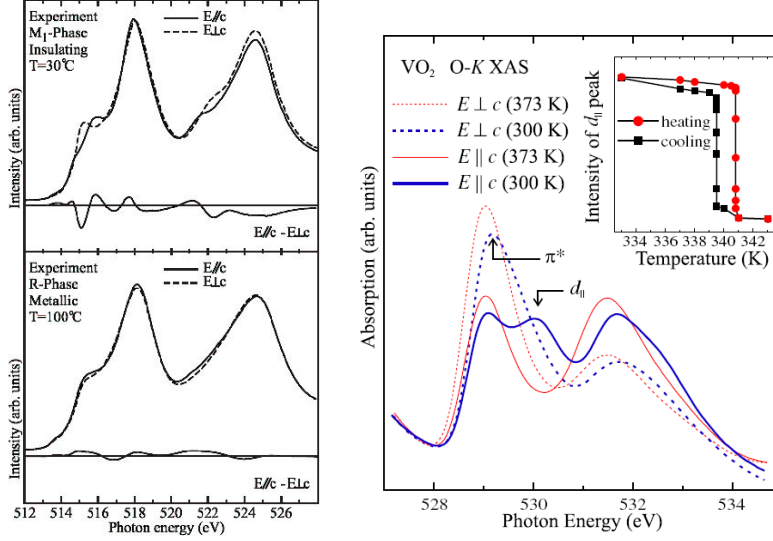


Figure 6.6: X-ray absorption spectra at the V $L_{2,3}$ edge (on the left) from Ref. [314], and at O K edge (on the right), from Ref. [293]. For both edges the spectra are taken with light polarization $\vec{E} \parallel c$ (solid lines) and $\vec{E} \perp c$ (dashed lines). For the V $L_{2,3}$ edge also the dichroic spectrum is presented, resulting from the difference between the two polarizations. In the insulating phase it has a larger amplitude. In the O K spectrum of the insulator with $\vec{E} \parallel c$, the additional d_{\parallel} peak at 530.1 eV is evidenced. The features at around 532 eV correspond to the e_g^{σ} states. The inset shows the hysteresis curve for the intensity of the d_{\parallel} peak. Not shown here, the O K spectrum, at higher energies (around 543 eV), would display also the hybridisation between O $2p$ and V $4sp$ states [317].

($2p \rightarrow 1s$) have been considered in the insulating phase [318] (see Fig. 6.5). The O $K\alpha$ spectrum, which directly measures the O $2p$ states, has a maximum at around 4 eV, in correspondence to a shoulder in the photoemission X-ray spectrum (where features due to O $2p$ states are partially hidden by their smaller cross section). The rest of the O $K\alpha$ and V $L\alpha$ spectra overlap in energy with the broad feature seen in the photoemission spectrum, confirming that is due to the hybridization between O $2p$ and V $3d$ states. Finally, the V $K\beta_5$ spectrum makes evident the hybridization between V $4p$ and O $2p$ or O $2s$ states.

6.3.2 Conduction states

X-ray absorption spectra [293, 317, 314, 324, 325], in an independent-particle picture, map the conduction bands above the Fermi level (see Eq. (1.35)). The absorption spectra collected at the O K ($1s \rightarrow 2p$) and V $L_{2,3}$ ($2p \rightarrow 3d$) edges probe the hybridization between the O $2p$ and V $3d$ unoccupied states

6. Vanadium dioxide

(see Fig. 6.6).

The XAS spectra show that the π^* states dominate the lower part of the conduction bands. From the metal to the insulator the π^* are shifted towards higher energies by about 0.2 eV. The leading edge of the photoemission spectrum for valence states (see Fig. 6.5) in the insulating phase is obtained as the middle point between the maximum of the $3d$ peak and the Fermi energy [293]. So it is located at a binding energy of around 0.4 eV. Adding this value to the 0.2 eV shift in the opposite direction of the leading edge of XAS insulating spectrum yields, in total, a gap of about 0.6 eV between the top valence and bottom conduction bands in the insulator.

In the V $L_{2,3}$ spectrum the spin-orbit splitting between the levels $2p_{3/2}$ and $2p_{1/2}$ is smaller (~ 6.6 eV) than the separation measured in photoemission (~ 7.4 eV, see also Tab. 6.2) and their intensity ratio is not 2:1 as expected [324][45]. This effect is due to the strong interaction between the core hole and the final state [62].

Most noticeably, the spectra for the insulating phase show a strong dependence on the polarization of the photons along the rutile c -axis. The metal is instead more isotropic. In particular, in the O K spectrum of the insulator an additional peak appears at a energy 1 eV higher with respect to the π^* peak. This new peak is visible only for a polarization $\vec{E} \parallel c$. It corresponds to the d_{\parallel} antibonding state, which is present only in the insulating phase. This state is mainly due to the overlap along the c -axis between V $3d$ orbitals and it is for this reason that it is visible only for a polarization $\vec{E} \parallel c$. The combination of photoemission and absorption spectra yields a total bonding-antibonding splitting of the d_{\parallel} state of about 2.5 eV. Finally, since for the π^* state there is a larger hybridization between O $2p$ and V $3d$ orbitals, the π^* peak has a higher intensity than the d_{\parallel} .

6.4 LDA ground-state calculations

The aim of my work has been the interpretation of the photoemission spectra that I have introduced in the previous section. But the starting point has been the calculation of the ground-state properties of VO_2 . This section presents the results of these calculations.

6.4.1 Pseudopotential generation

The first task in a plane-wave approach is the generation of reliable pseudopotentials that make easier (and often even feasible) the calculations. In particular, in the GW framework the use of pseudopotentials has been recently the subject of an intense debate [149][152][153][151][165] (see Sec. 3.3.3). Therefore, I will dedicate some space here to the discussion of the generation of the pseudopotentials for vanadium and oxygen, which I will use in the following calculations.

6.4 LDA ground-state calculations

State	Energy [eV]
1s	-5351.2
2s	-601.1
2p	-502.8
3s	-69.8
3p	-44.0
3d	-5.4
4s	-4.8

Table 6.3: Energy levels in the vanadium atom calculated in LDA.

The V atom has the electronic configuration $[\text{Ar}]3d^34s^2$. In an atomic LDA calculation the valence states are quite well separated in energy from the semicore states, which are the other states belonging to the third shell (see Tab. 6.3). A first possible choice for the pseudopotential for vanadium could then be to freeze in the atomic core all the states that are not explicitly valence.

In this case three main issues have to be considered in the generation of the V pseudopotential.

- i. Using pseudopotentials, the total electron density is decoupled into valence and core densities. The exact exchange-correlation term, E_{xc} , of the total DFT energy functional has a nonlinear functional dependence on the total density $\rho = \rho_v + \rho_c$. In the pseudopotential framework, the exchange-correlation term depends only on the valence density ρ_v . The exchange-correlation interaction between valence and core electrons is usually included in the pseudopotential as a term that depends linearly on the valence density. This linear decoupling between valence and core densities:

$$E_{xc}[\rho_v + \rho_c] = E_{xc}[\rho_v] + E_{xc}[\rho_c]$$

often turns out to be a reasonable approximation. But, if core and valence densities are not completely spatially separated, the nonlinear exchange and correlation interaction between them has to be treated explicitly, by including the so-called nonlinear core corrections in the pseudopotential [326].

- ii. The $3d$ state in the V atom is only weakly bound. Therefore, assuming transferability of the pseudopotentials, for the $3d$ pseudowavefunction it is better to choose as reference state a ionic configuration [115] instead of the neutral atom. In particular, for vanadium the ionic configuration $s^{0.75}p^{0.25}d^3$ has been used, which assures a better localization of the $3d$ wavefunction.

6. Vanadium dioxide

Pseudopotential	r_c^s	r_c^p	r_c^d	r_{nlc}	reference component
V ‘nlcc’	2.50	2.62	2.00	1.50	s
V ‘semico’	1.00	1.10	1.00		p
O	1.30	1.30	1.30		p

Table 6.4: Parameters employed in the generation of the different pseudopotential used in the following calculations. Cutoff radii for the different angular components are in atomic units. r_{nlc} is the radius for the partial core used in nonlinear core-corrections. I have found similar parameters as the V ‘semico’ pseudopotential in the one adopted in Ref. [334].

- iii. Considering for vanadium only the $3d$ and $4s$ states in valence could be problematic. In fact, the all-electron wavefunctions of the V atom for the valence states $3d$ and $4s$ and the semicore states $3s$ and $3p$ have a large spatial overlap (see Fig. 6.7). For this reason a better approximation would be to treat the semicore states explicitly as valence states, excluding them from the atomic frozen core. This turns out to be mandatory in particular for GW calculations, where in the exchange term it is rightly the spatial overlap between wavefunctions that really matters. The same situation has been found also for other transition metals, such as copper [327] or in the case of cadmium sulphide [150].

Pseudopotentials of the Troullier-Martins type have been chosen [328] in the fully separable Kleinman-Bylander form [329]. Using the `fhi98pp` code [330][331] to tune the cutoff radii, the transferability of these pseudopotentials has been optimized in order to find a compromise with the energy cutoff required for the convergence (the “softness” of the pseudopotential). After a proper choice of the reference component of the pseudopotential, the absence of spurious ghost states [332] has been carefully checked.

Two kinds of pseudopotentials for vanadium have been generated. In the first one (called ‘nlcc’ in the following) only $3d$ and $4s$ states are included in valence and a nonlinear core correction for the exchange-correlation potential is considered. For the second pseudopotential (called ‘semico’) also the $3s$ and $3p$ semicore states are added explicitly to the valence, leading, of course, to more demanding calculations. In the insulator with the ‘nlcc’ pseudopotential there are 68 valence electrons per unit cell; with the ‘semico’ pseudopotential they become 100.

The generation of the pseudopotential for oxygen is an easier task. Oxygen has an electronic configuration $[\text{He}]2s^22p^4$ and the core-valence partition is straightforward. Since already vanadium requires a high cutoff, the pseudopotential for oxygen can be created in such a way to privilege its transferability with respect to its softness. For this reason, cutoff radii for oxygen have been chosen smaller than, for instance, in Refs. [3][333].

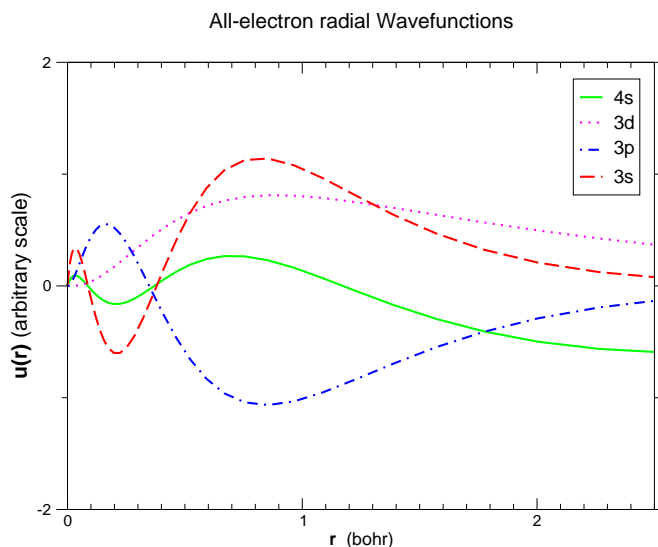


Figure 6.7: Radial all-electron LDA wavefunctions of the V atom. The absolute values of the wavefunctions of the semicore states $3s$ and $3p$ have their maximum where valence state $3d$ and $4s$ wavefunctions have theirs. Therefore this spatial overlap cannot be neglected, even though these states are quite well separated in energy (see Tab. 6.3).

6.4.2 Ground-state atomic structures

Various LDA calculations for VO_2 are available in literature. To test the quality of the pseudopotentials a comparison with them is hence possible. Both the ‘semico’ and ‘nlcc’ pseudopotentials (i.e. with or without semicore states in valence) have been employed. For all the following calculations I have made use of the Abinit package [335][336].

A $4 \times 4 \times 4$ Monkhorst-Pack grid [113] of \mathbf{k} points is enough to achieve a good convergence (within 2×10^{-4} Ha) in total energy calculations. This grid corresponds to 16 \mathbf{k} points in the irreducible wedge of the Brillouin zone for the insulator and 6 \mathbf{k} points for the metal. For the metal a Gaussian smearing of 0.01 Ha for the Fermi distribution has been adopted.

The calculation with the ‘semico’ pseudopotential is much more demanding. It requires an energy cutoff of 180 Ry to converge. Instead, the calculation with the ‘nlcc’ pseudopotential converges already with 100 Ry. In the latter case the wavefunctions are represented in a basis of around 13500 plane waves, in the former they become 32500.

The atomic structures have been calculated starting from the experimental ones. They have been fully relaxed until atomic forces and cell stresses have become smaller than 5×10^{-5} Ha/bohr.

Tab. 6.5 collects the geometrical structures for the monoclinic and rutile

6. Vanadium dioxide

Rutile	Exp.	Theo.	‘nlcc’	‘semico’
a	4.5546 Å	4.58 Å	4.659 Å	4.536 Å
c	2.8514 Å	2.794 Å	2.817 Å	2.754 Å
cell volume	59.2 Å ³	58.6 Å ³	61.1 Å ³	56.7 Å ³

Monoclinic	Exp.	Theo.	‘nlcc’	‘semico’
a	5.7517 Å	5.629 Å	5.659 Å	5.549 Å
b	4.5378 Å	4.657 Å	4.641 Å	4.522 Å
c	5.3825 Å	5.375 Å	5.420 Å	5.303 Å
α	122.646°	121.56°	121.46°	121.73°
cell volume	118.3 Å ³	120.1 Å ³	121.4 Å ³	113.2 Å ³

Table 6.5: Comparison between the structures calculated with the two different pseudopotentials, the theoretical results from Ref. [286], and the experimental data. The latter for the rutile are from Ref. [288], and for the monoclinic structure from Ref. [290].

phases, obtained using the two pseudopotentials, and compares them with the data (both experimental and theoretical) available in literature.

The LDA results for the lattice parameters are in good agreement with the experimental structure (within typical errors of few percents [337]). On one hand, this provides a confirmation of the reliability of the pseudopotentials. On the other hand, this shows that even for VO₂ LDA is a good approximation to calculate ground-state properties. In fact, VO₂ represents a severe test for LDA, because d orbitals are generally localized around the ions. VO₂ is hence quite distant from a situation where the charge density is homogeneous, as in the case of the jellium which LDA is built on.

The same conclusions were reached by Wentzcovitch *et al.* [286], who performed a Car-Parrinello molecular dynamics [338] simulation in LDA and found equilibrium structure in good agreement with the experiment (referred to as ‘Theo’ in the following). Wentzcovitch *et al.* [286] also have adopted a similar pseudopotential scheme, but it is not known which electrons have been included in valence (their cutoff is any case pretty low: only 64 Ry).

LDA has the tendency to overbind [339] and this is confirmed also by the results obtained with the ‘semico’ pseudopotential. The in principle less accurate ‘nlcc’ pseudopotential determines results even a bit closer to the experimental data, but yields equilibrium unit cell volumes that are, on the contrary, larger than the experimental ones. I performed also a test GGA calculation for the monoclinic structure. In this case, the resulting cell volume is 120.7 Å³, in agreement with the LDA results.

In any case, both LDA pseudopotentials properly describe also the dimerization of V atoms in the transition, as it is obtained by the calculation of

6.4 LDA ground-state calculations

	Exp.	Theo.	‘nlcc’	‘semico’
V-V (1)	2.62 Å	2.52 Å	2.57 Å	2.49 Å
V-V (2)	3.16 Å	3.14 Å	3.11 Å	3.10 Å

Table 6.6: V-V spacings along the c -axis in the monoclinic phase. In the rutile structure, the V atoms are equispaced along the axis and their distance corresponds to the lattice parameter c (see Tab. 6.5). Experimental data are from Ref. [290]. Theoretical data are from Ref. [286].

the V-V spacings in the monoclinic phase (see Tab. 6.6).

6.4.3 Kohn-Sham eigenvalues

Another way to assess the validity of the pseudopotentials is the calculation of the Kohn-Sham eigenvalues and their comparison with the results that can be found in literature.

The effect of pseudopotentials on the Kohn-Sham eigenvalues is twofold. First, since employing different pseudopotentials generally determines different lattice structure, this indirectly produces different Kohn-Sham results. Second, even fixed a lattice structure, for instance the experimental one, the choice of a pseudopotential has then a direct influence on the solution of the Kohn-Sham equations.

In this analysis I will consider only the monoclinic phase of VO₂. Results for the rutile phase are analogous. If the two different pseudopotentials are used adopting the same experimental equilibrium structure, the resulting Kohn-Sham eigenvalues remain pretty similar, especially around the Fermi level, as it is shown by Fig. 6.8. Differences between corresponding eigenvalues are never larger than about 0.1 eV for bands farther from the Fermi level.

On the contrary, the effects due to the different lattice structures are much larger, already around the Fermi level (see Fig. 6.9). While the bottom of the conduction bands is at the C point in all the cases, the position of the top of the valence bands varies with the structures in the ZD direction. Similarly, the bottom conduction band has at the Γ point a second minimum which is below the top valence only in two cases. The differences become even larger (of the order of 0.5 eV) for the other states, going farther from the Fermi level, both for conduction and valence bands.

A quantitative comparison, as done in Tab. 6.7, of the overlap in energy between the bottom conduction and top valence bands (which is defined as “negative gap”) in all these cases confirms that there is no much difference in using one pseudopotential or the other, once the lattice structure is fixed, but the discrepancies increase if, instead, the same pseudopotential is used starting from different geometries.

6. Vanadium dioxide

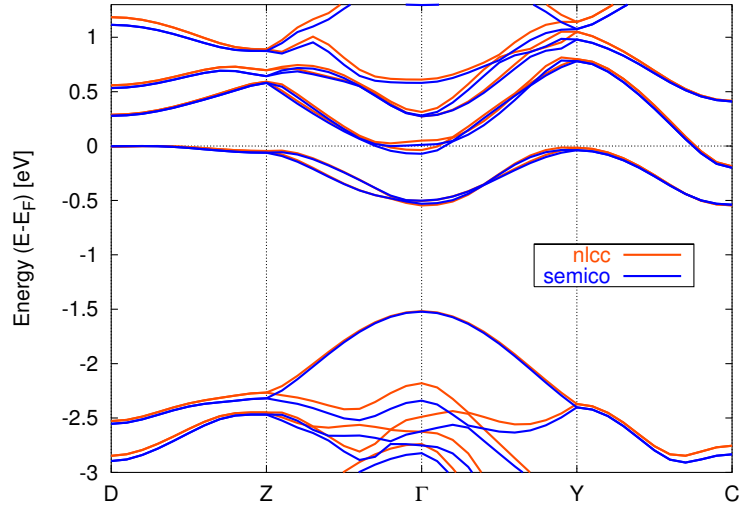


Figure 6.8: Kohn-Sham eigenvalues for monoclinic VO_2 calculated at the experimental ionic positions. Comparison between the results obtained with or without vanadium semicore states in valence (respectively ‘semico’ and ‘nlcc’ pseudopotentials). The differences are small, especially around the Fermi level. In all the band structures the different top valence are always aligned.

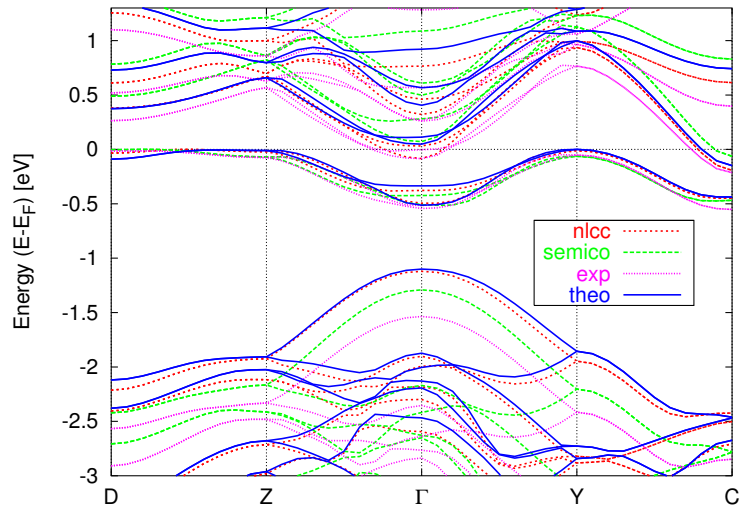


Figure 6.9: Kohn-Sham eigenvalues for monoclinic VO_2 calculated with the ‘semico’ pseudopotential using the different lattice structures of Tab. 6.5. The many curves in the picture show that the Kohn-Sham eigenvalues have a large dependence on the different structures employed in the calculations.

6.4 LDA ground-state calculations

Lattice	Pseudo	Gap
exp	nlcc	-0.19 eV
exp	semico	-0.20 eV
nlcc	semico	-0.19 eV
semico	semico	-0.06 eV
theo	semico	-0.15 eV

Table 6.7: Different values for the gap with different lattice structures (see Tab. 6.5) and with the different pseudopotentials for vanadium that have adopted in the calculations (see Tab. 6.4). A negative gap means that the bottom conduction and top valence band overlap, giving rise to a metallic band structure. The largest differences are obtained changing the lattice parameters.

From a physical point of view, these observations permit qualitatively to conclude that a strong electron-phonon coupling is indeed expected for the monoclinic vanadium oxide, since a small variation of the ionic position determines a large variation of the electronic properties of the system.

Concerning the reliability of the pseudopotentials, the fact that both give the same Kohn-Sham eigenvalues at a given lattice structure is a proof that the inclusion in valence of the semicore states $3s$ and $3p$ of vanadium doesn't modify the Kohn-Sham results. At the LDA level, considering only $3d$ states in valence is already enough to obtain a reliable band structure, if, for instance, the experimental lattice structure is used. On the contrary, of fundamental relevance is the requirement of a proper treatment of the exchange-correlation interaction between core and valence densities, through the inclusion of the nonlinear core corrections in the pseudopotential. A pseudopotential where these corrections are neglected yields a Kohn-Sham band structure completely different, already on a qualitative level, with a (positive) gap of 0.2 eV between valence and conduction states.

The validity of the pseudopotentials is finally assessed by a proper comparison with previous LDA calculations, which use different approaches. Wentzcovitch *et al.* [286] have adopted a similar pseudopotential plane-wave approach. Continenza *et al.* [340] and Eyert [271] used a different technique: an all-electron full-potential linearized-augmented plane-wave (FLAPW) method [341]. The latter author calculated the Kohn-Sham eigenvalues with the experimental geometry, the others with the theoretical structure of Wentzcovitch *et al.* ('Theo.' in Tab. 6.5).

They all show only the V $3d$ bands, but in all the three cases the band structures are extremely similar to the present results obtained with the corresponding ionic structures.

Wentzcovitch *et al.* found a slightly smaller negative gap (0.04 eV with respect to 0.15 eV here), but the shape of the band structure remains the same, with the top valence at Z and Y, and the bottom conduction at C.

6. Vanadium dioxide

The results of Eyert, obtained with the experimental lattice parameters, also compare very well, with the top valence in D and the bottom conduction in C and an overlap in energy of 0.1-0.2 eV. In the case of Continenza *et al.*, in particular, the band structure is perfectly coinciding with the solid blue curve of Fig. 6.9. In this comparison small differences could even be expected, since the method employed by Continenza *et al.* is not based on plane waves and, moreover, they didn't make use of pseudopotentials. The fact that the results are so similar provides a further demonstration of the validity of the generated pseudopotential for LDA calculations.

6.4.4 LDA validation of the molecular orbital picture

Even though Kohn-Sham eigenvalues cannot be interpreted as quasiparticle energies (see Sec. 2.2.1), they often yield the correct ordering of the bands, whose character can be hence analyzed. A combined study of the LDA band structures (see Fig. 6.10) and LDA density of states, projected on the different angular momentum components (see Fig. 6.11), can therefore provide a first-principle validation of the molecular orbital picture of Ref. [291].

The general classification of the electronic structure is similar in the two phases. In fact, for both the insulating and the metallic phases, three groups of bands can be identified. In the energy range between -7.6 and -1.5 eV below the Fermi level (only partially shown in the band-structure plots in Fig. 6.10), bands are mostly O $2p$, hybridized with V $3d$ states. The other two groups of bands, from -0.6 eV to 5.0 eV, are, on the contrary, mostly V $3d$. They show as well a not negligible contribution from O $2p$. These two groups have a small separation, visible in particular in the density of states, at 2.0 eV above the Fermi level. In the rutile phase, the first V $3d$ group is made of six bands and the second group of four bands. So the former can be identified with the set of t_{2g} states and the latter can be attributed to the e_g^σ states. In the monoclinic phase the number of bands for each group is doubled because the number of formula units per unit cell is also doubled. A further symmetry analysis of the different $3d$ states has been carried out by Eyert [271]. His results are in very good agreement with the ones shown here.

This LDA study confirms the predictions done on the basis of the molecular orbital picture of Ref. [291]. It provides the same description of the O $2p$ – V $3d$ hybridization and the same assignments to the different group of bands, even though the LDA electronic structures are metallic for both phases.

The effects of the phase transition on the electronic properties of VO₂ are evident in particular at the Fermi level. The band dispersion is generally smaller in the monoclinic phase, especially for the t_{2g} states, indicating that the bands are more localized. In the rutile phase there is a high density

of states around E_F . In particular, the density of states for the t_{2g} states has its maximum at the center of the corresponding group of bands. In the monoclinic phase, on the contrary, the two highest peaks show up on the two sides of this group, where the main part of the spectral weight is shifted to. This reflects the upshift of the π^* states and the splitting of the $d_{||}$ band into a bonding-antibonding pair, as expected from the molecular orbital description. The LDA estimate of the amplitude of this splitting is 1.3 eV.

It is clear from this analysis that LDA yields a metallic electronic structure also for the monoclinic phase of VO_2 rightly because it underestimates the $d_{||}$ splitting, which experimentally is more than 2.5 eV [293][319].

Is this a failure of LDA and a demonstration of the strongly electronic correlated character of VO_2 ? Or this result is simply due the fact that DFT in the Kohn-Sham formulation is not supposed to yield correct quasiparticle band structures and leads to a band gap underestimation? The answer to these questions will be the subject of a further analysis, based on the GW approximation, the state-of-the-art first-principle method to calculate quasiparticle excitations in solids.

6.5 Standard GW calculations

In a GW calculation the proper treatment of the semicore states ($3s$ and $3p$ in the case of vanadium) is of crucial importance. In fact, if the spatial overlap between semicore and valence states is large, its contribution to the bare-exchange self-energy term is expected to be large and cannot be neglected. This has been already shown for example in the case of cadmium sulphide [150], copper [342] and copper oxide [3][233]. In all these cases treating the exchange interaction between valence and semicore states at the LDA level in the pseudopotential resulted in a very large and unphysical upward shift of the valence d states, that in the case of copper oxide led even to the closure of the LDA gap. And, since the exchange self-energy doesn't depend on energy differences, the energy separation of those states, although large, doesn't have any relevance in this context. What really matters is their common spatial localisation that contributes to build up the density matrix on which the exchange operator depends.

These results made evident that in a GW calculation the semicore-valence exchange interaction is not properly taken into account by a pseudopotential that treats in a different manner states belonging to the same shell. For this reason, in all the calculations for the determination of quasiparticle properties of VO_2 , I have considered only the pseudopotential with semicore explicitly treated in valence.

For the monoclinic phase, convergence has been achieved using 200 bands (each represented on a basis of 5001 plane waves) for the calculation of the

6. Vanadium dioxide

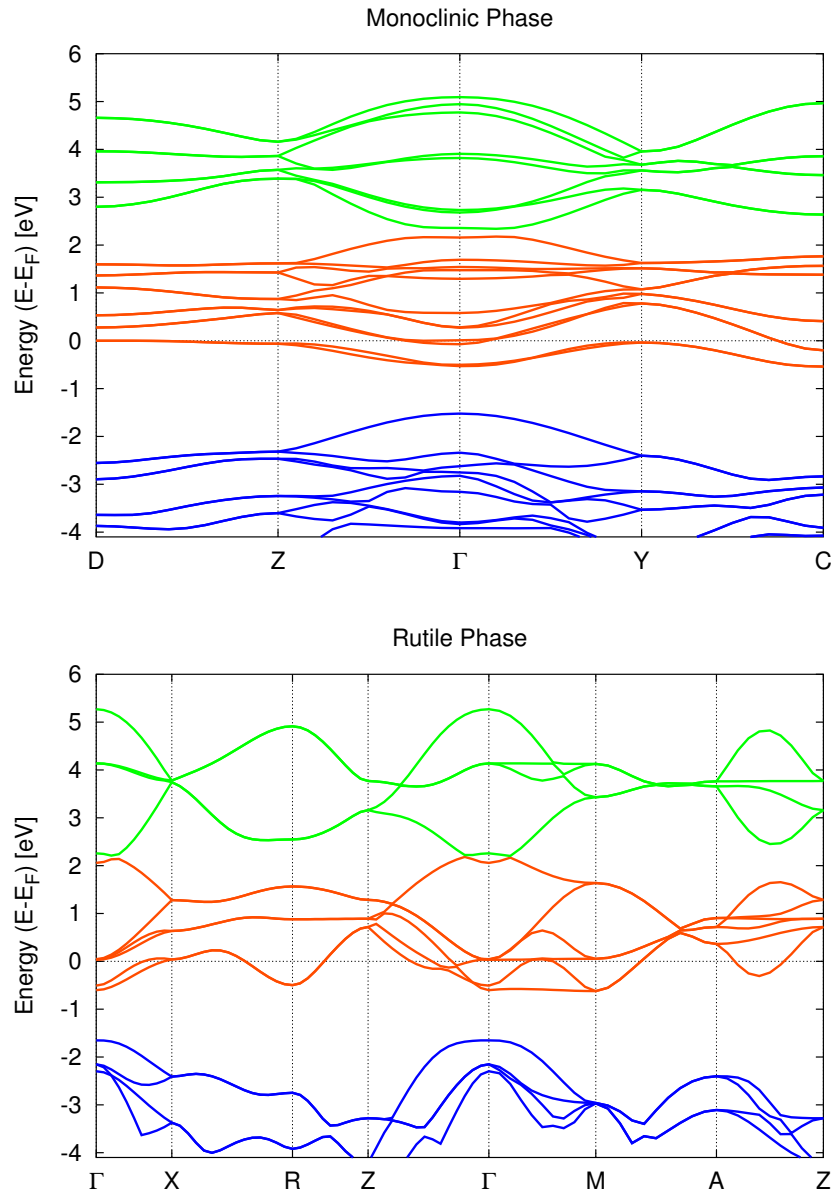


Figure 6.10: LDA band structure of the monoclinic and rutile phases of VO₂. For both the same color key is used. The topmost O 2p states are represented in blue; in red the t_{2g} states and in green the e_g^σ states.

6.5 Standard GW calculations

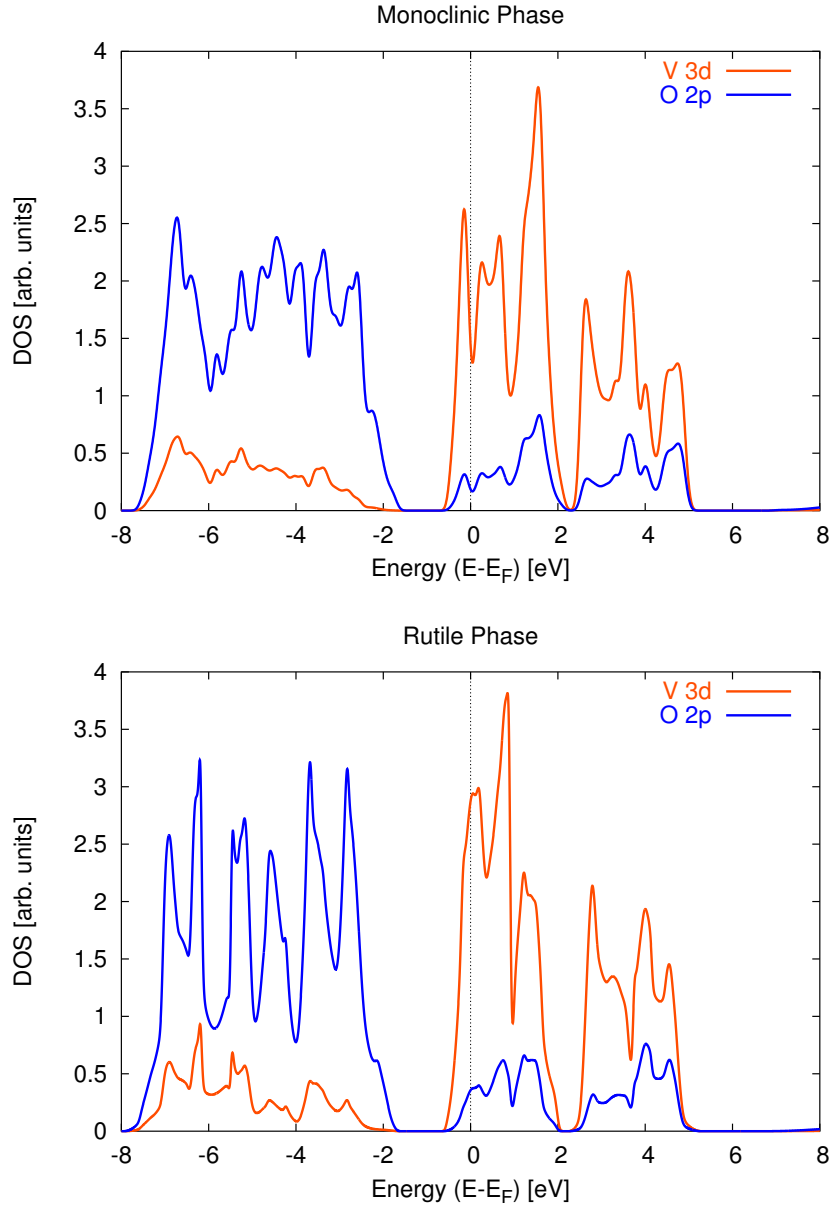


Figure 6.11: Projected density of states for the two phases. In these pictures only the main components near the Fermi level are shown. In this energy region, bands result from a hybridization between O $2p$ and V $3d$ orbitals, with different proportions of the two elements for the three group of bands that can be distinguished in these plots.

6. Vanadium dioxide

screening, and 150 bands (with 3001 plane waves) in the calculation of self-energy corrections. The inverse dielectric function $\epsilon_{\mathbf{G}\mathbf{G}'}^{-1}$, in the reciprocal space is a matrix of dimension 301. Parameters of similar size have been adopted also for the rutile phase. In both cases, the convergence has been checked also with respect to the number of \mathbf{k} points: a $4 \times 4 \times 4$ Monkhorst-Pack grid yields already converged results.

In the monoclinic phase the standard perturbative GW corrections (see Eq. (3.60)) determine a rigid upshift of the whole t_{2g} group of LDA bands of almost 1.6 eV and a similar 0.8 eV rigid upshift of the lower group of O $2p$ bands. Once the top valence of the LDA and GW band structures have been aligned, the global effect is then an increase of the gap between the occupied O $2p$ and t_{2g} bands. A similar effect can be found also for the metallic phase, with an increase of the O $2p - t_{2g}$ gap of almost 0.5 eV.

In the monoclinic and in the rutile phases the GW corrections have the same effect, as evidenced by Fig. 6.12. In both cases the t_{2g} group behaves as a whole. Hence, no gap is opened between the top valence and bottom conduction bands, which belong both to the group of t_{2g} states. The electronic structure of the monoclinic phase therefore remains metallic even in GW.

This failure of standard GW to reproduce the insulating character of the monoclinic phase seems supporting the hypothesis of strong correlation. In fact, for example, even germanium has a negative gap at the LDA level, but when GW corrections are considered in the same manner as in the present GW study of VO_2 , a good agreement with experiment is achieved.

On the other hand, the standard GW method is based on a series of hypotheses and approximations (see Sec. 3.3) that normally are valid for a vast range of materials, such as semiconductors and simple metals where GW is well grounded. But the same hypotheses might not be acceptable for vanadium dioxide. Therefore, before concluding that GW is not able to describe the electronic structure of VO_2 , one should check one by one all these approximations and verify whether they are still valid in the case of vanadium dioxide. It is rightly what I am going to discuss here.

First of all, standard GW corrections are usually evaluated as first-order perturbation with respect to LDA (see Eq. (3.60)). In this way one calculates only the diagonal matrix elements $\langle \varphi_{i\mathbf{k}} | \Sigma | \varphi_{i\mathbf{k}} \rangle$ to get the corrections to the LDA eigenvalues $\varepsilon_{i\mathbf{k}}$. The off-diagonal terms $\langle \varphi_{i\mathbf{k}} | \Sigma | \varphi_{j\mathbf{k}} \rangle$ are instead neglected. To check this assumption, a new band structure for the monoclinic phase has been obtained by diagonalizing the full matrix, calculated taking into account all the O $2p$ and V $3d$ states. These new GW corrections turn out to be very similar to the perturbative results (see Fig. 6.13 for a direct comparison). The qualitative effect remains the same: two upshifts of the t_{2g} and O $2p$ states of different sizes, which induce a further small increase of the gap between these two groups of bands. The diagonalization doesn't determine any difference in the relative positions of the top valence and the

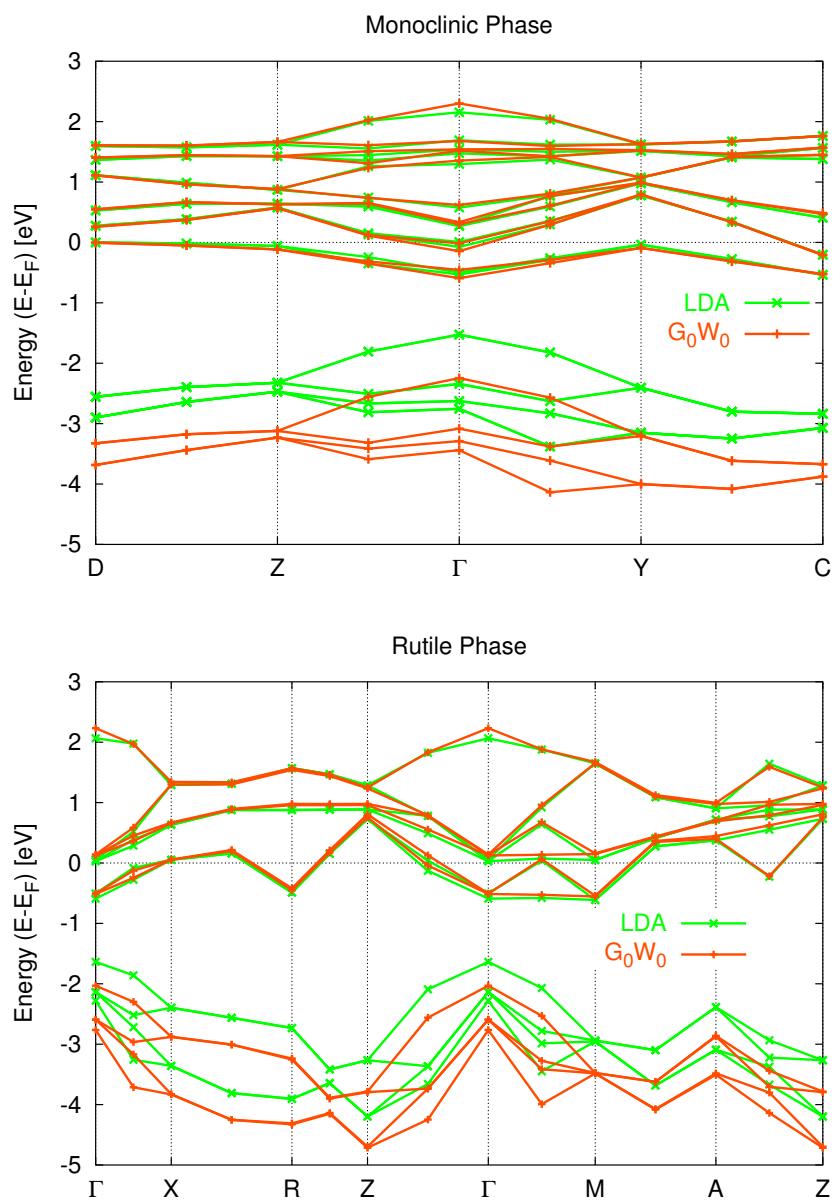


Figure 6.12: Comparison between LDA and perturbative G_0W_0 band structures for the monoclinic (upper panel) and rutile phases (bottom panel). The top valence in both cases has been aligned.

6. Vanadium dioxide

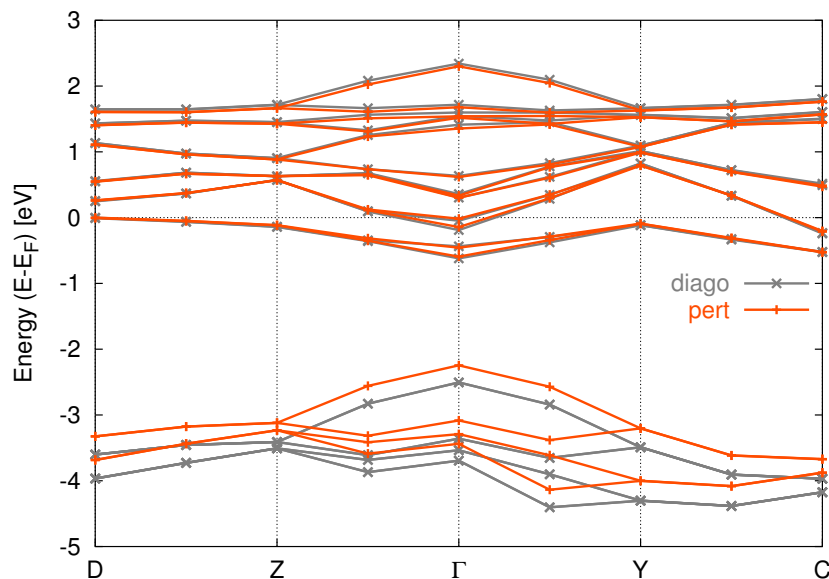


Figure 6.13: Comparison between the band structure, ‘pert’, from standard first-order perturbative GW and the band structure, ‘diago’, obtained by diagonalizing the full matrix $\langle \varphi_{i\mathbf{k}} | H_0 + \Sigma | \varphi_{j\mathbf{k}} \rangle$.

bottom conduction states, leaving the system metallic and confirming the validity of the first-order perturbation approach.

Moreover, the self-energy has a dynamical dependence that is linearized around the Kohn-Sham eigenvalues $\varepsilon_{i\mathbf{k}}$ on which the GW corrections are calculated (see Eq. (3.3.1)). To check the validity of this linearization, the expectation values $\langle \varphi_{i\mathbf{k}} | \Sigma(\omega) | \varphi_{i\mathbf{k}} \rangle$ have been calculated at 9 frequencies around $\varepsilon_{i\mathbf{k}}$. The renormalization factors, $Z_{i\mathbf{k}}$, that come out from this linearization, have been then obtained by linear interpolation. In this way the error made in the linearization can be evaluated. In all the cases it results smaller than 0.1 eV.

Therefore, after having assessed the validity of the approximations routinely adopted to solve the quasiparticle equation, the reliability of the standard GW self-energy itself has to be addressed.

One of the most relevant approximations usually made is the use of a plasmon-pole model (see Sec. 3.3.2) to simplify the evaluation of the frequency dependence of $W(\omega)$. But the loss function of vanadium dioxide is not characterized by one single peak [343] (see also Sec. 6.8), as for example in the case of bulk silicon [143][144]. One then could reasonably have some doubts concerning the plasmon-pole model approximation.

To verify the validity of this approximation, I explicitly calculated the

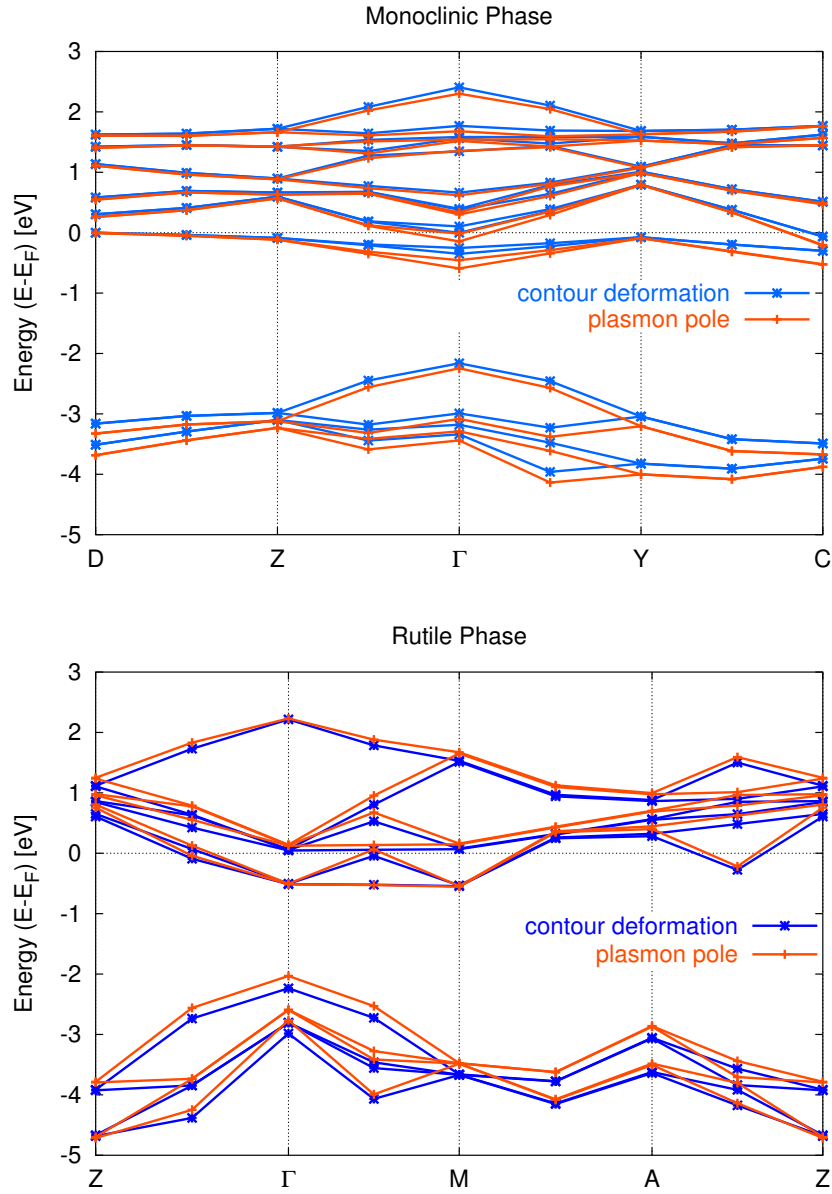


Figure 6.14: Comparison between band structures calculated in the plasmon pole approximation and using the contour deformation integral method, for both the monoclinic (upper panel) and rutile (bottom panel) phases.

6. Vanadium dioxide

convolution integral between G and $W_p = W - v$:

$$\Sigma(\omega) = \frac{i}{2\pi} \int d\omega' e^{i\eta\omega'} G(\omega + \omega') W_p(\omega') \quad (6.1)$$

by making use of the contour integral method (see Eq. (3.68)), which, once converged, doesn't require any further hypothesis on the dynamical behavior of the screened interaction. In the calculation of the contour integral, I sampled the real axis with up to 40 frequencies in the energy range 0-1.5 Ha, and the imaginary axis with 20 frequencies between 0 and 255 eV.

Also in this case, the band structures turn out to be very similar to the ones calculated in the plasmon-pole approximation, especially for the rutile phase (see Fig. 6.14). Remarkably, in the band structure of the monoclinic phase, the band dispersion of both the top valence and bottom conduction bands is reduced in this new GW band structure. In particular, the band dispersion of the top valence is halved with respect to the LDA one. This, moreover, leads to an appreciable reduction of the negative gap up to 0.05 eV. But the band structure is still metallic and its global shape remains qualitatively unchanged. Therefore, it is possible to state that the plasmon-pole approximation has a certain relevance, but it is not the main key to explain the failure of standard GW.

Having excluded all the other possibilities, a last important issue has to be considered with great care. It is the fact that the GW self-energy in the standard procedure is built by making use of LDA eigenvalues and wavefunctions. In particular, since in the case of the monoclinic phase, the LDA band structure is metallic, the screening in W can be dramatically overestimated on a LDA level. And therefore the GW gap corrections can be underestimated rightly for this reason: W entering the self-energy is too weak. This is a general shortcoming of the standard one-shot method [169] that calls for the analysis of the issue of self-consistency in GW calculations.

A simple way to make a first test is to apply a scissor operator to the LDA eigenvalues used in the construction of W . This means that all the conduction bands are rigidly shifted upwards by a quantity Δ in such a way to get an insulating LDA band structure and artificially avoid an overscreened W .

In fact, this is a first attempt to simulate a self-consistency in the quasiparticle eigenvalues. If it were only a matter of overscreening due to the use of LDA eigenvalues, a calculation where the quasiparticle eigenvalues are updated self-consistently, and the wavefunctions are kept at the LDA level, at a certain point should yield an insulating band structure with a screening reduced accordingly. The scissor operator is supposed to produce directly a similar insulating band structure and hence provide indications about the relevance of this self-consistency in the eigenvalues, before doing explicitly the full self-consistent calculation.

6.6 Self-consistent quasiparticle calculations

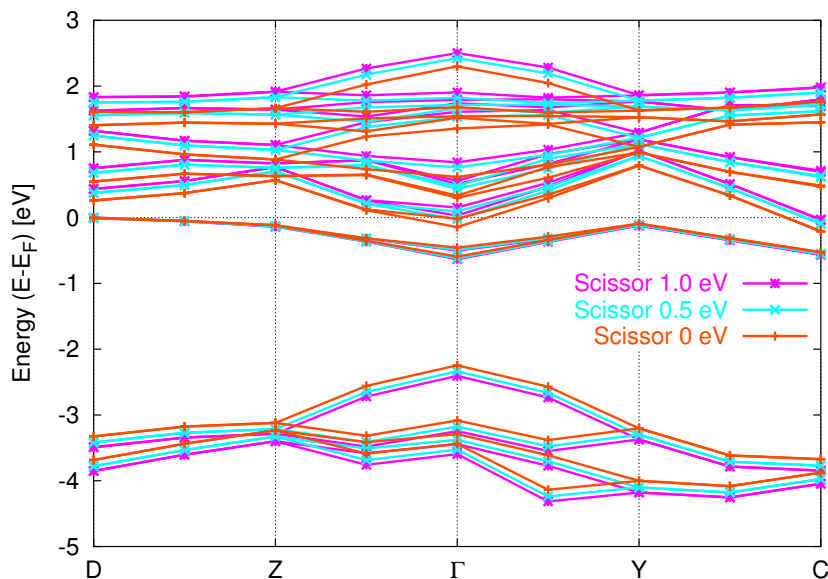


Figure 6.15: Comparison between the GW band structure obtained from the use of original LDA eigenvalues in W ('scissor 0 eV') and the band structures where a rigid upshift Δ has been applied to the conduction LDA bands that enter the screening for W (which is calculated using a plasmon-pole model). Two values: $\Delta=0.5$ eV and $\Delta=1.0$ eV have been used.

Two different values have been tried for Δ : 0.5 eV in one case and 1.0 eV in the other. In both cases the plasmon-pole model has been used in the calculation of the self-energy. But, even with such values, large enough to produce a fictitious insulating LDA band structure, there is not an appreciable gap opening between the bottom conduction and top valence (see Fig. 6.15). The effect of using such an insulating band structure in W is very small: with the largest Δ the conduction states are shifted upwards by only 0.1 eV.

Therefore, the conclusions that can be drawn from this analysis are that the use of LDA eigenvalues and the corresponding metallic band structure in the calculation of W is not the main reason of the failure of the standard GW calculation either. The explanation must be more subtle. This has to be the subject of a further analysis, where the issue of self-consistency, in particular, is directly taken into account.

6.6 Self-consistent quasiparticle calculations

From the previous analysis it turns out that the issue of a self-consistent calculation for the monoclinic phase of VO_2 has to be carefully considered.

6. Vanadium dioxide

This issue is related to the validity of the LDA starting point, a fact that has been shown to be potentially important in materials containing d electrons [169][233][344].

In fact, in the standard approach, G and W are calculated using LDA eigenvalues and wavefunctions. Therefore, a self-consistent calculation where the LDA starting point has no more relevance is important rightly to assess the validity of the quasiparticle band structure paradigm in VO_2 . If even in this case a metallic band structure is produced, this would mean that either it is the GW approximation itself that is not valid in this context and one should think of vertex corrections, or the electronic correlation in VO_2 is so strong to invalidate any possible one-quasiparticle band picture.

I have therefore performed self-consistent quasiparticle calculations, along the scheme implemented by F. Bruneval [3][141]. In this approach, self-consistency is obtained at the COHSEX level (see Sec. 3.5). The result is then used as input for a further perturbative GW calculation. The work of F. Bruneval has shown that this procedure yields results close to quasiparticle self-consistent GW [169] (see Eq. (3.70)), at a lower computational cost.

In the self-consistent COHSEX calculation, the number of plane waves used to represent the wavefunctions has to be increased a lot in order to avoid an error propagation in the self-consistent loop. In the monoclinic phase, for instance, convergence has been achieved only with 11999 plane waves. In order to get the final result, 22 iterations have been necessary: a very high number compared to what one is used to [141]. At each iteration the topmost 26 occupied bands (the $d_{||}$ top valence state and all the O $2p$ bands) and 26 empty states have been recalculated for all the \mathbf{k} points in the irreducible wedge of the Brillouin zone. To avoid undamped oscillations in the density, I have been obliged to use a very small mixing factor, $\alpha = 0.25$, in the density (see Eq. (3.82)). The calculations turned out to be extremely delicate within this respect. In particular, I had to find a way to avoid the occurrence of symmetry breakings and instabilities in the self-consistent loop, that led to a missed respect of the degeneracies in the energies at some \mathbf{k} points. The calculations had to be very accurate, in order to avoid a propagation of errors from one iteration to another.

The upper panel of figure 6.16 shows that the self-consistent COHSEX calculation finally *does* succeed in opening an indirect gap, 0.78 eV, in the band structure of the monoclinic phase. In particular, conduction bands undergo an upshift of almost 1 eV. The COHSEX calculation doesn't modify noticeably their dispersions. As in LDA, the top valence stays at D and the bottom conduction at C.

Perturbative GW starting from COHSEX wavefunctions and eigenvalues has then the effect to reduce a bit the gap, which becomes 0.65 eV. But the global shape of the band structure doesn't change much from the COHSEX results, as one can see looking at the bottom panel of Fig. 6.16. This final result is in very good quantitative agreement with the 0.6 eV experimental

6.6 Self-consistent quasiparticle calculations

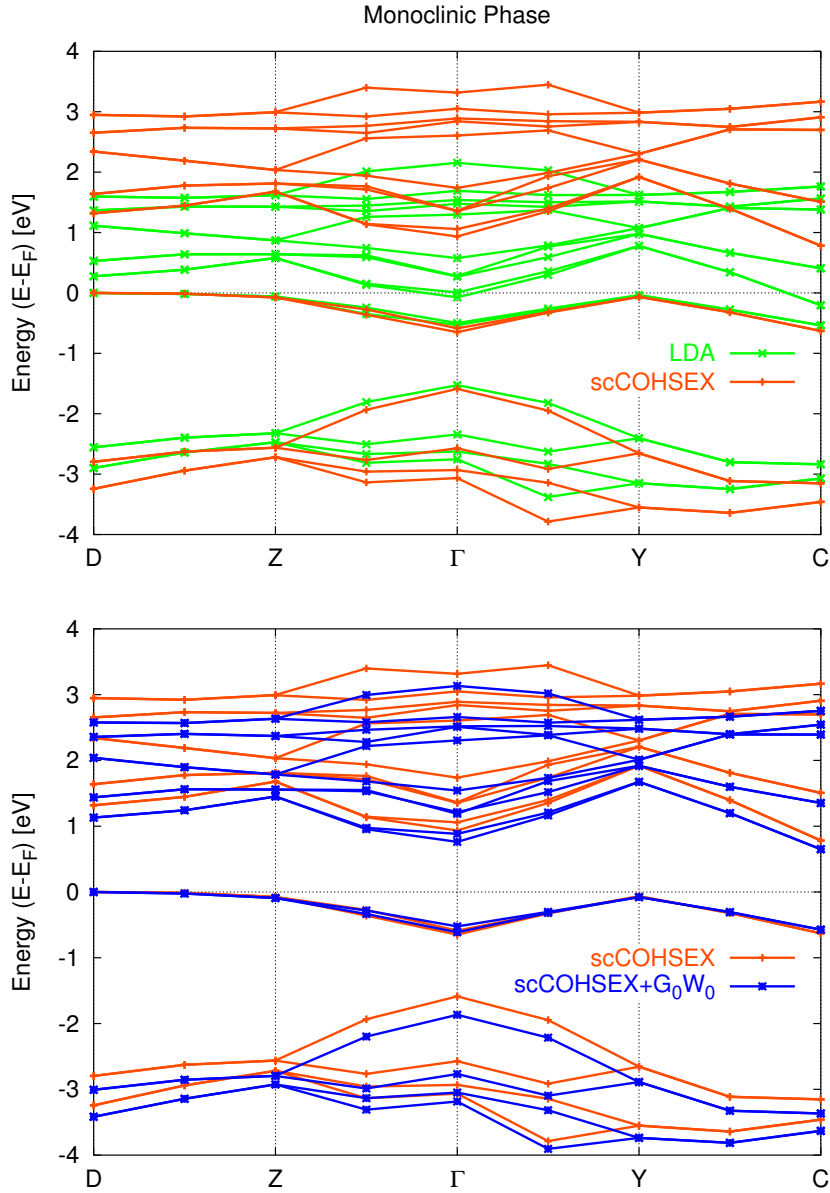


Figure 6.16: (Upper panel) Comparison for the monoclinic phase between LDA and self-consistent COHSEX band structures. In the latter a gap of 0.78 eV is opened. (Bottom panel) Perturbative GW corrections calculated on top of the COHSEX results. They induce small modifications to the band structure. In particular the band gap is reduced to 0.65 eV.

6. Vanadium dioxide

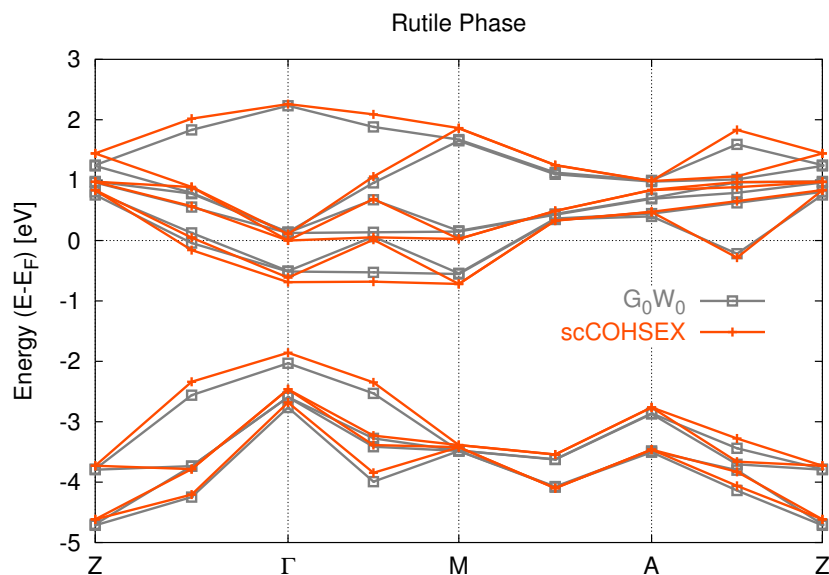


Figure 6.17: Comparison for the rutile phase between the band structures obtained from a standard perturbative GW calculation on top of LDA and a self-consistent COHSEX calculation. They turn out to be very similar.

value.

As expected, in the metallic phase the self-consistent COHSEX corrections are, on the contrary, much smaller and the final band structure is very similar to the results obtained by the perturbative GW on top of LDA (see Fig. 6.17).

Now, of course, the interesting question to which one would like to find an answer is why the self-consistent COHSEX is able to open such a gap in the band structure of the monoclinic VO_2 .

First of all, in order to identify the origin of this result, I have also done a COHSEX calculation where the wavefunctions are constrained to be the LDA ones and only the energies are updated self-consistently. But in this energy-only self-consistent COHSEX scheme, an almost zero gap, 0.02 eV, is found (Fig. 6.18). This is consistent with the calculation where a scissor operator was applied to the LDA eigenvalues entering the screened interaction W and which was not able to open the gap either.

It is therefore the change of the wavefunctions with respect to the LDA ones that turns out to be of utmost importance.

Looking at the angular-momentum projected densities of states in Fig. 6.19, one can immediately realize that the hybridization between O $2p$ and V $3d$ states remains unchanged going from LDA to COHSEX. Besides the splitting between the top valence and bottom conduction states, the other

6.6 Self-consistent quasiparticle calculations

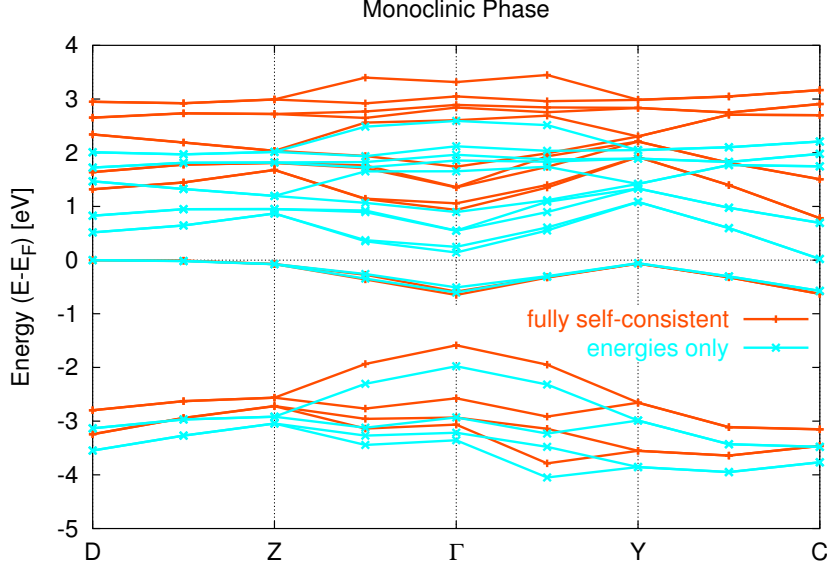


Figure 6.18: Comparison between the fully self-consistent COHSEX calculation of Fig. 6.16 and a COHSEX calculation where the self-consistency is limited to the energies and the wavefunctions are kept at the LDA level. The latter is not able to open an appreciable gap in the band structure of the monoclinic phase.

parts of the COHSEX electronic structure behave as a whole, with rigid shifts, downwards for the occupied group of O $2p$ bands, and upwards for the unoccupied group of t_{2g} bands.

I have then directly considered the projections of the COHSEX wavefunctions over the LDA states. To make the analysis easier, here I take into account only the \mathbf{k} points where the bands are not degenerate. For these \mathbf{k} points the maximum among the values of the projections $|c_{mn}^{\mathbf{k}}|^2$ of each COHSEX wavefunction $\phi_{n\mathbf{k}}^{\text{COHSEX}}$ over all the wavefunctions $\varphi_{m\mathbf{k}}^{\text{LDA}}$ of the LDA basis:

$$\max_m |c_{mn}^{\mathbf{k}}|^2 = \max_m |\langle \varphi_{m\mathbf{k}}^{\text{LDA}} | \phi_{n\mathbf{k}}^{\text{COHSEX}} \rangle|^2 \quad (6.2)$$

provides an indication of the variation of the COHSEX wavefunctions with respect to the LDA ones. If for a given COHSEX wavefunction $\phi_{n\mathbf{k}}^{\text{COHSEX}}$ the maximum is 1, it means that $\phi_{n\mathbf{k}}^{\text{COHSEX}}$ has remained exactly the same as the corresponding LDA wavefunction the self-consistent calculation has started from. If, in addition, the maximum is the diagonal term $|c_{nn}^{\mathbf{k}}|^2$, one can conclude that also the band ordering has not changed. Equivalently, the smallest the maximum of the projections $|c_{mn}^{\mathbf{k}}|^2$ is, the more different from the LDA starting point the COHSEX wavefunction has become.

These values are shown in Fig. 6.20. Most of them are very close to

6. Vanadium dioxide

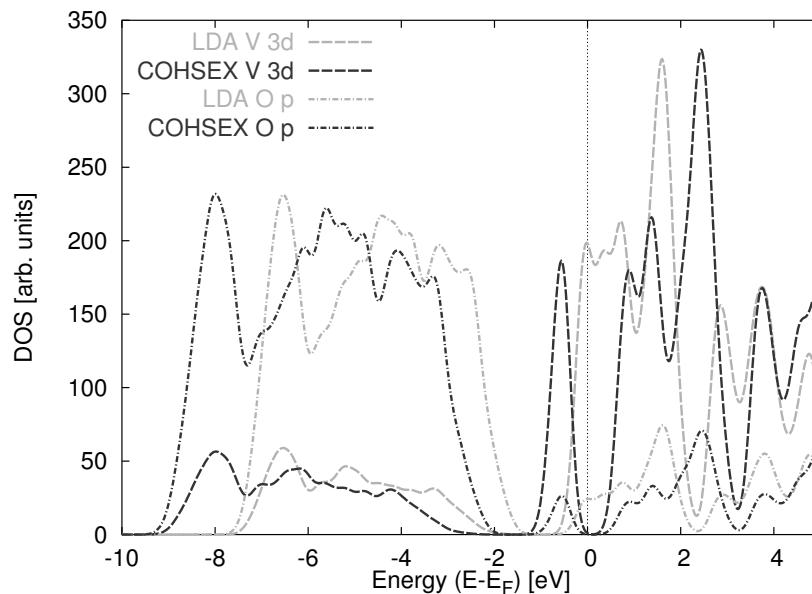


Figure 6.19: Projected densities of states for the monoclinic phase. Comparison between LDA and full-consistent COHSEX results for the O $2p$ and V $3d$ components. The hybridization between the two doesn't change.

1, meaning a complete overlap between COHSEX and LDA wavefunctions. But there is a not negligible number of them that are much smaller than 1, demonstrating a considerable change of the wavefunctions. For instance, in simple bulk systems the overlap between LDA and GW wavefunctions has been claimed to be greater than 0.999 by the first *ab initio* GW calculations [131].

This analysis shows that there is indeed a variation of the wavefunctions, but the mixing occurs among wavefunctions of the same kind. This also explains why the O $2p$ – V $3d$ hybridization doesn't change much, as shown by Fig. 6.19.

In particular, in VO_2 the largest number of small overlaps turns out to be for the top valence and bottom conduction wavefunctions (around $n=50$ in Fig. 6.20). These are hence the wavefunctions that change most. Since they play the major role in the opening of the band gap, they worth a further study.

Therefore, for these states I have plotted the LDA wavefunctions in real space and analyzed their variations in the self-consistent COHSEX calculation. In order to make this study simpler, in the upper panels (a)–(b) of Fig. 6.21 I rather consider the two partial electronic densities (which are

6.6 Self-consistent quasiparticle calculations

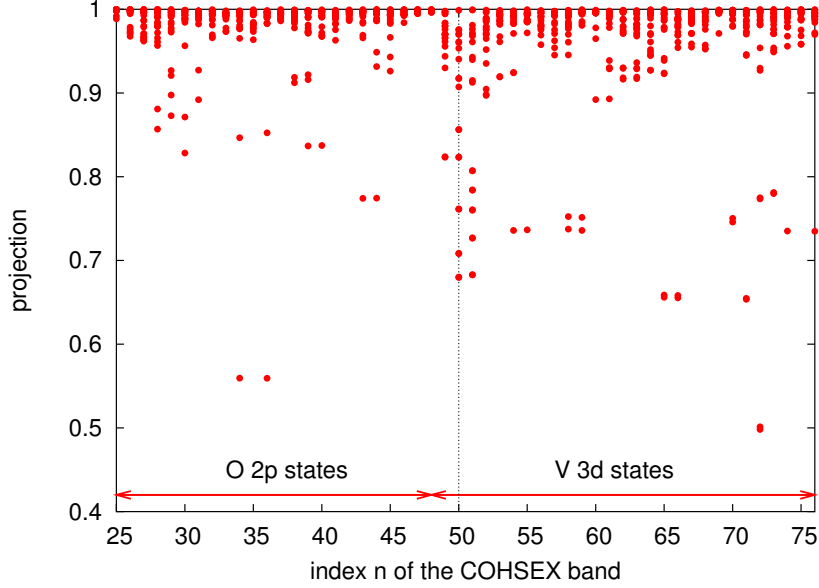


Figure 6.20: For each of the COHSEX wavefunctions $\phi_{n\mathbf{k}}^{\text{COHSEX}}$, a red dot indicates the maximum value of the projection of COHSEX wavefunction over all the LDA states $\varphi_{m\mathbf{k}}^{\text{LDA}}$ of the basis (see Eq. (6.2)). At each index n the different dots correspond to the different \mathbf{k} points that have been considered. Most of the projections are close to 1, but many of them are much smaller, showing a large change of the COHSEX wavefunctions with respect to the LDA ones. The vertical line for $n = 50$ separates occupied from empty states.

summed over all the \mathbf{k} points):

$$\begin{aligned}\rho_{\text{tv}}^{\text{LDA}}(r) &= \sum_{\mathbf{k}, i \in \text{tv}} |\varphi_{i\mathbf{k}}^{\text{LDA}}(r)|^2 \\ \rho_{\text{bc}}^{\text{LDA}}(r) &= \sum_{\mathbf{k}, i \in \text{bc}} |\varphi_{i\mathbf{k}}^{\text{LDA}}(r)|^2\end{aligned}\quad (6.3)$$

for the top valence (tv) and bottom conduction (bc) states.

A confirmation of the localized character of these wavefunctions is clearly found. Both are mainly V 3d states. In particular, the top valence shows to be the d_{\parallel} state, with a strong polarization along the c -axis (vertical direction in the pictures), due to its V-V bonding character. This is clearer if one considers the periodic images along the c -axis of the unit cell represented in Fig. 6.21 (a). The variations due to the COHSEX self-consistency are an almost completely specular mixing between these two states. The spatial regions where the top valence ρ_{tv} increases (yellow surfaces in Fig. 6.21 (c)) correspond to the regions where the bottom conduction ρ_{bc} decreases (purple surfaces in Fig. 6.21 (d)) – and vice versa. The global effect is an

6. Vanadium dioxide

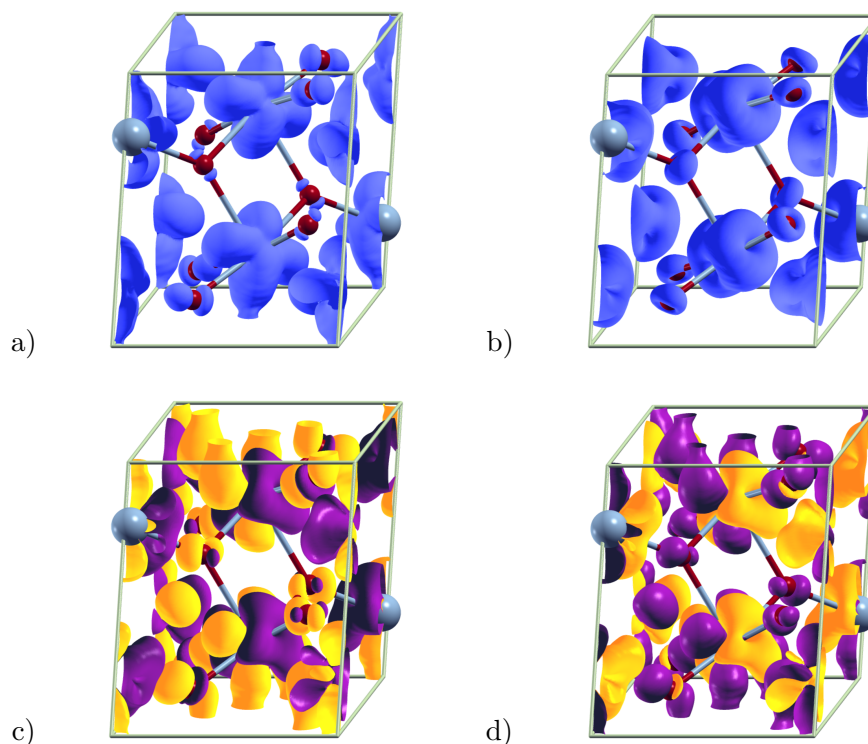


Figure 6.21: (Upper panels) Isosurfaces of LDA densities (see Eq. 6.3) for top valence (a) and bottom conduction (b) states. The isosurfaces are traced at a value $\rho^{\text{LDA}} = 0.005 \text{ a.u.}^{-3}$. (Bottom panels) Differences with respect to the COHSEX wavefunctions $|\rho^{\text{COHSEX}} - \rho^{\text{LDA}}| = 0.0005 \text{ a.u.}^{-3}$. Yellow surfaces are for positive variations and purple for negative ones. For a better interpretation of the pictures one should consider also the periodic images along the c -axis of the unit cell represented here.

enhancement of the anisotropy of the top valence state, which has a stronger $d_{||}$ character, becoming even more polarized along the c -axis.

This is the key that explains the failure of standard GW (upper panel of Fig. 6.12) in opening the gap and reproducing the photoemission spectrum for the insulating phase of VO_2 . At the same time, it provides a justification to the insufficiency of the energy-only self-consistent COHSEX calculation (see Fig. 6.18).

The opening of a gap is hence due to a subtle effect involving the wavefunctions immediately below and above the Fermi level. Their modifications induce large variations in the GW self-energy. The exchange term (X in Tab. 6.8) is a valid reference to estimate the effect of these spatial changes on the self-energy corrections. Since it doesn't depend on the energies, its variations reflect directly the spatial modifications of the wavefunctions. From LDA to COHSEX the exchange term is increased – in absolute value, the

6.7 Comparison with experiments and previous results

k point	X from LDA		X from COHSEX	
	top val	bot con	top val	bot con
D	-21.350	-15.715	-23.077	-14.650
C	-21.441	-14.892	-22.594	-13.979
Γ	-21.514	-15.498	-22.704	-14.496

Table 6.8: Expectation values of the Fock exchange term (in eV), calculated using LDA or COHSEX wavefunctions, for the top valence and bottom conduction states for a selection of representative \mathbf{k} points.

exchange is always negative – for the top valence and is reduced for the bottom conduction states (see Tab. 6.8). These differences are partially compensated by a change of the Hartree and correlation terms in the self-energy. The total effect of the variations of these three terms induces the 0.65 eV gap between the top valence and the bottom conduction, in good agreement with the experimental value of 0.6 eV [293].

6.7 Comparison with experiments and previous results

The previous analysis has shown the importance of performing self-consistent quasiparticle calculations. In the monoclinic phase of VO_2 , the Kohn-Sham LDA wavefunctions turn out to be a bad approximation of quasiparticle wavefunctions. This explains the failure of standard GW, which is built on top of LDA. COHSEX wavefunctions are instead a much better approximation to the GW wavefunctions, as it has been demonstrated also by F. Bruneval *et al.* in the case of bulk silicon, argon [141] and cuprous oxide [233].

As for VO_2 , in the insulating phase the system becomes more electronically one-dimensional with a stronger polarization along the c -axis and this leads to the gap opening. If this orbital redistribution is underestimated, as it happens in LDA, the system remains metallic. These observations are in agreement with the experimental findings from X-ray absorption spectra [293][314], which have shown a large anisotropy in the spectra of the insulating phase (see Fig. 6.6).

The gap is hence not a matter of treating strong electronic correlations beyond LDA. LDA+U, with e.g. $U=4.2$ eV [345], is indeed able to yield for the insulator a band gap in good agreement with experiment [346][347]. This result is interpreted as a demonstration of the important role played by local static electronic correlations in the monoclinic phase. But, on the other hand, LDA+U for a too high U yields a magnetic insulator and, in any case, is not capable to describe consistently the metallic phase. The failure

6. Vanadium dioxide

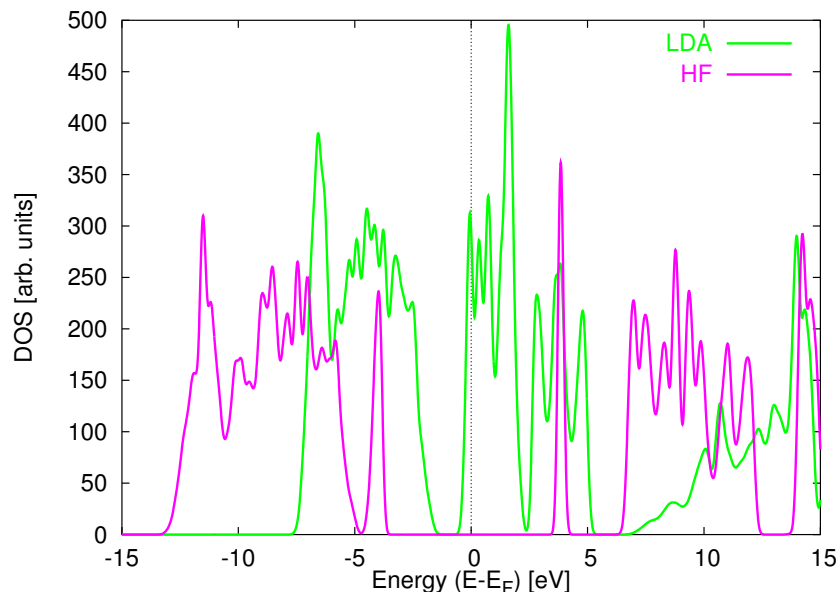


Figure 6.22: Comparison between LDA and self-consistent Hartree-Fock densities of states for the monoclinic phase of VO_2 . While the LDA DOS is metallic, the Hartree-Fock DOS shows a huge gap.

of LDA+U to reproduce the metallic character of the rutile phase has been explained [347] as caused by an overestimation of the electronic localisation as a result of the mean-field evaluation of the on-site Coulomb repulsion.

KS-DFT is not meant to yield quasiparticle band structures. And the fact that the monoclinic VO_2 has a metallic Kohn-Sham band structure in LDA is not related to strong correlation, as it is not either in the case of NiO [135][348] or YH_3 [349]. On the other side, DFT is an exact theory for the ground state and LDA is a good approximation also in this case. In particular, it provides lattice parameters in good agreement with experimental data (see Tab. 6.5).

Electronic correlation has however to be adequately treated. A Hartree-Fock calculation, where no correlation at all is taken into account, yields an insulator with the huge gap of 7.6 eV. As illustrated in Fig. 6.22, performing a self-consistent Hartree-Fock calculation the electronic structure changes completely with respect to LDA. Concerning the occupied states, the O $2p$ states result downshifted by several eV and their bandwidth becomes much larger. Moreover, the LDA gap between the O $2p$ and the $d_{||}$ band is closed. On the contrary, a gap is opened between the bottom conduction band and the rest of the t_{2g} states, which are raised by some eV. The resulting density of states is confuted by the experimental evidences.

The only difference between Hartree-Fock and GW is the screening of the

6.7 Comparison with experiments and previous results

Coulomb interaction. In particular, in the GW framework, W is screened at the RPA level. Therefore, the RPA turns out to be an already sufficient approximation to deal with electronic correlation in the description of the one-quasiparticle properties of VO_2 .

On the other hand, the frequency dependence of the self-energy is not very important for the determination of the quasiparticle energies. The completely static COHSEX approximation is already able to provide a correct qualitative description of the phase transition. In fact, the dynamical GW corrections on top the COHSEX results are really small (see the bottom panel of Fig. 6.16). This observation is in agreement with the conjectures of the DMFT studies [345][350][351]. In particular, Tomczak *et al.* [350] have considered the DMFT self-energy in a d_{\parallel} bonding-antibonding basis. They have shown that bonding and antibonding components are almost constant in frequency in the occupied and unoccupied parts of the spectrum, respectively. Their analysis is confirmed by the present COHSEX results.

However, whereas a static approximation is sufficient, the self-energy has in any case to be spatially nonlocal. In the metallic phase static correlations are negligible, as a consequence of a weak orbital polarization among t_{2g} states (in other words: the metal is electronically isotropic) [345]. The metal is correctly obtained in the framework of single-site DMFT [345][352][353], where dynamical correlations, beyond the static LDA+U model, are taken into account. On the other side, standard single-site DMFT turns out to be incapable to describe the insulating phase of VO_2 . With a low U no insulating phase is obtained. With a high U ($U > 5$ eV) an insulator is achieved, but at the price of creating also local magnetic moments, which are actually absent in the insulating VO_2 . Only calculations based on a cluster extension of DMFT [292] managed to obtain both phases consistently in a single picture. Contrarily to single-site DMFT, which is limited to a local description of V atoms, Biermann *et al.* [292] in their calculation considered the vanadium dimers as the key unit for the identification of the DMFT impurity, introducing in such a way a \mathbf{k} dependence in the DMFT self-energy. Using a value for U of 4 eV, they have been able to reproduce the main features of the photoemission spectra [293] of both phases. The failure of standard single-site DMFT is essentially due to its incapability to catch this fundamental spatial property of the self-energy. The nonlocality of Σ in the insulating VO_2 is in fact tightly linked to the strong spatial polarization of the V $3d$ states around the Fermi level.

The results presented here show that, once a self-consistent calculation is carried out, the band quasiparticle paradigm is still valid also for VO_2 . Remarkably, in order to obtain a quantitative agreement with experiments it is crucial to take into account the degrees of freedom beyond the t_{2g} orbital subset, to which DMFT calculations [292] are limited. In fact, a parameter-free COHSEX calculation where the self-consistency is limited to the t_{2g} still opens a gap, but only to 0.36 eV.

6. Vanadium dioxide

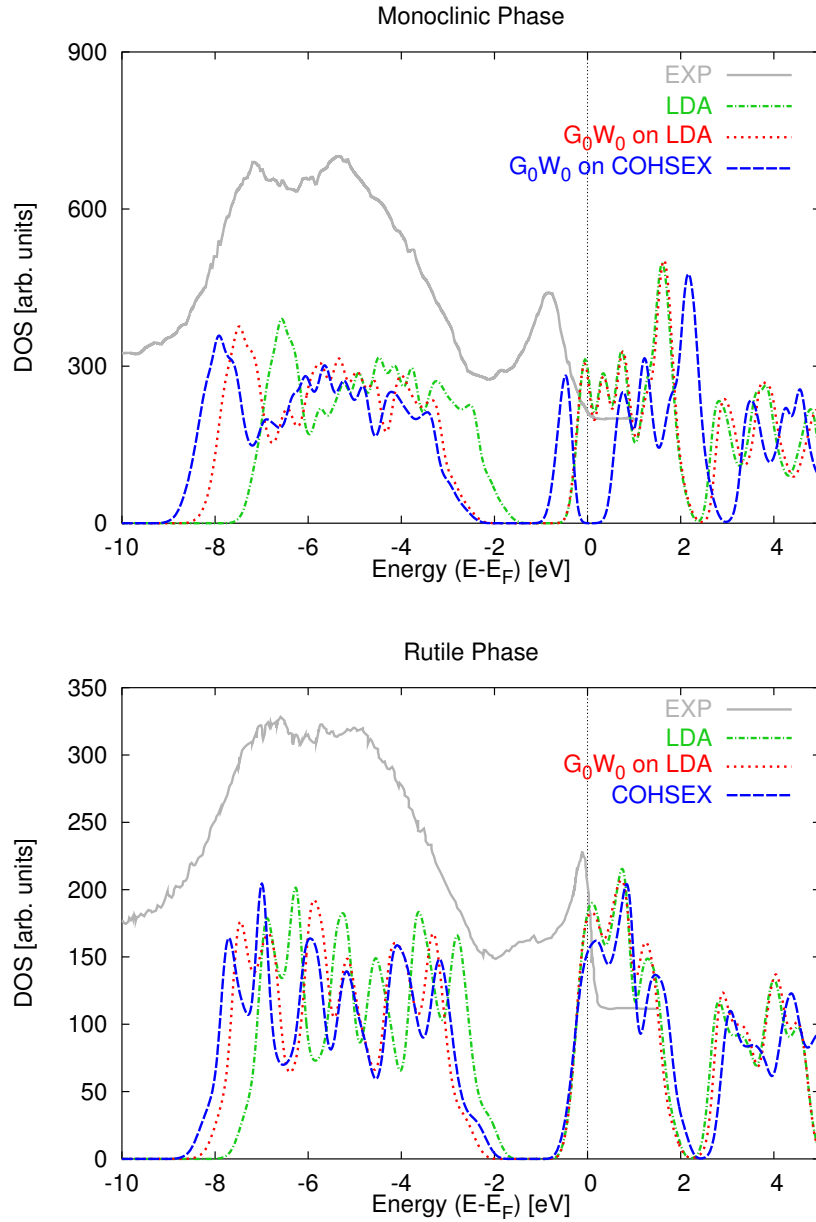


Figure 6.23: Comparison of the experimental photoemission spectra of Koethe *et al.* [293] (see also Fig. 6.4) with the densities of states calculated with different approximations for the monoclinic phase (upper panel) and the rutile (bottom panel).

6.7 Comparison with experiments and previous results

The full self-consistent calculations are in very good quantitative agreement with the photoemission spectra for both the insulating and the metallic phases, as shown by Fig. 6.23. In this comparison different factors have to be taken into account. From the theoretical point of view, a density of states is meant to reproduce only the quasiparticle properties of the system. For instance, finite lifetimes of quasiparticle excitations, that reveal quasiparticle interactions or collective excitations, are not included in this description. From the experimental point of view, the experiment has been done at a temperature much above $T = 0$ K. To roughly simulate the effects of the temperature, a Gaussian broadening of 0.15 eV has been applied to the plot of the densities of states. Moreover, as already discussed in Sec. 6.3.1, in the interpretation of the X-ray measurements, besides the experimental resolution, the fact that the photoelectron cross section is much larger for the V $3d$ than for the O $2p$ states has to be properly considered.

In any case, figure 6.23 clearly demonstrates that the final results (blue dashed lines in Fig. 6.23) are able to reproduce both the positions and the bandwidths of the different groups of peaks of the experimental spectrum for both the monoclinic and the rutile phases. In the energy range corresponding to the O $2p$ some discrepancies still remain. In both phases in the photoemission spectrum two main peaks are visible. On the contrary the theoretical densities of states are characterized by three main groups of peaks. But, considering the $3d$ projected density of states of Fig. 6.19, it is possible to see that the peak at the lowest binding energy is largely removed in that spectrum. These observations are confirmed also by the analysis of X-ray emission spectra (see Fig. 6.5) and by a comparison with UPS spectra [271], where this strong decrease in intensity around the top of the O $2p$ bands is instead absent. Moreover, the absolute position of the $d_{||}$ peak in the insulating phase is somewhat underestimated by the final calculations, but the $d_{||}$ bonding-antibonding separation, evaluated 2.5 eV, is in very good agreement with the experimental data [293][319]. Also in cluster-DMFT [292] the bonding $d_{||}$ peak is found at the same position as the COHSEX+GW result. In general, the comparison with the quasiparticle features of the spectral functions calculated in cluster-DMFT is very good, even though the latter study is limited only to the t_{2g} states around the Fermi level and contains adjustable parameters. Also the band structures, although calculated in completely different manners, compare pretty well. Discrepancies are limited to few details, like the dispersion of the topmost t_{2g} which is flatter in cluster DMFT [350][351] than in the plot of Fig. 6.16.

The same good agreement is found also with the model GW calculation performed by Continenza *et al.* [340] for the insulating phase. In their approach, the Gygi-Baldereschi [148] model for the screened interaction W and the self-energy has been used (see Sec. 3.3.2). They have been able to reproduce correctly the insulating character of the monoclinic phase, also thanks to the experimental information introduced in the model screening

6. Vanadium dioxide

function. In their calculation, the details of the band structure are somewhat different, since they used the theoretical lattice structure of Wentzcovitch *et al.* [286], but the differences remain of the same size as what has been already found at LDA level (see Fig. 6.9). Also in their case the GW corrections don't affect much the shape of the bands (see the upper panel of Fig. 6.16). Their qualitative picture agrees well with the present self-consistent quasiparticle calculations. The results illustrated in this section represent hence a fully parameter-free validation of their model calculations.

The bottom panel of Fig. 6.23 shows that the experimental spectrum for the metallic phase is already well reproduced by the LDA density of states. The task in this case for LDA was easier. The metal is electronically more isotropic than the insulator, and LDA and quasiparticle wavefunctions are much more similar. Further GW calculations induce only small changes, still improving the agreement with the experiment, especially concerning the position of the O $2p$ bands.

However, there is an interesting feature in the experimental photoemission spectrum of the metallic phase that is beyond the quasiparticle description. It is the satellite at a binding energy of 1.3 eV, which is interpreted in the context of DMFT models as lower Hubbard band [292][345]. A proper description of this feature would require the calculation of the complete spectral function $A(\omega)$. This calculation is extremely demanding in VO₂, especially if one is interested in features beyond quasiparticle properties. This kind of study in fact requires a higher degree of convergence in the various parameters and a calculation of the correct frequency dependence of Σ , beyond any plasmon-pole model. It turned out not to be feasible. Moreover, the GW approximation may not be sufficient for the description of the satellite [35].

Nevertheless, the physical interpretation of this satellite has been possible thanks to a calculation of the electron energy-loss spectrum. This will be the subject of Sec. 6.8.

6.7.1 X-ray absorption spectra

In the independent-particle theory X-ray absorption spectra provide a direct information about the density of unoccupied states, projected on atomic states according to dipole selection rules (see Sec. 1.2.2). In Fig. 6.24 I have compared the experimental O K XAS edge of Koethe *et al.* [293] (see also Fig. 6.6) with the calculated O p densities of states.

As already shown by previous calculations [271], one finds that at low energy the LDA DOS is in pretty good agreement with the experimental spectra. At high energy the agreement is less favorable, but, once the main features of the experimental spectra are better resolved [271], the agreement is still fair. The quasiparticle COHSEX corrections in the insulator instead induce a shift of the calculated spectra to higher energies. In this way the

6.7 Comparison with experiments and previous results

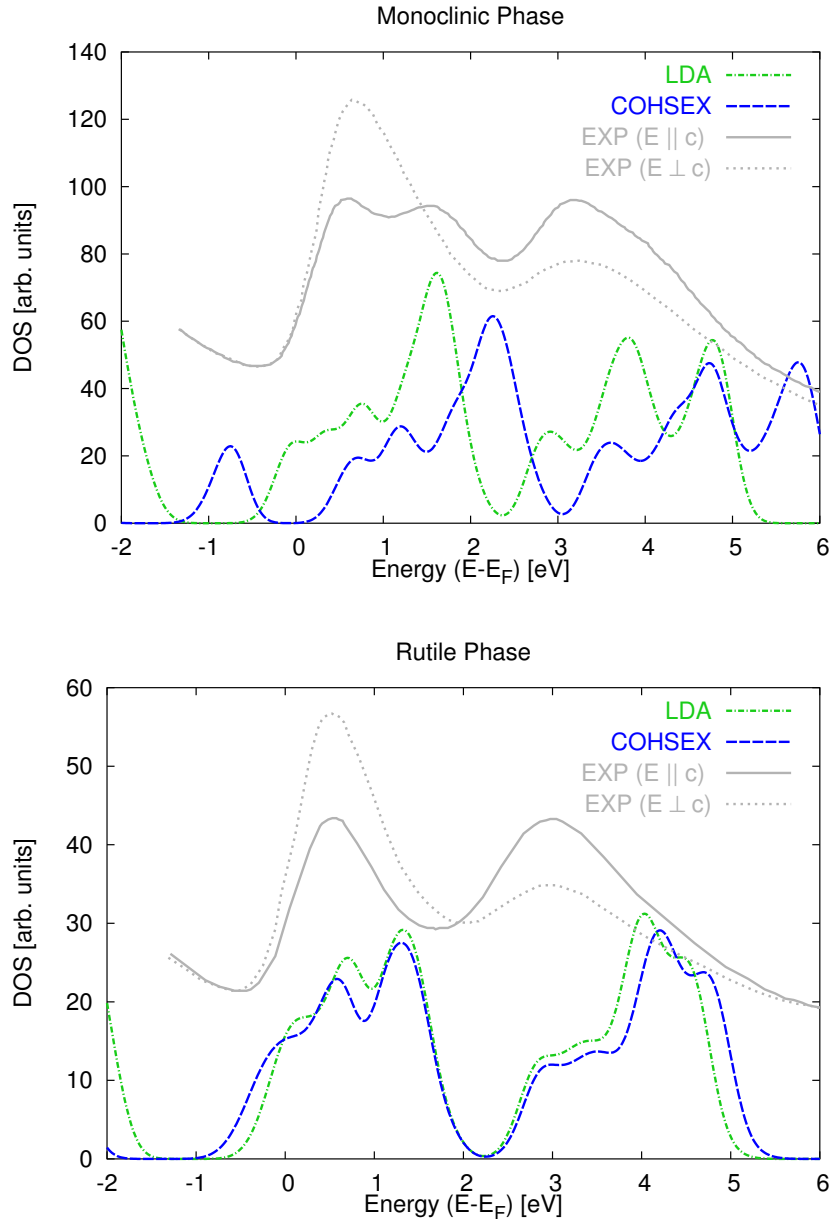


Figure 6.24: Comparison of the experimental X-ray absorption spectra at the O K edge of Koethe *et al.* [293] (see also the right panel of Fig. 6.6) with the O $2p$ projected densities of states calculated with different approximations for the monoclinic phase (upper panel) and the rutile (bottom panel).

6. Vanadium dioxide

COHSEX O p DOS results blueshifted with respect to the experimental XAS.

In fact, neither the ground-state LDA DOS nor the one-quasiparticle COHSEX DOS are in general suitable to describe X-ray absorption spectra. One should rather consider the presence of the (screened) core-hole [354], together with the excited electron in the appropriate conduction state. In the calculation of the X-ray absorption spectra one should hence take into account the local fields and the core-hole (excitonic) effects [45][355][356][357]. The fact that the LDA DOS is in good agreement with the experiment is probably due to a cancellation between quasiparticle corrections and excitonic effects, as these results demonstrate.

The calculation of these spectra, where the excitonic effects are properly taken into account, could be indeed another way to verify the results illustrated in the previous sections, but the inclusion of the core hole is computationally demanding.

6.8 Calculation of electron energy-loss spectra

In the final paragraph of this chapter I am going to deal with the calculation of the valence electron energy-loss spectrum of VO₂ for both phases. After a brief discussion about some issues concerning the method employed in the calculations, I will compare the results with the experimental spectra measured by Abe *et al.* [343]. The analysis of the EELS at low frequencies will be relevant in particular for the interpretation of the satellite in the photoemission spectrum of the metallic phase.

6.8.1 Methodological issues

Electron energy-loss spectra have been calculated in the framework of the time-dependent density-functional theory, using the Dp code [358]. They can be obtained from the calculation of ϵ^{-1} (see Eq. (5.36)), where $\epsilon^{-1} = 1 + v\chi$ and χ is the solution of the linear-response TDDFT Dyson equation (see Eq. (5.71)): $\chi = \chi_{KS} + \chi_{KS}(v + f_{xc})\chi$.

In the energy range 0-60 eV convergence has been reached with 300 bands represented by 7501 plane waves for the insulator, and 200 bands with 4003 plane waves for the metal. When local-field effects are included in the calculation, a matrix of order 301 is inverted for the monoclinic phase and order 201 for rutile. A $4 \times 4 \times 4$ and a $6 \times 6 \times 6$ shifted grids of \mathbf{k} points have been used respectively for the insulating and metallic phases.

Two methodological issues will be discussed in this paragraph. I will consider only the case of the monoclinic phase because for the rutile analogous results are found.

The first issue concerns the effect of the different pseudopotentials that include or not the vanadium semicore states $3s$ and $3p$ in valence (see Sec.

6.8 Calculation of electron energy-loss spectra

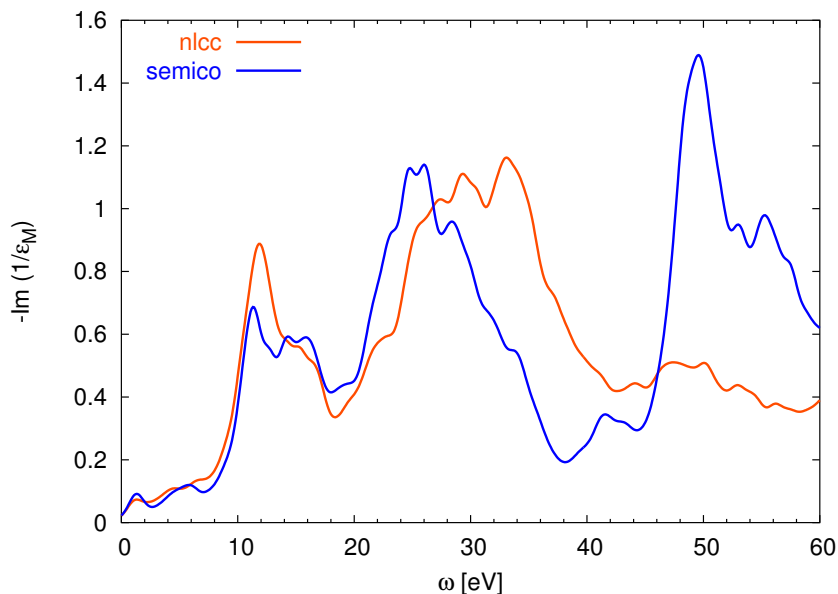


Figure 6.25: Comparison of EELS spectra at vanishing scattering vector \mathbf{q} for the monoclinic phase of VO_2 calculated with (‘semico’) or without (‘nlcc’) the inclusion of V semicore states $3s$ and $3p$ in valence.

6.4.2). Fig. 6.25 shows a comparison between the calculations effectuated with the ‘semico’ pseudopotential, where the semicore states are explicitly in valence, and with the ‘nlcc’ pseudopotential, where the effect of semicore states is treated indirectly via nonlinear core corrections. As expected, new structures appear at high loss energies ($E > 40$ eV) when the spectrum is calculated with the ‘semico’ pseudopotential. Since they correspond to excitations of V $3p$ states, it is normal that their excitations are absent in the case where they are kept frozen in the core. More surprising is the fact that the two spectra have quite different shapes even at lower energies ($20 \text{ eV} < E < 40 \text{ eV}$). This result is worth a further analysis.

Therefore, in Fig. 6.26 I have compared the real and imaginary parts of the dielectric function calculated with the two pseudopotentials. In the spectrum for ϵ_2 the peak due to the V $3p$ states is clearly visible with the ‘semico’ pseudopotential and absent with the ‘nlcc’ one. The rest of the spectra for ϵ_2 are instead pretty similar. So, it is the real part of ϵ_M that makes the difference in the EELS spectra. The fact that in one case ϵ_2 has one more peak implies, for the Kramers-Kronig relations, that also ϵ_1 has to follow the same behavior. While with ‘nlcc’ pseudopotential ϵ_1 is quite flat for $E > 30$ eV, with the ‘semico’ pseudopotential ϵ_1 continues to increase even beyond 30 eV. This behavior determines also a different EELS spectrum. The relevant conclusion that can be drawn from this analysis is

6. Vanadium dioxide

hence that one should use the pseudopotential that includes semicore states, even if the interest were limited only to the valence excitations ($E < 30$ eV). In fact, using the ‘nlcc’ pseudopotential would yield an overestimation of the valence plasmon energy of several eV.

L. Dash *et al.* [359] have carried out a calculation of the energy loss spectra for other transition metal oxide systems. In Cu_2O the inclusion of Cu semicore states in valence doesn’t affect the spectrum up to 60 eV. On the contrary, in TiO_2 a situation similar to VO_2 is found, even though in that case the effects are less pronounced. Also in the EELS spectrum of TiO_2 , a new peak due to the $3p$ states appears and also the plasmon peaks at lower energies are shifted by some eV.

The spectra reported in Fig. 6.25 are obtained in TDLDA. One of the advantages of theoretical spectroscopies is that in the calculation we can separate the different parts of the interaction and consider their effects one by one. In particular, in the case of the EELS of VO_2 , in Fig. 6.27 the effects of the different terms of the TDDFT Dyson equation, $\chi = \chi_{KS} + \chi_{KS}(v + f_{xc})\chi$, are shown (from now on, I’ll consider only results obtained with the ‘semico’ pseudopotential). The calculation based on an independent-particle picture ($\chi = \chi_{KS}$, i.e. $v = f_{xc} = 0$) would yield a huge overestimation of the V $3p$ peak (‘NLF’ curve in Fig. 6.27). The local fields have in fact a very large effect on that peak, because the V $3p$ states are very localized and polarizable. Local fields play a fundamental role in the calculation of EELS, especially in the semicore region. On the contrary the effects due to the exchange-correlation kernel are less important and limited to the semicore peak where local fields have the largest impact. The ‘RPA’ (where $f_{xc} = 0$) and ‘TDLDA’ curves in Fig. 6.27 are almost indistinguishable up to 40 eV.

Similar relevant local-field effects for the semicore plasmon have been found also in ZrO_2 [333] and TiO_2 [246]. The general conclusion about EELS calculations in TDLDA at vanishing \mathbf{q} has been demonstrated many times [2][221].

In the experiment the observed intensity depends on the collection angle β of the spectrometer. In the calculations, instead, the spectrum is obtained only at a certain scattering vector \mathbf{q} . In order to compare the calculated spectrum with the experimental result, one should proceed to a proper integration over the angle β . For instance, in the rutile phase at vanishing \mathbf{q} , once calculated the dielectric functions for \mathbf{q} parallel or perpendicular to the c -axis, one would have [246][333]:

$$I(E) \propto -\pi \text{Im} \{ \epsilon_{\perp}^{-1} \ln [1 + (\beta^2 \epsilon_{\perp} / \theta_E^2 \epsilon_{\parallel})] \} \quad (6.4)$$

where $\theta_E = mE/k_0^2$ (m is the relativistic mass of the impinging electron and k_0 the norm of its wave vector). Similar expressions apply in the monoclinic phase and at finite \mathbf{q} .

Since in this case the experimental collection angle β is not known [343], it is not possible to make a proper comparison with the experimental spectra

6.8 Calculation of electron energy-loss spectra

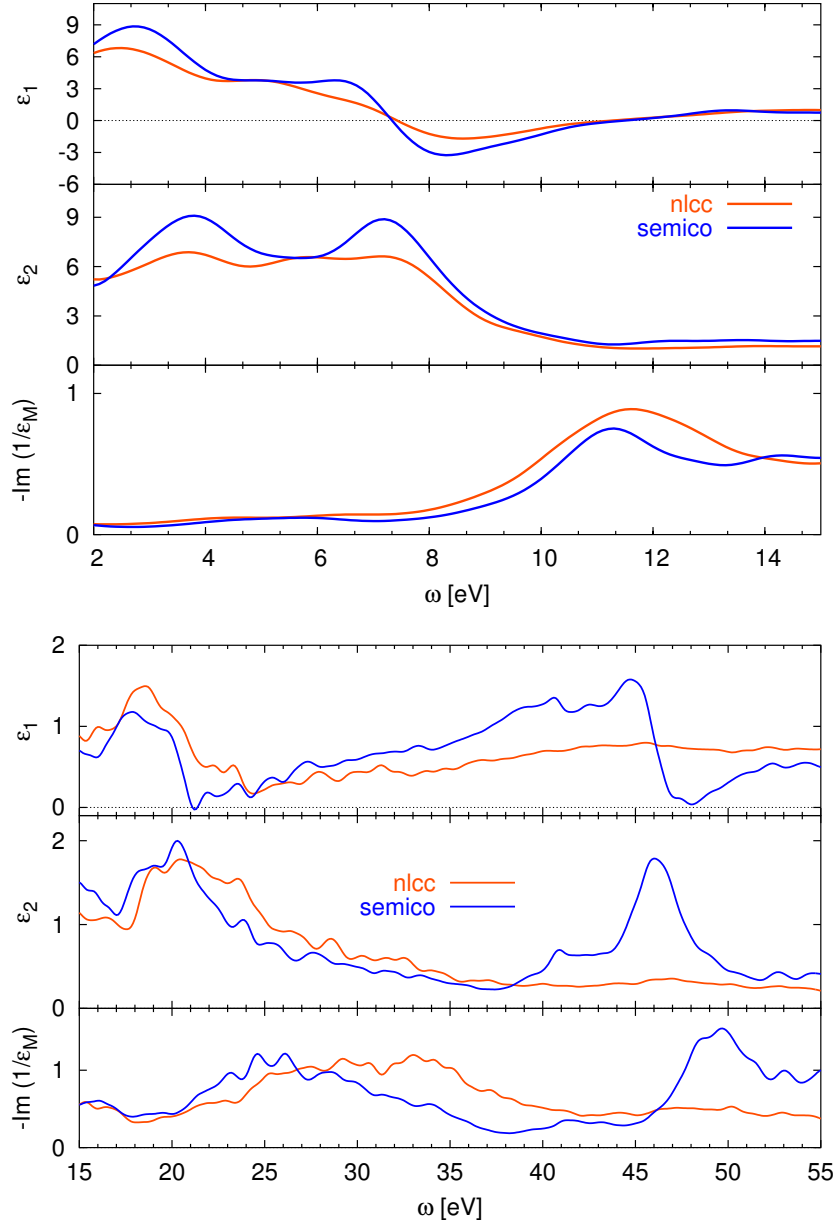


Figure 6.26: Analysis of the different behaviors of the real and imaginary parts of the dielectric function, $\epsilon_M = \epsilon_1 + i\epsilon_2$, that determine the EELS spectra (bottom panel), calculated with or without V semicore states in valence (see also Fig. 6.25).

6. Vanadium dioxide

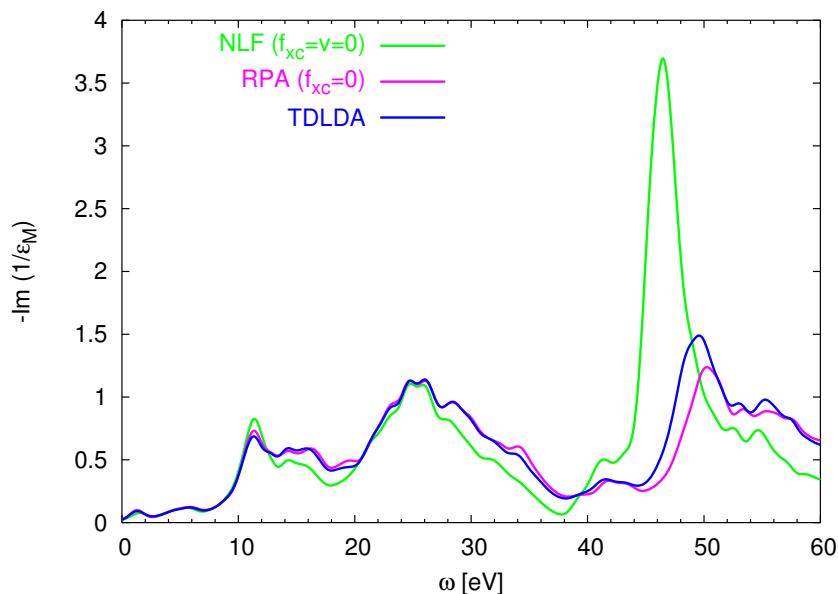


Figure 6.27: For the monoclinic phase, the TDLDA spectrum (where $f_{xc} = f_{xc}^{ALDA}$) is compared to the spectra obtained in RPA (where $f_{xc} = 0$, but local field effects are taken into account) and neglecting also local fields (that is $v = f_{xc} = 0$).

regarding the intensities of the peaks. Yet, an analysis of their positions is possible (see Fig. 6.28).

The agreement for both phases is in general very good and improves at high energies where the details of the band structures become less important. The peak in the loss spectra derive either by zeros of ϵ_1 that, in case also ϵ_2 is small, determine plasmon resonances, or by structures in ϵ_2 due to interband transitions. The attribution of the character of the different peaks turns out to be the same in the experimental and theoretical spectra and confirms the analysis of Abe *et al.* [343]. The peaks at about 5 eV, 43 eV and 52 eV are assigned to the transitions: O $2p \rightarrow$ V $3d$, and (for the latter two peaks) V $3p \rightarrow$ V $3d$. The peaks at 10 eV and around 25 eV are instead due to plasmons, since they are in correspondence to zeros of ϵ_1 .

6.8.2 The satellite in the photoemission spectrum of the metal

The energy loss spectra for the two phases are very similar at energies of some tenths of eV. The fingerprint of the transition can be instead found at lower energies, where the change of band structures around the Fermi energy clearly shows up. In particular in the experiment [343] a sharp peak is observed at 1.2 eV in the spectrum of the metallic phase and it is absent

6.8 Calculation of electron energy-loss spectra

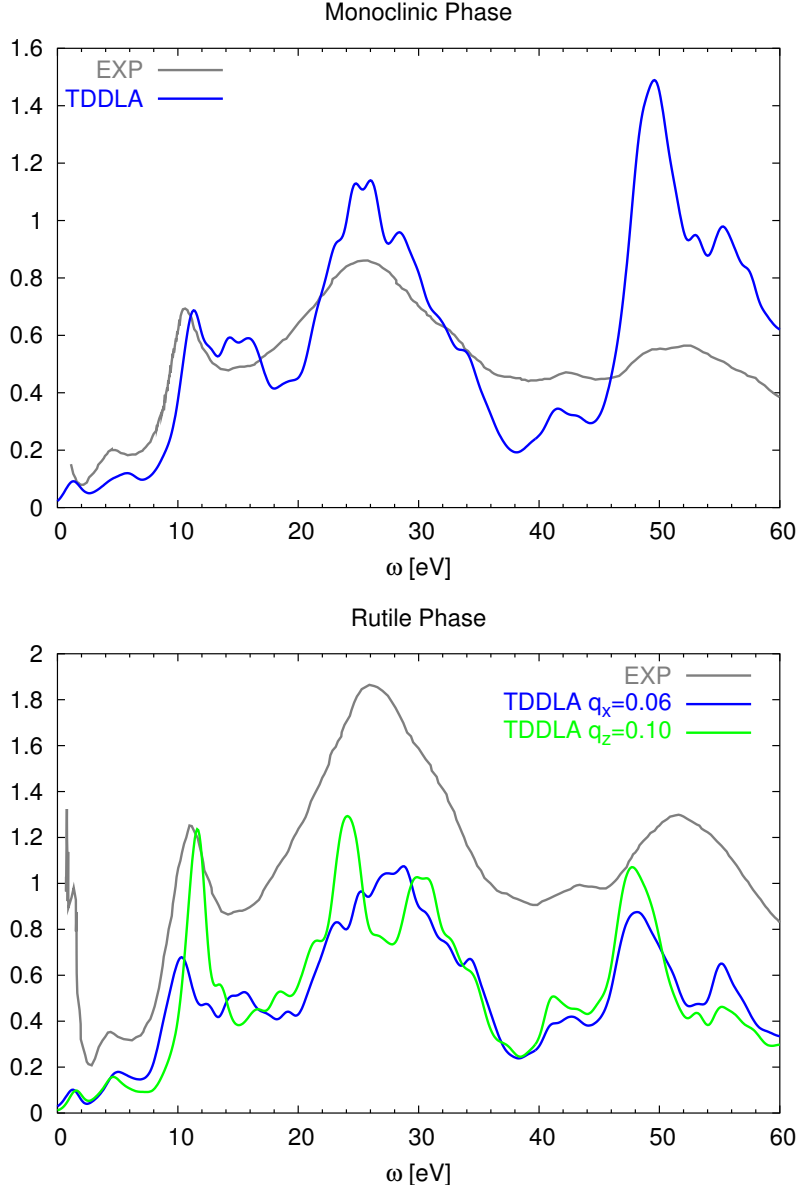


Figure 6.28: Comparison of TDDLA calculation with the experimental spectrum of Abe *et al.* [343]. In the experiment the integrated loss function (see Eq. (6.4)) is measured. Instead, in the calculation the integration over the collection angle β has not been done. Therefore the comparison is limited to the peak positions (the intensity is in arbitrary units). The agreement is very good. For the monoclinic phase (upper panel) a momentum transfer $\mathbf{q} \rightarrow 0$ is considered. For the rutile phase (bottom panel) the calculations are shown at two different \mathbf{q} (in Angstrom in the key).

6. Vanadium dioxide

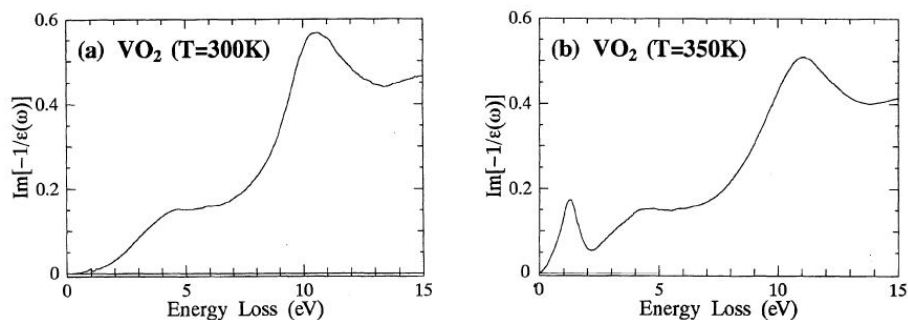


Figure 6.29: Experimental loss function for the insulating (on the left) and metallic phases (on the right). They have been obtained from the experimental measurements reported in Fig. 6.28 after having removed the contributions of the direct beam and multiple scattering. From Ref. [343].

in the insulating phase (see Fig. 6.29).

This observation is confirmed also by the thermoreflectance measurements of Bianconi *et al.* [360].

Consistently, in the same energy range, at a binding energy of 1.3 eV, the photoemission spectrum of Koethe *et al.* [293] shows a satellite in the metallic phase, which is not present in the insulating phase.

It is known that satellites in photoemission can be due to a coupling with plasmon resonances. In this case the impinging photon excites simultaneously a hole and a plasmon (see Fig. 1.3 and Sec. 1.2.1). This can be shown also analytically by considering, as done by Hedin [35] (and before him by Lundqvist [361][362] and Langreth [363]), a polaron model Hamiltonian:

$$\hat{H} = \epsilon_c c^\dagger c + \sum_q g_q (a_q + a_q^\dagger) c^\dagger c + \sum_q \omega_q a_q^\dagger a_q \quad (6.5)$$

that in this case describes the coupling between a single (localized) state ϵ_c with plasmons of energy $\omega_q = \omega_p + q^2/2$ (represented in (6.5) by the creation and annihilation operators a_q^\dagger, a_q). The exact solution [35][363] of this model yields a quasiparticle peak at $\omega = E_c$, solution of $E_c = \epsilon_c + \text{Re}\Sigma(E_c)$, and a series of satellites at energies $E_c - n\omega_p$ with $n = 1, 2, \dots$ (in the GW approximation, instead, one obtains a broad satellite starting at $\omega = E_c - \omega_p$ and extending to $\omega = -\infty$).

A complete description of photoemission spectra for a real system would require the *ab initio* calculation of the full spectral function, which is very cumbersome in vanadium dioxide. Nonetheless, a calculation of the plasmon in the energy loss spectra can provide physical insights to the explanation of the satellite in photoemission. This is what I will discuss in this paragraph.

I have carried out a calculation of the loss function in the energy region of interest for both the metallic and the insulating phases. There is no

6.8 Calculation of electron energy-loss spectra

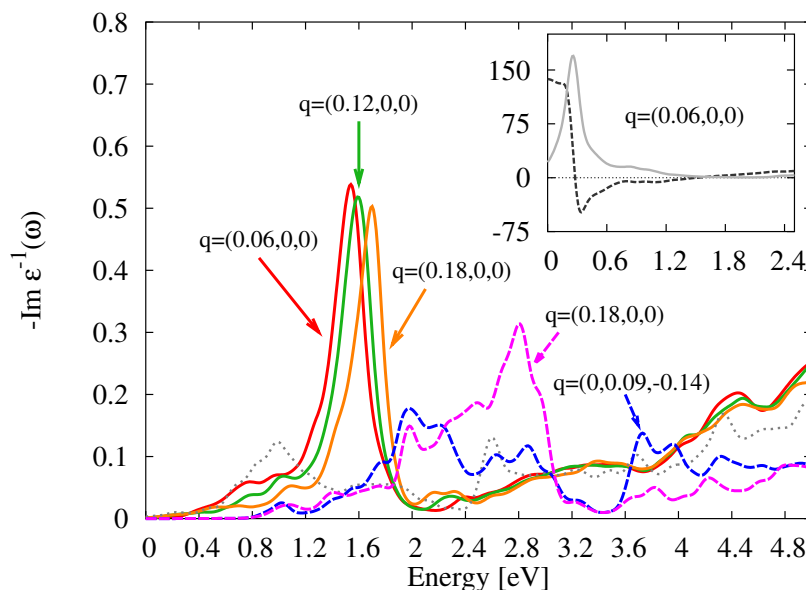


Figure 6.30: Calculated EELS of the metallic (solid lines) and insulating phases, for different values of \mathbf{q} (in atomic units). For both phases the spectra are obtained in RPA. In the case of the insulator the energies entering the independent-particle polarizability χ_{KS} are considered at the LDA level (dotted line), for $\mathbf{q}=(0,0.09,-0.14)$, or with COHSEX+GW corrections (dashed lines). In the inset: real and imaginary parts of ϵ (respectively dashed and solid) lines for the metallic phase.

difference between the results obtained in TDLDA or RPA, which is the approximation also used to calculate in GW the screening ϵ^{-1} of W and hence is more interesting in this context.

The RPA results for the metallic phase are shown (solid lines) in Fig. 6.30 in function of the momentum transfer \mathbf{q} . In agreement with the experimental results a sharp peak around 1.5 eV is found. On the basis of a Kramers-Kronig analysis of the experimental data, this peak in the EELS spectrum has been interpreted by Abe *et al* [343] as a $d-d$ interband transition. Our calculation, instead, clearly shows (see the inset of Fig. 6.30) that it is caused by a zero of ϵ_1 . Therefore this EELS peak has to be assigned to a plasmonic excitation, as stated also in Ref. [360]. This feature, in turn, is indeed due to a group of $d-d$ interband transitions visible in the spectrum of ϵ_2 at lower energy.

Since the LDA band structure is qualitatively wrong for the insulator, the energies used in the calculation of the loss function are the results of the self-consistent COHSEX+GW calculations. This approach is called GW-RPA. It corrects the main error of the usual RPA approach (named LDA-RPA, see the dotted curve in Fig. 6.30) and yields an energy loss spectrum in

6. Vanadium dioxide

good agreement with experiment. I also performed some test calculations to see the effect of the change of the wavefunctions, from LDA to COHSEX, for the insulating phase. In these preliminary results an enhancement of the damping of the plasmon peak towards high energies is found.

These findings for the loss function permit to assign the satellite at 1.3 eV binding energy in the experimental photoemission spectrum of the metallic phase to a plasmon satellite. Moreover they show that a RPA calculation is already sufficient to describe the difference between the metal and the insulator, where the plasmon peak is absent.

In the insulator, on the contrary, this sharp plasmon resonance is strongly damped and shifted to higher energies (see dashed lines of Fig. 6.30).

The results presented in this chapter show that in VO_2 the treatment of electronic correlation is adequate already at the RPA level, both in the quasiparticle framework and for the interpretation of the satellite beyond the quasiparticle picture. The key ingredient, in both cases, is the inverse dielectric function ϵ^{-1} that, on one side, provides directly the loss function that one needs to describe EELS spectra, and, on the other side, determines the screening of the Coulomb interaction that is used to build the self-energy in the GW approximation for the calculation of photoemission spectra.

The calculations have shown that also for VO_2 the LDA is a good approximation for the calculation of ground-state properties. On the contrary, the Kohn-Sham wavefunctions in the insulator are a bad approximation to the quasiparticle wavefunctions. In particular, they underestimate the polarization along the c -axis, which in turn leads to the gap opening. For this reason the system remains metallic even in the perturbative GW scheme. Remarkably, the self-consistent COHSEX calculations in vanadium dioxide change the description of the quasiparticle properties of the insulating phase not only on a quantitative level, by correcting the known LDA underestimation of the band gap, but also on a qualitative level, passing from a metallic LDA band structure to an insulating one.

The metallic phase, instead, is more electronically isotropic. In this case the LDA wavefunctions are a better approximation to the quasiparticle wavefunctions and hence the task for the perturbative GW approach is easier. Moreover, beyond the quasiparticle picture, the satellite in the metallic PES has been explained as a plasmon resonance in the EELS.

Therefore, these calculations provide the first parameter-free consistent explanation of the electronic properties of VO_2 . They demonstrate that a relatively simple physical interpretation of all the different features of the PES of the two phases is possible. Nevertheless, in order to make a direct comparison with the experimental PES one should calculate the trace of the spectral function. In vanadium dioxide this calculation has not been feasible. More-

6.8 Calculation of electron energy-loss spectra

over, even though the screening calculated at the RPA level, which enters the screened potential W used in the GW self-energy, is in good agreement with the experimental EELS, the GW approximation to the self-energy may be not sufficient to obtain the satellite in the spectral function in agreement with the experimental PES. One could still need to consider vertex corrections in the self-energy, beyond the GW approximation.

These limitations of the present first-principles GW approach has motivated a further part of work, aiming at introducing a scheme for the direct calculation of electronic spectra. This is the subject of the next chapter.

Chapter 7

Effective potentials and kernels for spectroscopy

The results presented in the previous chapter about vanadium dioxide have clearly put into evidence the advantages and the limits of the present ab initio MBPT approach. On the one side, thanks to its clear physical picture, it has been possible to explain the photoemission spectra of VO₂ in a simple way and without resorting to adjustable parameters. On the other side, the calculation of the spectral function, which would have required to determine with higher precision the frequency dependence of the self-energy, has not been practically feasible. This computational limitation has to be traced back to the fact that in MBPT one often calculates more information than needed. For instance, the trace of the spectral function can be obtained only after having calculated the whole Green's function.

Density-functional theory is instead an example of a method for a direct calculation of the quantity of interest, i.e. the electronic density. So, in this chapter, I will consider the Sham-Schlüter equation, that permits to establish a link between the MBPT and DFT worlds and use the physical information one can get from MBPT to find better approximations for the more efficient DFT. I will then introduce a new general scheme, based on a generalization of the Sham-Schlüter approach, for a direct calculation of the electronic spectra. This will lead me to define ad hoc reduced effective potentials and kernels that have the property of yielding the answer only to a limited question one can have (e.g. the calculation of the spectral function and not of the whole Green's function, which contains much more information). I will show how these effective potentials and kernels can be made simpler than the corresponding many-body quantities. Moreover, I will discuss the transformation of spatial nonlocality into frequency dependence that one encounters dealing with a reduced number of spatial degrees of freedom. I will present several examples of this scheme. I will in particular focus on the definition of a local, real and frequency-dependent effective potential for photoemission,

7. Effective potentials and kernels for spectroscopy

which has been the main motivation of this work. Studying exactly solvable model examples, I will show why the static and local exchange-correlation potential of DFT is instead not able to yield the same results as this new potential. I will compare the exact results with some approximations and underline that the linearization of the generalized Sham-Schlüter equation is an approximation that one has to validate with care case by case.

The results discussed in this chapter demonstrate that, if one were able to find working approximations, this new photoemission potential would represent an important simplification also for practical applications in order to obtain spectra both at the GW level and, even more interestingly, beyond GW, with the inclusion of vertex corrections.

7.1 Generalization of the Sham-Schlüter equation

The Kohn-Sham Green's function G_{KS} is the resolvent of the Kohn-Sham Hamiltonian:

$$\left[i \frac{\partial}{\partial t_1} - h_0(1) - V_H(1) - V_{xc}(1) \right] G_{KS}(1, 2) = \delta(1, 2). \quad (7.1)$$

Using the eigenfunctions and the eigenvalues of the Kohn-Sham equation (2.28), G_{KS} reads:

$$G_{KS}(\mathbf{r}_1, \mathbf{r}_2, \omega) = \sum_s \frac{\varphi_s(\mathbf{r}_1) \varphi_s^*(\mathbf{r}_2)}{\omega - \epsilon_s + i\eta \text{sgn}(\epsilon_s - \mu)}. \quad (7.2)$$

From the Kohn-Sham Green's function it is possible to calculate the electronic density as¹:

$$\rho(\mathbf{r}) = -i \int \frac{d\omega}{2\pi} e^{i\omega\eta} G_{KS}(\mathbf{r}, \mathbf{r}, \omega). \quad (7.4)$$

In fact the convergence factor $+i\omega\eta$ requires to close the contour in the upper half-plane, where the poles of the occupied states lie (see Eq. (7.2)), so:

$$-i \int \frac{d\omega}{2\pi} e^{i\omega\eta} G_{KS}(\mathbf{r}, \mathbf{r}, \omega) = \sum_s^{\text{occ}} |\varphi_s(\mathbf{r})|^2 = \rho(\mathbf{r}). \quad (7.5)$$

By definition the Kohn-Sham system produces the exact density of the real interacting system (see Eq. (2.29)), which can be obtained also from the full Green's function G (see Eq. (3.8)):

$$-i \int \frac{d\omega}{2\pi} e^{i\omega\eta} G(\mathbf{r}, \mathbf{r}, \omega) = \rho(\mathbf{r}). \quad (7.6)$$

¹ Equivalently (see Eq. (3.21)):

$$-\frac{1}{\pi} \int_{-\infty}^{\mu} d\omega \text{Im} G_{KS}(\mathbf{r}, \mathbf{r}, \omega) = \sum_s^{\text{occ}} |\varphi_s(\mathbf{r})|^2 = \rho(\mathbf{r}). \quad (7.3)$$

7.1 Generalization of the Sham-Schlüter equation

Combining Eq. (7.1) with the Dyson equation (3.30), it is possible to find a new Dyson equation, linking G_{KS} to G :

$$G(\mathbf{r}_1, \mathbf{r}_2, \omega) = G_{KS}(\mathbf{r}_1, \mathbf{r}_2, \omega) + \int d\mathbf{r}_3 d\mathbf{r}_4 G_{KS}(\mathbf{r}_1, \mathbf{r}_3, \omega) [\Sigma(\mathbf{r}_3, \mathbf{r}_4, \omega) - V_{xc}(\mathbf{r}_3) \delta(\mathbf{r}_3 - \mathbf{r}_4)] G(\mathbf{r}_4, \mathbf{r}_2, \omega). \quad (7.7)$$

The frequency integrals of G and G_{KS} yield the same exact density (see Eqs. (7.4)-(7.6)). Using this condition in the Dyson equation (7.7), one gets:

$$\int d\omega d\mathbf{r}_3 d\mathbf{r}_4 e^{i\omega\eta} G_{KS}(\mathbf{r}_1, \mathbf{r}_3, \omega) [\Sigma(\mathbf{r}_3, \mathbf{r}_4, \omega) - V_{xc}(\mathbf{r}_3) \delta(\mathbf{r}_3 - \mathbf{r}_4)] G(\mathbf{r}_4, \mathbf{r}_1, \omega) = 0. \quad (7.8)$$

Thanks to Eqs. (7.4) and (7.6) the other two terms in Eq. (7.7) cancel exactly. Eq. (7.8) can be solved for V_{xc} , obtaining:

$$\begin{aligned} \int d\mathbf{r}_3 V_{xc}(\mathbf{r}_3) \int d\omega e^{i\omega\eta} G_{KS}(\mathbf{r}_1, \mathbf{r}_3, \omega) G(\mathbf{r}_3, \mathbf{r}_1, \omega) = \\ = \int d\omega d\mathbf{r}_3 d\mathbf{r}_4 e^{i\omega\eta} G_{KS}(\mathbf{r}_1, \mathbf{r}_3, \omega) \Sigma(\mathbf{r}_3, \mathbf{r}_4, \omega) G(\mathbf{r}_4, \mathbf{r}_1, \omega). \end{aligned} \quad (7.9)$$

Eq. (7.9) represents an exact definition of V_{xc} in terms of G and Σ . It is a nonlinear integral equation for V_{xc} that has been derived for the first time by Sham and Schlüter in [89][364]. It has been then extended to the case of time-dependent potentials by van Leeuwen [365] (in this case one would define the equation on the Keldysh contour).

In practical applications, the Sham-Schlüter equation is used in its linearized version, where G is replaced by G_{KS} everywhere, including in the functional dependence of the self-energy: $\Sigma[G] \rightarrow \Sigma[G_{KS}]$. In this way Eq. (7.9) becomes:

$$\begin{aligned} \int d\mathbf{r}_3 V_{xc}(\mathbf{r}_3) \chi_{KS}(\mathbf{r}_1, \mathbf{r}_3, \omega = 0) = \\ = -\frac{i}{2\pi} \int d\omega d\mathbf{r}_3 d\mathbf{r}_4 e^{i\omega\eta} G_{KS}(\mathbf{r}_1, \mathbf{r}_3, \omega) \Sigma(\mathbf{r}_3, \mathbf{r}_4, \omega) G_{KS}(\mathbf{r}_4, \mathbf{r}_1, \omega), \end{aligned} \quad (7.10)$$

where the static density-density response function $\chi_{KS}(\omega = 0)$ has been introduced (see Eq. (5.73)). The linearized Sham-Schlüter equation (7.10) is still a nonlinear equation in V_{xc} .

Given a the self-energy, Eq. (7.10) permits to define the corresponding exchange-correlation potential V_{xc} . This potential yields the same density up to the first-order in the difference $\Sigma - V_{xc}$.

The linearized Sham-Schlüter equation is the central equation of the optimized effective potential method (see Sec. 2.2.3). In fact Eq. (7.10)

7. Effective potentials and kernels for spectroscopy

is the same equation as Eq. (2.37), which had been derived in the OEP framework. In particular, if one uses for Σ the exchange-only approximation $\Sigma = \Sigma_x$ where $\Sigma_x = iG_{KS}v$ (see Eq. (3.38)), then the exact-exchange approximation to V_{xc} is recovered (see Eq. (2.40)).

The linearized Sham-Schlüter equation (in both the static and time-dependent cases) has been derived also in a variational approach by Casida [366] and von Barth *et al.* [200]. This implies that if the self-energy is Φ -derivable (see Sec. 4.3), then also the exchange-correlation potential V_{xc} and the f_{xc} kernel derived from it are conserving. This means that the response functions calculated in this way obey conservation rules (for instance for the particle number, the total momentum, etc.).

The linearized Sham-Schlüter equation has been exploited in many different contexts. For instance, Godby, Sham and Schlüter [112][367] have used it to show that in *sp* semiconductors the LDA V_{xc} is very similar to the exchange-correlation potential calculated employing in (7.10) the GW self-energy. Niquet, Fuchs and Gonze [368] have demonstrated that V_{xc} obtained from Eq. (7.10) has the correct asymptotic behavior. For this reason Eguiluz *et al.* [369] in this way found an exchange-correlation potential that reproduces correctly the image potential at the jellium-vacuum interface, which is completely missed by the LDA potential. Tokatly and Pankratov [255] have derived from the linearized Sham-Schlüter equation (7.10) a diagrammatic expansion using G_{KS} as bare propagator. In this way they have been able also to study the properties of the exchange-correlation kernel f_{xc} .

The Sham-Schlüter equation permits to make a link between two worlds: DFT and MBPT. The density-functional theory is a very efficient scheme to calculate directly the electronic density $\rho(\mathbf{r})$. Using DFT one doesn't have to calculate the Green's function $G(\mathbf{r}, \mathbf{r}', \omega)$ to get ρ from it (see Eq. (7.6)). This is instead the case for other quantities of interest beyond the ground-state density, in particular for the spectral function $A(\omega)$ that one can presently obtain only after having calculated $G(\mathbf{r}, \mathbf{r}', \omega)$ (see Eq. (3.15)). This has been the main computational drawback in the calculation of the electronic properties of VO₂ in the previous chapter. Nevertheless, MBPT-based approaches have been successful also for VO₂ thanks to the physical intuition that helps in finding good approximations, based on the simple concept of elementary excitations, such as quasiparticles, plasmons, etc. which have largely used for the explanation of the properties of VO₂.

Hence, one would like to combine the advantages of both approaches: the clear physical picture of MBPT and the computational efficiency of DFT. The Sham-Schlüter equation, in particular, permits to exploit the physical information contained in the Green's function G to design better approximations for V_{xc} , beyond the LDA. Therefore, the main idea that I will develop in this chapter is that the Sham-Schlüter approach can be actually used in other contexts and for other quantities of interest beyond the electronic density. In particular, I will consider a generalization in two different directions:

7.1 Generalization of the Sham-Schlüter equation

- by considering other quantities, besides the electronic density, that can be calculated from the one-particle Green's function: in principle the expectation value of any one-particle operator (see Eq. (3.6)). For example, in the following I will discuss the definition of an effective potential that permits to obtain the trace of the spectral function that one needs to describe photoemission (see Sec. 1.2.1);
- by considering other Dyson equations involving other kinds of Green's functions. In particular, I will study the case of the response functions, which are a particular kind of two-particle Green's functions, that one needs to describe spectroscopy experiments involving neutral excitations (see Secs. 7.6-7.7).

This generalization of the Sham-Schlüter approach defines a very general scheme to design reduced potential and kernels aimed at obtaining directly certain quantities that can be otherwise calculated indirectly from some Green's function.

I illustrate here the general scheme for the case of the one-particle Green's function. Then, in the following sections, some practical applications will be discussed, also involving two-particle Green's functions.

I suppose that one wants to calculate the quantity T that is a part of the information carried by G . For instance, T can be the expectation value of a one-particle operator (see Eq. (3.6)), like the electronic density ρ . Symbolically I express this relation between T and G as: $T = p\{G\}$, which means: T is a "part" of G . I introduce another Green's function G_T that has the property of having the part $p\{.\}$ in common with G : $T = p\{G_T\} = p\{G\}$. I now suppose that G_T stems from an effective potential V_T , according to $G_T = (\omega - h_0 - V_H - V_T)$. If, in particular, G and G_T yield the same density (and hence the same Hartree potential V_H), a Dyson equation between G and G_T can be written as:

$$G = G_T + G_T(\Sigma - V_T)G. \quad (7.11)$$

It is also possible that G_T doesn't reproduce the correct density. In this case one should consider a further correction in the Dyson equation. But in the practical applications I won't deal with such situations. Since $p\{G_T\} = p\{G\}$, taking the part of interest $p\{.\}$ of the Dyson equation (7.11), one immediately finds:

$$p\{G_T(\Sigma - V_T)G\} = 0. \quad (7.12)$$

The aim is then to make an ansatz for the form of V_T with a simpler structure than Σ and for which one can still solve the equation (7.12). In this way the two equations (7.11)-(7.12) define two conditions that can be solved self-consistently in the two unknowns G_T and V_T . In this way one could use the simpler potential V_T to get the same result concerning the quantity T as if one used the more complicate self-energy.

7. Effective potentials and kernels for spectroscopy

In the example that T is the density ρ , V_T actually is the static and local exchange-correlation potential V_{xc} , which is much simpler than Σ , G_T is the Kohn-Sham Green's function G_{KS} and Eq. (7.12) is the Sham-Schlüter equation (7.8).

I will consider now some practical applications of this general scheme.

7.2 The photoemission potential

To first approximation, angular-integrated photoemission experiments measure the trace of the spectral function A (see Eq. (1.18)), which is the imaginary part of the Green's function (see Eq. (3.15)):

$$A(\mathbf{r}_1, \mathbf{r}_2, \omega) = \frac{1}{\pi} \text{sgn}(\mu - \omega) \text{Im}G(\mathbf{r}_1, \mathbf{r}_2, \omega). \quad (7.13)$$

Thanks to a first generalization of the Sham-Schlüter equation (7.9), I will define here an effective reduced potential, V_{SF} , that reproduces exactly the diagonal in real space of the spectral function: $A(\mathbf{r}, \mathbf{r}, \omega)$. In this way both the trace of A and the electronic density are reproduced (see Eq. (7.3)). The potential V_{SF} defines a new Green's function $G_{SF} = (\omega - h_0 - V_H - V_{SF})^{-1}$ that has the property:

$$\text{Im}G_{SF}(\mathbf{r}_1, \mathbf{r}_1, \omega) = \text{Im}G(\mathbf{r}_1, \mathbf{r}_1, \omega) \quad (7.14)$$

($\text{Im}G$ and $\text{Im}G_{SF}$ change sign at the same frequency and the factor $1/\pi$ in (7.13) here is irrelevant). A possible ansatz for the potential V_{SF} is a spatially local, but frequency dependent operator: $V_{SF} = V_{SF}(\mathbf{r}, \omega)$. Moreover, it is also possible to choose V_{SF} to be real.

In this way, the Dyson equation linking V_{SF} to Σ is:

$$\begin{aligned} G(\mathbf{r}_1, \mathbf{r}_2, \omega) &= G_{SF}(\mathbf{r}_1, \mathbf{r}_2, \omega) + \\ &+ \int d\mathbf{r}_3 d\mathbf{r}_4 G_{SF}(\mathbf{r}_1, \mathbf{r}_3, \omega) [\Sigma(\mathbf{r}_3, \mathbf{r}_4, \omega) - V_{SF}(\mathbf{r}_3, \omega) \delta(\mathbf{r}_3 - \mathbf{r}_4)] G(\mathbf{r}_4, \mathbf{r}_2, \omega). \end{aligned} \quad (7.15)$$

By plugging the condition (7.14) into (7.15), one gets:

$$\begin{aligned} \int d\mathbf{r}_3 d\mathbf{r}_4 \text{Im}[G_{SF}(\mathbf{r}_1, \mathbf{r}_3, \omega) \Sigma(\mathbf{r}_3, \mathbf{r}_4, \omega) G(\mathbf{r}_4, \mathbf{r}_1, \omega)] &= \\ = \int d\mathbf{r}_3 V_{SF}(\mathbf{r}_3, \omega) \text{Im}[G_{SF}(\mathbf{r}_1, \mathbf{r}_3, \omega) G(\mathbf{r}_3, \mathbf{r}_1, \omega)]. \end{aligned} \quad (7.16)$$

Solving this equation for V_{SF} , one finds the definition of V_{SF} in terms of G and Σ :

$$\begin{aligned} V_{SF}(\mathbf{r}_1, \omega) &= \int d\mathbf{r}_2 d\mathbf{r}_3 d\mathbf{r}_4 \zeta^{-1}(\mathbf{r}_1, \mathbf{r}_4, \omega) \times \\ &\times \text{Im}[G_{SF}(\mathbf{r}_4, \mathbf{r}_2, \omega) \Sigma(\mathbf{r}_2, \mathbf{r}_3, \omega) G(\mathbf{r}_3, \mathbf{r}_4, \omega)], \end{aligned} \quad (7.17)$$

7.2 The photoemission potential

where $\zeta(\mathbf{r}_1, \mathbf{r}_2, \omega) = \text{Im}[G_{SF}(\mathbf{r}_1, \mathbf{r}_2, \omega)G(\mathbf{r}_2, \mathbf{r}_1, \omega)]$. So a solution to Eq. (7.16) exists if ζ is invertible. When this is possible is a delicate question that I have not addressed. At the same time I have implicitly assumed to deal only with “ V -representable” $\text{Im}G(\mathbf{r}, \mathbf{r}, \omega)$.

Unless Σ is static and local, V_{SF} could not be chosen to be static. In the general case, the right-hand-side of Eq. (7.17) is frequency dependent. This also means that a local and static potential, like the Kohn-Sham potential V_{KS} of DFT, is not capable to reproduce the diagonal of the spectral function. Also a static and nonlocal ansatz for V_{SF} would not be correct. In this case instead of Eq. (7.16), one would get:

$$\begin{aligned} \int d\mathbf{r}_3 d\mathbf{r}_4 \text{Im}[G_{SF}(\mathbf{r}_1, \mathbf{r}_3, \omega)\Sigma(\mathbf{r}_3, \mathbf{r}_4, \omega)G(\mathbf{r}_4, \mathbf{r}_1, \omega)] = \\ = \int d\mathbf{r}_3 d\mathbf{r}_4 V_{SF}(\mathbf{r}_3, \mathbf{r}_4) \text{Im}[G_{SF}(\mathbf{r}_1, \mathbf{r}_3, \omega)G(\mathbf{r}_4, \mathbf{r}_1, \omega)], \end{aligned} \quad (7.18)$$

which is clearly not possible, unless Σ is static (and real). And in this case one would trivially have: $V_{SF} = \Sigma$.

Already Sham and Kohn in [140] suggested a local-density approximation to the self-energy. The resulting approximate self-energy gave rise to a local and dynamical potential [370]. The potential V_{SF} that I have just introduced, instead, is the local and dynamical potential that yields the *exact* diagonal of the imaginary part of the Green’s function G . It is not an approximation of the self-energy, as I will show in the following.

Through Eq. (7.17) it is possible to construct a fictitious system of independent particles moving in a local but frequency-dependent potential which reproduces $\text{Im}G(\mathbf{r}, \mathbf{r}, \omega)$ of the real system. Since also the electronic density $\rho(\mathbf{r})$ is correctly reproduced, this represents a generalization of the Kohn-Sham scheme of DFT.

Since they both yield the exact density and hence the same Hartree potential V_H , it is possible to write a Dyson equation linking G_{KS} and G_{SF} :

$$\begin{aligned} G_{SF}(\mathbf{r}_1, \mathbf{r}_2, \omega) = G_{KS}(\mathbf{r}_1, \mathbf{r}_2, \omega) + \\ + \int d\mathbf{r}_3 G_{KS}(\mathbf{r}_1, \mathbf{r}_3, \omega)[V_{SF}(\mathbf{r}_3, \omega) - V_{xc}(\mathbf{r}_3)]G_{SF}(\mathbf{r}_3, \mathbf{r}_2, \omega). \end{aligned} \quad (7.19)$$

Since:

$$-\frac{1}{\pi} \int_{-\infty}^{\mu} d\omega \text{Im}G_{KS}(\mathbf{r}, \mathbf{r}, \omega) = -\frac{1}{\pi} \int_{-\infty}^{\mu} d\omega \text{Im}G_{SF}(\mathbf{r}, \mathbf{r}, \omega) = \rho(\mathbf{r}), \quad (7.20)$$

one has:

$$\begin{aligned} \int d\mathbf{r}_3 V_{xc}(\mathbf{r}_3) \int_{-\infty}^{\mu} d\omega \text{Im}[G_{KS}(\mathbf{r}_1, \mathbf{r}_3, \omega)G_{SF}(\mathbf{r}_3, \mathbf{r}_1, \omega)] = \\ \int d\mathbf{r}_3 \int_{-\infty}^{\mu} d\omega V_{SF}(\mathbf{r}_3, \omega) \text{Im}[G_{KS}(\mathbf{r}_1, \mathbf{r}_3, \omega)G_{SF}(\mathbf{r}_3, \mathbf{r}_1, \omega)], \end{aligned} \quad (7.21)$$

7. Effective potentials and kernels for spectroscopy

and hence a new Sham-Schlüter equation for V_{xc} , defining the exchange-correlation potential V_{xc} in terms of V_{SF} .

The frequency ω enters the definition (7.17) of V_{SF} as a parameter. In other words, at each ω one has the definition of a local potential. Moreover, for each ω it is possible to introduce a set of Kohn-Sham equations for the new fictitious system of independent particles:

$$\left(-\frac{\nabla^2}{2} + V_{ext}(\mathbf{r}) + V_H(\mathbf{r}) + V_{SF}(\mathbf{r}, \omega)\right)\xi_i(\mathbf{r}, \omega) = \epsilon_i(\omega)\xi_i(\mathbf{r}, \omega). \quad (7.22)$$

In particular, since V_{SF} is real, the eigenvalues $\epsilon_i(\omega)$ are real and at each ω the eigenfunctions ξ_i form an orthonormal set. The Green's function associated to this system reads:

$$G_{SF}(\mathbf{r}_1, \mathbf{r}_2, \omega) = \sum_i \frac{\xi_i(\mathbf{r}_1, \omega)\xi_i^*(\mathbf{r}_2, \omega)}{\omega - \epsilon_i(\omega) + i\eta\text{sgn}(\epsilon_i(\omega) - \mu)}. \quad (7.23)$$

Whereas by definition

$$\text{Im}G_{SF}(\mathbf{r}, \mathbf{r}, \omega) = -\pi \sum_i \text{sgn}(\epsilon_i(\omega) - \mu)|\xi_i(\mathbf{r}, \omega)|^2\delta(\omega - \epsilon_i(\omega)) \quad (7.24)$$

is equal to $\text{Im}G(\mathbf{r}, \mathbf{r}, \omega)$, nothing general can be said about the poles of G_{SF} in (7.23). As the Kohn-Sham eigenvalues ϵ_i are not the one-particle excitation energies of the real system, the poles of G_{SF} , i.e. the solutions of the equation $\omega - \epsilon_i(\omega) = 0$, do not have to be the quasiparticle energies either. In other words, from G_{SF} it is possible, in principle, to describe the photoemission spectra, through the trace of the spectral function. But it is not possible to have access to the \mathbf{k} -dispersion of the quasiparticle bands that is measured in angular-resolved photoemission spectra.

The novelty of the potential V_{SF} that distinguishes it from the exchange-correlation potential of DFT is its frequency dependence. In particular, from the definition (7.17) of V_{SF} one can realize that a local potential can yield the correct spectral function only if it is frequency dependent. In the next section I am going to discuss rightly the frequency dependence of the new potential V_{SF} .

7.3 Transforming nonlocality into frequency dependence

In the next two sections I will consider two illustrative model systems defined by a self-energy Σ that permits to calculate exactly the corresponding Green's function G . The full Green's function G then will be the exact reference. I will prove how the effective potential is able to reproduce the trace of spectral function associated to the exact G . In both models, in particular,

7.3 Transforming nonlocality into frequency dependence

I will consider static nonlocal self-energies to show that, even in these cases, the resulting local effective potential is frequency dependent. The effective potential for the spectral function in these models can be also exactly calculated. Therefore it will be possible to additionally discuss how common approximations to the exact Sham-Schlüter equation perform with the new frequency-dependent potential.

7.3.1 A scissor operator in a two-level system

As a first illustrative example, I will study here a minimal model consisting of only two levels: one valence state $|v\rangle$ and one conduction state $|c\rangle$. In this case V_{SF} would be defined only in a discrete set of frequencies. Therefore, to exemplificative purposes, I will consider a slightly modified effective potential. In fact, by asking that a new potential \tilde{V}_{SF} reproduces the diagonal of G , and not only its imaginary part, one has a new Green's function \tilde{G}_{SF} such as: $\tilde{G}_{SF}(\mathbf{r}, \mathbf{r}, \omega) = G(\mathbf{r}, \mathbf{r}, \omega)$. The reduced potential \tilde{V}_{SF} is in general complex and is defined by:

$$\begin{aligned} \tilde{V}_{SF}(\mathbf{r}_1, \omega) = & \int d\mathbf{r}_2 d\mathbf{r}_3 d\mathbf{r}_4 \tilde{\zeta}^{-1}(\mathbf{r}_1, \mathbf{r}_4, \omega) \times \\ & \times \tilde{G}_{SF}(\mathbf{r}_4, \mathbf{r}_2, \omega) \Sigma(\mathbf{r}_2, \mathbf{r}_3, \omega) G(\mathbf{r}_3, \mathbf{r}_4, \omega), \end{aligned} \quad (7.25)$$

where $\tilde{\zeta}(\mathbf{r}_1, \mathbf{r}_2, \omega) = \tilde{G}_{SF}(\mathbf{r}_1, \mathbf{r}_2, \omega) G(\mathbf{r}_2, \mathbf{r}_1, \omega)$.

In the continuum limit, in any non one-dimensional system, the real part of the Green's function $\text{Re}G(\mathbf{r}, \mathbf{r}', \omega)$ diverges at $\mathbf{r} = \mathbf{r}'$, since it accounts also for the density of all the empty states. In fact, from a mathematical point of view [371], one has that in the limit $\mathbf{r} \rightarrow \mathbf{r}'$, the asymptotic form of the Dyson equation (3.27) becomes:

$$\nabla^2 G(\mathbf{r}, \mathbf{r}', \omega) = \delta(\mathbf{r} - \mathbf{r}'), \quad (7.26)$$

which, in the three-dimensional case, has the (real) solution:

$$G(\mathbf{r}, \mathbf{r}', \omega) = -\frac{1}{4\pi} \frac{1}{|\mathbf{r} - \mathbf{r}'|}, \quad (7.27)$$

which diverges for $\mathbf{r} = \mathbf{r}'$. So in this case one prefers to define directly the reduced potential V_{SF} that reproduces only the imaginary part of $G(\mathbf{r}, \mathbf{r}, \omega)$. But in the two-level model studied here this problem doesn't occur and one can rather consider the potential \tilde{V}_{SF} , defined in Eq. (7.25).

In *sp* semiconductor the main effect of GW corrections to the LDA Kohn-Sham eigenvalues is a rigid upshift of the conduction energies with respect to the valence ones [131]. This effect of the GW self-energy can be represented by the introduction of a "scissor operator" [372]:

$$\Sigma = V(\mathbf{r}) + \Delta \sum_c |c\rangle \langle c|, \quad (7.28)$$

7. Effective potentials and kernels for spectroscopy

where $|c\rangle$ are the conduction Kohn-Sham wavefunctions. The self-energy (7.28) is the sum of a local operator, V , and a nonlocal operator, T , the projector on the conduction states: $\Sigma = V + T$. Moreover Σ is static, since Δ is a (positive) number.

I will consider the self-energy (7.28) in the two-level model and calculate the exchange-correlation potential V_{xc} of DFT and the potential \tilde{V}_{SF} .

Inserting the self-energy (7.28) in the Sham-Schlüter equation (7.9) for V_{xc} one gets immediately the result: $V_{xc}(\mathbf{r}) = V(\mathbf{r})$. In fact, in order to contribute to V_{xc} , the nonlocal part of Σ should mix valence and conduction states (otherwise the frequency integration of the right-hand-side of Eq. (7.9) yields a result equal to zero).

So, in the two-level model the self-energy (7.28) can be equivalently rewritten as:

$$\Sigma = V_{xc}|v\rangle\langle v| + (V_{xc} + \Delta)|c\rangle\langle c|. \quad (7.29)$$

Written in this form, it is clear that the self-energy is diagonal in the space of Kohn-Sham wavefunctions $|i\rangle$. Σ is static and Hermitian. Therefore the quasiparticle wavefunctions associated to this self-energy are still the Kohn-Sham wavefunctions: $\phi_v = \varphi_v$ and $\phi_c = \varphi_c$. The only effect of Σ is a shift of the conduction energy of a value equal to Δ . The quasiparticle energies are in fact: $E_v = \epsilon_v$ and $E_c = \epsilon_c + \Delta$. The Kohn-Sham Green's function G_{KS} and the full Green's function G read:

$$G_{KS}(\mathbf{r}_1, \mathbf{r}_2, \omega) = \frac{\varphi_v(\mathbf{r}_1)\varphi_v^*(\mathbf{r}_2)}{\omega - \epsilon_v - i\eta} + \frac{\varphi_c(\mathbf{r}_1)\varphi_c^*(\mathbf{r}_2)}{\omega - \epsilon_c + i\eta}, \quad (7.30)$$

$$G(\mathbf{r}_1, \mathbf{r}_2, \omega) = \frac{\varphi_v(\mathbf{r}_1)\varphi_v^*(\mathbf{r}_2)}{\omega - \epsilon_v - i\eta} + \frac{\varphi_c(\mathbf{r}_1)\varphi_c^*(\mathbf{r}_2)}{\omega - (\epsilon_c + \Delta) + i\eta}. \quad (7.31)$$

With the self-energy (7.28) the effective potential \tilde{V}_{SF} is: $\tilde{V}_{SF}(\mathbf{r}, \omega) = V(\mathbf{r}) + U(\mathbf{r}, \omega) = V_{xc}(\mathbf{r}) + U(\mathbf{r}, \omega)$, where the term U stems from the nonlocal part T of the self-energy. It represents the correction beyond V_{xc} that one has to take into account to mimic the effect of the quasiparticle corrections on the Kohn-Sham eigenvalues. In other words, it is the responsible of the band gap opening.

For the two one-particle wavefunctions φ_i of the system, here I consider in particular the case of two plane waves. The generalized Sham-Schlüter equation (7.25) becomes a nonlinear equation in $U = U(\omega)$, i.e. a function constant in space, where:

$$U(\omega) = \Delta \frac{(\omega - \epsilon_v)(\omega - \epsilon_v - U(\omega))}{(\omega - \epsilon_v)(\omega - \epsilon_v - U(\omega)) + (\omega - \epsilon_c - \Delta)(\omega - \epsilon_v - U(\omega))}. \quad (7.32)$$

Eq. (7.32) is a quadratic equation in U . It hence yields two, in general complex, solutions, depending on the values of Δ and $\epsilon_g = \epsilon_c - \epsilon_v$. In Fig. 7.1 I consider the case of two real solutions. The first is a well-behaved

7.3 Transforming nonlocality into frequency dependence

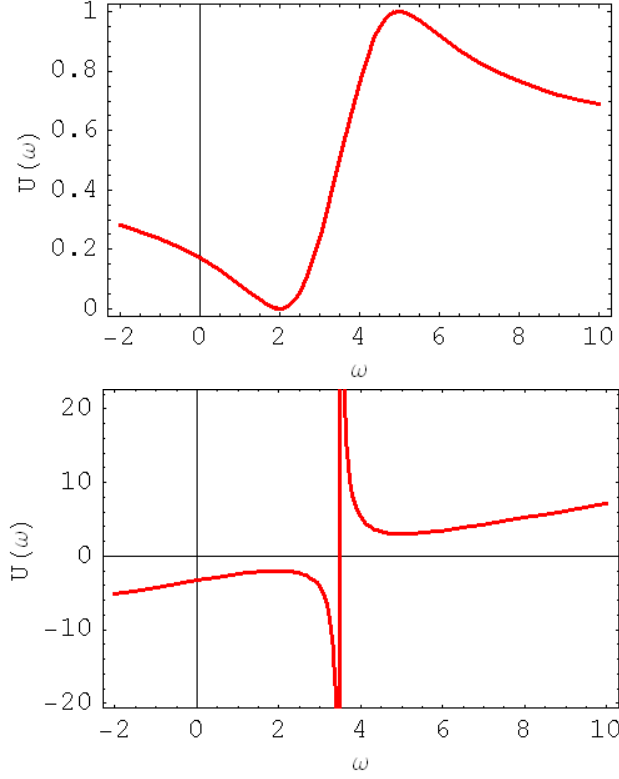


Figure 7.1: The two exact solutions of Eq. (7.32), corresponding to the following choice of the parameters defining the model: $\epsilon_v = 2$, $\epsilon_c = 4$ and $\Delta = 1$ (arbitrary units). In this case both solutions are real. The same values of ϵ_v , ϵ_c and Δ will be used also to represent the approximate solutions in the following figures. The continuous solution (upper panel) is always $0 < U(\omega) < \Delta$. The solution in the bottom panel has a discontinuity at the energy $(\epsilon_v + \epsilon_c + \Delta)/2$, corresponding to the energy in the middle of the gap, where $G(\omega) = 0$.

continuous solution, for which $U(\omega) = 0$ when $\omega = \epsilon_v$, and $U(\omega) = \Delta$ when $\omega = \epsilon_c + \Delta$. Moreover, in the limit $\omega \rightarrow \pm\infty$ it is $U(\omega) \rightarrow \Delta/2$. The second solution is discontinuous in the middle of the band gap, where $G = 0$. In both cases $U(\omega)$ turns out to be strongly frequency dependent. This means that the spatial nonlocality of the static self-energy (7.28) has been completely transformed into the frequency dependence of \tilde{V}_{SF} .

The rigid shift Δ in (7.28) corresponds to the derivative discontinuity of exchange-correlation potential in DFT (see Eq. (2.33)), i.e. the difference between the quasiparticle and the Kohn-Sham gaps. This simple two-level model shows that this discontinuity is accounted for by the local potential \tilde{V}_{SF} rightly through its frequency dependence.

The fact that more than one solution exists indicates that one could have chosen an even more restricted ansatz for \tilde{V}_{SF} in (7.25). Moreover,

7. Effective potentials and kernels for spectroscopy

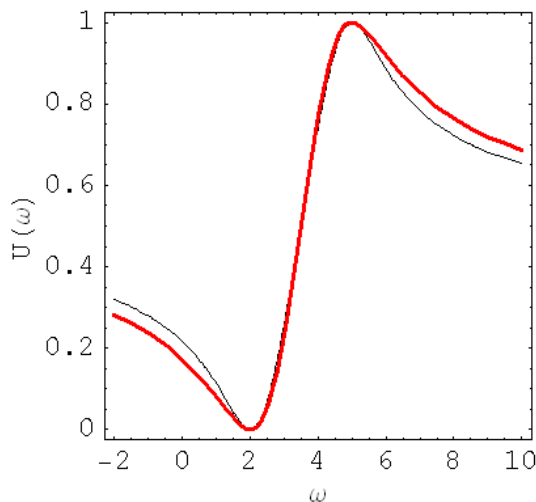


Figure 7.2: Comparison between the exact continuous solution of the upper panel of Fig. 7.1 (in red) and the self-consistent solution (in black) of Eq. (7.33). They are pretty similar.

one can easily understand that by adding more states to the model, the self-consistent equation leads to higher order polynomials and therefore to more and more solutions. It becomes then mandatory to try to restrict the solution. In particular, in the continuum limit it would be clearly problematic to work with the diagonal of G in real space, as discussed at the beginning of this section. But even in this case it is still possible to solve the generalized Sham-Schlüter equation (7.17), with the scissor-operator self-energy (7.28), for the real potential V_{SF} that yields only the *imaginary part* of the diagonal of G . If the wavefunctions $|v\rangle$ and $|c\rangle$ are still plane waves, this model corresponds to the simple Callaway homogeneous model for insulators [373]. In this case one finds that $V_{SF}(\omega) = 0$ for $\omega < \epsilon_v$ and $V_{SF}(\omega) = \Delta$ for $\omega > \epsilon_c + \Delta$. In the gap, between ϵ_v and $\epsilon_c + \Delta$, where $\text{Im}G = 0$, different solutions are possible for $V_{SF}(\omega)$. One can for instance impose that $V_{SF}(\omega)$ is a continuous function in ω . On the other hand, the static exchange-correlation potential V_{xc} of DFT cannot produce the correct band gap, because at $\omega = \epsilon_v$ and $\omega = \epsilon_v + \Delta$ it should assume different values, in correspondence to the derivative discontinuity Δ .

Eq. (7.32) yields the exact solutions of the generalized Sham-Schlüter equation for \tilde{V}_{SF} in the two-level model. Knowing the exact solutions, one can also verify how common approximations to the Sham-Schlüter equation perform for \tilde{V}_{SF} .

In particular, in the OEP approach in DFT one linearizes the Sham-Schlüter equation (7.9) by replacing G everywhere with G_{KS} . Here it is

7.3 Transforming nonlocality into frequency dependence

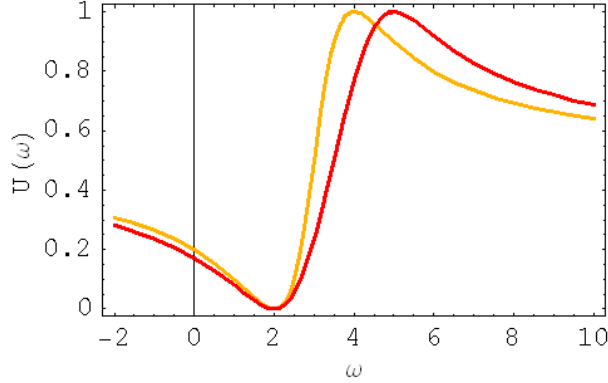


Figure 7.3: Comparison between the exact solution (see the upper panel of Fig. 7.1), in red, with the first-order solution of the linearized generalized Sham-Schlüter equation (see Eq. (7.35)), in orange. The latter has the maximum at the Kohn-Sham conduction energy $\omega = \epsilon_c$; the former at the quasiparticle energy $\omega = \epsilon_c + \Delta$.

possible to linearize analogously Eq. (7.25) by replacing G everywhere with \tilde{G}_{SF} . This linearized generalized Sham-Schlüter equation is still a nonlinear equation in U :

$$U(\omega) = \Delta \frac{(\omega - \epsilon_v - U(\omega))^2}{(\omega - \epsilon_v - U(\omega))^2 + (\omega - \epsilon_c - U(\omega))^2}. \quad (7.33)$$

Eq. (7.33) is a cubic equation in U . Since the coefficients of the polynomial in U are real, at least one solution is real. This solution can be found either by solving directly the third-order equation in U or by considering the fact that Eq. (7.33) is a quadratic equation in ω [371]. In the latter case the solution is:

$$\omega(U) = U + \epsilon_v + \frac{U\epsilon_g \pm \sqrt{U\epsilon_g^2(\Delta - U)}}{2U - \Delta}. \quad (7.34)$$

The function $\omega(U)$ is real for $U < \Delta$. So this corresponds to an approximation of the continuous solution of the exact Sham-Schlüter equation (see the upper panel of Fig. 7.1). In fact the two branches of $\omega(U)$ define one continuous function $U(\omega)$, which is very similar to the exact solution (see Fig. 7.2).

The linearized generalized Sham-Schlüter equation can be approximated to the first order, by setting \tilde{G}_{SF} equal to the zero-order Green's function, where $U = 0$. This corresponds to replace \tilde{G}_{SF} in the linearized generalized Sham-Schlüter equation with G_{KS} . In this way the linearized generalized Sham-Schlüter equation is no more a nonlinear equation in U , but an explicit definition of U . For this reason this approximation yields only one real

7. Effective potentials and kernels for spectroscopy

solution:

$$U(\omega) = \Delta \frac{(\omega - \epsilon_v)^2}{(\omega - \epsilon_v)^2 + (\omega - \epsilon_c)^2}. \quad (7.35)$$

This solution is quite different from the exact one (see Fig. 7.3). In particular it has a maximum at $\omega = \epsilon_c$, and not at $\omega = \epsilon_c + \Delta$ as the exact solution. This is due to the fact that the perturbation induced by the self-energy is not small and cannot be caught within a first-order perturbative approximation. Nevertheless, if, using this approximate solution, one calculates consistently the first-order perturbative correction to the Kohn-Sham eigenvalues (taking $U(\omega)$ at the corresponding Kohn-Sham eigenvalue instead of the quasiparticle energy) one still finds the correct quasiparticle energies:

$$E_v = \epsilon_v + Z_v U(\epsilon_v) = \epsilon_v \quad (7.36)$$

$$E_c = \epsilon_c + Z_c U(\epsilon_c) = \epsilon_c + \Delta \quad (7.37)$$

The linearization of the generalized Sham-Schlüter equation relies on the fact that the exact \tilde{G}_{SF} and the full G could be similar also outside the diagonal $\mathbf{r} = \mathbf{r}'$, where they are equal by definition. This assumption can be easily verified here, where both the exact \tilde{G}_{SF} and G are known. A simple illustrative way to make this comparison is to replace \tilde{G}_{SF} with G in the exact Sham-Schlüter equation (7.25), which becomes a non self-consistent equation in U :

$$U(\omega) = \Delta \frac{(\omega - \epsilon_v)^2}{(\omega - \epsilon_v)^2 + (\omega - \epsilon_c - \Delta)^2}. \quad (7.38)$$

In this case one finds a solution (see Fig. 7.4) similar to the exact continuous solution (see upper panel of Fig. 7.1). This implies that the Green's function \tilde{G}_{SF} obtained by the exact continuous potential \tilde{V}_{SF} is similar to G even outside the diagonal. This is not the case for the Green's function \tilde{G}_{SF} obtained from the second exact solution, which is equal to G only on the diagonal. As soon as one compares these two Green's functions outside the diagonal, they turn out to be very different.

The symmetric choice is to replace G in (7.25) with the *exact* \tilde{G}_{SF} calculated with the continuous potential $U(\omega)$ obtained by (7.32). Again, this approximation should not be meant as a self-consistent equation for U , but another explicit definition of an approximate $U(\omega)$. For this reason this approximation, where one uses the exact \tilde{G}_{SF} , is different with respect to the solution of Eq. (7.33) where \tilde{G}_{SF} is not the exact one. As expected, this approximate $U(\omega)$ is very similar to the exact continuous solution (see Fig. 7.4), confirming that the full Green's function G and the reduced Green's function \tilde{G}_{SF} , corresponding to the exact continuous solution, are similar.

Of course, in practical applications, where one knows neither the exact full Green's function G nor the exact \tilde{G}_{SF} , the only possible approximation, among the ones discussed here, would be just the linearization (7.33).

7.3 Transforming nonlocality into frequency dependence

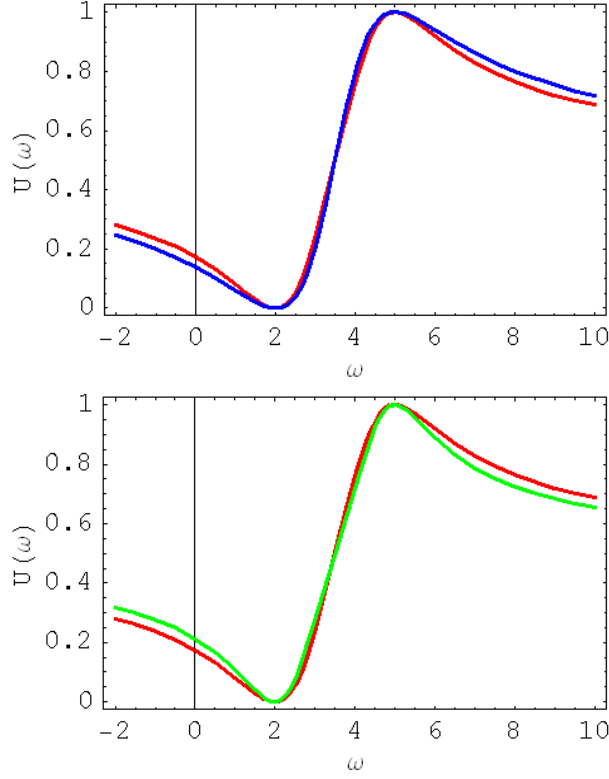


Figure 7.4: (Upper panel) Comparison between the exact continuous solution in the upper panel of Fig. 7.1, in red, and the solution, in blue, obtained by replacing \tilde{G}_{SF} with G in Eq. (7.25). (Bottom panel) Comparison with the symmetric approximation of Eq. (7.25), where G has been replaced by the exact \tilde{G}_{SF} associated with the continuous solution. In both cases, the agreement is good.

But here, where everything is exactly known, it has been interesting to consider also the other situations in order to discuss similarities and differences between G and \tilde{G}_{SF} , which in turn could be important also in practical applications.

7.3.2 Screened exchange in homogeneous electron gas

As a second example, I will consider in this section the homogeneous electron gas. Since it is an infinite three-dimensional system where $\text{Re}G(\mathbf{r}, \mathbf{r}, \omega) = \infty$, it is preferable to turn back to the effective potential V_{SF} , defined in Eq. (7.17), that reproduces only $\text{Im}G(\mathbf{r}, \mathbf{r}, \omega)$.

Moreover, I will consider static self-energies of the form: $\Sigma_\lambda(r - r') = iG(r - r', t - t^+)v_\lambda(r - r')$. So Σ has a statically screened-exchange form where the screened Coulomb potential is $v_\lambda(r - r') = v(r - r')e^{-|r - r'|/\lambda}$. For

7. Effective potentials and kernels for spectroscopy

a larger screening length λ , Σ is less screened and more effectively nonlocal. Therefore, λ tunes the effective range of the interaction: from $\lambda = 0$ ($\Sigma = 0$, Hartree approximation), to $\lambda = \infty$ (completely unscreened Hartree-Fock), all the intermediate values of λ can be considered, and, in particular, $\lambda_{TF} = (4p_F/\pi)^{-1/2}$ (Thomas-Fermi screening).

In order to ease the comparison of results issued by different self-energies Σ_λ , here it is convenient to set the zero of the Green's functions energy to the Fermi level. This corresponds to use the grand canonical ensemble at zero temperature, where the full Hamiltonian is $\hat{H}' = \hat{H} - \mu\hat{N}$ [374]. So in the following in all the Green's function stemming from different self-energies, the Fermi level will be at $\omega = 0$.

In homogeneous systems all local quantities (like V_{xc} and V_{SF}) are constant in space. In particular, the exchange-correlation potential of DFT is a number. From the Sham-Schlüter equation one has $V_{xc} = \Sigma(p = p_F, \omega = 0)$. This implies also that the DFT Kohn-Sham density of states, for any self-energy, differs from the Hartree DOS only for a rigid shift. The exchange-correlation potential V_{xc} is not meant to reproduce this property of the system, but only the electronic density. On the other hand, the potential V_{SF} retains a degree of freedom more than V_{xc} , that is its frequency dependence: $V_{SF} = V_{SF}(\omega)$. Therefore, the Green's function G_{SF} is:

$$G_{SF}(\omega, p) = \frac{2}{\omega + \mu - p^2/2 - V_{SF}(\omega) + i\eta \text{sgn}(\omega)}, \quad (7.39)$$

where the factor 2 accounts for spin degeneracy.

Also in this model it is possible to solve exactly the generalized Sham-Schlüter equations for $V_{SF}(\omega)$. In fact, from (7.39) one has:

$$\begin{aligned} \text{Im}G_{SF}(\mathbf{r}, \mathbf{r}, \omega) &= -2\pi \text{sgn}(\omega) \int \frac{d\mathbf{p}}{8\pi^3} \delta(\omega + \mu - p^2/2 - V_{SF}(\omega)) = \\ &= -\frac{\sqrt{2}}{\pi} \text{sgn}(\omega) \theta(\omega + \mu - V_{SF}(\omega)) \sqrt{\omega + \mu - V_{SF}(\omega)}. \end{aligned} \quad (7.40)$$

Requiring that this is equal to $\text{Im}G(\mathbf{r}, \mathbf{r}, \omega)$, one finds a unique local potential V_{SF} (for $V_{SF}(\omega) < \omega + \mu$):

$$V_{SF}(\omega) = \omega + \mu - \left(\frac{\pi}{\sqrt{2}} \text{Im}G(\mathbf{r}, \mathbf{r}, \omega) \right)^2. \quad (7.41)$$

When $\text{Im}G \neq 0$, from Eq. (7.41) one has automatically $V_{SF}(\omega) < \omega + \mu$. When $\text{Im}G = 0$, in order to get $\text{Im}G_{SF} = 0$ it is enough that $V_{SF}(\omega) > \omega + \mu$ and many (infinite) solutions are in principle possible.

Using Eq. (7.41), I have calculated the exact $V_{SF}(\omega)$ for different values of λ (see App. C.2). The spatial nonlocality of the static self-energies has been completely transformed into the frequency dependence of V_{SF} . In particular, looking at Fig. 7.5, one observes that the more nonlocal Σ_λ is,

7.3 Transforming nonlocality into frequency dependence

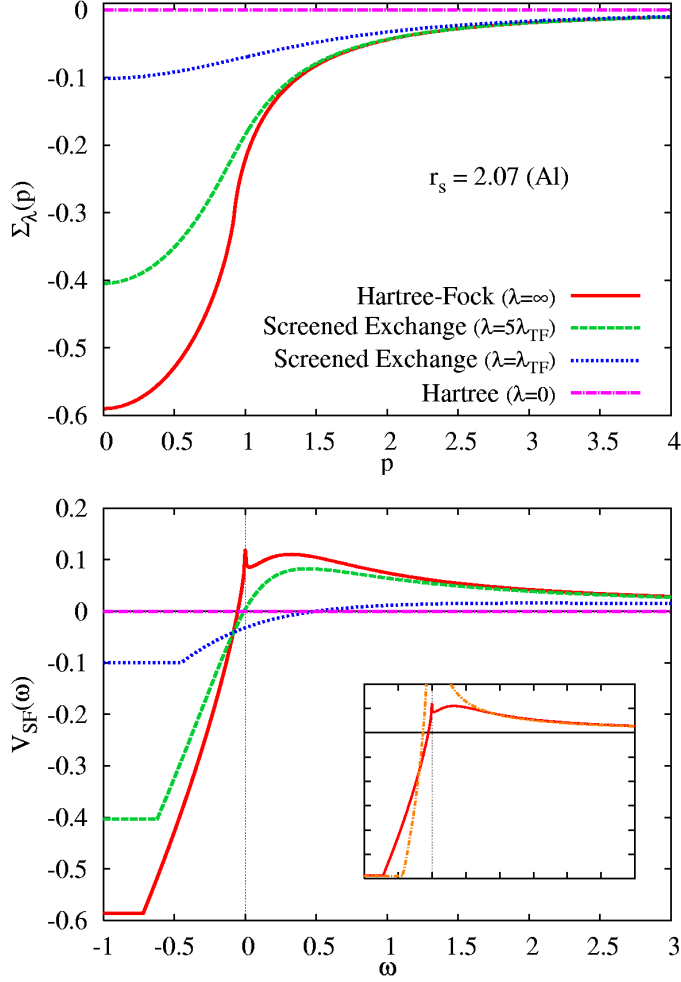


Figure 7.5: Transformation of nonlocal statically screened exchange self-energies $\Sigma_\lambda(p)$ (upper panel), see App. C.2, to the frequency-dependent local potentials $V_{SF}(\omega)$ (bottom panel), for different screening lengths λ in HEG ($\lambda_{TF} = (4p_F/\pi)^{-1/2}$ is the Thomas-Fermi length). A Wigner-Seitz radius r_s (see Eq. (1.40)) corresponding to the aluminum density has been considered. The key is common to both panels. The ω -dependence of V_{SF} is stronger for more nonlocal self-energies. Below band-edges, where $\text{Im}G = 0$, $V_{SF}(\omega)$ has been defined continuous and equal to a constant larger than $\omega + \mu$. In the inset: comparison between the exact solution (7.41) and the first-order perturbative solution of the linearized generalized Sham-Schlüter equation (7.46) in the Hartree-Fock case.

7. Effective potentials and kernels for spectroscopy

the more dynamical V_{SF} becomes. This frequency dependence is an essential property of V_{SF} , which radically distinguishes V_{SF} from the static V_{xc} .

So the effective potential V_{SF} , as the exchange-correlation potential V_{xc} in DFT, is neither an approximation to the self-energy nor a model self-energy. In particular, the frequency dependence of V_{SF} is not the frequency dependence of Σ . The frequency dependence of V_{SF} has instead two contributions. The first contribution (which has not been considered here) stems from the genuine frequency dependence of Σ , i.e. from dynamical correlations. Instead, the second contribution, which is that one considered here, owes its origin just in the reduction of the number of spatial degrees of freedom in V_{SF} with respect to Σ . V_{SF} is local and Σ is nonlocal. The spatial nonlocality of Σ becomes a further frequency dependence in V_{SF} .

Also in this case it is interesting to compare the exact solutions with some common approximations to the exact the Sham-Schlüter equation. In particular, I will examine here the approximation that consists in linearizing the Sham-Schlüter equation replacing G with G_{SF} everywhere in the situation where one considers the unscreened self-energy (i.e. $\lambda = \infty$). The equation to solve is:

$$V_{SF}(\omega) \text{Im} \int \frac{d\mathbf{p}}{(2\pi)^3} G_{SF}^2(\omega, p) = \text{Im} \int \frac{d\mathbf{p}}{(2\pi)^3} G_{SF}^2(\omega, p) \Sigma_x(p), \quad (7.42)$$

where $\Sigma_x(p)$ is the Fock exchange operator.

Once the integrals have been explicitly calculated (see App. C.1), Eq. (7.42) becomes:

$$V_{SF}(\omega) \frac{\pi}{2p_F} \frac{\text{Re}Q(\omega)}{|Q(\omega)|^2} = - \left(\frac{\text{Re}Q(\omega)}{|Q(\omega)|^2} + \frac{1}{2} \ln \left| \frac{Q(\omega) - 1}{Q(\omega) + 1} \right| \right), \quad (7.43)$$

where:

$$Q^2(\omega) = \frac{2}{p_F^2} \left(\omega + \mu - V_{SF}(\omega) + i\eta \text{sgn}(\omega) \right). \quad (7.44)$$

For $\omega + \mu - V_{SF}(\omega) < 0$, one has $\text{Re}Q(\omega) = 0$. In this case both the left-hand-side and the right-hand-side of (7.43) are 0 and there is an infinite number of solutions $V_{SF}(\omega)$. For $\text{Re}Q(\omega) \neq 0$ the solution to Eq. (7.43) is:

$$V_{SF}(\omega) = - \frac{2p_F}{\pi} \left(1 + \frac{|Q(\omega)|^2}{2\text{Re}Q(\omega)} \ln \left| \frac{Q(\omega) - 1}{Q(\omega) + 1} \right| \right). \quad (7.45)$$

The integral equation (7.42) has become a nonlinear equation in $V_{SF}(\omega)$. The first-order perturbative solution is obtained setting $V_{SF} = 0$ in Eq. (7.44), or, equivalently, $G_{SF} = G_H$ in (7.42). In this case one gets:

$$V_{SF} \left(\tilde{\omega} = \frac{\omega + p_F^2/2}{p_F^2/2} \right) = - \frac{2p_F}{\pi} \left(1 + \frac{\sqrt{\tilde{\omega}}}{2} \ln \left| \frac{\sqrt{\tilde{\omega}} - 1}{\sqrt{\tilde{\omega}} + 1} \right| \right), \quad (7.46)$$

7.3 Transforming nonlocality into frequency dependence

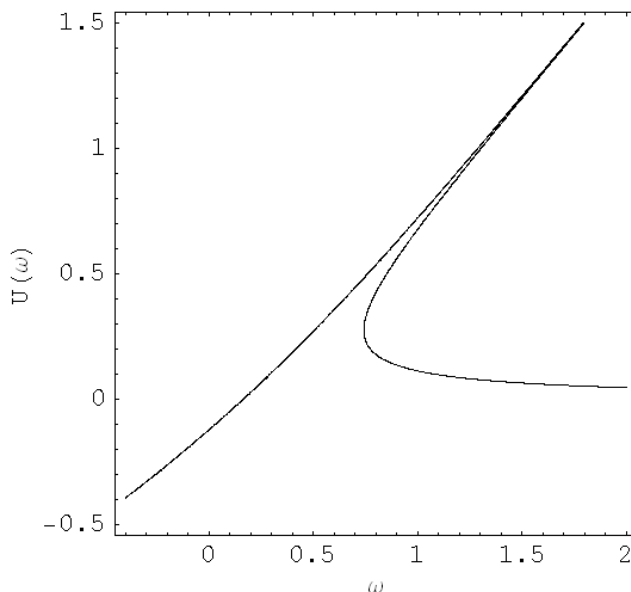


Figure 7.6: Exact solution of the linearized generalized Sham-Schlüter equation (7.45). The plot has been done for the same r_s value as the one used in the calculation of the exact $V_{SF}(\omega)$ in Fig. 7.5. Up to three possible solutions $V_{SF}(\omega)$ at fixed ω are found. Therefore the approximate solution (7.45) of the linearized generalized Sham-Schlüter equation reveals to be substantially different with respect to the exact result (the red curve in the bottom panel of Fig. 7.5).

which shows a logarithmic divergence at the Fermi energy $\omega = 0$ (see the inset of Fig. 7.5). From Eq. (7.40) this means that also the corresponding $\text{Im}G_{SF}(\mathbf{r}, \mathbf{r}', \omega)$ diverges for $\omega = 0$, which is evidently unphysical. This divergence is due to the fact that the Fock self-energy has an infinite spatial range and is not an analytic function at the Fermi energy (at $p = p_F$). And in fact the divergence in the approximate $V_{SF}(\omega)$ disappears when the screening of the Coulomb interaction is taken into account.

It is clear that an iterative solution of the linearized generalized Sham-Schlüter equation (7.42), starting from a divergent solution, is not expected to converge. Anyway, in the nonlinear equation (7.45) the frequency ω can be considered as a parameter. For each ω , one can solve the nonlinear equation in V_{SF} , using standard numerical methods, like the bisection method. The result is shown in Fig. 7.6.

Comparing this self-consistent linearized solution with the exact result (the red curve in the bottom panel of Fig. 7.5), one observes that the approximate solution reveals to be substantially different from the exact one over a wide range of energies. These results demonstrate that the linearization

7. Effective potentials and kernels for spectroscopy

of the Sham-Schlüter equation is a procedure that one has to validate case by case.

It is also interesting to compare the reduced effective potential $V_{SF}(\mathbf{r}, \omega)$ with the approaches of dynamical mean-field theory and spectral-density-functional theory (see Sec. 4.2-4.3), where one is analogously interested in calculating the spectral function $A(\omega)$ using simpler quantities than the full Green's function G . This will be the subject of the next section.

7.4 Spectral density-functional theory

The complex potential of SDFT $V_{SDFT}(\mathbf{r}, \mathbf{r}', \omega)$, introduced in Sec. 4.3, is in principle not known, because it is defined as a functional derivative of an unknown functional (see Eq. (4.37)). Instead, thanks to the generalized Sham-Schlüter approach, it is possible to get an exact alternative definition of V_{SDFT} in terms of quantities that are in principle known, such as G and Σ . This new result could be used to have new physical insights on V_{SDFT} .

The Dyson equation linking V_{SDFT} to Σ is:

$$G(\mathbf{r}_1, \mathbf{r}_2, \omega) = G_{SDFT}(\mathbf{r}_1, \mathbf{r}_2, \omega) + \int d\mathbf{r}_3 d\mathbf{r}_4 G_{SDFT}(\mathbf{r}_1, \mathbf{r}_3, \omega) [\Sigma(\mathbf{r}_3, \mathbf{r}_4, \omega) - V_{SDFT}(\mathbf{r}_3, \mathbf{r}_4, \omega)] G(\mathbf{r}_4, \mathbf{r}_2, \omega). \quad (7.47)$$

$V_{SDFT}(\mathbf{r}_1, \mathbf{r}_2, \omega)$ is the potential that yields $G(\mathbf{r}_1, \mathbf{r}_2, \omega) = G_{SDFT}(\mathbf{r}_1, \mathbf{r}_2, \omega)$ where $\Theta(\Omega_{loc}) = 1$, i.e. for $\mathbf{r}_1 \in \Omega_c$ and $\mathbf{r}_2 \in \Omega_{loc}$ (see Fig. 4.3). Using this condition in (7.47) one gets:

$$V_{SDFT}(\mathbf{r}_5, \mathbf{r}_6, \omega) = \int_{\Omega_C} d\mathbf{r}_1 \int_{\Omega_{loc}} d\mathbf{r}_2 \int d\mathbf{r}_3 d\mathbf{r}_4 \tilde{G}_{SDFT}^{-1}(\mathbf{r}_5, \mathbf{r}_1, \omega) \times \\ \times G_{SDFT}(\mathbf{r}_1, \mathbf{r}_3, \omega) \Sigma(\mathbf{r}_3, \mathbf{r}_4, \omega) G(\mathbf{r}_4, \mathbf{r}_2, \omega) \check{G}^{-1}(\mathbf{r}_2, \mathbf{r}_6, \omega). \quad (7.48)$$

Whereas G^{-1} and G_{SDFT}^{-1} are the full inverse, defined in the whole space (see App. A.4), \tilde{G}_{SDFT}^{-1} and \check{G}^{-1} , if they exist, are the local inverse in Ω_C and Ω_{loc} :

$$\int_{\Omega_C} d\mathbf{r}_3 \tilde{G}_{SDFT}^{-1}(\mathbf{r}_1, \mathbf{r}_3, \omega) G_{SDFT}(\mathbf{r}_3, \mathbf{r}_2, \omega) = \delta(\mathbf{r}_1 - \mathbf{r}_2), \quad (7.49)$$

$$\int_{\Omega_{loc}} d\mathbf{r}_3 G(\mathbf{r}_1, \mathbf{r}_3, \omega) \check{G}^{-1}(\mathbf{r}_3, \mathbf{r}_2, \omega) = \delta(\mathbf{r}_1 - \mathbf{r}_2). \quad (7.50)$$

Eq. (7.48) represents an exact definition of V_{SDFT} . It is an explicit expression for V_{SDFT} in terms of quantities that are in principle known. It is still a nonlinear equation in V_{SDFT} that has to be solved together with the Dyson equation (7.47).

7.5 Density-matrix functional theory

It is interesting here to compare V_{SDFT} with V_{SF} (see Eq. (7.17)). Whereas V_{SF} is a real and local operator, V_{SDFT} is a complex and non-local operator. V_{SDFT} doesn't coincide with Σ either, because V_{SDFT} is short-ranged. It is different from zero only in the region of space where $\Theta(\Omega_{loc}) = 1$, while Σ is defined in the whole space. Moreover, as it has been discussed in Sec. 7.3 for V_{SF} , also V_{SDFT} has a frequency dependence which is not the frequency dependence of Σ . In fact, the conversion of spatial non-locality into frequency dependence to a certain extent (depending on the range of Ω_{loc}) is true also for V_{SDFT} .

The effective potential V_{SDFT} in practical applications is always approximated using (cluster) DMFT. In cluster-DMFT one restricts the functional dependence of the Luttinger-Ward energy functional Γ_{LW} to G_{loc} (see Sec. 4.3). In this way, in the Sham-Schlüter equation (7.48) for V_{SDFT} all the Green's function are replaced by G_{loc} , included in the functional dependence of Σ . Therefore, in the cluster-DMFT approximation, $V_{SDFT}(\mathbf{r}_1, \mathbf{r}_2, \omega) = \Sigma(\mathbf{r}_1, \mathbf{r}_2, \omega)$, where Σ is built using G_{loc} instead of G . Using Eq. (7.48) one could instead directly define new approximations for V_{SDFT} . For example, in DFT Casida [366] and von Barth *et al.* [200] have derived the linearized Sham-Schlüter OEP equation (7.10) for V_{xc} by restricting the variational freedom of the Klein functional $\Gamma_K[G]$ to the domain of the Kohn-Sham Green's function G_{KS} . One could obtain a linearized generalized Sham-Schlüter equation also for V_{SDFT} in a similar manner.

7.5 Density-matrix functional theory

The density matrix is the key variable of density-matrix functional theory (see Sec. 2.1).

The density matrix $\gamma(\mathbf{r}, \mathbf{r}')$ (see Eq. (2.5)) can be calculated from the Green's function G as:

$$\gamma(\mathbf{r}, \mathbf{r}') = -i \int \frac{d\omega}{2\pi} e^{i\omega\eta} G(\mathbf{r}, \mathbf{r}', \omega). \quad (7.51)$$

So one could think to generalize the Sham-Schlüter equation also to calculate $\gamma(\mathbf{r}, \mathbf{r}')$ directly from a reduced potential V_{DM} . One would have:

$$\gamma_{DM}(\mathbf{r}, \mathbf{r}') = -i \int \frac{d\omega}{2\pi} e^{i\omega\eta} G_{DM}(\mathbf{r}, \mathbf{r}', \omega), \quad (7.52)$$

where $G_{DM} = (\omega - h_0 - V_H - V_{DM})^{-1}$.

But γ_{DM} in general cannot be made equal to γ . The former is associated to a Kohn-Sham system of independent particles, described by a Slater determinant. So γ_{DM} is idempotent [72]: $\gamma_{DM}^2 = \gamma_{DM}$. The latter is the true density-matrix of the real interacting system. So it is not idempotent [72]. In other words, a given density matrix cannot be at the same time V-representable and noninteracting V-representable.

7. Effective potentials and kernels for spectroscopy

The density matrix γ can be equal to γ_{DM} when the self-energy is static. In this case one could make the ansatz:

$$\begin{aligned} \int d\mathbf{r}_3 d\mathbf{r}_4 d\omega G_{DM}(\mathbf{r}_1, \mathbf{r}_3, \omega) V_{DM}(\mathbf{r}_3, \mathbf{r}_4) G(\mathbf{r}_4, \mathbf{r}_2, \omega) = \\ = \int d\mathbf{r}_3 d\mathbf{r}_4 d\omega G_{DM}(\mathbf{r}_1, \mathbf{r}_3, \omega) \Sigma(\mathbf{r}_3, \mathbf{r}_4) G(\mathbf{r}_4, \mathbf{r}_2, \omega). \end{aligned} \quad (7.53)$$

But in this one would find, trivially, $V_{DM} = \Sigma$.

Therefore, the density-matrix functional theory represents an example where the generalized Sham-Schlüter approach cannot be applied. This possible generalization of the Sham-Schlüter equation has been studied also by Casida in [366].

7.6 Time-dependent density-functional theory

So far, I have considered only Dyson equations involving one-particle Green's functions. In this and the following section I will show that the generalized Sham-Schlüter approach can be applied equivalently also to Dyson equations between response functions, which are a particular kind of two-particle Green's functions.

The Bethe-Salpeter equation for the four-point irreducible polarizability \tilde{L} reads (see Eq. (5.85)):

$$\begin{aligned} \tilde{L}(1, 2, 3, 4) = L_0(1, 2, 3, 4) + \\ + \int d5678 L_0(1, 2, 5, 6) \Xi(5, 6, 7, 8) \tilde{L}(7, 8, 3, 4), \end{aligned} \quad (7.54)$$

where $\Xi = i\delta\Sigma/\delta G$ is the excitonic four-point kernel. Equivalently in TDDFT the equation for the four-point irreducible polarizability 4P is:

$$\begin{aligned} {}^4P(1, 2, 3, 4) = L_0(1, 2, 3, 4) + \\ + \int d5678 L_0(1, 2, 5, 6) \delta(5, 6) \delta(7, 8) f_{xc}^{(2)}(5, 7) {}^4P(7, 8, 3, 4). \end{aligned} \quad (7.55)$$

In both cases the starting point is L_0 that already includes quasiparticle corrections. So in Eq. (7.55) only the excitonic term $f_{xc}^{(2)}$ of the exchange-correlation kernel of TDDFT appears (see Eq. (5.75)). The two Dyson equations (7.54) and (7.55) can be combined giving:

$$\begin{aligned} \tilde{L}(1, 2, 3, 4) = {}^4P(1, 2, 3, 4) + \\ + \int d5678 {}^4P(1, 2, 5, 6) [\Xi(5, 6, 7, 8) - \delta(5, 6) \delta(7, 8) f_{xc}^{(2)}(5, 7)] \tilde{L}(7, 8, 3, 4). \end{aligned} \quad (7.56)$$

7.6 Time-dependent density-functional theory

In TDDFT $f_{xc}^{(2)}$ is the two-point kernel that yields the correct two-point polarizability $P(1, 2) = {}^4P(1, 1, 2, 2) = \tilde{L}(1, 1, 2, 2)$. Using this condition in Eq. (7.56) one finds:

$$\begin{aligned} \int d5678 {}^4P(1, 1, 5, 6) \Xi(5, 6, 7, 8) \tilde{L}(7, 8, 2, 2) = \\ = \int d57 P(1, 5) f_{xc}^{(2)}(5, 7) P(7, 2), \end{aligned} \quad (7.57)$$

which can be solved for $f_{xc}^{(2)}$ leading to:

$$f_{xc}^{(2)}(3, 4) = \int d125678 P^{-1}(3, 1) {}^4P(1, 1, 5, 6) \Xi(5, 6, 7, 8) \tilde{L}(7, 8, 2, 2) P^{-1}(2, 4). \quad (7.58)$$

This is an exact equation for $f_{xc}^{(2)}$. It is equivalent to Eq. (5.81). In both cases the kernel $f_{xc}^{(2)}$ has been related to many-body quantities, finding an explicit exact expression. The exact kernel (7.58) can be approximated from a first-order linearization of the generalized Sham-Schlüter equation (7.57), setting $P(1, 2) = P_0(1, 2) = -iG(1, 2)G(2, 1)$, ${}^4P(1, 1, 2, 3) = L_0(1, 1, 2, 3) = -iG(1, 2)G(3, 1)$ and $\tilde{L}(1, 2, 3, 3) = L_0(1, 2, 3, 3) = -iG(1, 3)G(3, 2)$ (where G are ‘‘quasiparticle’’ Green’s functions). Moreover, as in standard BSE (see Sec. 5.3.1) Ξ is approximated by $-W$, where in W one takes a statically screened Coulomb interaction (see Eq. (5.55)). In this way one gets:

$$f_{xc}^{(2)}(1, 2) = \int d3456 P_0^{-1}(1, 3) G(3, 4) G(5, 3) W(4, 5) G(4, 6) G(6, 5) P_0^{-1}(6, 2), \quad (7.59)$$

which is rightly the many-body kernel (5.84) obtained in Sec. 5.4.1. In this case the linearization of the generalized Sham-Schlüter equation turns out to be a very good approximation for the calculation of optical spectra (see Fig. 5.1).

Remarkably, in (7.59) while W is static, the kernel $f_{xc}^{(2)}$ is in general frequency dependent. Therefore, also in this case we observe a conversion of spatial nonlocality into a frequency dependence, associated to a reduction of the number of degrees of freedom, when one passes from the four-point \tilde{L} to the two-point P and from the four-point Ξ to the two-point f_{xc} .

$f_{xc}^{(2)}$ is the kernel that reproduces the two-point diagonal part of the four-point irreducible correlation function \tilde{L} : $P(1, 2) = \tilde{L}(1, 1, 2, 2)$. In this sense it plays the same role as V_{SF} with respect to the diagonal part of G (see Sec. 7.2). But in TDDFT one obtains a further advantage. In fact, the Dyson equation between G and Σ involves two-point quantities. When the effective potential V_{SF} is introduced, the simplification is given by the fact that the V_{SF} has a reduced number of degrees of freedom with respect to Σ . But the Dyson equation between G_{SF} and V_{SF} still involves two-point quantities. Here, instead, a great advantage is already given by the structures of the

7. Effective potentials and kernels for spectroscopy

equations themselves. While the Bethe-Salpeter equation is a four-point equation, the TDDFT Dyson equation becomes a two-point equation. So the definition (7.58) of the TDDFT kernel already permits to obtain a great simplification.

Moreover, what is actually measured in experiments like absorption is not the whole two-point polarizability, but only a part of it. So one could think of a further reduced kernel aimed at reproducing only the part of interest of the two-point polarizability. This is what I will discuss in the next section.

7.6.1 The absorption kernel

The absorption spectrum is calculated from (see Eq. (5.37)):

$$\text{Abs}(\omega) = - \lim_{\mathbf{q} \rightarrow 0} \text{Im} \left\{ v_{\mathbf{G}=0}(\mathbf{q}) \int d\mathbf{r}_1 d\mathbf{r}_2 \bar{\chi}(\mathbf{r}_1, \mathbf{r}_2, \omega) e^{i\mathbf{q}(\mathbf{r}_1 - \mathbf{r}_2)} \right\}, \quad (7.60)$$

where $\bar{\chi}$ in TDDFT is obtained directly from the two-point Dyson equation $\bar{\chi} = P + P\bar{v}\bar{\chi}$ and in the BSE approach is obtained from the contraction of the four-point \bar{L} , calculated from the four-point Dyson equation: $\bar{L} = \tilde{L} + \tilde{L}\bar{v}\bar{L}$. So in an absorption spectrum one doesn't measure the whole polarizability $\bar{\chi}$, but only the $\mathbf{q} \rightarrow 0$ limit of $F(\mathbf{q}, \omega)$, where:

$$F(\mathbf{q}, \omega) = \int d\mathbf{r}_1 d\mathbf{r}_2 \bar{\chi}(\mathbf{r}_1, \mathbf{r}_2, \omega) e^{i\mathbf{q}(\mathbf{r}_1 - \mathbf{r}_2)}. \quad (7.61)$$

$F(\mathbf{q}, \omega)$ turns out to be the quantity of interest that is directly measured in the experiments. Therefore one could devise a kernel, f_{abs} , that yields only $F(\mathbf{q}, \omega)$, rather than the whole $\bar{\chi}$. In principle, this kernel f_{abs} could be even simpler than the TDDFT kernel f_{xc} , which has to yield the whole $\bar{\chi}$. Moreover, in this context, \mathbf{q} plays the role of a parameter. For a different \mathbf{q} in $F(\mathbf{q}, \omega)$ one has a different kernel f_{abs} .

In particular I will consider here the ansatz of a dynamical local kernel:

$$f_{abs}(\omega) \delta(5, 6) \delta(7, 8) \delta(5, 7) \quad (7.62)$$

This ansatz can be used in the Dyson equation connecting the four-point \bar{L} with the four point ${}^4\bar{\chi}$:

$$\begin{aligned} \bar{L}(1, 2, 3, 4) &= {}^4\bar{\chi}(1, 2, 3, 4) + \\ &+ \int d5678 {}^4\bar{\chi}(1, 2, 5, 6) \left[\Xi(5, 6, 7, 8) - \delta(5, 6) \delta(7, 8) \delta(5, 7) f_{abs} \right] \tilde{L}(7, 8, 3, 4). \end{aligned} \quad (7.63)$$

The choice of this ansatz is particularly appealing, since f_{abs} is completely spatially local (it is a contact potential). So this could be an important

7.6 Time-dependent density-functional theory

simplification with respect to the f_{xc} kernel, which is a two-point function. The frequency dependence of f_{abs} in part stems from the spatial nonlocality of f_{xc} , in the same way as the frequency dependence of V_{SF} is partly due to the spatial nonlocality of Σ .

Using the usual expression for Ξ (see Eq. (5.55)):

$$\Xi(1, 2, 3, 4) = -\frac{1}{2\pi} W(\mathbf{r}_1, \mathbf{r}_2, \omega = 0) \delta(t_1 - t_2) \delta(1, 3) \delta(2, 4), \quad (7.64)$$

and asking that f_{abs} reproduces $F(\mathbf{q}, \omega)$, from the Dyson equation (7.63) one gets:

$$\begin{aligned} -\frac{1}{2\pi} \int d1256^4 \bar{\chi}(1, 1, 5, 6) W(5, 6) \tilde{L}(5, 6, 2, 2) e^{i\mathbf{q}(\mathbf{r}_1 - \mathbf{r}_2)} = \\ = f_{abs} \int d125^4 \bar{\chi}(1, 1, 5, 5) \bar{L}(5, 5, 2, 2) e^{i\mathbf{q}(\mathbf{r}_1 - \mathbf{r}_2)}. \end{aligned} \quad (7.65)$$

In order to get a practical approximation for f_{abs} , Eq. (7.65) can be linearized similarly to Eq. (7.58), finding:

$$f_{abs} = -\frac{1}{2\pi} \frac{\int d1256 G(1, 5) G(6, 1) W(5, 6) G(5, 2) G(2, 6) e^{i\mathbf{q}(\mathbf{r}_1 - \mathbf{r}_2)}}{\int d125 G(1, 5) G(5, 1) G(5, 2) G(2, 5) e^{i\mathbf{q}(\mathbf{r}_1 - \mathbf{r}_2)}}. \quad (7.66)$$

For each frequency ω and momentum transfer \mathbf{q} , f_{abs} in (7.66) is given by the ratio of two numbers. The numerator of Eq. (7.66) is nothing else than the full kernel (7.59), without the terms P_0^{-1} , where, after a Fourier transform to the reciprocal space, one takes the head (the element $\mathbf{G} = 0, \mathbf{G}' = 0$) of the matrix $GWGG$. The denominator of Eq. (7.66) can be rewritten as:

$$-\int d5 \int d1 \left[-iG(1, 5) G(5, 1) e^{i\mathbf{q}\mathbf{r}_1} \right] \int d2 \left[-iG(5, 2) G(2, 5) e^{-i\mathbf{q}\mathbf{r}_2} \right]. \quad (7.67)$$

So it is given by the product of the wings (the elements $\mathbf{G} = 0$ or $\mathbf{G}' = 0$) of two polarizabilities P_0 written in the reciprocal space.

However, one could further improve the ansatz used here, thanks to the fact that the kernel f_{abs} has an implicit parametrical dependence on the momentum transfer \mathbf{q} . One could explicitly impose to f_{abs} a specific dependence on the momentum transfer \mathbf{q} in order to have a simpler mapping from the full TDDFT kernel f_{xc} . In particular, in Sec. 5.4.1 I discussed how the f_{xc} kernel of TDDFT has to be a long-range term. So one could exploit the available known physical information on f_{xc} to design a better ansatz for f_{abs} where the linearization procedure could lead to better results. In this sense a better ansatz for the reduced kernel f_{abs} could be:

$$\delta(5, 6) \delta(7, 8) \frac{f_{abs}(\omega)}{|\mathbf{r}_5 - \mathbf{r}_7|}, \quad (7.68)$$

7. Effective potentials and kernels for spectroscopy

which would have the same long-range term as the f_{xc} kernel in Eq. (7.59). In this case the denominator of Eq. (7.66) would become:

$$\int d1257G(1,5)G(5,1)v(5,7)G(7,2)G(2,7)e^{i\mathbf{q}(\mathbf{r}_1-\mathbf{r}_2)}, \quad (7.69)$$

which in the reciprocal space is still the products of the wings of two polarizabilities P_0 , one of which is now multiplied by the Coulomb potential v , stemming from the ansatz (7.69).

This equation has been implemented along this way by F. Sottile in the Dp code [358]. Remarkably, as one can see in the upper panel of Fig. 7.7, such a simple kernel is indeed able to reproduce the absorption spectrum of bulk silicon obtained with the full many-body kernel (7.59). But it fails in solid argon (bottom panel of Fig. 7.7), where strong bound excitonic effects are present [236]. In this case the linearization of the generalized Sham-Schlüter equation for f_{abs} turns out to be a too severe approximation.

7.7 Time-dependent current-density-functional theory

As it has been done in Sec. 7.6 with the f_{xc} kernel of TDDFT, the generalized Sham-Schlüter approach can be used also to obtain an exact expression for the $\overleftrightarrow{f}_{xc}$ kernel of TDCDFT. Moreover, along the lines of Eq. (7.59), a new approximation for $\overleftrightarrow{f}_{xc}$ will be suggested.

The irreducible current-current response function $\overleftrightarrow{P}_{\mathbf{jj}}$ can be calculated from the four-point irreducible correlation function \tilde{L} as (see Eq. (5.50)):

$$\overleftrightarrow{P}_{\mathbf{jj}}(1,3) = \frac{1}{2i} \frac{1}{2i} \left[(\nabla_1 - \nabla_2)(\nabla_3 - \nabla_4) \tilde{L}(1,2,3,4) \right]_{2=1^+,4=3^+}. \quad (7.70)$$

Analogously, from the irreducible four-point polarizability in TDCDFT $\overleftrightarrow{P}_{\mathbf{jj}}$ is obtained as:

$$\overleftrightarrow{P}_{\mathbf{jj}}(1,3) = \frac{1}{2i} \frac{1}{2i} \left[(\nabla_1 - \nabla_2)(\nabla_3 - \nabla_4)^4 P(1,2,3,4) \right]_{2=1^+,4=3^+}. \quad (7.71)$$

As in the TDDFT case (see Sec. 7.6), also here I assume that 4P is calculated from L_0 , where the quasiparticle corrections have already been included. So also in this case I will consider only the excitonic part $\overleftrightarrow{f}_{xc}^{(2)}$ of the exchange-correlation kernel $\overleftrightarrow{f}_{xc}$ of the TDCDFT. In TDCDFT the exact two-point kernel $\overleftrightarrow{f}_{xc}^{(2)}$ yields a current-current response function obtained from (7.70) which is the same as the current-current response function (7.71) calculated from the exact Bethe-Salpeter equation. Inserting the condition of equality

7.7 Time-dependent current-density-functional theory

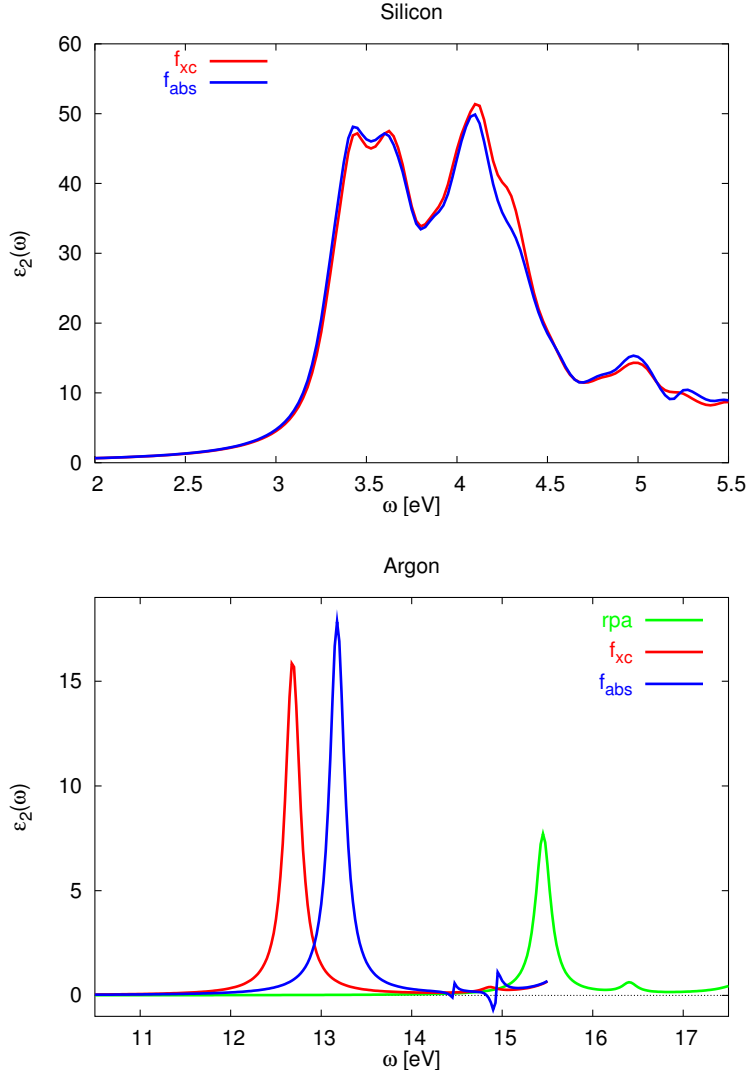


Figure 7.7: (Upper panel) Absorption spectrum of bulk silicon, calculated with 256 shifted \mathbf{k} points. Comparison between the full many-body f_{xc} kernel (see Eq. (7.59)) and the absorption kernel f_{abs} (7.66) for $\mathbf{q} = (0.0001, 0.0002, 0.0003)$. (Bottom panel) Absorption spectrum of solid argon, calculated with 2 \mathbf{k} points. With so few \mathbf{k} points the spectrum is far from being converged. But the strong bound exciton is already clearly visible. In this case the simple kernel f_{abs} is not stable and is not able to reproduce the spectrum obtained with the full many-body f_{xc} kernel, although it creates a bound exciton (for comparison in the picture also the absorption spectrum in RPA is represented). A scissor operator of 6 eV has been used.

7. Effective potentials and kernels for spectroscopy

between the two Eqs. (7.70)-(7.71) in the four-point Dyson equation (7.56), one gets:

$$(\nabla_1 - \nabla_2)(\nabla_3 - \nabla_4) \left\{ \int d5678^4 P(1, 2, 5, 6) [\Xi(5, 6, 7, 8) + \right. \\ \left. - \overleftrightarrow{f}_{xc}^{(2)}(5, 7) \delta(5, 6) \delta(7, 8)] \tilde{L}(7, 8, 3, 4) \right\} = 0, \quad (7.72)$$

that is:

$$\int d5678 (\nabla_1 - \nabla_2)^4 P(1, 2, 5, 6)|_{2=1+} \Xi(5, 6, 7, 8) (\nabla_3 - \nabla_4) \tilde{L}(7, 8, 3, 4)|_{4=3+} = \\ = \int d57 (\nabla_1 - \nabla_2)^4 P(1, 2, 5, 5)|_{2=1+} \overleftrightarrow{f}_{xc}^{(2)}(5, 7) (\nabla_3 - \nabla_4) \tilde{L}(7, 7, 3, 4)|_{4=3+}. \quad (7.73)$$

The generalized Sham-Schlüter equation (7.73) represents an exact definition of $\overleftrightarrow{f}_{xc}^{(2)}$, analogous to the one obtained for the $f_{xc}^{(2)}$ kernel in TDDFT (see Eq. (7.58)). In fact, one could use a unified quadrivector formalism, considering at the same time both TDDFT and TDCDFT.

Linearizing (7.73) one obtains a new approximation for $\overleftrightarrow{f}_{xc}^{(2)}$:

$$\overleftrightarrow{f}_{xc}^{(2)}(3, 4) = (\overleftarrow{P}_{0,j\rho})^{-1}(3, 1)^3 \overleftarrow{P}_{0,j\rho}(1, 5, 6) \times \\ \times W(5, 6)^3 \overrightarrow{P}_{0,\rho j}(5, 6, 2) (\overrightarrow{P}_{0,\rho j})^{-1}(2, 4), \quad (7.74)$$

where I have defined the independent-particle response functions as:

$$\overleftarrow{P}_{0,j\rho}(1, 3) = \frac{1}{2i} \left[(\nabla_1 - \nabla_2) L_0(1, 2, 3, 3^+) \right]_{2=1+}, \quad (7.75)$$

$$\overrightarrow{P}_{0,\rho j}(1, 3) = \frac{1}{2i} \left[(\nabla_3 - \nabla_4) L_0(1, 1^+, 3, 4) \right]_{4=3+}, \quad (7.76)$$

$${}^3\overleftarrow{P}_{0,j\rho}(1, 3, 4) = \frac{1}{2i} \left[(\nabla_1 - \nabla_2) L_0(1, 2, 3, 4) \right]_{2=1+}, \quad (7.77)$$

$${}^3\overrightarrow{P}_{0,\rho j}(1, 2, 3) = \frac{1}{2i} \left[(\nabla_3 - \nabla_4) L_0(1, 2, 3, 4) \right]_{4=3+}. \quad (7.78)$$

So far in TDCDFT $\overleftrightarrow{f}_{xc}$ has been mostly employed as a local functional of the current [265][266] (see Sec. 5.5). Recently also an approximation in the exact-exchange framework has been proposed [261][200], but it has been applied only to the homogeneous electron gas. From the experience in TDDFT we know that the screening of the Coulomb interaction is of fundamental importance in the f_{xc} kernel [375]. For this reason a pure TDEXX (without any further spatial cutoff in the Coulomb interaction [376])

7.7 Time-dependent current-density-functional theory

is not a good approximation for the calculation of absorption spectra in solids. As in the many-body TDDFT kernel of Sec. 7.6, in Eq. (7.74) instead the screening is taken into account, thanks to the presence of the statically screened W . So Eq. (7.74) represents an alternative approximation for the TDCDFT kernel whose validity one could try to explore.

All the examples presented in this chapter have demonstrated that the generalized Sham-Schlüter approach is a very powerful tool. It permits to define a general scheme for the introduction of ad hoc effective potentials and kernels aimed at the direct calculation of the quantities of interest, which otherwise would be calculated from contractions of one-particle or two-particle Green's functions. The general approach has been successfully applied in very different contexts, ranging from a potential for photoemission to a kernel for absorption, from SDFT to TDCDFT.

Chapter 8

Conclusions

Our point of view has radically changed since Dirac's times. It is true that the full solution of the many-body Schrödinger equation (1.1) is out of reach. But the calculation of the many-body wavefunction is usually not even desirable [377]. In fact one generally would like to find answers only to limited questions, like the excitation energies measured in a spectroscopy experiment. In order to reduce the complexity of the problem, a successful strategy is then to work directly with reduced quantities that are able to provide the particular searched answers.

A prominent example is the one-particle Green's function G , whose poles correspond to the quasiparticle excitations measured in photoemission. The Green's function G is the key quantity of many-body perturbation theory (MBPT), where one defines an effective Hamiltonian containing the self-energy, a nonlocal, dynamical and complex potential that accounts for relaxation, exchange and correlation effects in the electronic systems.

In this thesis I have made use of many-body methods to calculate the photoemission spectra of vanadium dioxide, which is a prototype material for the discussion of correlation effects in solids. In particular, I have adopted Hedin's GW approximation to Σ [127]. In this framework, I have shown that correlation effects in the photoemission spectra of both the metallic and the insulating phases of VO_2 are correctly reproduced, provided that quasiparticle energies and wavefunctions are calculated self-consistently. Moreover, I have discussed the failure of the standard perturbative GW method [130] to describe the spectrum of the insulating phase. This failure has essentially to be ascribed to the underestimation of the spatial anisotropy of the top-valence LDA wavefunctions which are used to calculate the GW perturbative corrections. In fact, the orbital switching of these states is the main responsible of the transition from the isotropic metal to the electronically more one-dimensional insulator. If this effect is not properly accounted for, as in LDA, then the system remains metallic. In order to get rid of the LDA starting point, I have performed a self-consistent calculation at the

8. Conclusions

COHSEX level, a static approximation of the GW self-energy. The result of the COHSEX calculation has been used as input for a fully dynamical final perturbative GW calculation. The resulting spectra are in good agreement with recent experiments [293].

Beyond the quasiparticle picture, the photoemission spectrum of the metallic phase displays a satellite feature, which is instead absent in the insulating phase. In the electron energy-loss spectrum of the metal a sharp peak is found at the same energy as the binding energy of the satellite in the PES. This peak disappears in the insulating spectrum. The calculations have proved that this peak in the EELS is associated to a zero of the real part of the dielectric function. So it is a plasmon. Therefore also the satellite in the photoemission spectrum can be explained as due to the plasmon resonance of the energy-loss function.

Hence the MBPT approach has demonstrated to be successful also in the case of vanadium dioxide. The intuitive physical many-body picture indeed permits to find working strategies, like the GW approximation. Therefore MBPT is used also when in principle one could employ more simplified approaches, in particular, DFT-based ones. The latter lead to more efficient schemes, but in these cases finding good approximations is more difficult. Many-body methods are computationally expensive because one calculates more information than needed. In the MBPT framework, measurable spectra are in fact obtained from contractions of one-particle or two-particle Green's functions. Nonetheless, this surplus of information can be actually extremely precious in helping to find good approximations for DFT-based schemes. The combination of the two approaches in the recent past has already proved to be a rewarding strategy [253]. For instance, it has been possible to derive from the Bethe-Salpeter equation an exchange-correlation kernel in TDDFT that is able to describe absorption and energy-loss spectra of a wide range of materials [207].

In this thesis I have studied the Sham-Schlüter equation, which permits to establish a direct link between the many-body and density-functional worlds. I have considered a possible generalization of the Sham-Schlüter approach for other quantities besides the electronic density. This generalization has permitted to formulate a very general scheme for the design of *ad hoc* effective potentials and kernels for a direct, and in principle exact, calculation of the answers to the limited questions one generally has. As a particular example of this general approach, I have introduced an effective “photoemission potential” that yields the trace of the spectral function which is measured in photoemission experiments. This effective potential turns out to be dynamical but local and real. In particular, I have shown in two model examples that an important contribution to its frequency dependence stems from the spatial nonlocality of the corresponding self-energy. I have discussed other generalizations of the Sham-Schlüter equation in various contexts: from spectral density-functional theory to linear response in

TDDFT and TDCDFT. I have proved that the conversion of spatial non-locality into frequency dependence is a general feature that one encounters whenever an effective potential or kernel with a reduced number of spatial degrees of freedom is introduced.

In studying possible approximations for these potentials and kernels I have recovered the many-body TDDFT kernel. I have also derived an analogous many-body kernel in the TDCDFT framework whose validity would be interesting to assess. Moreover, I have shown that an OEP-like linearization of the generalized Sham-Schlüter equation is a delicate operation that one has to validate case by case. This result leaves open the way to find working approximations, in particular for the photoemission potential. Currently I am exploring the possibility to formulate local approximations to it. The possibility to use a simplified potential, instead of the complicate self-energy, would be very useful, especially when self-consistency is important, as in the case of vanadium dioxide. At the same time, it could be helpful to exploit it also in calculations that need to include vertex corrections beyond the GW approximation (see also App. B).

A particularly important field of applications for the first-principles methods employed in this thesis is for sure constituted by strongly correlated systems. In this context, after the calculation of the electronic properties of VO_2 , one could address its optical spectra, that require to take into account excitonic effects, for instance using the Bethe-Salpeter approach or the simpler TDDFT scheme. Then, the next natural candidate to be studied could be vanadium sesquioxide (V_2O_3). Stoichiometric V_2O_3 , at ambient pressure, undergoes a transition from an antiferromagnetic insulator to a paramagnetic metal and represents the prototype of Mott-Hubbard insulator.

Extending the application of well grounded first-principles methods to the more correlated system, more complex physical aspects have to be taken into account. This implies that also the self-energy becomes a more complicate object to deal with. At the same time, the increased complexity requires to introduce simplified approaches in order to keep the problem practically tractable.

This is what I have started to learn in this thesis.

Appendix A

Derivation of some equations in MBPT

A.1 Equation of motion of the Green's function

The Hamiltonian of a system interacting via a two-particle Coulomb potential v can be written in second quantization as:

$$\hat{H} = \int d\mathbf{r}_1 \hat{\psi}^\dagger(\mathbf{r}_1) h_0(\mathbf{r}_1) \hat{\psi}(\mathbf{r}_1) + \frac{1}{2} \int d\mathbf{r}_1 d\mathbf{r}_2 \hat{\psi}^\dagger(\mathbf{r}_1) \hat{\psi}^\dagger(\mathbf{r}_2) v(|\mathbf{r}_1 - \mathbf{r}_2|) \hat{\psi}(\mathbf{r}_2) \hat{\psi}(\mathbf{r}_1), \quad (\text{A.1})$$

where h_0 is the one-particle term of the Hamiltonian $h_0(\mathbf{r}_1) = -\nabla_1^2/2 + V_{ext}(\mathbf{r}_1)$ and $\hat{\psi}(\mathbf{r}_1)$ are fermionic field operators that anticommute according to $\{\hat{\psi}(\mathbf{r}_1), \hat{\psi}(\mathbf{r}_2)\} = 0$ and $\{\hat{\psi}(\mathbf{r}_1), \hat{\psi}^\dagger(\mathbf{r}_2)\} = \delta(\mathbf{r}_1 - \mathbf{r}_2)$.

The equations of motion for the field operators in the Heisenberg picture are:

$$\begin{aligned} i \frac{\partial}{\partial t_1} \hat{\psi}(1) &= h_0(1) \hat{\psi}(1) + \int d2 v(1, 2) \hat{\psi}^\dagger(2) \hat{\psi}(2) \hat{\psi}(1), \\ i \frac{\partial}{\partial t_1} \hat{\psi}^\dagger(1) &= -h_0(1) \hat{\psi}^\dagger(1) - \hat{\psi}^\dagger(1) \int d2 v(1, 2) \hat{\psi}^\dagger(2) \hat{\psi}(2). \end{aligned} \quad (\text{A.2})$$

where 1 is a shorthand notation for $\mathbf{r}_1 t_1 \sigma_1$. Since:

$$i \frac{\partial}{\partial t} \hat{\psi}(1) = [\hat{\psi}(1), \hat{H}] = e^{i\hat{H}t} [\hat{\psi}(\mathbf{r}), \hat{H}] e^{-i\hat{H}t}, \quad (\text{A.3})$$

in order to get the first of (A.2), one has then to evaluate commutators like (see (A.1)): $[\hat{\psi}(\mathbf{r}), \hat{\psi}^\dagger(\mathbf{r}_1) \hat{\psi}(\mathbf{r}_1)]$ and $[\hat{\psi}(\mathbf{r}), \hat{\psi}^\dagger(\mathbf{r}_1) \hat{\psi}^\dagger(\mathbf{r}_2) \hat{\psi}(\mathbf{r}_2) \hat{\psi}(\mathbf{r}_1)]$. Analogously for the equation of motion for $\hat{\psi}^\dagger(1)$.

The Green's function is defined as (see Eq. (3.1)):

$$G(1, 2) = -i \langle N | T [\hat{\psi}(1) \hat{\psi}^\dagger(2)] | N \rangle, \quad (\text{A.4})$$

A. Derivation of some equations in MBPT

where $|N\rangle$ is the exact ground state of the interacting system and $\hat{\psi}$ are Heisenberg operators. From the definition of T -product:

$$G(1, 2) = -i[\theta(t_1 - t_2)\langle N|\hat{\psi}(1)\hat{\psi}^+(2)|N\rangle - \theta(t_2 - t_1)\langle N|\hat{\psi}^+(2)\hat{\psi}(1)|N\rangle]. \quad (\text{A.5})$$

Calculating the $\partial/\partial t_1$ derivative of G , for the first term in the right-hand-side of (A.5), one has:

$$\begin{aligned} \frac{\partial}{\partial t_1} \left[\theta(t_1 - t_2)\langle N|\hat{\psi}(1)\hat{\psi}^+(2)|N\rangle \right] &= \\ &= \left[\frac{\partial}{\partial t_1}\theta(t_1 - t_2) \right] \langle N|\hat{\psi}(1)\hat{\psi}^+(2)|N\rangle + \theta(t_1 - t_2)\langle N|\frac{\partial}{\partial t_1}\hat{\psi}(1)\hat{\psi}^+(2)|N\rangle. \end{aligned} \quad (\text{A.6})$$

Analogously for the second term. Since:

$$\frac{\partial}{\partial t_1}\theta(t_1 - t_2) = -\frac{\partial}{\partial t_1}\theta(t_2 - t_1) = \delta(t_1 - t_2), \quad (\text{A.7})$$

and, summing up the derivatives of the the two terms in Eq. (A.5), one has:

$$i\frac{\partial}{\partial t_1}G(1, 2) = -i(i)\delta(1, 2) - i\langle N|T\left[i\frac{\partial}{\partial t_1}\hat{\psi}(1)\hat{\psi}^+(2)\right]|N\rangle. \quad (\text{A.8})$$

Using the equation of motion (A.2) for the field operators in (A.8), one gets:

$$\begin{aligned} i\frac{\partial}{\partial t_1}G(1, 2) &= \delta(1, 2) - ih_0(1)\langle N|T[\hat{\psi}(1)\hat{\psi}^+(2)]|N\rangle + \\ &\quad - i \int d3 v(1, 3)\langle N|T[\hat{\psi}^+(3)\hat{\psi}(3)\hat{\psi}(1)\hat{\psi}^+(2)]|N\rangle. \end{aligned} \quad (\text{A.9})$$

Since field operators inside the T-product can be exchanged:

$$\begin{aligned} T[\hat{\psi}^+(3^+)\hat{\psi}(3)\hat{\psi}(1)\hat{\psi}^+(2)] &= T[\hat{\psi}(3)\hat{\psi}(1)\hat{\psi}^+(3^+)\hat{\psi}^+(2)] \\ T[\hat{\psi}(3)\hat{\psi}(1)\hat{\psi}^+(3^+)\hat{\psi}^+(2)] &= -T[\hat{\psi}(1)\hat{\psi}(3)\hat{\psi}^+(3^+)\hat{\psi}^+(2)], \end{aligned} \quad (\text{A.10})$$

and, defining the two-particle Green's function as:

$$G_2(1, 2, 3, 4) = (-i)^2\langle N|T[\hat{\psi}(1)\hat{\psi}(2)\hat{\psi}^+(4)\hat{\psi}^+(3)]|N\rangle, \quad (\text{A.11})$$

one finally obtains:

$$\left[i\frac{\partial}{\partial t_1} - h_0(1) \right] G(1, 2) = \delta(1, 2) - i \int d3 v(1, 3)G_2(1, 3, 2, 3^+). \quad (\text{A.12})$$

A.2 Schwinger's functional derivative

In presence of an external perturbing potential V_{per} , the total Hamiltonian becomes:

$$\hat{H}_{tot} = \hat{H} + \hat{H}_1, \quad (\text{A.13})$$

where \hat{H} is given by Eq. (A.1) and the perturbation is:

$$\hat{H}_1 = \int d1 \hat{\psi}^\dagger(1) V_{per}(1) \hat{\psi}(1). \quad (\text{A.14})$$

The perturbation V_{per} will be made vanish at the end of the derivation.

In this case it is more convenient to adopt an interaction picture [119], where operators still evolve according to the unperturbed hamiltonian \hat{H} (see (A.3)) and states evolve between two times t and t' according to:

$$|\Psi(t')\rangle = \hat{U}(t', t) |\Psi(t)\rangle, \quad (\text{A.15})$$

where the time-evolution operator $\hat{U}(t, t')$ has been introduced.

The time-evolution operators form a unitary group and satisfy the equations of motion:

$$\begin{aligned} i \frac{\partial}{\partial t} \hat{U}(t, t') &= \hat{H}_1(t) \hat{U}(t, t'), \\ i \frac{\partial}{\partial t'} \hat{U}(t, t') &= -\hat{U}(t, t') \hat{H}_1(t), \end{aligned} \quad (\text{A.16})$$

with the boundary condition $\hat{U}(t, t) = 1$. The formal solution to these equations is:

$$\hat{U}(t, t') = T \exp \left(-i \int_{t'}^t dt_1 \hat{H}_1(t_1) \right). \quad (\text{A.17})$$

In this way the Green's function is redefined as [127][119]:

$$G(1, 2) = -i \frac{\langle N | T [\hat{U}(-\infty, +\infty) \hat{\psi}(1) \hat{\psi}^\dagger(2)] | N \rangle}{\langle N | \hat{U}(-\infty, +\infty) | N \rangle}, \quad (\text{A.18})$$

where $|N\rangle$ is some state of the system with $\hat{H}_1 = 0$. This definition coincides with Eq. (3.1) when $\hat{H}_1 = 0$ and $|N\rangle$ is the ground state.

I will now demonstrate that for $t < t_1 < t'$, or $t' < t_1 < t$:

$$\frac{\delta \hat{U}(t, t')}{\delta V_{per}(1)} = -i \text{sgn}(t - t') \hat{U}(t, t_1) \hat{\psi}^\dagger(1) \hat{\psi}(1) \hat{U}(t_1, t'). \quad (\text{A.19})$$

If t_1 doesn't belong to the interval $[t, t']$ (or $[t', t]$), then the derivative is 0. Note that when $t = t'$, (A.19) is nomore defined.

A. Derivation of some equations in MBPT

When the perturbing potential changes as: $V_{per} \rightarrow V'_{per} = V_{per} + \delta V_{per}$, the evolution operator changes as: $\hat{U} \rightarrow \hat{U} + \delta\hat{U}$. The first of the equations of motion (A.16) has to be rewritten as:

$$i \frac{\partial}{\partial t} [\hat{U}(t, t') + \delta\hat{U}(t, t')] = [\hat{H}_1(t) + \delta\hat{H}_1(t)] [\hat{U}(t, t') + \delta\hat{U}(t, t')]. \quad (\text{A.20})$$

Keeping only the first-order terms, one has:

$$i \frac{\partial}{\partial t} \delta\hat{U}(t, t') = \delta\hat{H}_1(t) \hat{U}(t, t') + \hat{H}_1(t) \delta\hat{U}(t, t'). \quad (\text{A.21})$$

It can be verified that the solution of (A.21) is, for $t > t'$:

$$\delta\hat{U}(t, t') = -i \int_{t'}^t dt_1 \hat{U}(t, t_1) \delta\hat{H}_1(t_1) \hat{U}(t_1, t'), \quad (\text{A.22})$$

which, once the functional derivative is performed, proves (A.19) for $t' < t_1 < t$. The same procedure can be similarly applied for the second of (A.16), for which it holds analogously:

$$i \frac{\partial}{\partial t'} \delta\hat{U}(t, t') = -\hat{U}(t, t') \delta\hat{H}_1(t') - \delta\hat{U}(t, t') \hat{H}_1(t'). \quad (\text{A.23})$$

Now, combining this result with the following general rule for the functional derivatives [119]:

$$\frac{\delta}{\delta v(y)} \left[\frac{N[v(x)]}{D[v(x)]} \right] = \frac{1}{D^2[v(x)]} \left[\frac{\delta N[v(x)]}{\delta v(y)} D[v(x)] - N[v(x)] \frac{\delta D[v(x)]}{\delta v(y)} \right], \quad (\text{A.24})$$

it is possible to evaluate $\delta G(12)/\delta V_{per}(3)$, with the result [126][378]:

$$\frac{\delta G(1, 2)}{\delta V_{per}(3)} = G(3, 3^+) G(1, 2) - G_2(1, 3, 2, 3^+). \quad (\text{A.25})$$

A.3 The Dyson equation

The equation of motion of the full Green's function G and the Hartree Green's function G_H are:

$$\left[i \frac{\partial}{\partial t_1} - h_0(1) - V_H(1) \right] G(1, 2) = \delta(1, 2) + \int d3 \Sigma(1, 3) G(3, 2), \quad (\text{A.26})$$

$$\left[i \frac{\partial}{\partial t_1} - h_0(1) - V_H(1) \right] G_H(1, 2) = \delta(1, 2). \quad (\text{A.27})$$

The Hartree Green's function is the resolvent of the Hartree Hamiltonian (built with the exact density of the system):

$$G_H^{-1}(1, 2) = \left[i \frac{\partial}{\partial t_1} - h_0(1) - V_H(1) \right] \delta(1, 2). \quad (\text{A.28})$$

A.4 Derivative of the identity

Inserting (A.28) in (A.26) leads to:

$$\int d3[G_H^{-1}(1, 3) - \Sigma(1, 3)]G(3, 2) = \delta(12). \quad (\text{A.29})$$

Multiplying (A.29) on the right with $G^{-1}(24)$, one has:

$$G_H^{-1}(1, 2) - \Sigma(1, 2) = G^{-1}(1, 2). \quad (\text{A.30})$$

Finally, the Dyson equation:

$$G(1, 2) = G_H(1, 2) + \int d34G_H(1, 3)\Sigma(3, 4)G(4, 2) \quad (\text{A.31})$$

is obtained by multiplying (A.30) on the left with $G_H(3, 1)$ and on the right with $G(2, 4)$.

A.4 Derivative of the identity

A Green's function G and its inverse G^{-1} are defined by:

$$\int d3G^{-1}(1, 3)G(3, 2) = \delta(1, 2). \quad (\text{A.32})$$

Deriving (A.32) with respect to the external potential V_{per} yields:

$$\int d3G^{-1}(1, 3)\frac{\delta G(3, 2)}{\delta V_{per}(4)} = - \int d3\frac{\delta G^{-1}(1, 3)}{\delta V_{per}(4)}G(3, 2), \quad (\text{A.33})$$

which can be solved for $\delta G/\delta V_{per}$:

$$\frac{\delta G(1, 2)}{\delta V_{per}(3)} = - \int d45G(1, 4)\frac{\delta G^{-1}(4, 5)}{\delta V_{per}(4)}G(5, 2). \quad (\text{A.34})$$

It is interesting to note that by adding to (A.34) an arbitrary function C that satisfies $G^{-1}C = 0$ another solution of (A.33) can be found [379]. But if we consider G for the ground state only, then C must be zero.

A.5 Hedin's equations

The definition of the time-ordered screening

$$\epsilon^{-1}(1, 2) = \frac{\delta V_{tot}(1)}{\delta V_{per}(2)}, \quad (\text{A.35})$$

where V_{tot} is the total classic potential, sum of the Hartree potential V_H and the perturbing potential V_{per} , permits to rewrite the equation (3.33) for the self energy Σ

$$\Sigma(1, 2) = -i \int d34v(1^+, 3)G(1, 4)\frac{\delta G^{-1}(4, 2)}{\delta V_{per}(3)} \quad (\text{A.36})$$

A. Derivation of some equations in MBPT

as:

$$\begin{aligned}\Sigma(1, 2) &= -i \int d345 v(1^+, 3) G(1, 4) \frac{\delta G^{-1}(4, 2)}{\delta V_{tot}(5)} \frac{\delta V_{tot}(5)}{\delta V_{per}(3)} = \\ &= -i \int d345 v(1^+, 3) G(1, 4) \frac{\delta G^{-1}(4, 2)}{\delta V_{tot}(5)} \epsilon^{-1}(5, 3).\end{aligned}\quad (\text{A.37})$$

Defining the screened potential W and the (irreducible) vertex as (see also Eq. (3.40)):

$$W(1, 2) = \int d3 \epsilon^{-1}(1, 3) v(3, 2), \quad (\text{A.38})$$

$$\Gamma(1, 2, 3) = -\frac{\delta G^{-1}(1, 2)}{\delta V_{tot}(3)}, \quad (\text{A.39})$$

one gets:

$$\Sigma(1, 2) = i \int d34 G(1, 3) W(1, 4) \Gamma(3, 2, 4). \quad (\text{A.40})$$

As for the reducible vertex $\tilde{\Gamma}$ (see Eq. (3.37)), thanks to the Dyson equation (3.29) $G^{-1} = G_H^{-1} - \Sigma$, the equation (A.39) for vertex Γ can be rewritten as:

$$\Gamma(1, 2, 3) = \delta(1, 3) \delta(1, 2) + \int d4567 \frac{\delta \Sigma(1, 2)}{\delta G(4, 5)} G(4, 6) \Gamma(6, 7, 3) G(7, 5). \quad (\text{A.41})$$

Moreover, from the definition (A.35) of ϵ^{-1} , one can explicitly write:

$$\epsilon^{-1}(1, 2) = \delta(1, 2) + \int d3 v(1, 3) \chi(3, 2), \quad (\text{A.42})$$

where the reducible polarizability $\chi(32) = \delta\rho(1)/\delta V_{per}(2)$ has been introduced. Using the chain rule:

$$\chi(1, 2) = \int d3 \frac{\delta\rho(1)}{\delta V_{tot}(3)} \frac{\delta V_{tot}(3)}{\delta V_{per}(2)}, \quad (\text{A.43})$$

the (irreducible) polarizability $P(1, 3) = \delta\rho(1)/\delta V_{tot}(3)$ can be similarly defined. The combination of (A.35) and (A.43):

$$\chi(1, 2) = \int d3 P(1, 3) \epsilon^{-1}(3, 2), \quad (\text{A.44})$$

used together with (A.28), yields a Dyson equation linking χ to P :

$$\chi(1, 2) = P(1, 2) + \int d34 P(1, 3) v(3, 4) \chi(4, 2). \quad (\text{A.45})$$

It is important to remind that the polarizabilities appearing in these equations are all time-ordered quantities. The fact that the density ρ is $\rho(1) =$

A.6 How to get a two-point Bethe-Salpeter equation?

$-iG(1, 1^+)$ and the derivative of the identity (A.34) performed with respect to V_{tot} permit to write an equation for P :

$$P(1, 2) = -i \int d34 G(1, 3) \Gamma(3, 4, 2) G(4, 1^+). \quad (\text{A.46})$$

Finally, combining its definition (A.38) with Eqs. (A.42) and (A.44), one obtains a Dyson equation also for W :

$$W(1, 2) = v(1, 2) + \int d34 v(1, 3) P(3, 4) W(4, 2). \quad (\text{A.47})$$

The four equations (A.40), (A.41), (A.46) and (A.47), together with the Dyson equation (3.30), constitute the closed set of Hedin's equations.

A.6 How to get a two-point Bethe-Salpeter equation?

The Bethe-Salpeter equation is a four-point equation, as extensively discussed in Sec. 5.3. Nevertheless, in this section I will show how it is possible to derive a two-point approximation to the exact BSE simply by making the hypothesis that the ‘‘quasiparticle Green's function’’ G_{QP} stems from a local potential. G_{QP} is defined as the Kohn-Sham Green's function where the Kohn-Sham eigenvalues are replaced by the quasiparticle energies, which include GW corrections.

The Bethe-Salpeter equation reads (sums over repeated indexes are understood):

$$L(1, 2, 3, 4) = L_0(1, 2, 3, 4) + L_0(1, 2, 5, 6) [v(5, 7) \delta(5, 6) \delta(7, 8) + \Xi(5, 6, 7, 8)] L(7, 8, 3, 4). \quad (\text{A.48})$$

The many-body excitonic kernel

$$\Xi(5, 6, 7, 8) = i \frac{\delta \Sigma(5, 6)}{\delta G(7, 8)} \quad (\text{A.49})$$

is usually approximated by taking $\Sigma(5, 6) = iG(5, 6)W(5, 6)$. In this way one gets:

$$L(1, 2, 3, 4) = L_0(1, 2, 3, 4) + L_0(1, 2, 5, 6) [v(5, 7) \delta(5, 6) \delta(7, 8) - W(5, 6) \delta(5, 7) \delta(6, 8)] L(7, 8, 3, 4). \quad (\text{A.50})$$

But in actual calculations $\Sigma(5, 6) = iG_{QP}(5, 6)W(5, 6)$, where W is the RPA screened interaction and G_{QP} is the ‘‘quasiparticle’’ Green's function. Here

A. Derivation of some equations in MBPT

I will explicitly show how the BSE is modified by taking into account the derivative of $iG_{QP}(5, 6)W(5, 6)$.

Using the chain rule $\delta\Sigma/\delta G = (\delta\Sigma/\delta G_{QP})(\delta G_{QP}/\delta G)$ and neglecting, as usual, the derivative $\delta W/\delta G$, one has:

$$\frac{\delta\Sigma(5, 6)}{\delta G(7, 8)} = \frac{\delta\Sigma(5, 6)}{\delta G_{QP}(9, 10)} \frac{\delta G_{QP}(9, 10)}{\delta G(7, 8)} = iW(5, 6)\delta(5, 9)\delta(6, 10) \frac{\delta G_{QP}(9, 10)}{\delta G(7, 8)}. \quad (\text{A.51})$$

Making the hypothesis that G_{QP} stems from a local potential, one has

$$\frac{\delta G_{QP}(9, 10)}{\delta G(7, 8)} = -iG_{QP}(5, 9)\chi_{QP}^{-1}(9, 10)\delta(7, 10)\delta(8, 10)G_{QP}(9, 6). \quad (\text{A.52})$$

So the direct term $W(5, 6)\delta(5, 7)\delta(6, 8)$ in the original BSE (A.50) turns out to be replaced by:

$$iW(5, 6)G_{QP}(5, 9)\chi_{QP}^{-1}(9, 7)G_{QP}(9, 6)\delta(7, 8). \quad (\text{A.53})$$

Defining the new kernel $f(5, 6, 7) = iW(5, 6)G_{QP}(5, 9)\chi_{QP}^{-1}(9, 7)G_{QP}(9, 6)$, the Bethe-Salpeter equation becomes:

$$L(1, 2, 3, 4) = L_0(1, 2, 3, 4) + L_0(1, 2, 5, 6)[v(5, 7)\delta(5, 6)\delta(7, 8) + f(5, 6, 7)\delta(7, 8)]L(7, 8, 3, 4). \quad (\text{A.54})$$

This equation has a three-point kernel instead of a four-point kernel, as the original one (see Eq. (A.50)). Therefore it can be contracted directly to a two-point equation, by considering $\chi(1, 2) = L(1, 1, 2, 2)$. This contraction immediately gives:

$$\chi(1, 2) = P_0(1, 2) + P_0^{(3)}(1; 5, 6)[v(5, 7)\delta(5, 6) + f(5, 6, 7)]\chi(7, 2). \quad (\text{A.55})$$

Introducing the identity $\delta(1, 3) = P_0(1, 4)P_0^{-1}(4, 3)$, (A.55) can be rewritten as:

$$\chi(1, 2) = P_0(1, 2) + P_0(1, 4)P_0^{-1}(4, 3)P_0^{(3)}(3; 5, 6)[v(5, 7)\delta(5, 6) + f(5, 6, 7)]\chi(7, 2), \quad (\text{A.56})$$

which is the two-point equation:

$$\chi(1, 2) = P_0(1, 2) + P_0(1, 3)F(3, 4)\chi(4, 2), \quad (\text{A.57})$$

having introduced the kernel $F(3, 4) = P_0^{-1}(3, 5)P_0^{(3)}(5; 6, 7)[v(6, 4)\delta(6, 7) + f(6, 7, 4)]$.

Appendix B

Density functional in the Dyson equation

In Sec. 5.4.1 I have shown how F. Bruneval *et al.* [253] have introduced the density-functional concept in the many-body framework, finding a simpler equation for the vertex function Γ . Analogously, here I will discuss that, thanks to the Runge-Gross theorem, it is possible also to rewrite the Dyson equation between G_H and G .

The self-energy is implicitly defined by (see Eq. (3.26)):

$$\int d4\Sigma(3, 4)G(4, 2) = i \int d4v(3, 4) \frac{\delta G(3, 2)}{\delta V_{per}(4)}. \quad (\text{B.1})$$

Here $\delta G(3, 2)/\delta V_{per}(4)$ is nothing else than a three-point reducible polarizability χ^3 (see Eq. (A.43)). So the Dyson equation (B.4) can be rewritten as:

$$G(1, 2) = G_H(1, 2) + \int d3456 G_H(1, 3)v(3, 5)\chi(5, 6)\chi^{-1}(6, 4)\chi^3(3, 2; 4) \quad (\text{B.2})$$

where the identity $\chi\chi^{-1} = 1$ has been inserted.

The scope of MBPT is the calculation of the Green's function G . The important observation to make here is that in Eq. (B.2) there is no need to introduce the self-energy in order to calculate G . From Eq. (B.2) the Green's function G can be obtained by making use only of response functions, whose calculation has been discussed in Chapter 5.

Moreover, thanks to the Runge-Gross theorem (see Sec. 5.4), it is possible to use the chain rule $\delta G/\delta V_{per} = (\delta G/\delta \rho)(\delta \rho/V_{per})$ in Eq. (B.1) and get:

$$\begin{aligned} \int d4\Sigma(3, 4)G(4, 2) &= i \int d45v(3, 4) \frac{\delta G(3, 2)}{\delta \rho(5)} \frac{\delta \rho(5)}{\delta V_{per}(4)} = \\ &= i \int d45v(3, 4)\chi(5, 4) \frac{\delta G(3, 2)}{\delta \rho(5)}. \end{aligned} \quad (\text{B.3})$$

B. Density functional in the Dyson equation

where, contrary to TDDFT, χ , like all the other quantities used here, is a time-ordered polarizability. Inserting this relation into the Dyson equation (3.30):

$$G(1, 2) = G_H(1, 2) + \int d34 G_H(1, 3) \Sigma(3, 4) G(4, 2), \quad (\text{B.4})$$

one has the final result

$$G(12) = G_H(1, 2) + i \int d345 G_H(1, 3) v(3, 4) \chi(5, 4) \frac{\delta G(3, 2)}{\delta \rho(5)}. \quad (\text{B.5})$$

where $G_H = [\omega - h_0 - V_H(1, 2)]^{-1}$ is the resolvent of the Hartree term of the full Hamiltonian (i.e. it is built using the exact electronic density, not the density obtained in the Hartree approximation).

The interesting result found here is that also in this other equation for G the self-energy Σ doesn't appear anymore. All the many-body effects are hidden in the term $\delta G / \delta \rho$. If one were able to find a good approximation for this term, one would obtain G directly, without using Σ . A first approximation of this term could be $\delta G / \delta \rho = G_{KS} \chi_{KS}^{-1} G_{KS}$, stemming from the approximation $G = G_{KS}$ in $\delta G / \delta \rho$. χ_{KS}^{-1} has poles that lie between the poles of χ_{KS} , which are in correspondence to the Kohn-Sham one-particle transitions. As shown by F. Sottile *et al.* [236], when these poles are in the quasiparticle band gap, they give rise to spurious structures in the absorption spectra. A better approximation to $\delta G / \delta \rho$ would be instead to use a quasiparticle Green's function G_{QP} and get: $\delta G / \delta \rho = G_{QP} P_0^{-1} G_{QP}$ with the hypothesis that G_{QP} derives from a local potential. G_{QP} is built with Kohn-Sham eigenfunctions and eigenvalues with self-energy corrections included and P_0 has poles in correspondence to differences between quasiparticle energies.

Appendix C

Integral equations

If the self-energy Σ and the full Green's function G are assigned, the generalized Sham-Schlüter equation

$$\begin{aligned} \int d\mathbf{r}_3 V_{SF}(\mathbf{r}_3, \omega) \text{Im}[G_{SF}(\mathbf{r}_1, \mathbf{r}_3, \omega)G(\mathbf{r}_3, \mathbf{r}_1, \omega)] = \\ = \int d\mathbf{r}_3 d\mathbf{r}_4 \text{Im}[G_{SF}(\mathbf{r}_1, \mathbf{r}_3, \omega)\Sigma(\mathbf{r}_3, \mathbf{r}_4, \omega)G(\mathbf{r}_4, \mathbf{r}_1, \omega)] \end{aligned} \quad (\text{C.1})$$

together with the Dyson equation:

$$\begin{aligned} G(\mathbf{r}_1, \mathbf{r}_2, \omega) = G_{SF}(\mathbf{r}_1, \mathbf{r}_2, \omega) + \\ + \int d\mathbf{r}_3 d\mathbf{r}_4 G_{SF}(\mathbf{r}_1, \mathbf{r}_3, \omega)[\Sigma(\mathbf{r}_3, \mathbf{r}_4, \omega) - V_{SF}(\mathbf{r}_3, \omega)\delta(\mathbf{r}_3 - \mathbf{r}_4)]G(\mathbf{r}_4, \mathbf{r}_2, \omega) \end{aligned} \quad (\text{C.2})$$

constitute a set of two equations for two unknowns, G_{SF} and V_{SF} , that have to be solved self-consistently.

In particular, Eq. (C.1) is a Fredholm integral equation of the first kind in V_{SF} . For each frequency ω , it can be cast in the form:

$$\int dx_2 A(x_1, x_2)U(x_2) = F(x_1). \quad (\text{C.3})$$

If the kernel A can be written as:

$$A(x_1, x_2) = \sum_i D_i(x_1)H_i(x_2), \quad (\text{C.4})$$

it follows:

$$\int dx_2 A(x_1, x_2)U(x_2) = \sum_i D_i(x_1) \int dx_2 H_i(x_2)U(x_2) = F(x_1), \quad (\text{C.5})$$

C. Integral equations

whence the necessary condition:

$$F(x_1) = \sum_i \alpha_i D_i(x_1), \quad (\text{C.6})$$

where $\alpha_i = \langle H_i | U \rangle$. The general solution of Eq. (C.4) is [380]:

$$U(x_1) = \sum_i \beta_i H_i(x_1), \quad (\text{C.7})$$

with:

$$\beta = \Gamma^{-1} \alpha, \quad (\text{C.8})$$

where $\Gamma_{ij} = \langle H_i | H_j \rangle$. So Γ_{ij} must define an invertible matrix. In fact, putting $U(x_2) = \sum_j \beta_j H_j(x_2)$ in Eq. (C.4) one finds:

$$\int dx_2 \sum_i D_i(x_1) H_i(x_2) \sum_j \beta_j H_j(x_2) = \sum_{ij} D_i(x_1) \beta_j \Gamma_{ij} = F(x_1), \quad (\text{C.9})$$

which, compared with (C.6), yields: $\alpha_i = \sum_j \Gamma_{ij} \beta_j$ and therefore (C.8). Moreover, if $\tilde{U}(x_2) = U(x_2) + \Phi(x_2)$ with $\langle H_i | \Phi \rangle = 0 \forall i$, then also \tilde{U} is a solution of Eq. (C.4).

C.1 Linearization of the generalized Sham-Schlüter equation in HEG

In this section I will explicitly calculate the integrals in the linearized generalized Sham-Schlüter equation (7.42) for V_{SF} in the homogeneous electron gas in the situation where the self-energy is the exchange Fock operator.

The equation to solve is:

$$V_{SF}(\omega) \text{Im} \int \frac{d\mathbf{p}}{(2\pi)^3} G_{SF}^2(\omega, p) = \text{Im} \int \frac{d\mathbf{p}}{(2\pi)^3} G_{SF}^2(\omega, p) \Sigma_x(p), \quad (\text{C.10})$$

where $\Sigma_x(p)$ is:

$$\Sigma_x(p) = - \int \frac{d\mathbf{p}'}{(2\pi)^3} \theta(p_F - p') \frac{4\pi}{|\mathbf{p} - \mathbf{p}'|}. \quad (\text{C.11})$$

Setting $k = p/p_F$, one has explicitly [50]:

$$\Sigma_x(k) = - \frac{p_F}{\pi} \left(1 + \frac{1 - k^2}{2k} \ln \left| \frac{1 + k}{1 - k} \right| \right), \quad (\text{C.12})$$

which is nonanalytic in $k = 1$ (see Eq. (1.36)). I will follow here the derivation of I. Tokatly [371]. The Green's function $G_{SF}(\omega, p)$ (7.39) can be rewritten as:

$$G_{SF}(\omega, k) = \frac{2}{p_F^2} \frac{2}{Q^2(\omega) - k^2}, \quad (\text{C.13})$$

C.1 Linearization of the generalized Sham-Schlüter equation

where $k = p/p_F$ and $Q^2(\omega) = (2/p_F^2)[\omega + \mu - V_{SF}(\omega) + i\eta \text{sgn}(\omega)]$. So, for the left-hand-side of Eq. (C.10), one has:

$$\begin{aligned} \int \frac{d\mathbf{p}}{(2\pi)^3} G_{SF}^2(\omega, p) &= \frac{4}{p_F^4} \frac{1}{2} \int_{-\infty}^{+\infty} p_F dk \frac{4\pi p_F^2 k^2}{8\pi^3} \frac{4}{(Q^2 - k^2)^2} = \\ &= \frac{4}{\pi^2 p_F} \int_{-\infty}^{+\infty} dk \frac{k^2}{(Q^2 - k^2)^2} = \\ &= \frac{4}{\pi^2 p_F} \int_{-\infty}^{+\infty} dk \frac{k^2}{(Q+k)^2(Q-k)^2}. \end{aligned} \quad (\text{C.14})$$

I use the residue theorem to calculate the last integral. The contribution deriving from the upper semicircle centered at the origin and radius R vanishes for $R \rightarrow \infty$ since the integrand behaves like $1/k^2$ for $k \rightarrow \infty$ [381]. The integrand has a second-order pole for $k = \pm Q$. If $\text{Im}Q > 0$ I close the contour in the upper complex half-plane. This contour includes the pole $k = Q$. The residue is:

$$\left[\frac{d}{dk} \frac{k^2}{(Q+k)^2} \right]_{y=Q} = \frac{1}{4Q}. \quad (\text{C.15})$$

If $\text{Im}Q < 0$ I close the contour in the lower complex half-plane. This contour includes the pole $k = -Q$. The residue at $k = -Q$ has the opposite sign with respect to the residue at $k = Q$, which is compensated by the fact that the contour is now closed in the clockwise direction. So:

$$\int \frac{d\mathbf{p}}{(2\pi)^3} G_{SF}^2(\omega, p) = \frac{4}{\pi^2 p_F} \frac{2\pi i}{4Q} = \frac{2i}{\pi p_F Q}. \quad (\text{C.16})$$

For the right-hand-side of Eq. (C.10) one has to calculate the integral:

$$\begin{aligned} -4 \int \frac{d\mathbf{k}}{8\pi^3} \frac{d\mathbf{q}}{8\pi^3} \theta(1-q) \frac{4\pi}{|\mathbf{k}-\mathbf{q}|} \frac{4}{(k^2 - Q^2)^2} = \\ = -\frac{4}{\pi^3} \int_0^1 dq q^2 \int_0^\pi d\theta \sin \theta \int_{-\infty}^{+\infty} dk \frac{k^2}{(k^2 - Q^2)^2 (k^2 + q^2 - 2kq \cos \theta)}, \end{aligned} \quad (\text{C.17})$$

where $k = p/p_F$ and $q = p'/p_F$. The last term can be rewritten as:

$$\frac{k^2}{(k^2 - Q^2)^2 (k^2 + q^2 - 2kq \cos \theta)} = \frac{k^2}{(k - Q)^2 (k + Q)^2 (k - qe^{i\theta})(k + qe^{i\theta})}. \quad (\text{C.18})$$

The integral in k can be done using the residue theorem. For $\text{Im}Q > 0$ I close the contour in the upper half-plane. There are two poles: the second-order pole $k = Q$ and the first-order pole $k = qe^{i\theta}$. For $\text{Im}Q < 0$, the contour is in the lower half-plane, the residues have opposite sign, and the integration

C. Integral equations

is in the opposite direction. So the result is the same. The integral over the residue of the pole $k = qe^{i\theta}$ is zero:

$$\begin{aligned} \int_0^\pi d\theta \frac{2\pi i q^2 e^{i2\theta} \sin \theta}{(q^2 e^{i2\theta} - Q^2)^2 q (e^{i\theta} - e^{-i\theta})} &= \int_0^\pi d\theta \frac{\pi q e^{i2\theta}}{(q^2 e^{i2\theta} - Q^2)^2} = \\ &= \frac{\pi}{2} \int_0^{2\pi} d\phi \frac{q e^{i\phi}}{(q^2 e^{i\phi} - Q^2)^2} = \frac{\pi}{2i} \oint_{|z|=1} dz \frac{q}{(q^2 z - Q^2)^2} = 0. \end{aligned} \quad (\text{C.19})$$

The residue of the second-order pole in $k = Q$ is:

$$\left[\frac{d}{dk} \frac{k^2}{(k+Q)^2 (k^2 + q^2 - 2kq \cos \theta)} \right]_{y=Q} = \frac{q^2 - Q^2}{4Q(q^2 - 2qQ \cos \theta)^2}. \quad (\text{C.20})$$

So:

$$-4 \int \frac{d\mathbf{k}}{8\pi^3} \frac{d\mathbf{q}}{8\pi^3} \theta(1-q) \frac{4\pi}{|\mathbf{k}-\mathbf{q}|} \frac{4}{(k^2 - Q^2)^2} = \quad (\text{C.21})$$

$$= -\frac{4}{\pi^3} \frac{2\pi i}{4Q} \int_0^1 dq q^2 \int_0^\pi d\theta \sin \theta \frac{q^2 - Q^2}{(q^2 - 2qQ \cos \theta)^2} = \quad (\text{C.22})$$

$$= -\frac{2i}{\pi^2 Q} \int_0^1 dq q^2 \int_{-1}^{+1} dx \frac{q^2 - Q^2}{(q^2 + Q^2 - 2Qqx)^2} = \quad (\text{C.23})$$

$$= -\frac{4i}{\pi^2 Q} \int_0^1 dq q^2 \frac{q^2}{q^2 - Q^2}, \quad (\text{C.24})$$

which yields the final result:

$$-\frac{4i}{\pi^2 Q} \left[1 - \frac{Q}{2} \ln \left| \frac{Q+1}{Q-1} \right| \right]. \quad (\text{C.25})$$

Hence Eq. (C.10) results:

$$V_{SF}(\omega) \text{Im} \left\{ \frac{2i}{\pi p_F Q(\omega)} \right\} = -\text{Im} \left\{ \frac{4i}{\pi^2 Q(\omega)} \left[1 - \frac{Q(\omega)}{2} \ln \left| \frac{Q(\omega)+1}{Q(\omega)-1} \right| \right] \right\}, \quad (\text{C.26})$$

and then (see Eq. (7.43)):

$$V_{SF}(\omega) \frac{\pi}{2p_F} \frac{\text{Re}Q(\omega)}{|Q(\omega)|^2} = -\left(\frac{\text{Re}Q(\omega)}{|Q(\omega)|^2} + \frac{1}{2} \ln \left| \frac{Q(\omega)-1}{Q(\omega)+1} \right| \right). \quad (\text{C.27})$$

In particular, if $\text{Re}Q(\omega) = 0$ both sides are 0.

C.2 Screened-exchange self-energy in HEG

In this section I will calculate the general form of the screened-exchange self-energy in the homogeneous electron gas that is plotted, for some values of

C.2 Screened-exchange self-energy in HEG

the screening length λ , in the top panel of Fig. 7.5. The self-energy defined in the real space reads:

$$\Sigma_\lambda(\mathbf{r} - \mathbf{r}') = iG(\mathbf{r} - \mathbf{r}', t - t^+) \frac{1}{|\mathbf{r} - \mathbf{r}'|} e^{-|\mathbf{r} - \mathbf{r}'|/\lambda} \quad (\text{C.28})$$

and in the Fourier space (introducing $k_\lambda = \lambda^{-1}$):

$$\begin{aligned} \Sigma_\lambda(p) &= - \int \frac{d\mathbf{q}}{8\pi^3} \frac{4\pi\theta(p_F - q)}{|\mathbf{p} - \mathbf{q}|^2 + k_\lambda^2} = - \frac{1}{\pi} \int_0^{p_F} q^2 dq \int_{-1}^{+1} \frac{dx}{p^2 + q^2 - 2pqx + k_\lambda^2} = \\ &= - \frac{1}{\pi} \left\{ \int_0^{p_F} dq \frac{q^2}{2pq} \ln[(p+q)^2 + k_\lambda^2] - \int_0^{p_F} dq \frac{q^2}{2pq} \ln[(p-q)^2 + k_\lambda^2] \right\} = \\ &= - \frac{1}{2p\pi} \left\{ \left[\frac{1}{2} k_\lambda^2 \ln[(p+q)^2 + k_\lambda^2] - 2pk_\lambda \tan^{-1} \left(\frac{p+q}{k_\lambda} \right) + \right. \right. \\ &\quad \left. \left. - \frac{1}{2} (p+q)^2 + 2p(p+q) + \frac{1}{2} (q^2 - p^2) \ln[(p+q)^2 + k_\lambda^2] \right] + \right. \\ &\quad \left. - \left[\frac{1}{2} k_\lambda^2 \ln[(p-q)^2 + k_\lambda^2] - 2pk_\lambda \tan^{-1} \left(\frac{p-q}{k_\lambda} \right) + \right. \right. \\ &\quad \left. \left. - \frac{1}{2} (p-q)^2 + 2p(p-q) + \frac{1}{2} (q^2 - p^2) \ln[(p-q)^2 + k_\lambda^2] \right] \right\}_0^{p_F}. \end{aligned} \quad (\text{C.29})$$

The final result is [382]:

$$\begin{aligned} \Sigma_\lambda(p) &= - \frac{1}{2p\pi} \left\{ \frac{1}{2} (p_F^2 + k_\lambda^2 - p^2) \ln \left[\frac{(p+p_F)^2 + k_\lambda^2}{(p-p_F)^2 + k_\lambda^2} \right] + \right. \\ &\quad \left. + 2pk_\lambda \left[\tan^{-1} \left(\frac{p-p_F}{k_\lambda} \right) - \tan^{-1} \left(\frac{p+p_F}{k_\lambda} \right) \right] + 2p_F p \right\}. \end{aligned} \quad (\text{C.30})$$

In particular, in the limit $\lambda \rightarrow \infty$, that is $k_\lambda \rightarrow 0$, the Hartree-Fock self-energy $\Sigma_\lambda(p)$ is recovered:

$$\begin{aligned} \Sigma_\lambda(p) &\rightarrow - \frac{1}{2p\pi} \left(\frac{1}{2} (p_F^2 - p^2) 2 \ln \left| \frac{p+p_F}{p-p_F} \right| + 2p_F p \right) = \\ &= - \frac{p_F}{\pi} \left(1 + \frac{p_F^2 - p^2}{2p_F p} \ln \left| \frac{p+p_F}{p-p_F} \right| \right) = \Sigma_x(p). \end{aligned} \quad (\text{C.31})$$

Using the self-energy (C.30) it is possible to calculate $\text{Im}G(\mathbf{r}, \mathbf{r}', \omega)$ and then use Eq. (7.41) to obtain V_{SF} .

List of Publications

- *Transforming Nonlocality into a Frequency Dependence: A Shortcut to Spectroscopy*
Matteo Gatti, Valerio Olevano, Lucia Reining, and Ilya V. Tokatly
Phys. Rev. Lett. **99**, 057401 (2007)
- *Understanding Correlations in Vanadium Dioxide from first principles*
Matteo Gatti, Fabien Bruneval Valerio Olevano, and Lucia Reining
Phys. Rev. Lett. (accepted)
- *Design of effective potentials and kernels for spectroscopy*
Matteo Gatti, Valerio Olevano, Lucia Reining, and Ilya V. Tokatly
(in preparation)
- *Self-consistent quasiparticle calculations of electronic excitations in VO₂*
Matteo Gatti, Fabien Bruneval Valerio Olevano, and Lucia Reining
(in preparation)
- *Dynamical local density approximation for photoemission spectroscopy*
Matteo Gatti, Valerio Olevano, Lucia Reining, and Ilya V. Tokatly
(in preparation)
- *A many-body kernel for time-dependent current-density-functional theory*
Matteo Gatti
(in preparation)

Bibliography

- [1] See e.g. <http://www.etsf.eu>.
- [2] G. Onida, L. Reining, and A. Rubio, *Rev. Mod. Phys.* **74**, 601 (2002).
- [3] F. Bruneval, Ph.D. thesis, École Polytechnique, Palaiseau (France), 2005.
- [4] F. Sottile, Ph.D. thesis, École Polytechnique, Palaiseau (France), 2003.
- [5] S. Albrecht, Ph.D. thesis, École Polytechnique, Palaiseau (France), 1999.
- [6] P. A. M. Dirac, *Proc. Roy. Soc. A* **123**, 714 (1929).
- [7] F. Scott Fitzgerald, *The Great Gatsby* (Charles Scribner's Sons, New York (USA), 1925).
- [8] T. Kuhn, *The structure of scientific revolutions* (University of Chicago Press, Chicago (USA), 1962).
- [9] M. Born and R. Oppenheimer, *Ann. Phys.* **84**, 457 (1927).
- [10] H. Jahn and E. Teller, *Proc. Roy. Soc. A* **161**, 220 (1937).
- [11] E. Morin, *La Méthode, La connaissance de la connaissance (vol. 3)* (Éditions du Seuil, Paris (France), 1986).
- [12] W. D. Knight, K. Clemenger, W. A. de Heer, W. A. Saunders, M. Y. Chou, and M. L. Cohen, *Phys. Rev. Lett.* **52**, 2141 (1984).
- [13] H. W. Kroto, *Nature* **329**, 529 (1987).
- [14] M. Doverstål, B. Lindgren, U. Sassenberg, and H. Yu, *Phys. Scr.* **43**, 572 (1991).
- [15] N. W. Ashcroft and N. D. Mermin, *Solid state physics* (Holt, Rinehart and Winston, New York, 1976).
- [16] W. Kohn, *Rev. Mod. Phys.* **71**, S59 (1999).

Bibliography

- [17] F. Bloch, *Z. Phys.* **52**, 553 (1928).
- [18] A. H. Wilson, *Proc. Roy. Soc. A* **133**, 458 (1931).
- [19] M. L. Cohen and V. Heine, in *Solid State Physics*, edited by H. Ehrenreich, F. Seitz, and D. Turnbull (Academic Press, New York, 1970), Vol. 24.
- [20] G. E. Moore, *Electronics* **38**, (1965).
- [21] W. Kohn, *Phys. Rev.* **133**, A171 (1964).
- [22] I. Souza, T. Wilkens, and R. M. Martin, *Phys. Rev. B* **62**, 1666 (2000).
- [23] R. Resta, *Phys. Rev. Lett.* **96**, 137601 (2006).
- [24] R. Resta, *Rev. Mod. Phys.* **66**, 899 (1994).
- [25] L. Landau, *Sov. Phys. JETP* **3**, 920 (1957).
- [26] L. Landau, *Sov. Phys. JETP* **5**, 101 (1957).
- [27] D. Pines, *The many-body problem* (W. A. Benjamin, Inc., New York, 1961).
- [28] R. Q. Hood, M. Y. Chou, A. J. Williamson, G. Rajagopal, R. J. Needs, and W. M. C. Foulkes, *Phys. Rev. Lett.* **78**, 3350 (1997).
- [29] H. Hertz, *Ann. Phys.* **17**, 983 (1887).
- [30] A. Einstein, *Ann. Phys.* **31**, 132 (1905).
- [31] C.-O. Almbladh and L. Hedin, in *Handbook on Synchrotron Radiation*, edited by E. E. Koch (North-Holland, Amsterdam, 1983).
- [32] C.-O. Almbladh, *J. Phys.: Conference Ser.* **35**, 127 (2006).
- [33] G. Onida, Lecture notes, 2003, unpublished.
- [34] L. Hedin, J. Michiels, and J. Inglesfield, *Phys. Rev. B* **58**, 15565 (1998).
- [35] L. Hedin, *J. Phys.: Condens. Matter* **11**, R489 (1999).
- [36] A. Zangwill, *Physics at surfaces* (Cambridge University Press, Cambridge, 1988).
- [37] G. Panaccione, M. Altarelli, A. Fondacaro, A. Georges, S. Huotari, P. Lacovig, A. Lichtenstein, P. Metcalf, G. Monaco, F. Offi, L. Paolasini, A. Poteryaev, O. Tjernberg, and M. Sacchi, *Phys. Rev. Lett.* **97**, 116401 (2006).

-
- [38] A. Damascelli, Z. Hussain, and Z.-X. Shen, *Rev. Mod. Phys.* **75**, 473 (2003).
- [39] J. D. Jackson, *Classical electrodynamics* (John Wiley & Sons, New York, 1962).
- [40] G. Grosso and G. Pastori Parravicini, *Solid state physics* (Academic Press, San Diego, 2000).
- [41] H. Lüth, *Solid surfaces, interfaces and thin films* (Springer-Verlag, Berlin, 2001).
- [42] R. Del Sole and R. Girlanda, *Phys. Rev. B* **48**, 11789 (1993).
- [43] J. E. Müller and J. W. Wilkins, *Phys. Rev. B* **29**, 4331 (1984).
- [44] R. Broglia, G. Colò, G. Onida, and H. Roman, *Solid state physics of finite systems: metal clusters, fullerenes, atomic wires* (Springer-Verlag, Berlin, 2004).
- [45] M. Haverkort, Ph.D. thesis, Universität zu Köln, Köln (Germany), 2005.
- [46] J. J. Rehr and R. C. Albers, *Rev. Mod. Phys.* **72**, 621 (2000).
- [47] D. Hartree, *Proc. Cambridge Philos. Soc.* **24**, 89 (1928).
- [48] V. Fock, *Z. Phys.* **61**, 126 (1930).
- [49] K. Burke, *The ABC of DFT*, 2003, (unpublished), <http://dft.rutgers.edu/kieron/beta>.
- [50] G. D. Mahan, *Many-particle physics* (Plenum Press, New York, 1981).
- [51] M. Gell-Mann and K. A. Brueckner, *Phys. Rev.* **106**, 364 (1957).
- [52] T. Koopmans, *Physica* **1**, 104 (1933).
- [53] R. W. Godby and I. D. White, *Phys. Rev. Lett.* **80**, 3161 (1998).
- [54] R. W. Godby and P. García-González, in *A primer in Density Functional Theory*, edited by C. Fiolhais, F. Nogueira, and M. A. L. Marques (Springer-Verlag, Berlin, 2003).
- [55] G. Giuliani and G. Vignale, *Quantum theory of the electron liquid* (Cambridge University Press, Cambridge, 2005).
- [56] E. Wigner, *Trans. Farad. Soc.* **34**, 678 (1938).
- [57] N. F. Mott, *Proc. Phys. Soc. A* **62**, 416 (1949).

Bibliography

- [58] J. Hubbard, Proc. Roy. Soc. A **276**, 238 (1963).
- [59] J. C. Slater, Phys. Rev. **82**, 538 (1951).
- [60] R. E. Peierls, *Quantum theory of solids* (Oxford University Press, Oxford, 1955).
- [61] A. Georges, cond-mat/0403123.
- [62] J. Zaanen, G. A. Sawatzky, J. Fink, W. Speier, and J. C. Fuggle, Phys. Rev. B **32**, 4905 (1985).
- [63] G. A. Sawatzky and J. W. Allen, Phys. Rev. Lett. **53**, 2339 (1984).
- [64] A. Fujimori, I. Hase, H. Namatame, Y. Fujishima, Y. Tokura, H. Eisaki, S. Uchida, K. Takegahara, and F. M. F. de Groot, Phys. Rev. Lett. **69**, 1796 (1992).
- [65] R. M. Dreizler and E. K. U. Gross, *Density functional theory* (Springer-Verlag, Berlin, 1990).
- [66] K. Capelle, cond-mat/0211443.
- [67] R. van Leeuwen, Adv. Quant. Chem. **43**, 24 (2003).
- [68] M. Levy, Proc. Nat. Acad. Sci. USA **76**, 6062 (1979).
- [69] N. N. Lathiotakis, N. Helbig, and E. K. U. Gross, Phys. Rev. B **75**, 195120 (2007).
- [70] N. Helbig, N. N. Lathiotakis, M. Albrecht, and E. K. U. Gross, Europhys. Lett. **77**, 67003 (2007).
- [71] T. L. Gilbert, Phys. Rev. B **12**, 2111 (1975).
- [72] E. K. U. Gross, E. Runge, and O. Heinonen, *Many-particle theory* (Adam Hilger, Bristol, 1991).
- [73] P. Hohenberg and W. Kohn, Phys. Rev. **136**, B864 (1964).
- [74] W. Kohn and L. J. Sham, Phys. Rev. **140**, A1133 (1965).
- [75] J. T. Chayes, L. Chayes, and M. B. Ruskai, J. Stat. Phys. **38**, 497 (1985).
- [76] R. Dreizler, in *A primer in Density Functional Theory*, edited by C. Fiolhais, F. Nogueira, and M. A. L. Marques (Springer-Verlag, Berlin, 2003).

-
- [77] R. van Leeuwen and E. K. U. Gross, in *Time-dependent density functional theory*, edited by M. A. L. Marques, C. A. Ullrich, F. Nogueira, A. Rubio, K. Burke, and E. K. U. Gross (Springer, Heidelberg, 2006).
- [78] M. Lüders, M. A. L. Marques, N. N. Lathiotakis, A. Floris, G. Profeta, L. Fast, A. Continenza, S. Massidda, and E. K. U. Gross, *Phys. Rev. B* **72**, 024545 (2005).
- [79] E. H. Lieb, *Int. J. Quantum Chem.* **24**, 243 (1982).
- [80] E. Smargiassi and P. A. Madden, *Phys. Rev. B* **49**, 5220 (1994).
- [81] L. H. Thomas, *Proc. Camb. Phil. Soc.* **23**, 542 (1927).
- [82] E. Fermi, *Rend. Accad. Lincei* **6**, 602 (1927).
- [83] P. A. M. Dirac, *Proc. Camb. Phil. Soc.* **26**, 376 (1930).
- [84] C. F. von Weizsacker, *Z. Phys.* **96**, 431 (1935).
- [85] E. Engel and R. M. Dreizler, *J. Phys. B: At. Mol. Opt. Phys.* **22**, 1901 (1989).
- [86] C.-O. Almbladh and U. von Barth, *Phys. Rev. B* **31**, 3231 (1985).
- [87] X. Gonze, P. Ghosez, and R. W. Godby, *Phys. Rev. Lett.* **74**, 4035 (1995).
- [88] J. P. Perdew and M. Levy, *Phys. Rev. Lett.* **51**, 1884 (1983).
- [89] L. J. Sham and M. Schlüter, *Phys. Rev. Lett.* **51**, 1888 (1983).
- [90] D. M. Ceperley and B. J. Alder, *Phys. Rev. Lett.* **45**, 566 (1980).
- [91] J. P. Perdew and Y. Wang, *Phys. Rev. B* **45**, 13244 (1992).
- [92] O. Gunnarsson and B. I. Lundqvist, *Phys. Rev. B* **13**, 4274 (1976).
- [93] R. O. Jones and O. Gunnarsson, *Rev. Mod. Phys.* **61**, 689 (1989).
- [94] J. P. Perdew, K. Burke, and M. Ernzerhof, *Phys. Rev. Lett.* **77**, 3865 (1996).
- [95] Y. M. Niquet, M. Fuchs, and X. Gonze, *Phys. Rev. A* **68**, 032507 (2003).
- [96] J. F. Dobson and J. Wang, *Phys. Rev. Lett.* **82**, 2123 (1999).
- [97] M. Fuchs and X. Gonze, *Phys. Rev. B* **65**, 235109 (2002).
- [98] A. Marini, P. García-González, and A. Rubio, *Phys. Rev. Lett.* **96**, 136404 (2006).

Bibliography

- [99] H. Rydberg, B. I. Lundqvist, D. C. Langreth, and M. Dion, *Phys. Rev. B* **62**, 6997 (2000).
- [100] J. P. Perdew and A. Zunger, *Phys. Rev. B* **23**, 5048 (1981).
- [101] A. Görling and M. Levy, *Phys. Rev. A* **50**, 196 (1994).
- [102] Z. Szotek, W. M. Temmerman, D. Ködderitzsch, A. Svane, L. Petit, and H. Winter, *Phys. Rev. B* **74**, 174431 (2006).
- [103] R. T. Sharp and G. K. Horton, *Phys. Rev.* **90**, 317 (1953).
- [104] J. D. Talman and W. F. Shadwick, *Phys. Rev. A* **14**, 36 (1976).
- [105] E. Engel, in *A primer in Density Functional Theory*, edited by C. Fiolhais, F. Nogueira, and M. A. L. Marques (Springer-Verlag, Berlin, 2003).
- [106] J. B. Krieger, Y. Li, and G. J. Iafrate, *Phys. Lett. A* **146**, 256 (1990).
- [107] M. Städele, J. A. Majewski, P. Vogl, and A. Görling, *Phys. Rev. Lett.* **79**, 2089 (1997).
- [108] M. Städele, M. Moukara, J. A. Majewski, P. Vogl, and A. Görling, *Phys. Rev. B* **59**, 10031 (1999).
- [109] R. J. Magyar, A. Fleszar, and E. K. U. Gross, *Phys. Rev. B* **69**, 045111 (2004).
- [110] M. Grüning, A. Marini, and A. Rubio, *J. Chem. Phys.* **124**, 154108 (2006).
- [111] M. Grüning, A. Marini, and A. Rubio, *Phys. Rev. B* **74**, 161103 (2006).
- [112] R. W. Godby, M. Schlüter, and L. J. Sham, *Phys. Rev. B* **36**, 6497 (1987).
- [113] H. J. Monkhorst and J. D. Pack, *Phys. Rev. B* **13**, 5188 (1976).
- [114] S. Botti, Ph.D. thesis, Università di Pavia, Pavia (Italy), 2002.
- [115] G. B. Bachelet, D. R. Hamann, and M. Schlüter, *Phys. Rev. B* **26**, 4199 (1982).
- [116] R. P. Feynman, *Phys. Rev.* **56**, 340 (1939).
- [117] A. L. Fetter and J. D. Walecka, *Quantum theory of Many-Particle Systems* (MacGraw-Hill, New York, 1971).

- [118] L. Hedin and S. Lundqvist, in *Solid State Physics*, edited by H. Ehrenreich, F. Seitz, and D. Turnbull (Academic Press, New York, 1969), Vol. 23.
- [119] G. Strinati, *Rivista del Nuovo Cimento* **11**, (12)1 (1988).
- [120] W. G. Aulbur, L. Jönsson, and J. W. Wilkins, *Solid State Phys.* **54**, 1 (1999).
- [121] F. Aryasetiawan and O. Gunnarsson, *Rep. Prog. Phys.* **61**, 237 (1998).
- [122] B. Farid, in *Electron correlation in the solid state*, edited by N. H. March (Imperial College Press, London, 1995).
- [123] V. M. Galitskii and A. B. Migdal, *Sov. Phys. - JETP* **7**, 96 (1958).
- [124] H. Lehmann, *Nuovo Cimento* **11**, 342 (1954).
- [125] G. C. Wick, *Phys. Rev.* **80**, 268 (1950).
- [126] J. Schwinger, *Proc. Nat. Accad. Sci.* **37**, 452 (1951).
- [127] L. Hedin, *Phys. Rev.* **139**, A796 (1965).
- [128] W. Nelson, P. Bokes, P. Rinke, and R. W. Godby, *Phys. Rev. A* **75**, 032505 (2007).
- [129] G. Strinati, H. J. Mattausch, and W. Hanke, *Phys. Rev. B* **25**, 2867 (1982).
- [130] M. S. Hybertsen and S. G. Louie, *Phys. Rev. Lett.* **55**, 1418 (1985).
- [131] M. S. Hybertsen and S. G. Louie, *Phys. Rev. B* **34**, 5390 (1986).
- [132] R. W. Godby, M. Schlüter, and L. J. Sham, *Phys. Rev. B* **37**, 10159 (1988).
- [133] R. Del Sole, L. Reining, and R. W. Godby, *Phys. Rev. B* **49**, 8024 (1994).
- [134] J.-L. Li, G.-M. Rignanese, E. K. Chang, X. Blase, and S. G. Louie, *Phys. Rev. B* **66**, 035102 (2002).
- [135] J.-L. Li, G.-M. Rignanese, and S. G. Louie, *Phys. Rev. B* **71**, 193102 (2005).
- [136] P. Rinke, A. Qteish, J. Neugebauer, C. Freysold, and M. Scheffler, *New J. Phys.* **7**, 126 (2005).
- [137] A. Qteish, P. Rinke, M. Scheffler, and J. Neugebauer, *Phys. Rev. B* **74**, 245208 (2006).

Bibliography

- [138] F. Fuchs, J. Furthmüller, F. Bechstedt, M. Shishkin, and G. Kresse, cond-mat/0604447.
- [139] M. van Schilfgaarde, T. Kotani, and S. Faleev, Phys. Rev. Lett. **96**, 226402 (2006).
- [140] L. J. Sham and W. Kohn, Phys. Rev. **145**, 561 (1966).
- [141] F. Bruneval, N. Vast, and L. Reining, Phys. Rev. B **74**, 045102 (2006).
- [142] P. C. Martin, *Measurements and correlation functions* (Gordon and Breach, New York, 1968).
- [143] J. Stiebling, Z. Phys. B **31**, 35 (1978).
- [144] V. Olevano and L. Reining, Phys. Rev. Lett. **86**, 5962 (2001).
- [145] R. W. Godby and R. J. Needs, Phys. Rev. Lett. **62**, 1169 (1989).
- [146] W. von der Linden and P. Horsch, Phys. Rev. B **37**, 8351 (1988).
- [147] S. Lebègue, B. Arnaud, M. Alouani, and P. E. Blochl, Phys. Rev. B **67**, 155208 (2003).
- [148] F. Gygi and A. Baldereschi, Phys. Rev. Lett. **62**, 2160 (1989).
- [149] W. Ku and A. G. Eguiluz, Phys. Rev. Lett. **89**, 126401 (2002).
- [150] M. Rohlfing, P. Krüger, and J. Pollmann, Phys. Rev. Lett. **75**, 3489 (1995).
- [151] K. Delaney, P. Garcia-Gonzalez, A. Rubio, P. Rinke, and R. W. Godby, Phys. Rev. Lett. **93**, 249701 (2004).
- [152] C. Friedrich, A. Schindlmayr, S. Blügel, and T. Kotani, Phys. Rev. B **74**, 045104 (2006).
- [153] M. L. Tiago, S. Ismail-Beigi, and S. G. Louie, Phys. Rev. B **69**, 125212 (2004).
- [154] B. Holm and U. von Barth, Phys. Rev. B **57**, 2108 (1998).
- [155] C. Verdozzi, R. W. Godby, and S. Holloway, Phys. Rev. Lett. **74**, 2327 (1995).
- [156] A. Schindlmayr, T. J. Pollehn, and R. W. Godby, Phys. Rev. B **58**, 12684 (1998).
- [157] W.-D. Schöne and A. G. Eguiluz, Phys. Rev. Lett. **81**, 1662 (1998).

- [158] A. Stan, N. E. Dahlen, and R. van Leeuwen, *Europhys. Lett.* **76**, 298 (2006).
- [159] M. Shishkin and G. Kresse, *Phys. Rev. B* **75**, 235102 (2007).
- [160] P. García-González and R. W. Godby, *Phys. Rev. B* **63**, 075112 (2001).
- [161] A. Schindlmayr, P. García-González, and R. W. Godby, *Phys. Rev. B* **64**, 235106 (2001).
- [162] U. von Barth and B. Holm, *Phys. Rev. B* **54**, 8411 (1996).
- [163] E. L. Shirley, *Phys. Rev. B* **54**, 7758 (1996).
- [164] R. T. M. Ummels, P. A. Bobbert, and W. van Haeringen, *Phys. Rev. B* **57**, 11962 (1998).
- [165] M. van Schilfgaarde, T. Kotani, and S. V. Faleev, *Phys. Rev. B* **74**, 245125 (2006).
- [166] M. Marsili, Ph.D. thesis, Università di Roma Tor Vergata, Roma (Italy), 2005.
- [167] T. Kotani, M. van Schilfgaarde, and S. V. Faleev, *cond-mat/0611002*.
- [168] A. N. Chantis, M. van Schilfgaarde, and T. Kotani, *cond-mat/0610528*.
- [169] S. V. Faleev, M. van Schilfgaarde, and T. Kotani, *Phys. Rev. Lett.* **93**, 126406 (2004).
- [170] A. Seidl, A. Görling, P. Vogl, J. A. Majewski, and M. Levy, *Phys. Rev. B* **53**, 3764 (1996).
- [171] Z. Zanolli, F. Fuchs, J. Furthmüller, U. von Barth, and F. Bechstedt, *Phys. Rev. B* **75**, 245121 (2007).
- [172] V. I. Anisimov, F. Aryasetiawan, and A. I. Lichtenstein, *J.Phys.: Condens. Matter* **9**, 767 (1997).
- [173] A. Georges and G. Kotliar, *Phys. Rev. B* **45**, 6479 (1992).
- [174] G. Kotliar, S. Y. Savrasov, K. Haule, V. S. Oudovenko, O. Parcollet, and C. A. Marianetti, *Rev. Mod. Phys.* **78**, 865 (2006).
- [175] V. I. Anisimov, J. Zaanen, and O. K. Andersen, *Phys. Rev. B* **44**, 943 (1991).
- [176] V. I. Anisimov, I. V. Solovyev, M. A. Korotin, M. T. Czyżyk, and G. A. Sawatzky, *Phys. Rev. B* **48**, 16929 (1993).

Bibliography

- [177] A. I. Liechtenstein, V. I. Anisimov, and J. Zaanen, *Phys. Rev. B* **52**, R5467 (1995).
- [178] V. I. Anisimov and O. Gunnarsson, *Phys. Rev. B* **43**, 7570 (1991).
- [179] K. Held, I. A. Nekrasov, G. Keller, V. Eyert, N. Blümer, A. K. McMahhan, R. T. Scalettar, T. Pruschke, V. I. Anisimov, and D. Vollhardt, *Phys. St. Sol. (b)* **243**, 2599 (2006).
- [180] F. Aryasetiawan, K. Karlsson, O. Jepsen, and U. Schönberger, *Phys. Rev. B* **74**, 125106 (2006).
- [181] M. Springer and F. Aryasetiawan, *Phys. Rev. B* **57**, 4364 (1998).
- [182] F. Aryasetiawan, M. Imada, A. Georges, G. Kotliar, S. Biermann, and A. I. Lichtenstein, *Phys. Rev. B* **70**, 195104 (2004).
- [183] T. J. Pollehn, A. Schindlmayr, and R. W. Godby, *J. Phys.: Condens. Matter* **10**, 1273 (1998).
- [184] G. Baym and L. P. Kadanoff, *Phys. Rev.* **124**, 287 (1961).
- [185] M. Springer, F. Aryasetiawan, and K. Karlsson, *Phys. Rev. Lett.* **80**, 2389 (1998).
- [186] P. W. Anderson, *Phys. Rev.* **124**, 41 (1961).
- [187] A. Georges, G. Kotliar, W. Krauth, and M. J. Rozenberg, *Rev. Mod. Phys.* **68**, 13 (1996).
- [188] G. Kotliar and D. Vollhardt, *Phys. Today* **57**, (3) 53 (2004).
- [189] W. Metzner and D. Vollhardt, *Phys. Rev. Lett.* **62**, 324 (1989).
- [190] E. Müller-Hartmann, *Z. Phys. B* **74**, 507 (1989).
- [191] V. I. Anisimov, A. I. Poteryaev, M. A. Korotin, A. O. Anokhin, and G. Kotliar, *J. Phys.: Condens. Matter* **9**, 7359 (1997).
- [192] A. I. Lichtenstein and M. I. Katsnelson, *Phys. Rev. B* **57**, 6884 (1998).
- [193] F. Lechermann, A. Georges, A. Poteryaev, S. Biermann, M. Posternak, A. Yamasaki, and O. K. Andersen, *Phys. Rev. B* **74**, 125120 (2006).
- [194] L. V. Pourovskii, B. Amadon, S. Biermann, and A. Georges, *cond-mat/0705.2161*.
- [195] G. Kotliar, S. Y. Savrasov, G. Pálsson, and G. Biroli, *Phys. Rev. Lett.* **87**, 186401 (2001).

- [196] T. Maier, M. Jarrell, T. Pruschke, and M. H. Hettler, *Rev. Mod. Phys.* **77**, 1027 (2005).
- [197] S. Y. Savrasov and G. Kotliar, *Phys. Rev. B* **69**, 245101 (2004).
- [198] J. M. Luttinger and J. C. Ward, *Phys. Rev.* **118**, 1417 (1960).
- [199] G. Baym, *Phys. Rev.* **127**, 1391 (1962).
- [200] U. von Barth, N. E. Dahlen, R. van Leeuwen, and G. Stefanucci, *Phys. Rev. B* **72**, 235109 (2005).
- [201] A. Klein, *Phys. Rev.* **121**, 950 (1961).
- [202] R. Chitra and G. Kotliar, *Phys. Rev. B* **62**, 12715 (2000).
- [203] R. Chitra and G. Kotliar, *Phys. Rev. B* **63**, 115110 (2001).
- [204] S. Biermann, F. Aryasetiawan, and A. Georges, *Phys. Rev. Lett.* **90**, 086402 (2003).
- [205] S. Biermann, F. Aryasetiawan, and A. Georges, cond-mat/0401653.
- [206] P. Sun and G. Kotliar, *Phys. Rev. Lett.* **92**, 196402 (2004).
- [207] S. Botti, A. Schindlmayr, R. Del Sole, and L. Reining, *Rep. Progr. Phys.* **70**, 357 (2007).
- [208] J. Berger, Ph.D. thesis, Rijksuniversiteit Groningen, Groningen (The Netherlands), 2006.
- [209] P. Romaniello, Ph.D. thesis, Rijksuniversiteit Groningen, Groningen (The Netherlands), 2006.
- [210] R. Kubo, *J. Phys. Soc. Japan* **12**, 570 (1957).
- [211] H. Kramers, *Atti Cong. Intern. Fisica*, (Transactions of Volta Centenary Congress) Como **2**, 545 (1927).
- [212] R. Kronig, *J. Opt. Soc. Am.* **12**, 547 (1926).
- [213] R. Del Sole and E. Fiorino, *Phys. Rev. B* **29**, 4631 (1984).
- [214] H. Ehrenreich, in *The Optical Properties of Solids: Proceedings of the International School of Physics "Enrico Fermi"*, edited by J. Tauc (Academic Press, New York, 1966).
- [215] S. L. Adler, *Phys. Rev.* **126**, 413 (1962).
- [216] N. Wiser, *Phys. Rev.* **129**, 62 (1963).

Bibliography

- [217] A. G. Marinopoulos, L. Reining, V. Olevano, A. Rubio, T. Pichler, X. Liu, M. Knupfer, and J. Fink, Phys. Rev. Lett. **89**, 076402 (2002).
- [218] A. G. Marinopoulos, L. Reining, A. Rubio, and N. Vast, Phys. Rev. Lett. **91**, 046402 (2003).
- [219] M. Gatti and G. Onida, Phys. Rev. B **72**, 045442 (2005).
- [220] S. Baroni and R. Resta, Phys. Rev. B **33**, 7017 (1986).
- [221] F. Aryasetiawan, O. Gunnarsson, M. Knupfer, and J. Fink, Phys. Rev. B **50**, 7311 (1994).
- [222] F. Sottile, F. Bruneval, A. G. Marinopoulos, L. K. Dash, S. Botti, V. Olevano, N. Vast, A. Rubio, and L. Reining, Int. J. Quant. Chem. **102**, 684 (2005).
- [223] E. E. Salpeter and H. A. Bethe, Phys. Rev. **84**, 1232 (1951).
- [224] W. Hanke and L. J. Sham, Phys. Rev. B **21**, 4656 (1980).
- [225] W. Hanke and L. J. Sham, Phys. Rev. B **12**, 4501 (1975).
- [226] A. Marini and R. Del Sole, Phys. Rev. Lett. **91**, 176402 (2003).
- [227] F. Bechstedt, K. Tenelsen, B. Adolph, and R. Del Sole, Phys. Rev. Lett. **78**, 1528 (1997).
- [228] G. Onida, L. Reining, R. W. Godby, R. Del Sole, and W. Andreoni, Phys. Rev. Lett. **75**, 818 (1995).
- [229] S. Albrecht, G. Onida, and L. Reining, Phys. Rev. B **55**, 10278 (1997).
- [230] S. Albrecht, L. Reining, R. Del Sole, and G. Onida, Phys. Rev. Lett. **80**, 4510 (1998).
- [231] L. X. Benedict, E. L. Shirley, and R. B. Bohn, Phys. Rev. Lett. **80**, 4514 (1998).
- [232] M. Rohlfing and S. G. Louie, Phys. Rev. Lett. **80**, 3320 (1998).
- [233] F. Bruneval, N. Vast, L. Reining, M. Izquierdo, F. Sirotti, and N. Barrett, Phys. Rev. Lett. **97**, 267601 (2006).
- [234] G. Strinati, Phys. Rev. Lett. **49**, 1519 (1982).
- [235] R. Haydock, Comput. Phys. Comm. **20**, 11 (1980).
- [236] F. Sottile, M. Marsili, V. Olevano, and L. Reining, cond-mat/0705.3140, (accepted in Phys. Rev. B (R)).

- [237] M. Rohlfing, M. Palumbo, G. Onida, and R. Del Sole, Phys. Rev. Lett. **85**, 5440 (2000).
- [238] M. Bruno, M. Palumbo, A. Marini, R. D. Sole, and S. Ossicini, Phys. Rev. Lett. **98**, 036807 (2007).
- [239] E. Runge and E. K. U. Gross, Phys. Rev. Lett. **52**, 997 (1984).
- [240] R. van Leeuwen, N. E. Dahlen, G. Stefanucci, C.-O. Almbladh, and U. von Barth, in *Time-dependent density functional theory*, edited by M. A. L. Marques, C. A. Ullrich, F. Nogueira, A. Rubio, K. Burke, and E. K. U. Gross (Springer, Heidelberg, 2006).
- [241] R. van Leeuwen, Phys. Rev. Lett. **80**, 1280 (1998).
- [242] R. van Leeuwen, Phys. Rev. Lett. **82**, 3863 (1999).
- [243] A. Zangwill and P. Soven, Phys. Rev. Lett. **45**, 204 (1980).
- [244] E. K. U. Gross and W. Kohn, Phys. Rev. Lett. **55**, 2850 (1985).
- [245] M. A. L. Marques, A. Castro, and A. Rubio, J. Chem. Phys. **115**, 3006 (2001).
- [246] N. Vast, L. Reining, V. Olevano, P. Schattschneider, and B. Jouffrey, Phys. Rev. Lett. **88**, 037601 (2002).
- [247] H.-C. Weissker, J. Serrano, S. Huotari, F. Bruneval, F. Sottile, G. Monaco, M. Krisch, V. Olevano, and L. Reining, Phys. Rev. Lett. **97**, 237602 (2006).
- [248] L. Reining, V. Olevano, A. Rubio, and G. Onida, Phys. Rev. Lett. **88**, 066404 (2002).
- [249] F. Sottile, V. Olevano, and L. Reining, Phys. Rev. Lett. **91**, 056402 (2003).
- [250] G. Adragna, R. Del Sole, and A. Marini, Phys. Rev. B **68**, 165108 (2003).
- [251] G. Adragna, Ph.D. thesis, Università di Roma Tor Vergata, Roma (Italy), 2002.
- [252] A. Marini, R. Del Sole, and A. Rubio, Phys. Rev. Lett. **91**, 256402 (2003).
- [253] F. Bruneval, F. Sottile, V. Olevano, R. D. Sole, and L. Reining, Phys. Rev. Lett. **94**, 186402 (2005).

Bibliography

- [254] R. Stubner, I. V. Tokatly, and O. Pankratov, Phys. Rev. B **70**, 245119 (2004).
- [255] I. V. Tokatly and O. Pankratov, Phys. Rev. Lett. **86**, 2078 (2001).
- [256] I. V. Tokatly, R. Stubner, and O. Pankratov, Phys. Rev. B **65**, 113107 (2002).
- [257] O. Pulci, A. Marini, M. Palummo, and R. Del Sole, (2007), (unpublished).
- [258] D. Varsano, Ph.D. thesis, UPV-EHU, San Sebastian (Spain), 2006.
- [259] N. T. Maitra, I. Souza, and K. Burke, Phys. Rev. B **68**, 045109 (2003).
- [260] S. K. Ghosh and A. K. Dhara, Phys. Rev. A **38**, 1149 (1988).
- [261] R. van Leeuwen, in *The Fundamentals of Electron Density, Density Matrix and Density Functional Theory in Atoms, Molecules and the Solid State*, edited by N. Gidopoulos and S. Wilson (Kluwer, Dordrecht, 2003).
- [262] R. van Leeuwen, in *Progress in Nonequilibrium Green's Functions II*, edited by M. Bonitz and D. Semkat (World Scientific, Singapore, 2003).
- [263] M. van Faassen, Ph.D. thesis, Rijksuniversiteit Groningen, Groningen (The Netherlands), 2005.
- [264] G. Vignale, Phys. Rev. B **70**, 201102 (2004).
- [265] G. Vignale and W. Kohn, Phys. Rev. Lett. **77**, 2037 (1996).
- [266] G. Vignale, C. A. Ullrich, and S. Conti, Phys. Rev. Lett. **79**, 4878 (1997).
- [267] M. van Faassen, P. L. de Boeij, R. van Leeuwen, J. A. Berger, and J. G. Snijders, Phys. Rev. Lett. **88**, 186401 (2002).
- [268] P. Romaniello and P. L. de Boeij, Phys. Rev. B **71**, 155108 (2005).
- [269] J. A. Berger, P. L. de Boeij, and R. van Leeuwen, Phys. Rev. B **75**, 035116 (2007).
- [270] C. A. Ullrich and K. Burke, J. Chem. Phys. **121**, 28 (2004).
- [271] V. Eyert, Ann. Phys. (Leipzig) **11**, 650 (2002).
- [272] C. N. Berglund and H. J. Guggenheim, Phys. Rev. **185**, 1022 (1969).
- [273] L. A. Ladd and W. Paul, Solid State Comm. **7**, 425 (1969).

- [274] G. I. Petrov, V. V. Yakovlev, and J. A. Squier, *Opt. Lett.* **27**, 655 (2002).
- [275] F. J. Morin, *Phys. Rev. Lett.* **3**, 34 (1959).
- [276] J. M. Gregg and R. M. Bowman, *Appl. Phys. Lett.* **71**, 3649 (1997).
- [277] G. Stefanovich, A. Pergament, and D. Stefanovich, *J. Phys.: Condens. Matter* **12**, 8837 (2000).
- [278] S. Lysenko, V. Vikhnin, F. Fernandez, A. Rua, and H. Liu, *Phys. Rev. B* **75**, 075109 (2007).
- [279] H. Liu, O. Vasquez, V. R. Santiago, L. Diaz, A. J. Rua, and F. E. Fernandez, *J. Elect. Mat.* **34**, 491 (2005).
- [280] M. Dragoman and A. Cismaru, *Appl. Phys. Lett.* **88**, 073503 (2006).
- [281] B.-J. Kim, Y. W. Lee, B.-G. Chae, S. J. Yun, S.-Y. Oh, H.-T. Kim, and Y.-S. Lim, *Appl. Phys. Lett.* **90**, 023515 (2007).
- [282] L. Jiang and W. N. Carr, *J. Micromech. Microeng.* **14**, 833 (2004).
- [283] D. Xiao, K. W. Kim, G. Lazzi, and J. M. Zavada, *J. Appl. Phys.* **99**, 113106 (2006).
- [284] T. Manning, I. Parkin, M. Pemble, D. Sheel, and D. Vernardou, *Chem. Mater.* **16**, 744 (2004).
- [285] A. Zylbersztein and N. F. Mott, *Phys. Rev. B* **11**, 4383 (1975).
- [286] R. M. Wentzcovitch, W. W. Schulz, and P. B. Allen, *Phys. Rev. Lett.* **72**, 3389 (1994).
- [287] *International tables for crystallography*, edited by T. Hahn (Springer, Dordrecht (The Netherlands), 2005), Vol. A.
- [288] D. B. McWhan, M. Marezio, J. P. Remeika, and P. D. Dernier, *Phys. Rev. B* **10**, 490 (1974).
- [289] D. Kucharczyk and T. Niklewski, *J. Appl. Cryst.* **12**, 370 (1979).
- [290] J. Longo and P. Kierkegaard, *Acta Chem. Scand.* **24**, 420 (1970).
- [291] J. B. Goodenough, *J. Sol. St. Chem.* **3**, 490 (1971).
- [292] S. Biermann, A. Poteryaev, A. I. Lichtenstein, and A. Georges, *Phys. Rev. Lett.* **94**, 026404 (2005).

Bibliography

- [293] T. C. Koethe, Z. Hu, M. W. Haverkort, C. Schussler-Langeheine, F. Venturini, N. B. Brookes, O. Tjernberg, W. Reichelt, H. H. Hsieh, H.-J. Lin, C. T. Chen, and L. H. Tjeng, *Phys. Rev. Lett.* **97**, 116402 (2006).
- [294] P. B. Allen, R. M. Wentzcovitch, W. W. Schulz, and P. C. Canfield, *Phys. Rev. B* **48**, 4359 (1993).
- [295] M. M. Qazilbash, K. S. Burch, D. Whisler, D. Shrekenhamer, B. G. Chae, H. T. Kim, and D. N. Basov, *Phys. Rev. B* **74**, 205118 (2006).
- [296] O. Gunnarsson, M. Calandra, and J. E. Han, *Rev. Mod. Phys.* **75**, 1085 (2003).
- [297] M. Marezio, D. B. McWhan, J. P. Remeika, and P. D. Dernier, *Phys. Rev. B* **5**, 2541 (1972).
- [298] J. P. Pouget, H. Launois, T. M. Rice, P. Dernier, A. Gossard, G. Villeneuve, and P. Hagenmuller, *Phys. Rev. B* **10**, 1801 (1974).
- [299] J. P. Pouget, H. Launois, J. P. D'Haenens, P. Merenda, and T. M. Rice, *Phys. Rev. Lett.* **35**, 873 (1975).
- [300] T. M. Rice, H. Launois, and J. P. Pouget, *Phys. Rev. Lett.* **73**, 3042 (1994).
- [301] R. M. Wentzcovitch, W. W. Schulz, and P. B. Allen, *Phys. Rev. Lett.* **73**, 3043 (1994).
- [302] H.-T. Kim, Y. W. Lee, B.-J. Kim, B.-G. Chae, S. J. Yun, K.-Y. Kang, K.-J. Han, K.-J. Yee, and Y.-S. Lim, *Phys. Rev. Lett.* **97**, 266401 (2006).
- [303] A. Cavalleri, T. Dekorsy, H. H. W. Chong, J. C. Kieffer, and R. W. Schoenlein, *Phys. Rev. B* **70**, 161102 (2004).
- [304] A. Cavalleri, M. Rini, H. H. W. Chong, S. Fourmaux, T. E. Glover, P. A. Heimann, J. C. Kieffer, and R. W. Schoenlein, *Phys. Rev. Lett.* **95**, 067405 (2005).
- [305] A. Cavalleri, C. Tóth, C. W. Siders, J. A. Squier, F. Ráksi, P. Forget, and J. C. Kieffer, *Phys. Rev. Lett.* **87**, 237401 (2001).
- [306] D. Maurer, A. Leue, R. Heichele, and V. Müller, *Phys. Rev. B* **60**, 13249 (1999).
- [307] M. Gupta, A. J. Freeman, and D. E. Ellis, *Phys. Rev. B* **16**, 3338 (1977).
- [308] F. Gervais and W. Kress, *Phys. Rev. B* **31**, 4809 (1985).

-
- [309] J. R. Brews, Phys. Rev. B **1**, 2557 (1970).
- [310] H. Terauchi and J. B. Cohen, Phys. Rev. B **17**, 2494 (1978).
- [311] G. I. Petrov, V. V. Yakovlev, and J. Squier, Appl. Phys. Lett. **81**, 1023 (2002).
- [312] R. Srivastava and L. L. Chase, Phys. Rev. Lett. **27**, 727 (1971).
- [313] J. C. Parker, Phys. Rev. B **42**, 3164 (1990).
- [314] M. W. Haverkort, Z. Hu, A. Tanaka, W. Reichelt, S. V. Streltsov, M. A. Korotin, V. I. Anisimov, H. H. Hsieh, H.-J. Lin, C. T. Chen, D. I. Khomskii, and L. H. Tjeng, Phys. Rev. Lett. **95**, 196404 (2005).
- [315] R. Eguchi, M. Taguchi, M. Matsunami, K. Horiba, K. Yamamoto, Y. Ishida, A. Chainani, Y. Takata, M. Yabashi, D. Miwa, Y. Nishino, K. Tamasaku, T. Ishikawa, Y. Senba, H. Ohashi, Y. Muraoka, Z. Hiroi, and S. Shin, cond-mat/0607712.
- [316] K. Okazaki, H. Wadati, A. Fujimori, M. Onoda, Y. Muraoka, and Z. Hiroi, Phys. Rev. B **69**, 165104 (2004).
- [317] R. Zimmermann, R. Claessen, F. Reinert, P. Steiner, and S. Hüfner, J. Phys.: Condens. Matter **10**, 5697 (1998).
- [318] E. Z. Kurmaev, V. M. Cherkashenko, Y. M. Yarmoshenko, S. Bartkowski, A. V. Postnikov, M. Neumann, L.-C. Duda, J. H. Guo, J. Nordgren, V. A. Perelyaev, and W. Reichelt, J. Phys.: Condens. Matter **10**, 4081 (1998).
- [319] S. Shin, S. Suga, M. Taniguchi, M. Fujisawa, H. Kanzaki, A. Fujimori, H. Daimon, Y. Ueda, K. Kosuge, and S. Kachi, Phys. Rev. B **41**, 4993 (1990).
- [320] G. A. Sawatzky and D. Post, Phys. Rev. B **20**, 1546 (1979).
- [321] R. J. Powell, C. N. Berglund, and W. E. Spicer, Phys. Rev. **178**, 1410 (1969).
- [322] E. Goering, M. Schramme, O. Müller, H. Paulin, M. Klemm, M. den-Boer, and S. Horn, Physica B **230-232**, 996 (1997).
- [323] A. Shigemoto, S. Suga, A. Sekiyama, S. Imada, A. Yamasaki, A. Irizawa, S. Kasai, T. Muro, Y. Saitoh, Y. Ueda, and K. Yoshimura, J. of Electron Spectrosc. Relat. Phenom. **144-147**, 837 (2005).
- [324] M. Abbate, F. M. F. de Groot, J. C. Fuggle, Y. J. Ma, C. T. Chen, F. Sette, A. Fujimori, Y. Ueda, and K. Kosuge, Phys. Rev. B **43**, 7263 (1991).

Bibliography

- [325] F. M. F. de Groot, M. Grioni, J. C. Fuggle, J. Ghijsen, G. A. Sawatzky, and H. Petersen, *Phys. Rev. B* **40**, 5715 (1989).
- [326] S. G. Louie, S. Froyen, and M. L. Cohen, *Phys. Rev. B* **26**, 1738 (1982).
- [327] A. Marini, G. Onida, and R. Del Sole, *Phys. Rev. B* **64**, 195125 (2001).
- [328] N. Troullier and J. L. Martins, *Phys. Rev. B* **43**, 1993 (1991).
- [329] L. Kleinman and D. M. Bylander, *Phys. Rev. Lett.* **48**, 1425 (1982).
- [330] M. Fuchs and M. Scheffler, *Comput. Phys. Commun.* **119**, 67 (1999).
- [331] <http://www.fhi-berlin.mpg.de/th/fhi98md/fhi98PP>.
- [332] X. Gonze, R. Stumpf, and M. Scheffler, *Phys. Rev. B* **44**, 8503 (1991).
- [333] L. K. Dash, N. Vast, P. Baranek, M.-C. Cheynet, and L. Reining, *Phys. Rev. B* **70**, 245116 (2004).
- [334] V. Brázdová, M. V. Ganduglia-Pirovano, and J. Sauer, *Phys. Rev. B* **69**, 165420 (2004).
- [335] X. Gonze, G.-M. Rignanese, M. Verstraete, J.-M. Beuken, Y. Pouillon, R. Caracas, F. Jollet, M. Torrent, G. Zerah, M. Mikami, P. Ghosez, M. Veithen, J.-Y. Raty, V. Olevano, F. Bruneval, L. Reining, R. Godby, G. Onida, D. Hamann, and D. Allan, *Zeit. Kristallogr.* **220**, 558 (2005).
- [336] <http://www.abinit.org>.
- [337] S. Kurth, J. P. Perdew, and P. Blaha, *Int. J. Quantum Chem.* **75**, 889 (1999).
- [338] R. Car and M. Parrinello, *Phys. Rev. Lett.* **55**, 2471 (1985).
- [339] M. Fuchs, M. Bockstedte, E. Pehlke, and M. Scheffler, *Phys. Rev. B* **57**, 2134 (1998).
- [340] A. Continenza, S. Massidda, and M. Posternak, *Phys. Rev. B* **60**, 15699 (1999).
- [341] H. J. F. Jansen and A. J. Freeman, *Phys. Rev. B* **30**, 561 (1984).
- [342] A. Marini, G. Onida, and R. Del Sole, *Phys. Rev. Lett.* **88**, 016403 (2001).
- [343] H. Abe, M. Terauchi, M. Tanaka, S. Shin, and Y. Ueda, *Jpn. J. Appl. Phys.* **36**, 165 (1997).
- [344] P. Rinke, M. Scheffler, A. Qteish, M. Winkelkemper, D. Bimberg, and J. Neugebauer, *Appl. Phys. Lett.* **89**, 161919 (2006).

- [345] A. Liebsch, H. Ishida, and G. Bihlmayer, *Phys. Rev. B* **71**, 085109 (2005).
- [346] X. Huang, W. Yang, and U. Eckern, *cond-mat/9808137*.
- [347] M. A. Korotin, N. A. Skorikov, and V. I. Anisimov, *Phys. Met. Metallography* **94**, 17 (2002).
- [348] F. Aryasetiawan and O. Gunnarsson, *Phys. Rev. Lett.* **74**, 3221 (1995).
- [349] P. van Gelderen, P. A. Bobbert, P. J. Kelly, and G. Brocks, *Phys. Rev. Lett.* **85**, 2989 (2000).
- [350] J. M. Tomczak and S. Biermann, *J. Phys: Condens. Matter* **19**, 365206 (2007).
- [351] J. M. Tomczak, F. Aryasetiawan, and S. Biermann, *cond-mat/0704.0902*.
- [352] M. S. Laad, L. Craco, and E. Müller-Hartmann, *Europhys. Lett.* **69**, 984 (2005).
- [353] M. S. Laad, L. Craco, and E. Müller-Hartmann, *Phys. Rev. B* **73**, 195120 (2006).
- [354] A. L. Ankudinov, B. Ravel, J. J. Rehr, and S. D. Conradson, *Phys. Rev. B* **58**, 7565 (1998).
- [355] E. L. Shirley, *Phys. Rev. Lett.* **80**, 794 (1998).
- [356] A. L. Ankudinov, Y. Takimoto, and J. J. Rehr, *Phys. Rev. B* **71**, 165110 (2005).
- [357] A. Scherz, E. K. U. Gross, H. Appel, C. Sorg, K. Baberschke, H. Wende, and K. Burke, *Phys. Rev. Lett.* **95**, 253006 (2005).
- [358] <http://www.dp-code.org>.
- [359] L. Dash, F. Bruneval, V. Trinité, N. Vast, and L. Reining, *Computat. Mater. Sci.* **38**, 482 (2007).
- [360] A. Bianconi, S. Stizza, and R. Bernardini, *Phys. Rev. B* **24**, 4406 (1981).
- [361] B. I. Lundqvist, *Phys. Kondens. Materie* **6**, 193 (1967).
- [362] B. I. Lundqvist, *Phys. Kondens. Materie* **6**, 206 (1967).
- [363] D. C. Langreth, *Phys. Rev. B* **1**, 471 (1970).
- [364] L. J. Sham, *Phys. Rev. B* **32**, 3876 (1985).

Bibliography

- [365] R. van Leeuwen, Phys. Rev. Lett. **76**, 3610 (1996).
- [366] M. E. Casida, Phys. Rev. A **51**, 2005 (1995).
- [367] R. W. Godby, M. Schlüter, and L. J. Sham, Phys. Rev. Lett. **56**, 2415 (1986).
- [368] Y. M. Niquet, M. Fuchs, and X. Gonze, J. Chem. Phys. **118**, 9504 (2003).
- [369] A. G. Eguiluz, M. Heinrichsmeier, A. Fleszar, and W. Hanke, Phys. Rev. Lett. **68**, 1359 (1992).
- [370] W. E. Pickett and C. S. Wang, Phys. Rev. B **30**, 4719 (1984).
- [371] I. V. Tokatly, private communication.
- [372] G. A. Baraff and M. Schlüter, Phys. Rev. B **30**, 3460 (1984).
- [373] J. Callaway, Phys. Rev. **116**, 1368 (1959).
- [374] R. Mattuck, *A Guide to Feynman Diagrams in the Many-body Problem* (McGraw-Hill, London, 1967).
- [375] F. Bruneval, F. Sottile, V. Olevano, and L. Reining, J. of Chem. Phys. **124**, 144113 (2006).
- [376] Y.-H. Kim and A. Görling, Phys. Rev. Lett. **89**, 096402 (2002).
- [377] W. Kohn, Rev. Mod. Phys. **71**, 1253 (1999).
- [378] P. C. Martin and J. Schwinger, Phys. Rev. **115**, 1342 (1959).
- [379] R. van Leeuwen and N. E. Dahlen, in *The Electron Liquid Model in Condensed Matter Physics*, edited by G. Giuliani and G. Vignale (IOS Press, Amsterdam, 2004).
- [380] J. Guy and A. Salès, *Integral equations in everyday practice* (Lavoisier, Paris, 1991).
- [381] J. Bak and D. J. Newman, *Complex analysis* (Springer, Berlin, 1997).
- [382] Y. M. Poluektov, Russ. Phys. J. **46**, 1229 (2004).

List of Figures

1.1	Mass-abundance distribution of carbon clusters with the number of carbon atoms.	3
1.2	Pair-correlation function $\bar{g}(\mathbf{r}, \mathbf{r}')$ and exchange-correlation hole $\rho_{xc}(\mathbf{r}, \mathbf{r}')$ in bulk silicon.	7
1.3	Si $2p$ and Si $2s$ photoemission spectra of the Si(111)7x7 surface. Plasmon satellites.	11
1.4	Schematic representation of an ARPES experiment.	13
1.5	One-particle excitation spectrum. Independent particles vs. quasiparticles.	20
1.6	Photoemission spectra of different metallic d^1 compounds.	24
2.1	Exchange-correlation hole in bulk silicon. LDA vs. Monte-carlo calculation.	35
3.1	Hedin's pentagon.	48
3.2	Band gaps in perturbative GW. Comparison with experiment.	51
3.3	Comparison between the Lehmann representation and the quasiparticle pole representation.	53
3.4	Path of the contour integration for $\Sigma_c(\omega)$	55
3.5	Band gaps in the QPscGW scheme. Comparison with experiment.	59
3.6	Real part of the screened potential $W_p(\tau)$ in aluminum.	60
3.7	Flowchart of self-consistent COHSEX calculations.	65
4.1	DOS in the Hubbard model for for different U/W values. DMFT results.	75
4.2	Self-consistent scheme of the LDA+DMFT method.	77
4.3	Definition of the "on-site" G_{loc} in real space.	80
5.1	Absorption spectrum of bulk silicon. BSE and many-body TDDFT kernel.	101
6.1	Atomic structures of rutile and monoclinic VO_2	106
6.2	Structural distortion in the phase transition.	107

List of Figures

6.3	Band scheme of VO ₂ in the molecular orbital picture.	109
6.4	PES of both phases of VO ₂	112
6.5	XES of monoclinic VO ₂	114
6.6	XAS (V L _{2,3} and O K edges) of both phases of VO ₂	115
6.7	All-electron LDA radial wavefunctions in the vanadium atom.	119
6.8	Kohn-Sham eigenvalues for monoclinic VO ₂ . Effect of the pseudopotentials at given lattice structure.	122
6.9	Kohn-Sham eigenvalues for monoclinic VO ₂ . Effect of the pseudopotentials through the lattice structure.	122
6.10	LDA band structures for both phases.	126
6.11	LDA O 2 <i>p</i> and V 3 <i>d</i> DOS for both phases.	127
6.12	LDA vs. perturbative G ₀ W ₀ band structures.	129
6.13	G ₀ W ₀ . Perturbative corrections vs. diagonalization of the full GW Hamiltonian.	130
6.14	G ₀ W ₀ . Plasmon pole vs. contour deformation frequency integration.	131
6.15	G ₀ W ₀ . Effect of scissor operator in <i>W</i>	133
6.16	LDA vs. self-consistent COHSEX band structures. COHSEX+GW band structure.	135
6.17	Perturbative GW vs. self-consistent COHSEX band structures for the rutile phase.	136
6.18	Fully consistent COHSEX vs. energy-only COHSEX band structures.	137
6.19	LDA vs. COHSEX O 2 <i>p</i> and V 3 <i>d</i> DOS.	138
6.20	Projections of the COHSEX wavefunctions over the LDA ones.	139
6.21	LDA top-valence and bottom-conduction wavefunctions and their variation with respect to the COHSEX ones.	140
6.22	LDA vs. Hartree-Fock DOS.	142
6.23	Experimental PES vs. DOS for both phases.	144
6.24	Experimental XAS vs. O <i>p</i> DOS for both phases.	147
6.25	EELS for monoclinic VO ₂ . Effect of the pseudopotentials.	149
6.26	Real and imaginary parts of ϵ . Effect of the pseudopotentials.	151
6.27	EELS for monoclinic VO ₂ . Different approximations.	152
6.28	Experimental integrated loss function vs. TDLDA for both phases of VO ₂	153
6.29	Experimental loss function.	154
6.30	Calculated EELS. The metallic phase has a plasmon peak at around 1.5 eV.	155
7.1	Scissor model. Exact solutions.	169
7.2	Scissor model. Exact vs. solutions from linearization of the generalized Sham-Schlüter equation.	170
7.3	Scissor model. Exact vs. first-order solutions of the linearized generalized Sham-Schlüter equation.	171

7.4	Scissor model. Similarity of G and \tilde{G}_{SF}	173
7.5	HEG. Transformation of nonlocal statically screened exchange self-energies into frequency-dependent local potentials $V_{SF}(\omega)$	175
7.6	HEG. Solution of the linearized generalized Sham-Schlüter equation for V_{SF} corresponding to a Fock self-energy.	177
7.7	Comparison between the absorption kernel f_{abs} and the full many-body kernel for bulk silicon and solid argon.	185

Notations and units

I provide here a list of abbreviations and symbols used, with the reference to the pages where they are defined

Acronym	Definition	Pag.
PES	Photoemission spectroscopy/spectrum	7
ARPES	Angular-resolved photoemission spectroscopy/spectrum ...	12
EELS	Electron energy-loss spectroscopy/spectrum	14
Abs	Absorption	13
DOS	Density of states	11
MBPT	Many-body perturbation theory	41
HF	Hartree-Fock	17
RPA	Random-phase approximation	49
GW	GW approximation	49
G_0W_0	Perturbative (“one-shot”) GW scheme	50
QP	Quasiparticle	52
SEX	Screened-exchange approximation	59
COHSEX	Coulomb-hole and screened-exchange approximation	60
QPscGW	Quasiparticle self-consistent GW approximation	58
BSE	Bethe-Salpeter equation	91
DFT	Density-functional theory	30
KS	Kohn-Sham	32
LDA	Local-density approximation	34
EXX	Exact-exchange approximation	37
OEP	Optimized effective potential method	36
TDDFT	Time-dependent density-functional theory	95
TDCDFT	Time-dependent current-density-functional theory	103
LFE	Local-field effects	88
NLF	Without local-field effects	89
TDLDA	Time-dependent local-density approximation	98
LDA+U	LDA+U method	68
DMFT	Dynamical mean-field theory	72
SDFT	Spectral density-functional theory	79
HEG	Homogeneous electron gas (jellium)	17

Symbol	Definition	Pag.
1	Shorthand notation for $\mathbf{r}_1 t_1$	41
$ N\rangle$ or $\Psi(\mathbf{r}_1, \dots, \mathbf{r}_N)$	Many-body wavefunction	1
$\psi(\mathbf{r})$	Single-particle (Bloch) wavefunction	3
$\varphi(1)$	Kohn-Sham orbital	33
$\phi(\mathbf{r})$	Quasiparticle wavefunction	52
$\rho(1)$	Electronic particle density	5,28,42,160,96
$\gamma(\mathbf{r}, \mathbf{r}')$	One-particle density matrix	28
$\rho_2(\mathbf{r}, \mathbf{r}')$	Pair density	5,28
$D_2(\mathbf{r}_1, \mathbf{r}_2; \mathbf{r}'_1, \mathbf{r}'_2)$	Two-particle density matrix	28
$\rho_{xc}(\mathbf{r}, \mathbf{r}')$	Exchange-correlation hole	5
$\bar{g}(\mathbf{r}, \mathbf{r}')$	Pair-correlation function	6
E	Total electronic energy	1,28
E_0	Ground-state energy	27,28,31,40,43
E_{cut}	Cutoff energy	39
E_{gap}	Band gap	19,34
ϵ_s	Kohn-Sham eigenvalue	33
E_s	Quasiparticle energy	52
Z	Renormalization factor	53
$J_{\mathbf{p}}(\omega)$	Photocurrent	9
$\alpha(\omega)$	Absorption coefficient	13
$n = n_1 + in_2$	Refractive index	13
$\epsilon_M = \epsilon_1 + i\epsilon_2$	Macroscopic dielectric function	14
$\epsilon_2^{(T)}(\mathbf{q}, \omega)$	Imaginary part of the transversal dielectric function	14
$\epsilon_2^{(L)}(\mathbf{q}, \omega)$	Imaginary part of the longitudinal dielectric function	15
$L(\omega)$	Loss function	14

Symbol	Definition	Pag.
$v(\mathbf{r}_1 - \mathbf{r}_2)$	Coulomb interaction	1
$\bar{v}(\mathbf{r}_1 - \mathbf{r}_2)$	v without the macroscopic component	89
$h_0(1)$	One-particle term of the Hamiltonian	45
$\Sigma(1, 2)$	Self-energy	46
$V_{ext}(1)$	External potential	1
$V_{per}(1)$	External perturbing potential	45
$V_{tot}(1)$	Total classical potential	49
$V_H(1)$	Hartree potential	17
$V_x(\mathbf{r}, \mathbf{r}')$ or $\Sigma_x(\mathbf{r}, \mathbf{r}')$	Fock exchange potential/self-energy	17,47
$\Sigma_c(1, 2)$	Correlation part of the self-energy	54
$W(1, 2)$	Screened potential	48
$W_p(1, 2)$	Polarization potential	60
$V_{KS}(1)$	Kohn-Sham potential	32
$V_{xc}(1)$	Exchange-correlation potential	32
Δ	Discontinuity of V_{xc}	34
$V_{SF}(\mathbf{r}, \omega)$	Photoemission potential (effective potential for $A(\mathbf{r}, \mathbf{r}, \omega)$)	165
$\tilde{V}_{SF}(\mathbf{r}, \omega)$	Effective potential for $G(\mathbf{r}, \mathbf{r}, \omega)$	167
$V_{SDFT}(1, 2)$	SDFT effective potential	79
$\hat{\psi}(1)$	Field operator in the Heisenberg picture	41
$\hat{\psi}(\mathbf{r})$	Field operator in the Schrödinger picture	193
$\hat{U}(t, t')$	Time-evolution operator	195
$G(1, 2)$	Green's function	41
$G^R(1, 2)$	Retarded Green's function	42
$G^A(1, 2)$	Advanced Green's function	42
$G_2(1, 2, 3, 4)$	Two-particle Green's function	194
$A(\mathbf{r}_1, \mathbf{r}_2, \omega)$	Spectral function	10,44
$f_s(\mathbf{r})$	Lehmann amplitude	43
$\Phi(\mathbf{r}, z)$	Right eigenfunction associated to G	52
$\tilde{\Phi}(\mathbf{r}, z)$	Left eigenfunction associated to G	52
$G_H(1, 2)$	Hartree Green's function	46
$G_{KS}(1, 2)$	Kohn-Sham Green's function	160
$G_{SF}(1, 2)$	Green's function associated to V_{SF}	165
$\xi(\mathbf{r}, \omega)$	Eigenfunction associated to G_{SF}	166
$\tilde{G}_{SF}(1, 2)$	Green's function associated to \tilde{V}_{SF}	167
$G_{SDFT}(1, 2)$	SDFT Green's function	79

Symbol	Definition	Pag.
$\tilde{\Gamma}(1, 2, 3)$	Reducible vertex	47
$\Gamma(1, 2, 3)$	Irreducible vertex	49
$\epsilon(1, 2)$	Microscopic dielectric function	48
$\chi(12)$	Reducible polarizability	198
$P(1, 2)$	Irreducible polarizability	49
$P_0(1, 2)$	Irreducible RPA polarizability	49
$L(1, 2, 3, 4)$	Two-particle correlation function	90
$\tilde{L}(1, 2, 3, 4)$	Irreducible two-particle correlation function	100
$L_0(1, 2, 3, 4)$	Independent-particle two-particle correlation function	91
$\chi_{KS}(1, 2)$	Kohn-Sham polarizability	97
${}^4P(1, 2, 3, 4)$	Four-point TDDFT irreducible polarizability	101
$\mathbf{j}(1)$	Paramagnetic density current	85
$\mathbf{J}(1)$	Total density current	85
$\mathbf{A}_{per}(1)$	Perturbing vector potential	85
$\mathbf{A}_{KS}(1)$	Kohn-Sham vector potential	103
$\mathbf{A}_{xc}(1)$	Exchange-correlation vector potential	103
$\mathbf{A}_H(1)$	Hartree vector potential	103
$\chi_{\rho\rho}(1, 2)$	Density-density response function (generally written as $\chi(1, 2)$)	86
$\bar{\chi}(1, 2)$	Modified density-density response function	89
$\overleftrightarrow{\chi}_{\mathbf{j}\mathbf{j}}(1, 2)$	Current-current response function	86
$\overleftarrow{\chi}_{\rho\mathbf{j}}(1, 2)$	Density-current response function	86
$\overleftarrow{\chi}_{\mathbf{j}\rho}(1, 2)$	Current-density response function	86
$\overleftarrow{\chi}_{\mathbf{j}\mathbf{j},KS}(1, 2)$	Kohn-Sham current-current response function	104
$\overrightarrow{P}_{0,\mathbf{j}\rho}(1, 2)$	Independent-particle current-density response function ...	186
$\overrightarrow{P}_{0,\rho\mathbf{j}}(1, 2)$	Independent-particle density-current response function ...	186
$\Xi(1, 2, 3, 4)$	Many-body BSE kernel	91
$f_{xc}(1, 2)$	TDDFT exchange-correlation kernel	97
$f_{xc}^{(1)}(1, 2)$	Quasiparticle correction term of f_{xc}	99
$f_{xc}^{(2)}(1, 2)$	Excitonic term of f_{xc}	99
$\overleftrightarrow{f}_{abs}(\omega)$	Absorption kernel	182
$\overleftrightarrow{f}_{xc}(1, 2)$	TDCDFT tensor exchange-correlation kernel	104
$\overleftarrow{f}_{xc}^{(2)}(1, 2)$	Excitonic term of $\overleftrightarrow{f}_{xc}$	186

Symbol	Definition	Pag.
t	Hopping term	21
U	Hubbard on-site Coulomb parameter	21
J	Exchange interaction parameter	69
$G_{loc}(\omega)$	On-site Green's function	72
$G_{imp}(\omega)$	Impurity-model Green's function	73
$G_{0,imp}(\omega)$	Noninteracting impurity-model Green's function	73
$\Sigma_{imp}(\omega)$	Impurity-model self-energy	73
$\Delta(\omega)$	Hybridization function	74
$\Gamma_{LW}[G]$	Luttinger-Ward functional	78
$\Phi[G]$	Exchange-correlation interaction functional	78
$\Gamma_{DFT}[\rho]$	DFT functional	79
$\Phi_{DFT}[\rho]$	Exchange-correlation interaction DFT functional	79
$\Gamma_{SDFT}[G_{loc}]$	SDFT functional	80
$\Phi_{SDFT}[G_{loc}]$	Exchange-correlation interaction SDFT functional	80
r_s	Wigner-Seitz radius	17
r_c^l	Cutoff radius for atomic radial wavefunction with angular momentum l	40
Ω_c	Unit-cell volume	39
$\Omega_{\mathbf{k}}$	Brillouin-zone volume	39

Units

If not otherwise specified, atomic units are adopted:

$$\hbar = m_e = e^2 = 4\pi\epsilon_0 = 1$$

Name	Atomic unit	SI unit
Length	a_0 (bohr)	5.29×10^{-11} m
Mass	m_e	9.11×10^{-31} Kg
Energy	Ha (hartree)	27.212 eV = 4.36×10^{-18} J
Time	\hbar/Ha	2.42×10^{-17} s

“Woran arbeiten Sie?” wurde Herr K. gefragt.
Herr K. antwortete: “Ich habe viel Mühe,
ich bereite meinen nächsten Irrtum vor”
(Bertolt Brecht, Geschichten vom Herrn Keuner)